

# UNIVERSITY OF LONDON THESIS

Degree PhD Year 2007 Name of Author QURESHI, Uzma

# Host Thin Films Incorporating Nanoparticles

A thesis submitted to the University of London in partial fulfilment of the requirements for the degree of Doctor of Philosophy

**Uzma Qureshi**

University College London

July 2007





ProQuest LLC
789 East Eisenhower Parkway
P.O. Box 1346
Ann Arbor, MI 48106-1346

I Uzma Qureshi, confirm that the work presented in this thesis is my own. Where information has been derived from other sources, I confirm that this has been indicated in the thesis.

## Abstract

The focus of this research project was the investigation of the functional properties of thin films that incorporate a secondary nanoparticulate phase. In particular to assess if the secondary nanoparticulate material enhanced a functional property of the coating on glass. In order to achieve this, new thin film deposition methods were developed, namely use of nanopowder precursors, an aerosol assisted transport technique and an aerosol into atmospheric pressure chemical vapour deposition system.

Aerosol assisted chemical vapour deposition (AACVD) was used to deposit 8 series of thin films on glass. Five different nanoparticles; silver, gold, ceria, tungsten oxide and zinc oxide were tested and shown to successfully deposit thin films incorporating nanoparticles within a host matrix.

Silver nanoparticles were synthesised and doped within a titania film by AACVD. This improved solar control properties. A unique aerosol assisted chemical vapour deposition (AACVD) into atmospheric pressure chemical vapour deposition (APCVD) system was used to deposit films of Au nanoparticles and thin films of gold nanoparticles incorporated within a host titania matrix. Incorporation of high refractive index contrast metal oxide particles within a host film altered the film colour. The key goal was to test the potential of nanopowder forms and transfer the suspended nanopowder via an aerosol to a substrate in order to deposit a thin film. Discrete tungsten oxide nanoparticles or ceria nanoparticles within a titanium dioxide thin film enhanced the self-cleaning and photo-induced super-hydrophilicity. The nanopowder precursor study was extended by deposition of zinc oxide thin films incorporating Au nanoparticles and also ZnO films deposited from a ZnO nanopowder precursor. Incorporation of Au nanoparticles within a $VO_2$ host matrix improved the thermochromic response, optical and colour properties. Composite $VO_2/TiO_2$ and Au nanoparticle/$VO_2/TiO_2$ thin films displayed three useful properties; photocatalysis, photo-induced super-hydrophilicity and thermochromism.

# Table of Contents

## Chapter 6: Cerium Dioxide, Cerium Dioxide – Titanium Dioxide Composite and Cerium Dioxide – Gold Composite Thin Films on Glass Prepared By Aerosol Assisted Chemical Vapour Deposition 144

---

## Table of Figures

## Table of Tables

## Acknowledgements

I thank my supervisor, Professor Ivan Parkin who has guided me for the past three years – his ideas, input and exceptional supervision have enabled me to succeed with this project. This has enabled me to mature and excel to my full potential.

I would like to thank my secondary supervisor Dr Claire Carmalt for additional support and also my industrial supervisor Dr Simon Hurst who has allowed me to make use of many analytical instruments at Pilkington Glass. I was also guided by Drs Chris Blackman, Russel Binions and Geoffrey Hyett who have been a vital source of guidance and help, and also Mr Robert Palgrave who introduced me to the nanoparticle chemistry behind this project. I'd like to thank Drs Russel Binions and Troy Manning for helping me with the mechanical side of CVD and teaching me how to use alan keys and screw drivers! Additional thanks go to Dr Russel Binions for completing all colour analysis and Swanepoel methods to determine film thickness.

In addition I am also very grateful for the help given by Mr Dave Knap, Mr Jo Nolan, and Roy in solving all my CVD related problems.

I would also like to thank Pilkington Glass for both supplying the glass substrates, chemicals and funding for this project.

The love and support of my parents and family has enabled me to complete this project, and I cannot thank them enough.

Dr Jemma Bhoday has always inspired me and brought out my tenacious side – thank you for supporting me. Specials thanks go to Dr Cindy Lin, Caroline Ward, Dr Amee Ramesh and Ifat Shah.

And last but not least all those in the Materials research laboratory, for their company and friendship.

# Host Thin Films Incorporating Nanoparticles

## Chapter 1: Introduction and Literature Review

### 1.1 Introduction to This Thesis

This thesis details the investigation of the functional properties of thin films that incorporate a secondary nanoparticulate phase. The aim of this work was to assess the potential of nanoparticulates when incorporated into thin films on glass. In particular to see if the secondary nanoparticulate phase has the ability to enhance photocatalytic efficiency, solar control properties, colour, durability, conductivity, electrochromic response, thermochromic response, antibacterial properties and hardness.

Firstly, an introduction to how thin films are commonly prepared and an outline of the processes involved in AACVD will be given. A brief description of the basic properties of nanoparticles and their potential applications will be followed by examples of thin films with nanoparticles incorporated into a host matrix. A summary of the results of previous workers will be given with which to compare the results obtained in the experimental sections of this report.

The experimental sections will consist of examining the production of pure nanoparticulate thin films and thin films that incorporate a secondary nanoparticulate phase.

### 1.2 Methods of Preparing Thin Films on Glass

#### 1.2.1 Film Deposition

There are many ways in which films can be deposited on different substrate types and the film deposited depends on the reaction conditions such as the substrate, precursors, the thermal energy and transport method. More importantly, the reaction kinetics of the

process need to be considered. Films can be epitaxial, polycrystalline or amorphous. The main forms of film growth reported in this thesis were by CVD and sol-gel synthesis. We shall now briefly discuss sol-gel and PVD methods to deposit thin films, and thereafter analyse in detail aerosol assisted chemical vapour deposition and also atmospheric pressure chemical vapour deposition[1].

## 1.2.2 Sol Gel Methods

There are two types of sol-gel synthesis; dip-coating and spin-coating. Solutions of metal alkoxides[2] or of the desired precursors are prepared; the precursor is usually dissolved in the parent alcohol to form the sol and the coatings are then formed. It follows that the thin film thickness is dependant upon the number of layers deposited. Most often, the film is then hydrolysed and heated to yield crystalline coatings. The sol-gel methods are multi-stage and in regard to float glass an off-line process.

## 1.2.3 Physical Vapour Deposition

Physical vapour deposition involves energetically removing atoms or molecules from a target in a chamber under reduced pressure conditions typically less than $10^{-3}$ atmospheres[3]. These atoms/molecules/ions can then react with the gases present to form a thin film; this occurs by condensation of the atoms and ionised species. The desired thickness and composition of the thin film can be chosen by tuning the amount of material removed from the target and the amount of reactive gas present in the deposition chamber. Researchers use a number of energy sources/methods to remove atoms from a metal source including laser ablation, RF magnetron sputtering, DC magnetron sputtering and ion beam sputtering. Additional targets can be added to the chamber in order to "dope" into a film or alternatively co-deposit a composite film.

### 1.2.4 Chemical Vapour Deposition

Chemical vapour deposition is effectively the deposition of a thin film via a chemical route[1] using gaseous precursors. There are many types of CVD, namely atmospheric pressure chemical vapour deposition (APCVD), plasma enhanced CVD (PECVD) and aerosol assisted chemical vapour deposition (AACVD). The steps in the CVD process are shown in Figure 1. Growth of thin films occurs in the following basic manner:

Transport of the reactive species to the reaction site.
Gas phase reaction.
Adsorption onto the substrate surface
Nucleation on the substrate surface.
Reaction and desorption of by-products
Film growth.

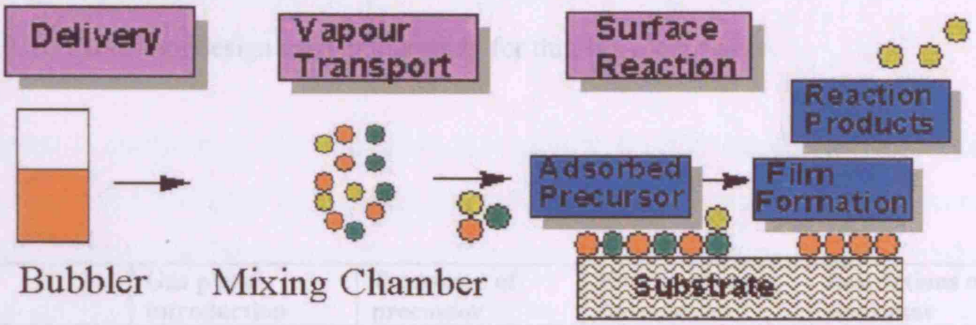


Figure 1. The chemical vapour deposition process steps[4].

In this project, AACVD and a new combined atmospheric pressure/aerosol assisted chemical vapour deposition (AP/AACVD) routes were used. AACVD uses an aerosol to transport the solvated precursor to the reactor chamber[5]. Aerosol assisted CVD is the preferred method since the process and coaters could in principle be incorporated into float-glass production lines. Furthermore, this process allows the use of precursors that

are not so volatile and thermally stable e.g. low melting solids and volatile liquids. This is often the case for nanoparticle based precursors where it is difficult to transport these by other CVD routes. In the AACVD experiment the reaction chamber is at or near atmospheric pressure. A high substrate temperature favours film formation, though each film type needs tailored reactions parameters. Figure 2 shows the design of a typical horizontal bed CVD reactor and Table 1 lists some examples of common CVD techniques and highlights the different methods used to achieve deposition.

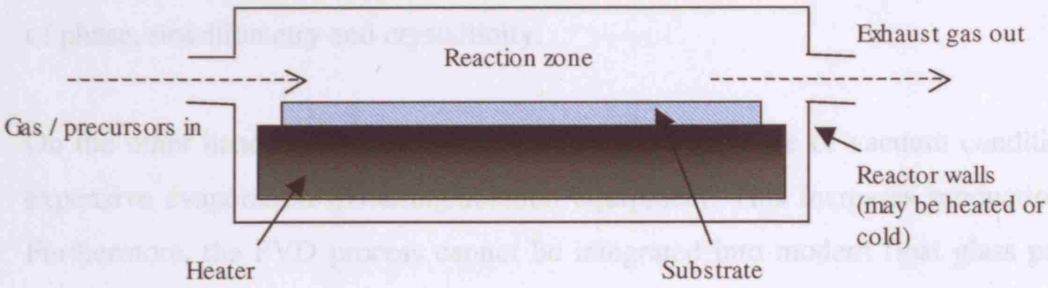


Figure 2. CVD reactor design used in this study for thin film deposition[6].

| Name | Gas phase introduction | Transport of precursor | Energy source for reaction | Restrictions on precursor |
|---|---|---|---|---|
| **Atmospheric pressure CVD** | Heating | Gas flow | Heated substrate | Must be volatile and thermally stable |
| **Low pressure CVD** | Heating at reduced pressure | Vacuum pump | Heated substrate | Must be volatile |
| **Plasma enhanced CVD** | Heating | Gas flow | Electrical discharge | Must be volatile and thermally stable |
| **Aerosol assisted CVD** | Aerosol generation | Gas flow | Heated substrate | Must be soluble |

Table 1. Comparison of CVD techniques.

## 1.2.5 Advantages and Disadvantages of CVD/PVD and Sol-Gel Methods

This thesis concentrates on thin film deposition for window coating applications and so the main disadvantage of the Sol-gel process for applications this project concentrates on is that it is not easily integrated into float-glass productions lines for deposition onto glass windows. This is because a lengthy process is required involving coating the substrate and precursor formation. This is time consuming and often not economical as a large area of glass needs to be coated, often up to 3.5 metres in width[7]. However the Sol-gel process is industrially used due to a number of preferred factors such as control of phase, stoichiometry and crystallinity.

On the other hand, PVD methods require reduced pressure or vacuum conditions and expensive evaporation/sputtering/ablation equipment. This increases production costs. Furthermore, the PVD process cannot be integrated into modern float glass processes due to the slow rate of growth. However a wide range of industrial coatings including sputtered Silver stacks are grown by PVD.

The preferred methods of choice used in this project, namely atmospheric pressure and aerosol assisted CVD give fast growth rates. The process is economical as precursors are readily available, the equipment easily constructed and to reduce costs further, no vacuum atmospheres are needed. The thickness of the film can be easily tailored and the changeover to new precursors for different coating functions is relatively easy. These factors make AACVD and APCVD methods attractive when wishing to prepare coated float-glass[8].

## 1.2.6 Film Growth Mechanisms

There are two mains types of reactions that occur in the CVD reactor and 3 main types of film growth; the main reaction types are vapour phase growth (homogeneous) and vapour-solid interface growth (heterogeneous). There are two main sites that this

growth can occur – either the substrate or the reactor walls. In the research reported in this thesis, a cold-walled reactor is used and growth occurs predominantly on the substrate as the reactor walls are not heated[9].

There are three main ways by which CVD films grow on a substrate, Figure. 3[10]. The Volmer - Weber mechanism (Figure 3a) involves nucleation followed by three dimensional island growth. This mechanism occurs when the films atoms are more strongly bound to each other than to the substrate. The Frank - van der Merve mechanism (Figure 3b) proceeds in a layer-by-layer fashion due to the film atoms being more strongly bound to the substrate than to each other. The Stranski - Kastanov mechanism (Figure 3c) is intermediate to the other two mechanisms, after one or two monolayers further growth is in the form of islands.

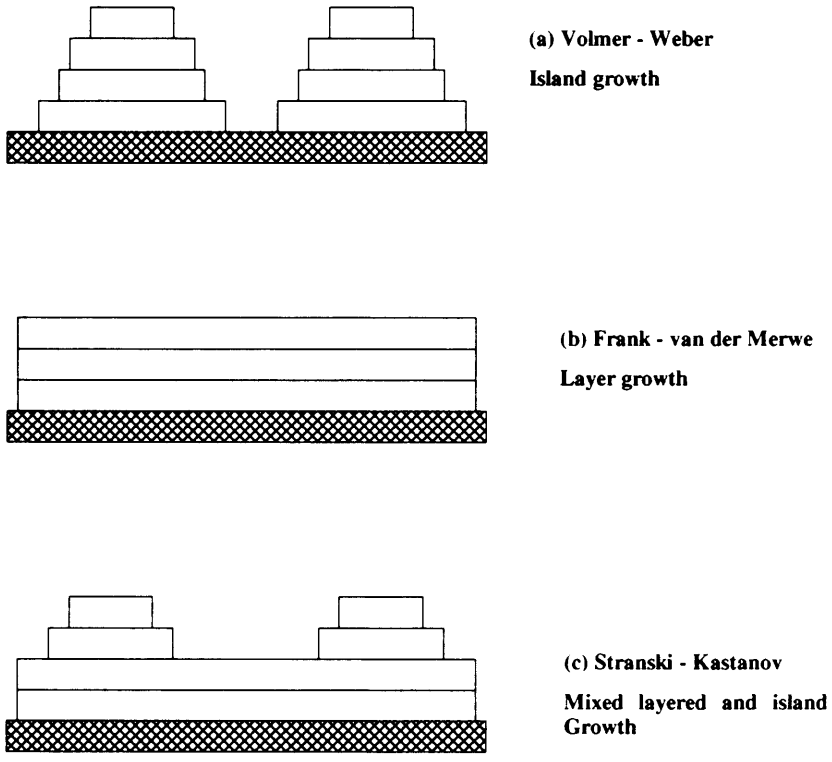


Figure 3. Growth mechanisms for thin films[10].

## 1.2.7 The Rate of Film Growth

Two main factors control the CVD reaction kinetics; these are vapour phase mass transport and surface reaction kinetics[11]. The first, vapour phase mass transport controlled growth is limited by the rate at which reactants can be delivered to the substrate surface. The latter, surface kinetic controlled growth is limited by the rate of reactions at the substrate. The relationship between growth rate and temperature is shown in Figure 4 where at very high temperatures growth rate may even decrease due to the depletion of reactants and/or an increase in the rate of desorption[12].

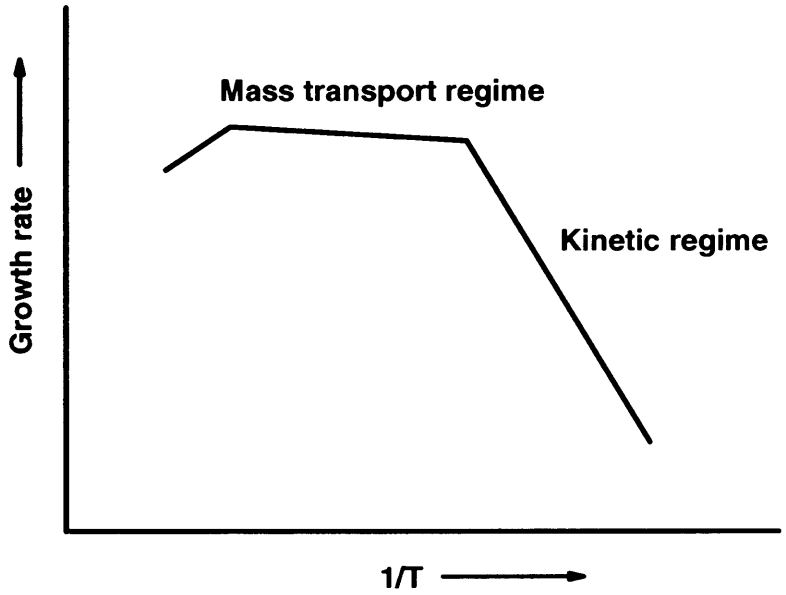


Figure 4. Sketch of the relationship between the film growth rate and substrate temperature in a CVD process.

To reach the substrate surface, the gaseous precursors must come across a boundary layer that may exist due to differences in reaction parameters such as concentration, temperature and velocity of the gaseous precursors (Figure 5)[13]. The continuum flow system occurs when the ratio of the gas mean free path to characteristic reactor dimension (Knudsen number, $K_n$) is less than 1. Upon reaching the substrate, frictional forces cause a decrease in the flow of the gaseous precursors. As the precursors undergo deposition reactions, their concentration profile also decreases. It follows that the temperature of the gas increases due to increasing contact with the hot surface.

These profiles all depend upon how far along the substrate film growth occurs or whether a film forms at all[14]. Another important process to consider is the thermophoretic effect. This is the effect of a temperature gradient on the nanoparticles; where the particles move from a hot surface to a cold one. All these processes contribute to the deposition kinetics for CVD reactions.

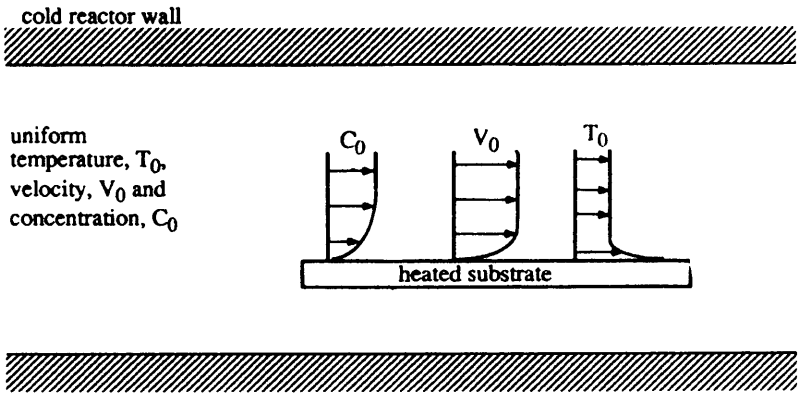


Figure 5. Precursor concentration, gas velocity and temperature profiles for a cold wall, horizontal bed CVD reactor to illustrate boundary layers above the substrate during a CVD reaction[15].

## 1.3 Properties of Nanoparticles

A nanoparticle is classed as a material having at least one dimension that is less than a few hundred nanometres whereas nanotechnology is the manipulation and science that occurs at this scale. In order to visualise just how small this scale is, its best to refer to some examples: A human hair strand is approximately 0.4 mm in width - a nanoparticle is 80,000 smaller than this width and a million times smaller than a full stop. Figure 6 shows some representations of everyday objects such as biological cells compared to the nanoscale[16].

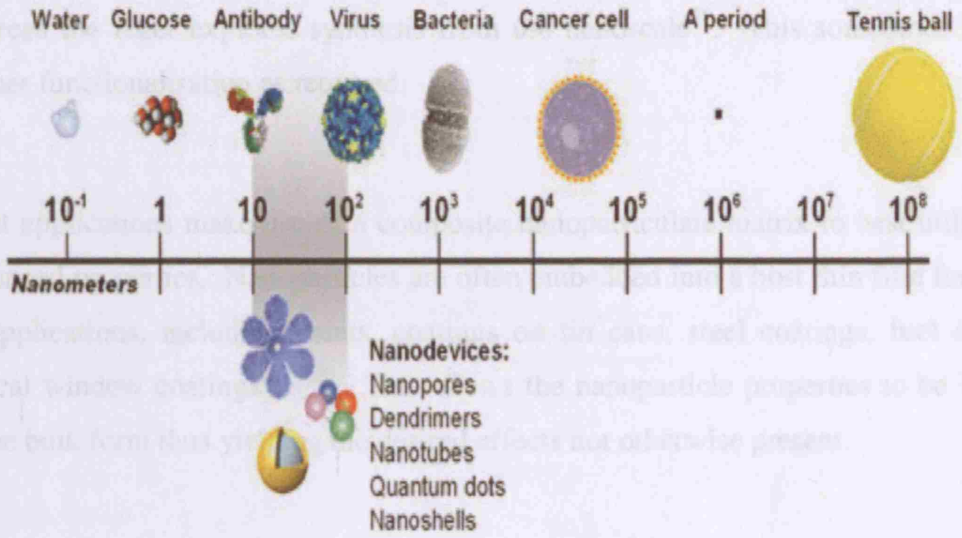


Figure 6. Representation of everday objects at the nanoscale[1].

Nanotechnology has been in rapid development for some time now[17] and researchers have been looking at the enhanced properties and potential applications from this field. Nanoparticles are increasingly being used in industry, some common examples includes the use of silver nanoparticles in socks[18] and underwear to kill bacteria, magnetic nanoparticles to enhance disk storage[19], in paints to tune the reflectivity[20], adhesion, colour[21], steel coatings to enhance corrosion resistance[22] and even components of a microchips- deposition of circuits and components at the nanoscale onto the chip to increase efficiency[23]. Carbon nanotubes, which have a sheet like structure to allow easy flow of electrons are used to increase the conduction of electrons at the nanoscale[24].

A crucial property that must be considered for nanoparticles is the surface area to volume ratio of the materials. A high surface area to volume ratio allows much more exposure of the material and this has applications in catalysis where enhanced efficiency generates more revenue and saves time.

The study of nanoscience is involved in many areas, such as engineering, computing, biology, medicine, materials science, chemistry and physics. There are two main

approaches to this field- a top down and a bottom up approach[25]. The former looks at yielding nanoparticles from the bulk form, e.g. etching and lithography at the nanoscale, whereas the latter explores synthesis from the nanoscale[26]. This sometimes involves further functionalisation as required.

Most applications make use of a composite nanoparticulate matrix to best utilise these enhanced properties. Nanoparticles are often embedded into a host thin film for a range of applications, including paints, coatings on tin cans, steel coatings, fuel cells and optical window coatings[27,28,29]. This allows the nanoparticle properties to be imparted to the bulk form thus yielding the desired effects not otherwise present.

There is still much research to be completed on nanotechnology, and many challenges lie ahead. One of the causes for concern are the long term health impacts of the use of particles at such a small scale- researchers are yet to discover how these nanoparticles affect the body if inhaled through exposure[30].

## 1.4 Quantum Dots

When considering nanoparticle science, it is important to realise that band gaps play an important part. A band gap is the energy space that separates the valence and conduction bands and is unique for each material. The band gap is of a fixed value, but at the nanoscale, quantum confinement occurs[31]. This is when the electronic excitations are able to experience the presence of particle boundaries and respond to particle size change by adjusting their energy level distribution; instead of the continuous spectra seen for bulk materials, discrete atomic like states are seen (Figure 7)[32]. This process is known as the quantum size effect and materials that exhibit this are often referred to as quantum dots.

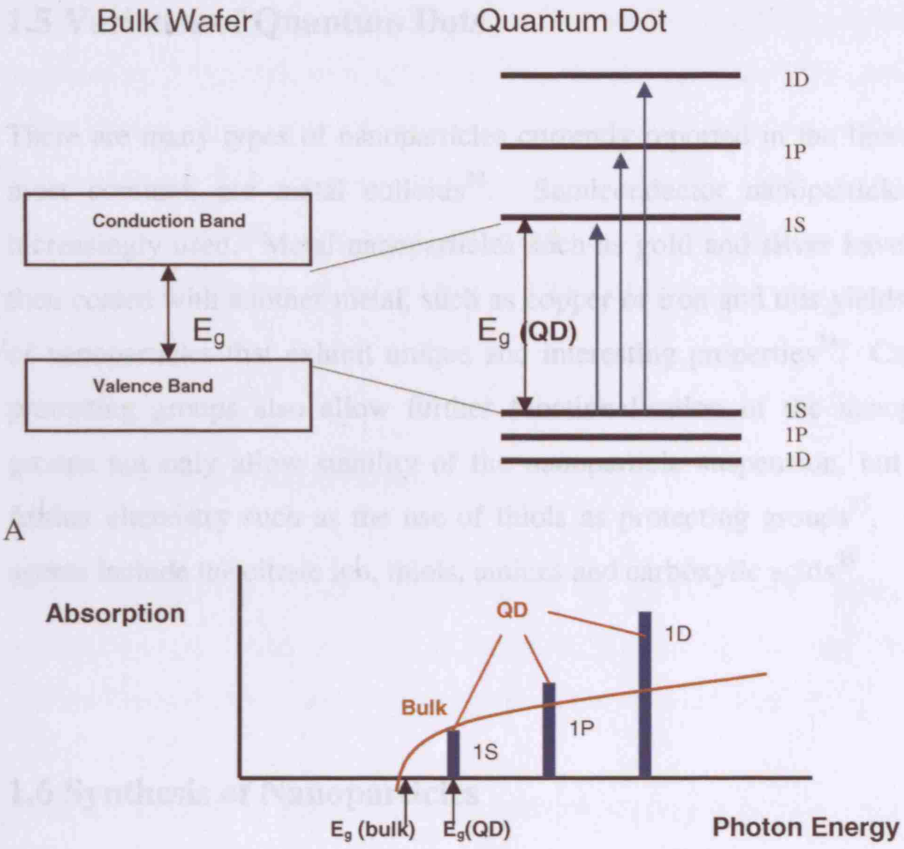


Figure 7 A) Representation of a semiconductor material (bulk form) with continuous conduction and valence bands separated by a fixed energy gap $E_g$, commonly known as the band gap of the material. A quantum dot (QD) has discrete atomic like states that are determined by the QD radius and B) The continuous absorption spectrum of a bulk semiconductor (curved line) as compared to the discrete absorption spectrum of a QD (vertical bars)[32].

The band gap for semiconductor nanoparticles is usually observed with ease, whereas for metallic nanoparticles this is often not the case[32]. This is because the Fermi level spacing for metallic nanoparticles is proportional to the number of electrons in the nanoparticles, and so it follows that if the number of electrons in a nanoparticle is only 1, then the band gap is only observable at very low temperatures[32].

## 1.5 Varieties of Quantum Dots

There are many types of nanoparticles currently reported in the literature. One of the most common are metal colloids[33]. Semiconductor nanoparticles are also being increasingly used. Metal nanoparticles such as gold and silver have been grown, and then coated with another metal, such as copper or iron and this yields alternating shells of nanoparticles that exhibit unique and interesting properties[34]. Capping groups and protecting groups also allow further functionalisation of the nanoparticles- capping groups not only allow stability of the nanoparticle suspension, but can also provide further chemistry such as the use of thiols as protecting groups[35]. Common capping agents include the citrate ion, thiols, amines and carboxylic acids[35].

## 1.6 Synthesis of Nanoparticles

Much work has been completed on the preparation and characterisation of stable dispersions of nanoparticles made of silver, gold and other Noble metals[36]. A variety of synthesis techniques have been used, including the use of a microwave to generate nanoparticle species[37]. Chemical reduction is a routine bench chemistry method, and a very efficient process - a typical experiment generates nanoparticles in 20 minutes. More complex routes are also used, such as reactions involving an inert atmosphere and Schlenk line. More innovative routes include the use of chemical vapour deposition and electroplating techniques to deposit nanoparticles onto a solid substrate[38]. Wolf *et al* have studied this with Au, Pt and Ir embedded in a titania host matrix and the films were deposited by electroplating[39]. Some work has been published on the incorporation of nanoparticles into thin-films by spin-coating[40].

As mentioned in 1.4, surfactants, capping groups and protective groups are commonly employed to impart stability into the system. In solution or suspension, nanoparticles have a tendency to agglomerate or fall out of solution[32]. Here, a balance of attractive and repulsive forces occur- electrostatic repulsion ensures that the nanoparticles are kept apart, whereas the high surface energy favours aggregation. Protecting groups can aid

dispersion by allowing a uniform distribution of the nanoparticles throughout the suspension. The pH, concentration and temperature are also crucial considerations when designing nanoparticle synthesis techniques and it has been proven that lower concentrations and temperatures enhance stability[41]. For example, aqueous gold nanoparticles are stable at room temperatures up to 2 mM for many months whereas titania nanoparticles survive for roughly 12 hours in an organic solvent at 4 °C[42].

## 1.7 Metallic Nanoparticles

Metal nanoparticles were first reported by Faraday, who synthesised red/purple solutions of colloidal gold[43]. Since then, Turkevich has extended this study and researched in detail the mechanisms behind the colloid chemistry[44].

Both semiconductor and metallic nanoparticles have similar absorption peaks as shown by their optical absorption spectra[32]. However, the primary absorption for metal nanoparticles is due to a surface plasmon and not, as with semiconductor particles, due to transitions between quantized energy states[32]. Over a hundred years ago, Mie modelled this plasmon resonance and was able to explain the mechanism by which it worked and how it was tuneable under different conditions[45]. This phenomenon will now be discussed in detail as this thesis explores how a surface plasmon changes under a range of conditions.

### 1.7.1 Surface Plasmon Resonance

A surface plasmon resonance is a visible light absorption caused by oscillation of conduction band electrons at the surface of the particles[46,47]. It can be tuned by the size, composition and shape of the nanoparticle and these changes cause a shift in the wavelength of the absorption.

The surface plasmon resonance band arises from the polarisation of free electrons as a result of an electric field of the incident light. A net charge difference is induced at the nanoparticle surface, the surface charge then works on restoring this balance. Excitation of dipolar oscillations of the electrons then occur (Figure 8)[48]. Dipolar surface plasmon resonance occurs when the particle concerned is smaller than the wavelength of the incoming light and when the frequency of the oscillation is equal to the frequency of the resonant light.

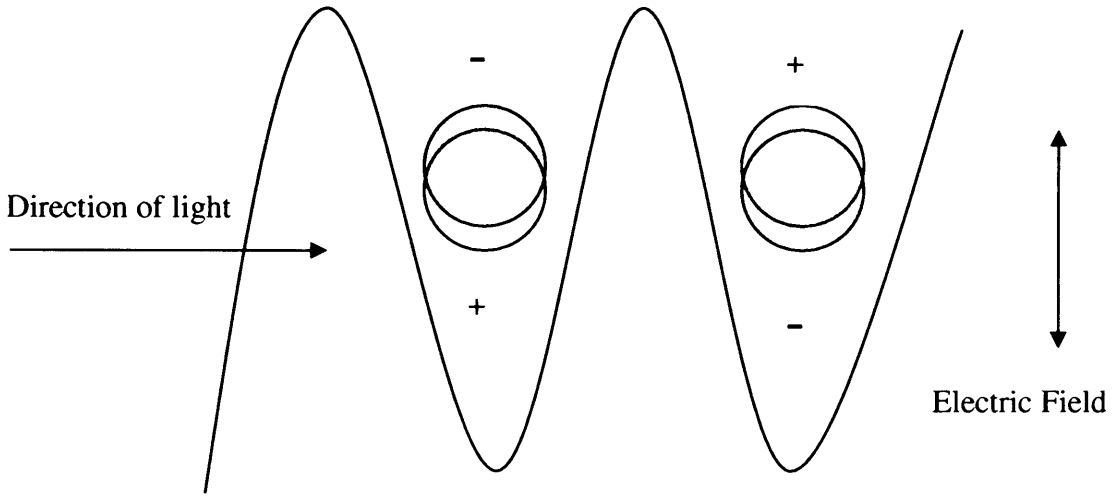


Figure 8. The excitation of a surface plasmon resonance by the electric field of incoming light. The grey area represents surface electron density of the metal nanoparticle.

The few metals that exhibit the phenomenon include silver, gold, copper, titanium and chromium. Out of these metals, gold and silver are more commonly researched and applied. Gold nanoparticles exhibit a surface plasmon resonance band at approximately 500 nm[49]. This band then redshifts with increasing particle size (Figure 9). Silver on the other hand shows a surface plasmon peak at 400 nm[50]. Figure 10A shows the change in the plasmon resonance peak for four different gold-silver alloys. There is a red shift of the plasmon with increasing gold composition (Figure 10B).

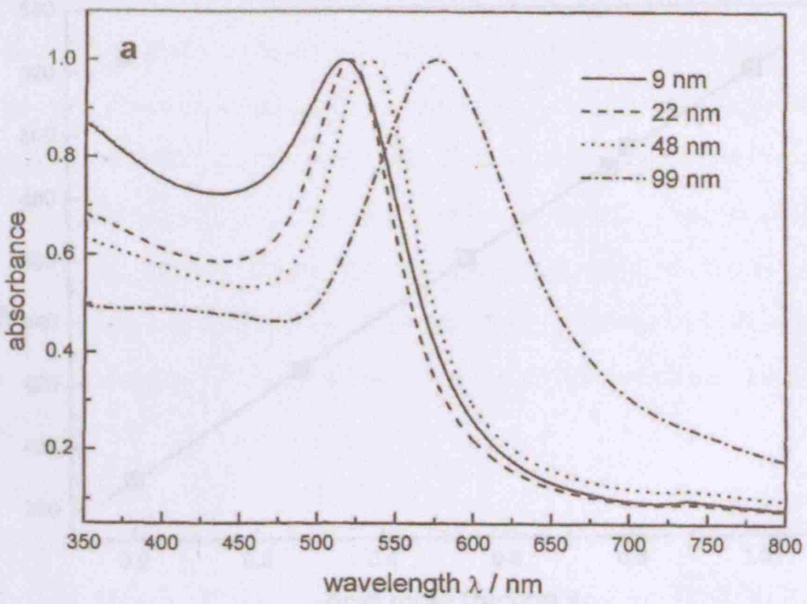


Figure 9. UV absorption spectra of 4 gold nanoparticle suspensions of dimension 9, 22, 48 and 99 nm[32].

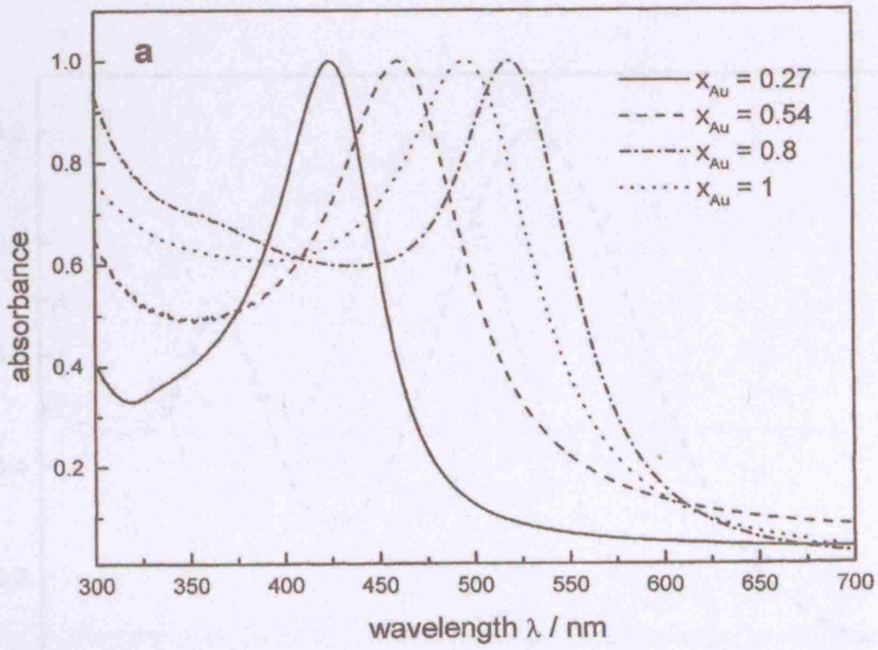


Figure 10A. UV spectra of four colloidal gold-silver alloy nanoparticle solutions (gold mole fraction $x_{Au}$)[32].

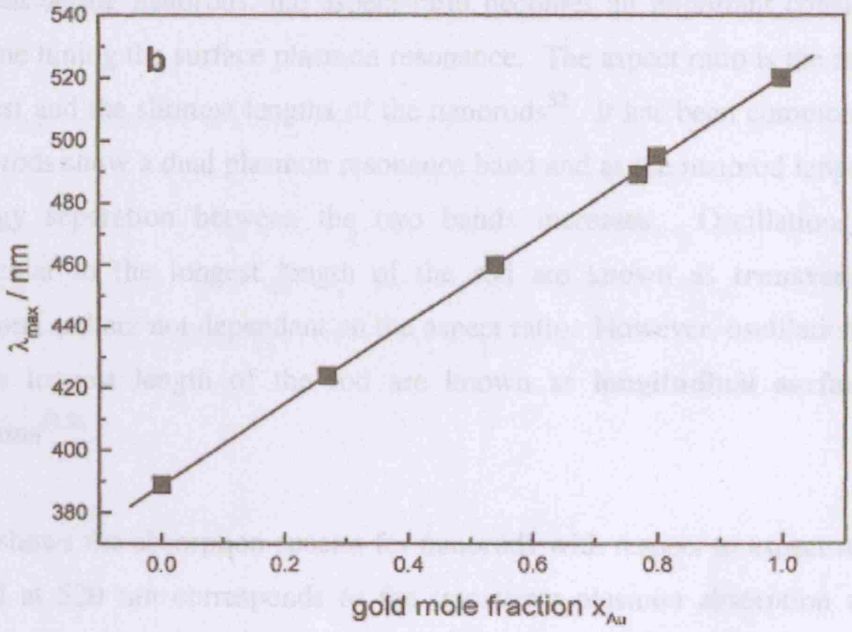


Figure 10B. Plot of the absorption maximum as a function of gold mole fraction[32].

This enables the fine tuning of the surface plasmon resonance between 400 – 500 nm. Changing the nanoparticle shape can extend this range further into the infra-red to a longer wavelength. Elongation in one dimension causes the plasmon resonance to split into 2 bands (Figure 11A)[51].

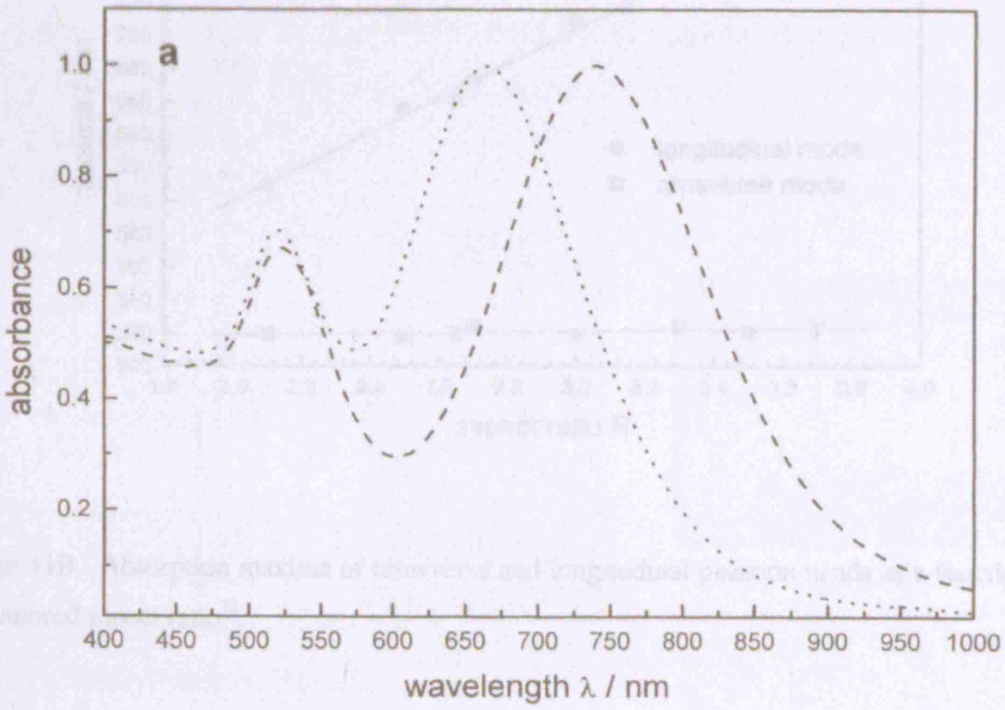


Figure 11A. UV absorption with two plasmon bands for elongated particles[32].

When considering nanorods, the aspect ratio becomes an important consideration for further fine tuning the surface plasmon resonance. The aspect ratio is the ratio between the longest and the shortest lengths of the nanorods[52]. It has been commonly observed that nanorods show a dual plasmon resonance band and as the nanorod length increases, the energy separation between the two bands increases. Oscillations that occur perpendicular to the longest length of the rod are known as **transverse plasmon absorptions** and are not dependant on the aspect ratio. However, oscillations that occur along the longest length of the rod are known as **longitudinal surface plasmon absorptions**[51,52].

Fig 11B shows the absorption spectra for nanorods with respect to aspect ratios. Here, The band at 520 nm corresponds to the transverse plasmon absorption whereas the second red shifted band is for the longitudinal plasmon absorption[32].

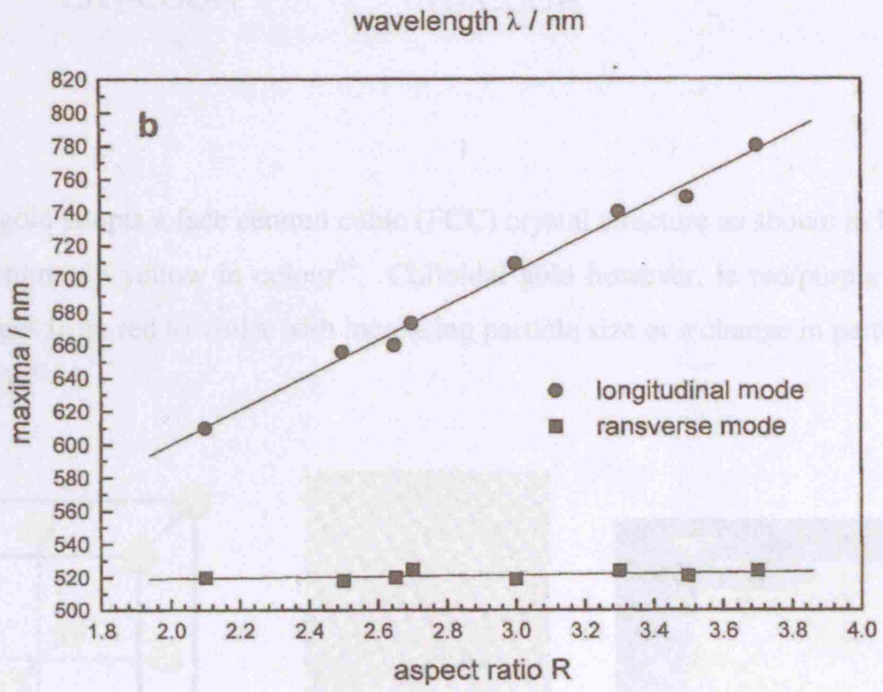


Figure 11B. Absorption maxima of transverse and longitudinal plasmon bands as a function of the nanorod aspect ratio[32].

## 1.7.2 Synthesis of Gold Nanoparticles and Their Thin Film Deposition

The most used synthetic technique to yield gold nanoparticles involves the reduction of auric acid by sodium citrate[53]. Many reactions using this technique have been reported in the literature and the synthesis can be used for other metals such as platinum. The mechanism for this reaction has been studied, and interestingly, an intermediate step is involved prior to the formation of the gold nanoparticles[32].

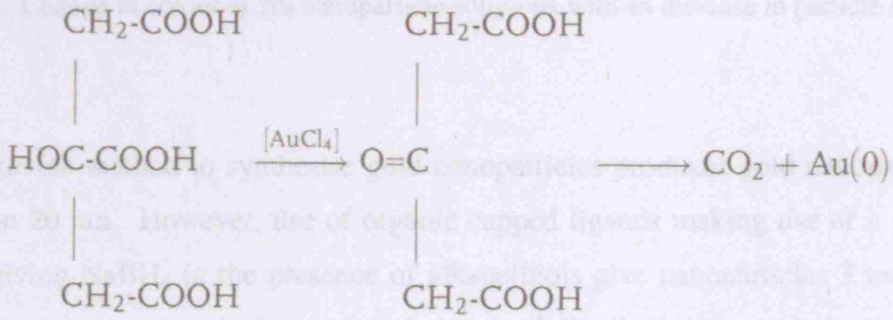


Metallic gold adopts a face centred cubic (FCC) crystal structure as shown in Figure 12, and is commonly yellow in colour[54]. Colloidal gold however, is red/purple in colour and changes from red to violet with increasing particle size or a change in particle shape (Figure 13)[55].

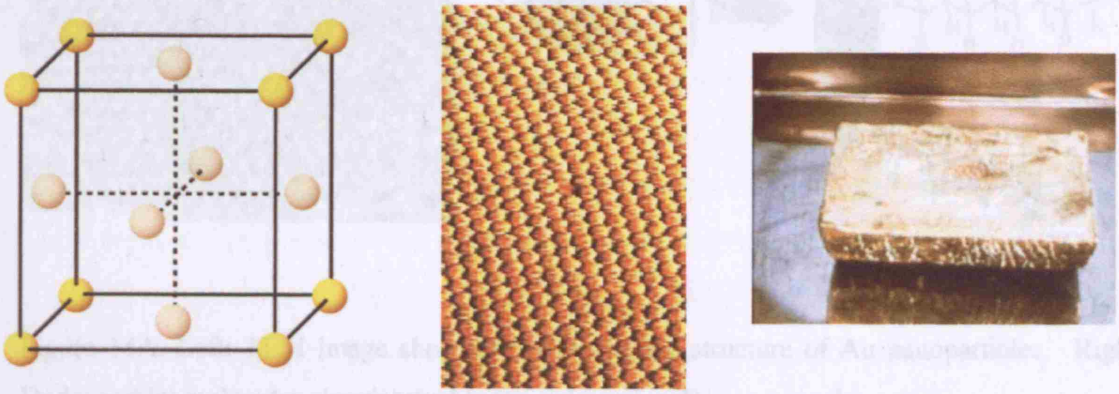

Figure 12. Representations of gold[56].

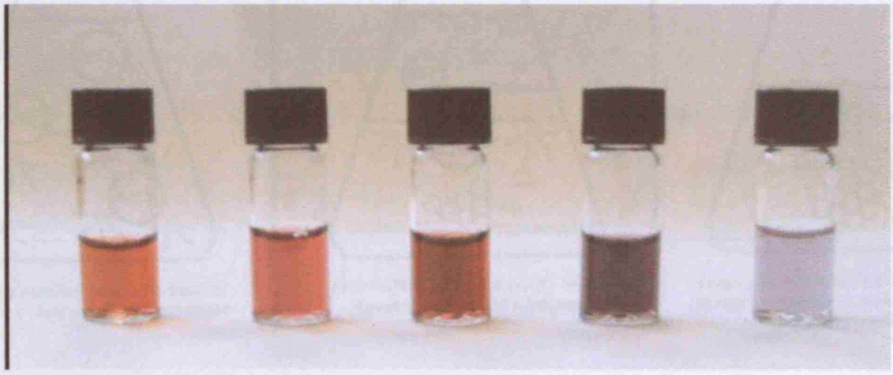

Figure 13. Change in colour of Au nanoparticle solutions with an increase in particle size[57].

The Turkevich method to synthesise gold nanoparticles produces gold nanoparticles of dimension 20 nm. However, use of organic capped ligands making use of a reduction step involving $NaBH_4$ in the presence of alkanethiols give nanoparticles 3 nm in size. This is through the control of nanoparticle size and distribution through the use of thiol capping groups; gold nanoparticles bind strongly to sulfur (Figure 14)[32].

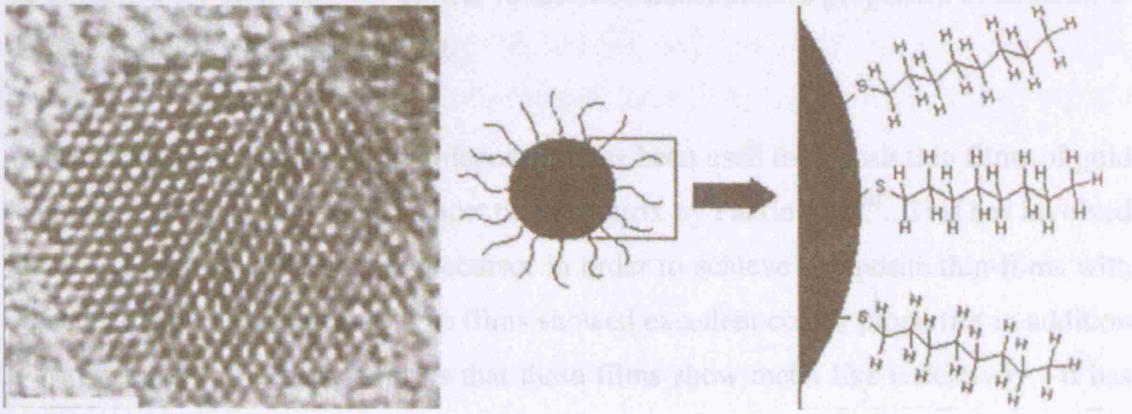

Figure 14A. Left: TEM image showing the crystalline structure of Au nanoparticles. Right: Dodecanthiol molecules chemisorbed to the gold surface[32].

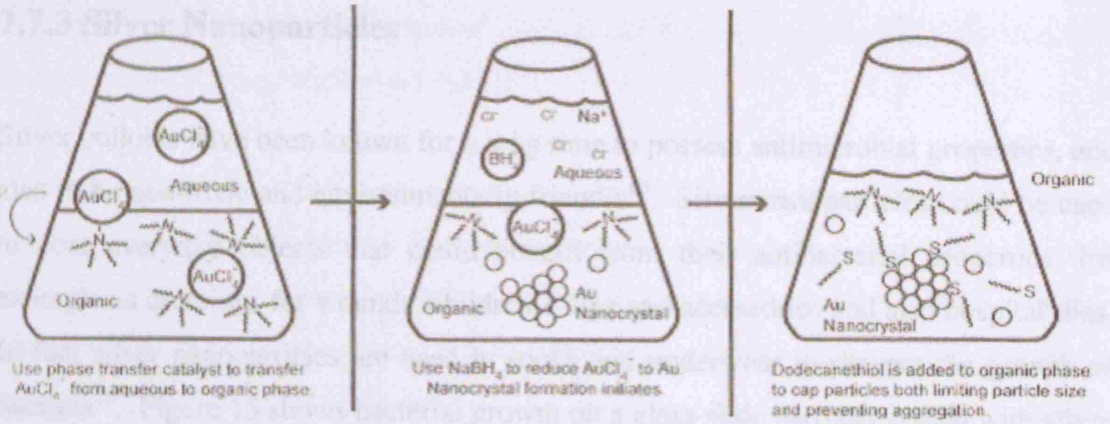


Figure 14B. Gold nanoparticle synthesis using a two phase reduction technique developed by Brust *et al*[32].

Many researchers have reported the deposition of thin films of gold nanoparticles[58]. Many of these techniques have used common capping groups in order to control the size distribution of the gold nanoparticles. Some of these thin films have found applications in catalysis and gas sensing[59]. One of the main advantages of these film types is their high conductivity- the films are non-metallic in nature and retain their nanoparticulate nature upon transfer to the thin film. The enhanced electrical conduction is due to activated electron hopping throughout the lattice[58]. However, these coatings could also be exploited for their superior optical reflectance/transmittance properties in addition to colour for use as a window coating.

Aerosol assisted chemical vapour deposition has been used to deposit thin films of gold nanoparticles embedded within a host titania matrix by Parkin *et al*[60]. This has involved the use of auric acid as a CVD precursor in order to achieve composite thin-films with embedded gold nanoparticles. The films showed excellent colour properties in addition to dichromism. A further point is that these films show metal like reflectivity. It has been proven that a variety of host matrices can be used; Pemble *et al* have used AACVD to deposit gold nanoparticle and zinc oxide thin films[61]. Laser assisted CVD had been used to deposit gold/titania composite films[62]. Besides these reports, there are no other researchers who have completed work with AACVD in order to deposit nanocomposite thin films of gold and titania.

### 1.7.3 Silver Nanoparticles

Silver colloids have been known for a long time to possess antimicrobial properties, and also to be non-toxic and environmentally friendly[63]. Silver nanoparticles could be used to coat everyday objects that could benefit from their antibacterial properties, for example as dressings for wounds, children's toys and accessories and also hospital tiles. In fact silver nanoparticles are used in socks and underwear to prevent the growth of bacteria[18]. Figure 15 shows bacterial growth on a glass-slide partially coated with silver nanoparticles, the coated area does not contain any bacterial growth.

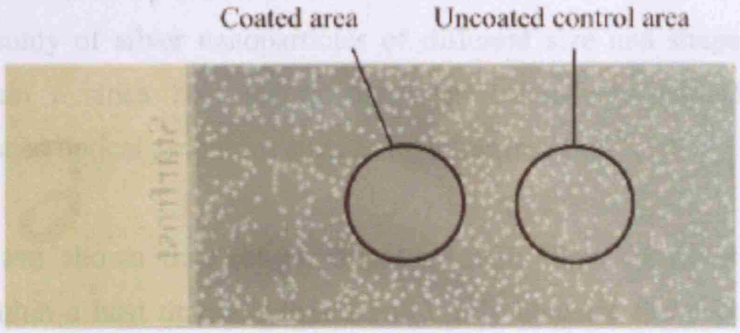


Figure 15. Bacterial growth on a glass slide- the area coated with silver nanoparticles does not grow bacteria[64].

As with gold nanoparticle synthesis techniques, uniform silver nanoparticles can be synthesised via the reduction of a suitable salt, usually $AgNO_3$ or silver acetate and the analogous chemistry developed for gold can be used for silver[65].

Sun and Xia have reported the synthesis of monodisperse silver nanocubes (100 nm) by reduction of silver nitrate with ethylene glycol[66]. Here, ethylene glycol is both a reducing agent and solvent and *poly*(vinylpyrrolidone) is used as a capping agent. They showed that the size of the silver nanocrystals can be controlled by the experimental conditions such as temperature, metal salt concentration, metal/stabiliser ratio, and growth time[67]. Under certain conditions, large quantities of highly symmetric silver nanocubes with size ranging from 50 to 100 nm can be obtained. Recently, highly mono-disperse myristate capped silver nanoparticles have been reported[68]. However,

there are no reports of the transfer of these silver nanoshapes onto glass for thin film formation by chemical vapour deposition[69].

Aerosol assisted chemical vapour deposition (AACVD) has previously been used to deposit metallic silver coatings from silver carboxylates and also silver sulphides from silver thiolates[70]. These silver coatings show useful transmission-reflection properties and sulphide films have potential for use in ion insertion batteries or as lubricants[71]. However, the majority of work on silver nanoparticle thin films has been via the sol-gel process[72].

Thin films of silver nanoparticles have also been found to exhibit a photovoltaic effect[73]. The study of silver nanoparticles of different size and shape combinations embedded within a silica host matrix has been extensively studied- these films displayed enhanced optical properties such as high transmission[74].

Parkin *et al* have shown that sol-gel deposited thin films of silver nanoparticles incorporated within a host titania matrix significantly enhance the photocatalysis and antimicrobial properties of titania[75]. No work has yet been reported on the AACVD of silver nanoparticles and nanoshapes incorporated within a host titania matrix.

## 1.7.4 $Fe_2O_3$ Nanoparticles

Nanoparticles of magnetic metals and oxides have become increasingly popular amongst the scientific community and their unique physical and chemical properties have been widely researched[76]. In particular $Fe_2O_3$ nanoparticles can be used to increase disk space storage and even improve picture quality in magnetic resonance imaging[77].

Many different methods have been reported for $Fe_2O_3$ nanoparticle synthesis ranging from sol-gel reactions to complex redox reactions making use of a Schlenk line[32]. In general, researchers have found that use of various capping groups, surfactants and

intensive reaction steps all under an argon atmosphere allow better control of the end nanoparticle quality, size, composition and monodispersity[32].

Use of Fe(III) acetylacetonate [$Fe(acac)_3$] as a precursor to produce $Fe_2O_3$ nanoparticles is now very common[78]. Alcohol reduction is used along with many capping agents. Sun and Zeng have successfully synthesised $Fe_2O_3$ nanoparticles with high control using a refluxing solvent method (Figure 16)[79].

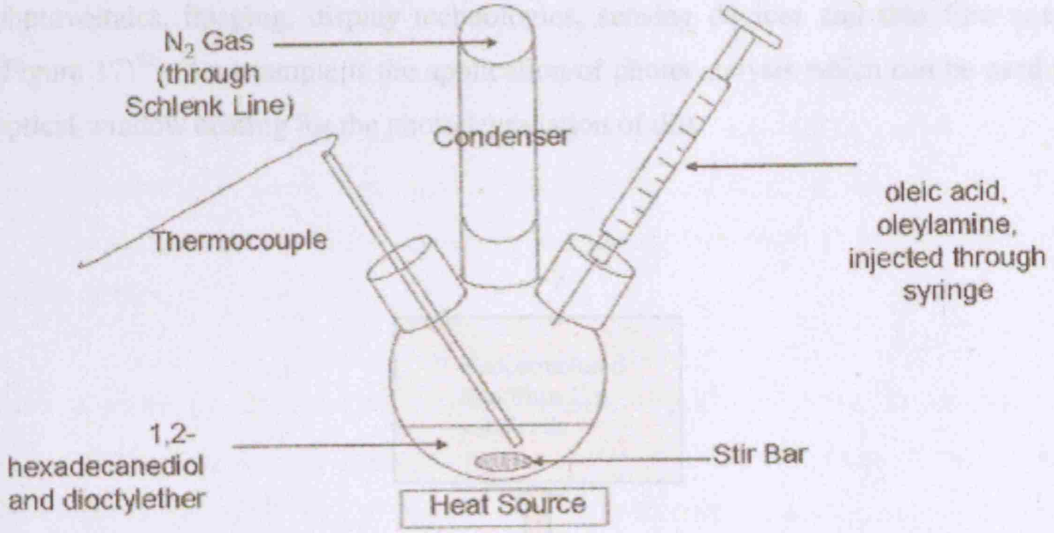


Figure 16. Synthesis of $Fe_2O_3$ nanoparticles through the use of a coordinating solvent at high temperatures[32].

There are no reports to date of any attempt to deposit iron oxide nanoparticles by AACVD or their subsequent incorporation into a titania host matrix. However, the electronic transport and magnetic properties of iron oxide nanoparticles has for a long time been used in thin film devices[77]. The thin films for this purpose are synthesized by sol-gel, magnetron-sputtering, and physical vapour deposition techniques[80]. An aerosol assisted CVD based route to deposit iron nanoparticle thin films would be of great commercial importance due to the enhance conductivity of the reported iron nanoparticle thin films. Furthermore, embedding these iron oxide nanoparticles into a

titania host matrix could also give rise to interesting properties for window coating applications.

## 1.8 Semiconductor Nanoparticles

As with metallic nanoparticles, semiconductor nanomaterials exhibit enhanced properties that scale with size. Semiconductor nanoparticles are important materials industrially and have applications in many everyday items such as electronics, photovoltaics, imaging, display technologies, sensing devices and thin film coatings (Figure 17)[81]. An example is the application of photocatalysis which can be used in an optical window coating for the photodegradation of dirt.

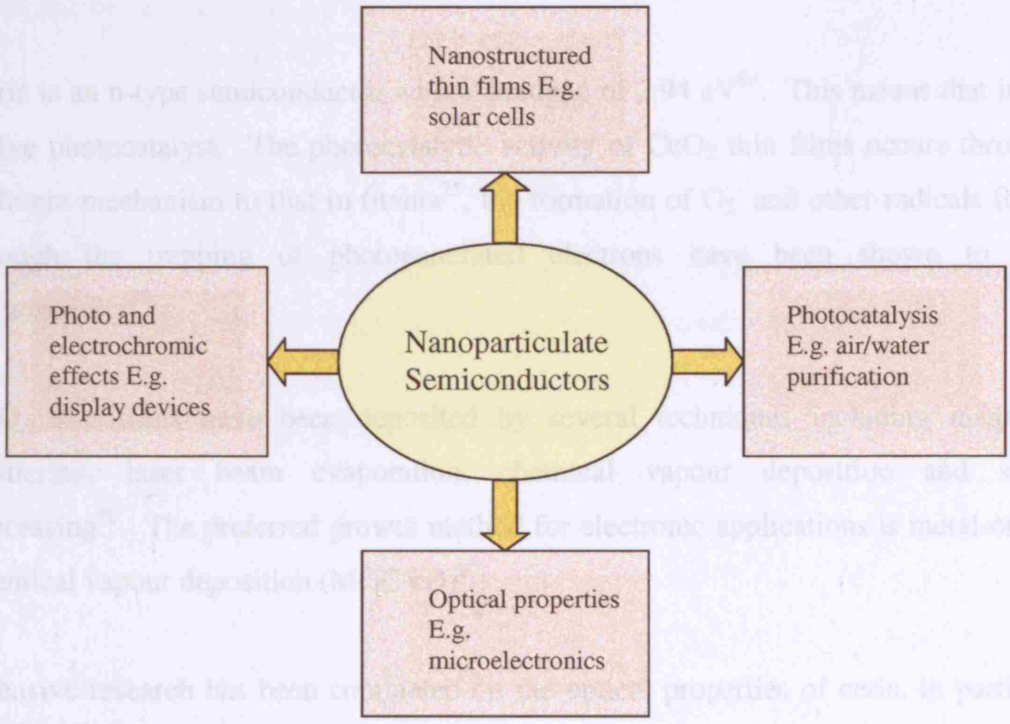


Figure 17. Applications of semiconductor nanoparticles[82].

More importantly, semiconductor nanoparticles, such as $TiO_2$, have tuneable band gaps. Band gaps increase as particle size decreases, so the band edge is "blue shifted". Semiconductor nanopowders are increasingly being applied in fields such as ceramics and powder metallurgy[32].

## 1.8.1 $CeO_2$ Nanoparticles

Cerium oxide (cubic $CeO_2$) is a very promising material for future applications and much work is being completed in exploiting its properties[83]. It has a high refractive index (2.20[84]) and excellent transmission (80 % [85]) in the visible and infrared regions. Furthermore ceria is mechanically stable i.e. adhesive and stable against mechanical abrasion, chemical attack and high temperatures[86]. Another useful property of ceria includes being a dielectric oxide, which has further uses such as in high temperature superconductors[87].

Ceria is an n-type semiconductor with a bandgap of 2.94 eV[88]. This means that it is an active photocatalyst. The photocatalytic activity of $CeO_2$ thin films occurs through a different mechanism to that in titania[75], the formation of $O_2^-$ and other radicals formed through the trapping of photogenerated electrons have been shown to cause photoactivity[89].

$CeO_2$ thin films have been deposited by several techniques including magnetron sputtering, laser beam evaporation, chemical vapour deposition and sol-gel processing[90]. The preferred growth method for electronic applications is metal-organic chemical vapour deposition (MOCVD)[90].

Intensive research has been completed on the optical properties of ceria, in particlular absorbance, reflectance and transmittance. More work has yet to be completed on the influence of nanostructures on properties such as grain boundaries, defects, oxygen vacancies, crystallite size and how these affect the optical properties of the ceria thin films[91].

In particular, researchers are interested in utilising these optical properties for use in electrochromic appliances. Electrochromic materials change their optical properties in response to an electrical signal. Thin films of ceria have been deposited by physical vapour deposition methods in order to aid this study. This process allows films of high quality to be grown. Researchers are currently analysing ceria thin films properties and relating these to the deposition parameters and electrochromic behaviour[92].

A range of other ceria thin films have been deposited, and these include $CeO_2$ thin films deposited on Ni metal[93], on $Al_2O_3$ (1-102) and $TiO_2$ (001) single crystal substrates by MOCVD[94]. Ceria had also been deposited electrochemically on $ZrO_2$ and $Al_2O_3$ thin films formed on stainless steel[95] and sapphire by molecular beam epitaxy[96]. Physical vapour deposition of ceria onto ITO coated glass, Si wafers and fused silica has also produced films of the desired quality[97]. There are no reports on the AACVD of ceria nanoparticles or their subsequent incorporation into a titania host matrix- it would be desirable to deposit ceria/titania composite films that are superior to titania anatase film by an aerosol assisted route.

## 1.8.2 $WO_3$ Nanoparticles

Tungsten trioxide is a yellow powder with a structure consisting of corner sharing $WO_6$ octahedra[98]. Tilting of the $WO_6$ octahedra and displacement of the tungsten atoms away from the centre of the octahedra does occur. Figure 18 shows the tetragonal phase of $WO_3$. In order of increasing temperature, the following crystal phases are observed[99].

| | |
|---|---|
| 0 to 230 K | monoclinic(II) $\varepsilon$-$WO_3$ |
| 230 to 290 K | triclinic $\delta$-$WO_3$ |
| 290 to 600 K | monoclinic(I) $\gamma$-$WO_3$ |
| 600 to 1010 K | orthorhombic $\beta$-$WO_3$ |
| 1010 to 1170 K | tetragonal $\alpha$-$WO_3$ |

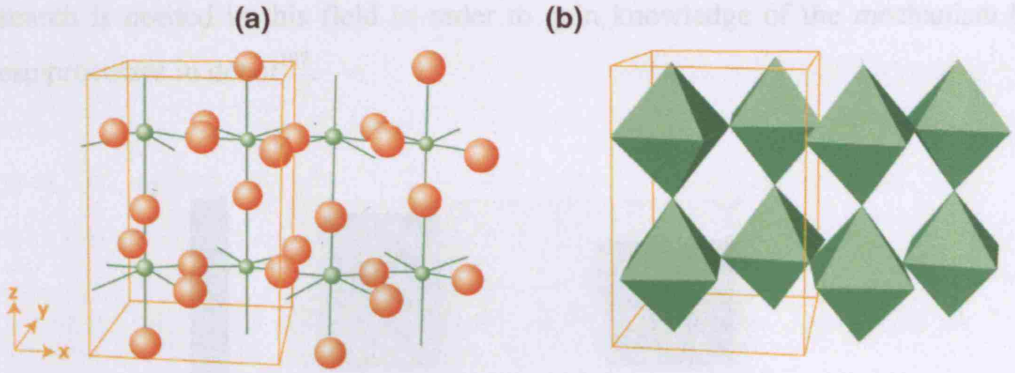


Figure 18. Structure of tetragonal α-$WO_3$. (a) Shows tungsten atoms in green and oxygen atoms in red; (b) depicts the corner-shared $WO_6$ octahedra. The unit cell is highlighted in orange[100].

Shear planes are commonly observed in $WO_3$ due to partial reduction of the structure and oxygen deficiencies[101], which play an important part in the electronic properties exhibited by tungsten oxide.

It has been found that CVD deposited films of $WO_3$ exhibit the monoclinic phase[102]. Monoclinic $WO_3$ has has a bandgap of 2.8 eV, amorphous $WO_3$ has a band gap of 3.3 eV. The most utilised application for tungsten oxide thin films is that of electrochromism[103]. Photochromism is also used and is the reversible change in optical absorption of a material in response to irradiation by light. Photochromism is caused by a series of reduced tungsten phases and a phase change occurs where thin films change from a yellow ($WO_3$) to a blue colour ($WO_{3-x}$). The yellow phase represents stoichiometric $WO_3$ whereas the blue phase is due to a partially reduced phase $WO_{3-x}$. Enhanced conductivity and a broad absorption band at approximately 600-1000 nm is often seen for the blue reduced phase[104].

Researchers have found that CVD prepared $WO_3$ films deposited under a deficiency of oxygen are blue rather than yellow[105] (Figure 19). A valence charge transfer mechanism is responsible for both the blue colour, this is a polaron transition; hopping of electrons between neighbouring metal ions of different oxidation states[106] but further

research is needed in this field in order to gain knowledge of the mechanism behind these processes in detail[107].

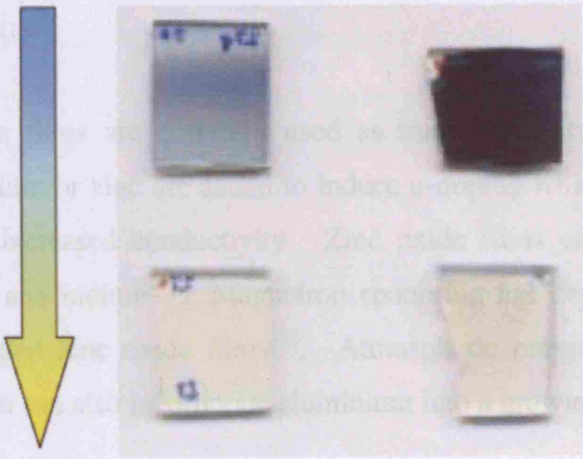

Figure 19. $WO_3$ displays photochromism – the reversible change in optical absorption of a material in response to irradiation by UV light whereby a transition occurs from a yellow "bleached" state to a dark blue "coloured" state[108].

There have been no reports to date on the deposition of tungsten oxide nanoparticle thin films alongside a host matrix by aerosol assisted CVD. Many other thin films processes such as PVD and sol-gel techniques have been used to deposit tungsten oxide composite thin films[109]. Parkin *et al* have shown gold nanoparticles within a host thin film tungsten oxide matrix significantly enhance the photochromism, photocatalysis and optical properties[110].

## 1.8.3 ZnO Nanoparticles

Zinc oxide has a hexagonal wurtzite structure with a wide band gap of 3.3 eV[111]. This means that it has potential to be used in a range of applications such as liquid crystal displays, energy-efficient windows, and solar cell technology[112]. Zinc oxide has been used to grow thin films that are highly transparent (>80 %) and conductive as compared to commercial rivals such as fluorine doped tin oxide films[113]. Furthermore zinc is

relatively inexpensive and readily available. One property of zinc oxide that has been exploited is in solar cells as it is resistant to reduction by a hydrogen-containing plasma[114]. Another crucial property is its ability to remain white when exposed to UV light. To compliment this further, ZnO exhibits the piezoelectric effect and is thermochromic[115].

Zinc oxide thin films are currently used as transparent conducting devices[116]. Here aluminium, indium or zinc are added to induce n-doping which in turn results in oxygen vacancies and increased conductivity. Zinc oxide films can be doped with fluorine, boron, gallium and indium[117]. Magnetron sputtering has deposited aluminum, gallium, and indium doped zinc oxide films[118]. Atmospheric pressure metal-organic chemical vapor deposition can also incorporate aluminium into a growing ZnO film[119].

ZnO layers are mainly deposited by sputter deposition and chemical vapor deposition (CVD)[120]. The latter method allows the growth of a rough layer, which has applications in solar cells as this allows the efficient diffusion of light by scattering. On the other hand, crystalline ZnO films with very smooth surfaces have also been deposited by sputtering (Zhu et al)[121].

Zinc oxide has mild antimicrobial properties[122]. It would be interesting to research these effects in a thin film co-deposited with a silver nanoparticle since ZnO also exhibits photocatalytic acitivity comparable to titania. There are many reports in the literature for zinc oxide nanoparticle synthesis and the synthesis of ZnO nanopowders. Sun *et al* have researched the photoinduced hydrophilicity of both anatase and zinc oxide thin films- they have reported that both give rise to similar contact angle measurements upon irraditiation with UV light[123]. There are no reports on the deposition of ZnO thin films from nanopowder precursors and this warrants further investigation.

## 1.9 Host Matrices – Thin Film Properties

### 1.9.1 Titania (Anatase)

Titania exists in three common forms- anatase, rutile and brookite and all three phases are known to display similar chemical behaviour and physical properties[124]. However, the main difference between the three is their structure. This work has concentrated on the anatase crystal type formed at 400 – 600 °C. Above 915 °C anatase converts to the rutile phase.

Titania anatase, has a structure consisting of octahedra that share four edges hence the four fold axis (Figure 20).

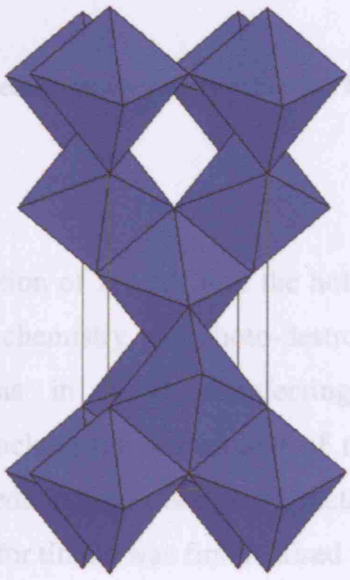

Figure 20. Titania anatase structure[125].

The band gaps for rutile and anatase are 3.06 and 3.23 eV which correspond to UV wavelengths of 405 nm and 385 nm respectively[126]. When $TiO_2$ is irradiated with UV light with energy greater than or equal to its band gap, an electron is excited from the valence band into the conduction band[127]. This leaves a positively charged hole in the valence band. The electron and hole migrate to the surface where they can either

recombine or undergo redox reactions with adsorbed species. This process is known as photocatalysis and is shown in Figure 21.

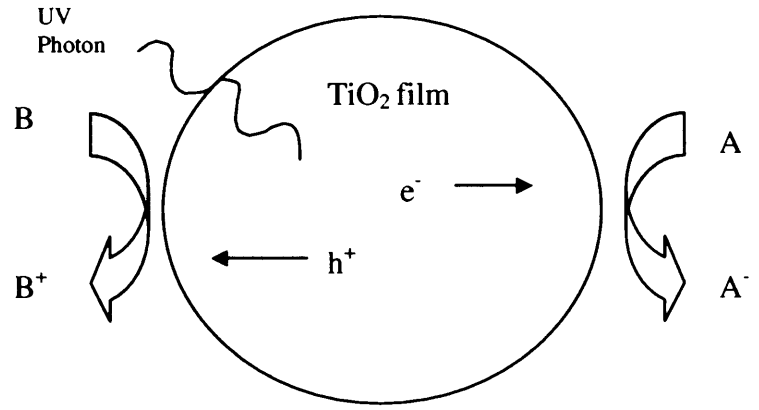


Figure 21. Complex oxidation/reduction chemistry when a $TiO_2$ particle is irradiated with UV light.

The electron causes the reduction of A to $A^-$ and the hole causes the oxidation of B to $B^+$. This oxidation/reduction chemistry will photo-destroy virtually all organic matter. This has found applications in water disinfecting, waste treatment and air purification[128]. Other uses include the destruction of micro-organisms e.g. bacteria, viruses, cancer cells and the reduction of trace heavy metals in industrial waste streams. The photocatalytic behaviour for titania was first realised in 1968 and it has been proven that anatase exhibits the greatest photocatalytic activity[129]. Commercially, photocatalysis relies on sunlight, especially the UV portion (340-285 nm) and harvests less than 1 % solar radiation at the earth's surface[130].

The following reactions occur during this process (sequence adapted from[131]):

- An electron and hole are produced upon excitation of titania with UV Light.

$$TiO_2 + hv \rightarrow e^- + h^+ \quad (1)$$

- One possible route is recombination of the charges generating thermal energy.

$$e^- + h^+ \rightarrow heat \quad (2)$$

- The photogenerated electron can be trapped at a surface site

$$e^- \rightarrow e^-_{surf} \quad (3)$$

- Adsorbed oxygen can be reduced to the superoxide anion by the electron

$$O_2 + e^-_{surf} \rightarrow O_2^{\bullet-} \quad (4)$$

- The photogenerated hole can be trapped on the surface of the lattice

$$h^+ \rightarrow h_{surf} \quad (5)$$

- The hole can oxidise any adsorbed species S.

$$h^+ + S \rightarrow S^{\bullet+} \quad (6)$$

- A surface hydroxide anion reacts with a hole to produce a surface hydroxyl radical.

$$h^+ + Ti\text{-}OH^-_{surf} \rightarrow Ti\text{-}OH^{\bullet}_{surf} \quad (7)$$

- The hydroxyl radical oxidises the adsorbed molecule, S.

$$Ti\text{-}OH^{\bullet}_{surf} + S + H_2O \rightarrow Ti\text{-}OH^-_{surf} + {}^{\bullet}S\text{-}OH + H^+ \quad (8)$$

- The trapped electron reduces the hydroxyl radical to a surface hydroxide anion.

$$e^-_{surf} + Ti\text{-}OH^{\bullet}_{surf} \rightarrow Ti\text{-}OH^-_{surf} + heat \quad (9)$$

In reactions (6) and (8), S is an adsorbed molecule in an air-saturated aqueous environment which can undergo oxidation reactions. The use of inorganic coatings on the titania particle relies on the inhibition of reactions (3), (5) or (7) and the enhancement of reactions (2) and (9).

### 1.9.2 Zinc Oxide

Please refer to section 1.8.3 for zinc oxide properties.

### 1.9.3 Vanadium Oxide ($VO_2$)

Intelligent window coatings respond to an external stimulus with increasing sophistication on an "as needs" basis. An example of this class of material includes thermochromic coatings[132], these are coatings that change their reflectance – transmittance properties with temperature and also undergo a semiconductor to metal transition as a result of the temperature change. Many materials are known to show this behaviour, and common examples include transition metal oxides such as $Ti_2O_3$, $Fe_3O_4$, $Mo_9O_{26}$[132, 133] and in several forms of vanadium oxide, $V_nO_{2n-1}$. Vanadium dioxide to date is the material of choice for various applications due to the tuneable transition temperature and electric, magnetic and optical properties at 70°C[134].

The phase change associated with $VO_2$ is from the monoclinic to tetragonal phase[135]. Here, a change in the optical properties occurs i.e. a decrease in the transmission and increase in reflectance/conductance due to the metal-like characteristics of the new phase. Researchers have increasingly looked at vanadium oxide for application as a window coating[136]. Below $T_c$ (0 – 68°C), the material is transparent. This allows sunlight to pass through the window, maximising the heating effect and warming the room. Above $T_c$ (68 - 200°C) the coating becomes very reflective, rejecting part of the IR portion of sunlight from entering the room. Interestingly the coating remains

transparent (Figure 22). This is very economical as electrical heating and air condition expenses are reduced.

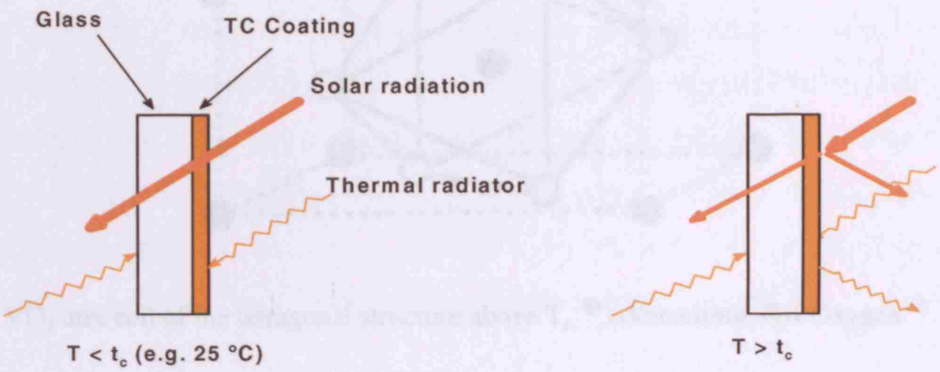


Fig 22: Representation of how $VO_2$ acts as an intelligent window coating[137]

The thermochromic transition temperature for vanadium dioxide thin films can be altered as desired by doping. This introduces new energy levels into the band gap, easing the phase transition. The thermochromic switching temperature ($T_c$) of vanadium (IV) dioxide is 70°C[138] and it has been found that high valent transition metal dopants reduce the $T_c$ for window coating applications in temperate climates. These elements include niobium, molybdenum or tungsten[139]. On the other hand, the transition temperature is increased by doping with trivalent cations (e.g. $Cr^{3+}$ and $Al^{3+}$)[140]. The most dramatic reduction in $T_c$ for vanadium (IV) dioxide films is with tungsten, where $T_c$ has been reduced to 25°C for thin films prepared by physical vapour deposition (PVD) and also by sol-gel and dip-coating methods[141].

### 1.9.3.1 Structure and Properties of Vanadium Dioxide Films – The Metal-Insulator Transition

The metal to insulator phase transition (MIT) has been studied by many scientists and much work has been completed by Goodenough[142] and Morin[143]. In the tetragonal high

temperature phase, the $V^{4+}$ ion with one 3d electron per atom is in the centre of the octahedron (Figure 23) [144].

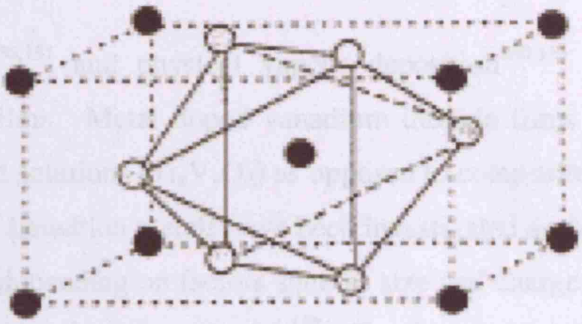

Fig 23: $VO_2$ unit cell of the tetragonal structure above $T_c$, ● =Vanadium, ○ = Oxygen[145]

The tetragonal structure has equidistant vanadium atoms in chains of edge sharing $VO_6$ octahedra. The low temperature monoclinic phase involves $V^{4+}$-$V^{4+}$ pairing with alternating shorter and longer $V^{4+}$-$V^{4+}$ distance along the *c* axis[146, 147]. When the MIT occurs, the planes of vanadium atoms in the monoclinic structure displace by 0.043 nm, breaking the $V^{4+}$-$V^{4+}$ pairs (Figure 24) [148].

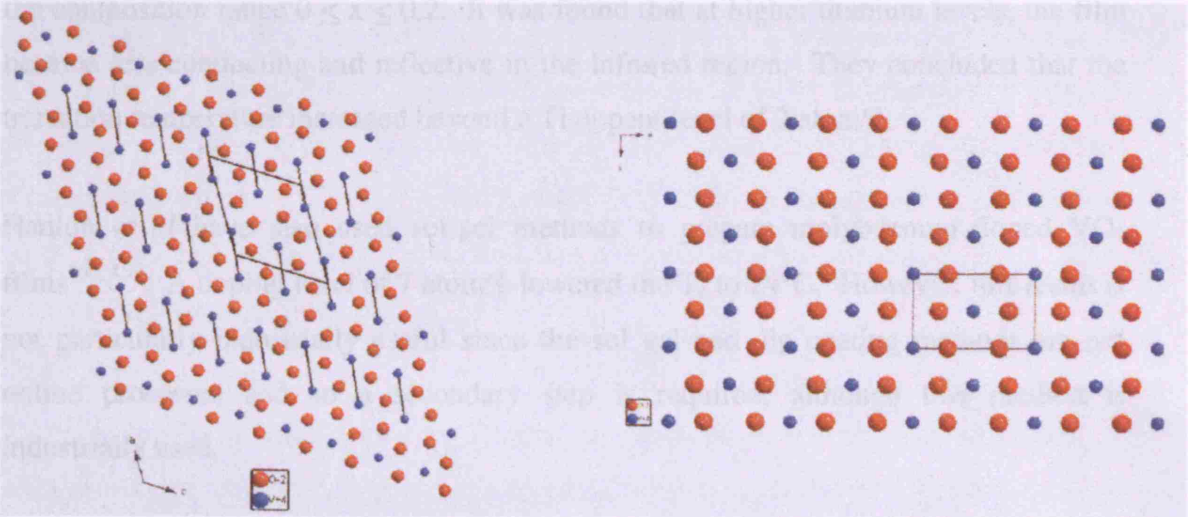

Fig 24. Schematic of a) monoclinic $VO_2$ with V-V pairs and b) tetragonal $VO_2$[149].

### 1.9.3.2 Previous Research - Development of Doped $VO_2$ Thin Films

The sol-gel process[150,151] and physical vapour deposition[150,151] have been used to prepare doped $VO_2$ films. Metal doped vanadium dioxide films prepared by sol-gel methods result in solid solutions ($Ti_xV_yO_2$) as opposed to composite films ($TiO_2$ - $VO_2$). The entire first row of transition metals have been investigated as dopants into $VO_2$, and are known to alter $T_c$ depending on factors such as size and charge of the dopant ion or changes in electron carrier density on doping[152]. The thickness of the thin films has also been shown to influence the thermochromic transition temperatures[153].

Doped $M_xVO_2$ films (M = $W^{6+}$, $Nb^{5+}$, $Ti^{4+}$, $Cr^{3+}$ or $Al^{3+}$) have been prepared by Beteille *et al* by mixing a vanadium alkoxide and a metal salt in an alcoholic solution[154]. The switching temperature decreases when the film is doped with high valent cations ($W^{6+}$) and increases with low valent cations ($Al^{3+}$, $Cr^{3+}$). Interestingly, $T_c$ reduces for low Ti-dopant concentrations (5 atom%) and increases for high Ti-dopant levels (20 atom%).

Beteille *et al* extended their research and attempted the sol-gel synthesis of $TiO_2$ doped vanadium dioxide films[155]. $V_{1-x}Ti_xO_2$ thin films were deposited from $V^V$ and $Ti^{IV}$ alkoxide solutions. The thermal behaviour of sol-gel deposited $V_{1-x}Ti_xO_2$ was studied in the composition range $0 \leq x \leq 0.2$. It was found that at higher titanium levels, the film became less conducting and reflective in the infrared region. They concluded that the transition temperature increased beyond a Ti dopant level of 2 atom%.

Hanlon *et al* have also used sol-gel methods to prepare molybdenum doped $VO_2$ films[156, 157]. A doping level of 7 atom% lowered the $T_c$ to 24°C. However, this result is not particularly industrially useful since the sol gel and dip coating methods are not online processes and so a secondary step is required, although this method is industrially used.

Gold doped $VO_2$ thin films have been successfully synthesised via the sol-gel process by Cavanna *et al*[158]. A solid solution ($Au_xV_yO_2$) resulted and it was found that at 0.25

atom% Au, the transition temperature reduced to 61°C, and for 0.5 atom% Au, the transition temperature lowered further to 57°C. The greatest decrease in the transition temperature was for 1.25 atom% Au, where $T_c$ was found to be 49°C. This is represented in Figure 25.

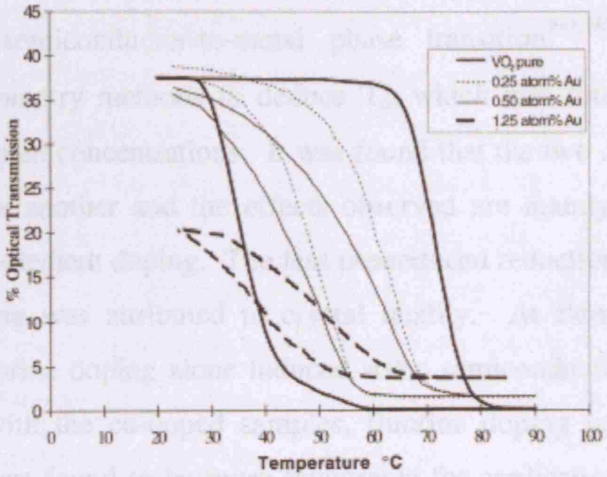


Fig 25. Reduction in $T_c$ with increasing Au dopant percentage[159]

In comparison to the sol-gel process, it has been found by Parkin *et al* that the APCVD reaction of $VCl_4$ and water yields thin films of a range of vanadium oxides on glass substrates[160]. These include $VO_2$, $VO_x$ (x = 2 – 2.5), $V_6O_{13}$ and $V_2O_5$. They found that higher deposition temperatures encouraged the formation of phases e.g. $VO_2$ which are less oxygen rich, whilst increasing the concentration of $VCl_4$ promoted the formation of oxygen rich phases such as $V_6O_{13}$. The films were analysed by Raman microscopy, X-ray diffraction, Rutherford backscattering, UV absorption spectroscopy and scanning electron microscopy. The $VO_2$ films formed exhibited reversible switching behaviour at 68°C corresponding to a monoclinic ($MoO_2$ structure) to tetragonal ($TiO_2$, rutile structure) phase transition.

In an extension to their research, Parkin and co-workers investigated thin films of tungsten doped vanadium (IV) dioxide on glass substrates via the APCVD of vanadium (IV) chloride, tungsten (VI) ethoxide and water at 550-650°C[151]. It was found that tungsten doping caused a decrease in the thermochromic phase transition temperature

comparable to sol-gel studies. A maximum tungsten loading of approximately 5% could be obtained using the tungsten ethoxide precursor. A tungsten loading of 3 atom% lead to a $T_c$ value of 5°C.

Tungsten and fluorine co-doping of $VO_2$ has been studied by Burkhardt *et al* who have found that there is clear evidence for an interaction of fluorine and tungsten in $VO_2$ which affects the semiconductor-to-metal phase transition[161,162,163]. They used photoelectron spectrometry methods to deduce $T_c$, which was found to be 0 - 33°C depending on the dopant concentrations. It was found that the two doping elements act independently of one another and the effects observed are mainly as a result of the summation of single-element doping. The less pronounced reduction in $T_c$ compared to single element doping was attributed to crystal quality. At fluorine concentrations below 2 atom%, fluorine doping alone induced some semiconducting character to the $VO_2$ films, whilst with the co-doped samples, fluorine doping induced the metallic phase. Co-doping was found to be more favourable for applications such as window coatings since tungsten doping alone does not provide a wanted colour for the $VO_2$ films. Furthermore, when doping with fluorine alone, sufficient values for $T_c$ are not reached without heavily reducing the switching of the energy transmittance. Hence co-doping provides films with the desired $T_c$ as well as enhanced transmittance in the visible spectral range, while still maintaining switching[164].

## 1.10 Literature Summary

The use of CVD to grow thin films of nanoparticles has recently been developed. Films of Si and diamond nanoparticles amongst others have been produced by CVD[32]. The nanoparticles are formed from suitable precursors in the CVD reactor, meaning that their physical properties such as size, shape and uniformity are determined by the CVD conditions[32]. Nanoparticles have been coated onto substrates by spin coating and other physical techniques[32]. Further investigation of the functional properties of thin films that incorporate a secondary nanoparticulate phase is required.

The aim of this work is to assess the potential of gold, silver, ceria, iron oxide, zinc oxide and $WO_3$ nanoparticulates when incorporated into host thin films on glass. In particular to see if the secondary nanoparticulate phase has the ability to enhance photocatalytic efficiency, solar control properties, colour, durability, conductivity, electrochromic response, antibacterial properties and hardness.

The primary aim of this research project was the investigation of the functional properties of thin films that incorporate a secondary phase, such as a metal oxide or metallic nanoparticles. In order to achieve this it was necessary to develop methods whereby nanoparticles could be reproducibly incorporated into thin films, resulting in composite films with properties that are mostly combinations of the properties of bulk film and nanoparticle. In addition, unique properties, arising from cooperative effects between nanoparticle and host thin film were anticipated. This approach allowed for the growth of films in which properties such as refractive index, electrical conductivity and electronic structure were widely tuneable.

The size and shape of the nanoparticles as well as the mode of deposition becomes crucial when tailoring the properties of semiconductor films. For many practical applications nanoparticles will need to be incorporated into thin films because to be useful, devices will need to be based on assemblies of nanoparticles. There are some problems associated with the use of high temperature processing of nanoparticles into films, since if the deposition or processing technique is at too high a temperature the nanoparticles will have a natural tendency to agglomerate into larger units- and thereby reduce their surface free energy or react with their surroundings and loose functional properties. Methods have been devised to avoid these problems including surface passivation with molecular protecting groups or the incorporation of the nanoparticles into a host matrix that lends stability – such as a nanoparticle-polymer composite. Nanoparticles in solution often have a surface charge, which helps prevent aggregation through electrostatic repulsion. Their stability is a balance between electrostatics keeping the particles apart and surface energy effects that favour aggregation. Unstable nanoparticles coalesce and usually drop out of solution. Electrostatic repulsion is increased in solutions of high or low pH. It has been shown that the size, morphology, stability, and properties of these nanoparticles have a strong dependence on the

specificity of the preparation method and the experimental conditions. Some work has been published on the incorporation of nanoparticles into sol-gel or polymer based thin films by spin-coating. This method is limited in its ability to prepare composite films of materials that require higher temperature processing, e.g. photocatalytic films, smooth transparent conducting oxide layers, and indeed semiconductor structures in general as well as stable optical coatings on substrates such as glass. It is proposed that the aerosol assisted CVD (AACVD) method is potentially capable of overcoming these limitations. The method involves the preparation of a precursor solution phase containing both the chemical precursors for the growth of the target film, and appropriate nanoparticles. This method is particularly suited to CVD growth using precursors that posses little or no vapour pressure at accessible temperatures. Previously, discrete metal oxide particles have been incorporated within a host matrix by AACVD using a simple mixed alkoxide system and a composite film results rather than solid solution formation. With this background in mind, this project explored a new programme of study into the use of this novel AACVD growth technology for the production of a range of new or improved materials having applications in optical coatings.

The overall aim of this project was to design and fabricate metal, metal compound and composite nanoparticles as potential new materials for a range of thin films and coatings having applications in areas such as self-cleaning and photocatalytic surfaces, transparent electrical conductors for photovoltaic devices, interference structures, photochromic materials, solar control coatings and novel decorative coatings. In order to achieve this aim it was also necessary to develop a new generation of chemical vapour deposition (CVD) based coating processes for use with nanoparticulate materials and their precursors.

# Chapter 2: Experimental

This section reports on the experimental techniques used in this research study, ranging from the synthesis of all nanoparticle types and an account of how the different types of chemical vapour depositions techniques were used, namely aerosol assisted chemical vapour deposition (AACVD), atmospheric pressure chemical vapour deposition (APCVD) and aerosol assisted into atmospheric pressure chemical vapour deposition (AA/APCVD). All analysis techniques reported in this thesis will be presented and the method of sample preparation in order to carry out the analysis will also be accounted for. Further details on film deposition and specific reaction parameters will be detailed in subsequent chapters.

## 2.1 The Chemical Vapour Deposition (CVD) Reactor

A common reactor was used for all CVD reaction types by both AACVD and APCVD. This reactor consisted of a glass substrate and supported top plate, the top plate was either quartz or glass. This set up was encapsulated within a cylindrical quartz tube, Figure 26, open at both ends to allow flexibility within the reactor and ease of re-construction and cleaning. The two ends of the quartz tube were capped at each end by a stainless steel plate. Attached to one end of the quartz tube was a brass manifold. The function of this part was to allow the continuous and uniform flow of gas across the entire cross section of the reactor. The reactor was designed so that the gas passed between the substrate and top-plate, the flow of gas was kept within the 10 mm separation between the glass substrate and the top-plate. The glass substrates were cut to size in order to fit the dimensions of the reactor, a standard size of 150 by 45 by 4 mm was used. The substrate was heated by the graphite heater block on which the substrate rested. In order to ensure that the glass does not fuse with the deposited film, the substrates were pre-coated with a 50 nm thick $SiO_2$ barrier layer (glass supplied by Pilkington).

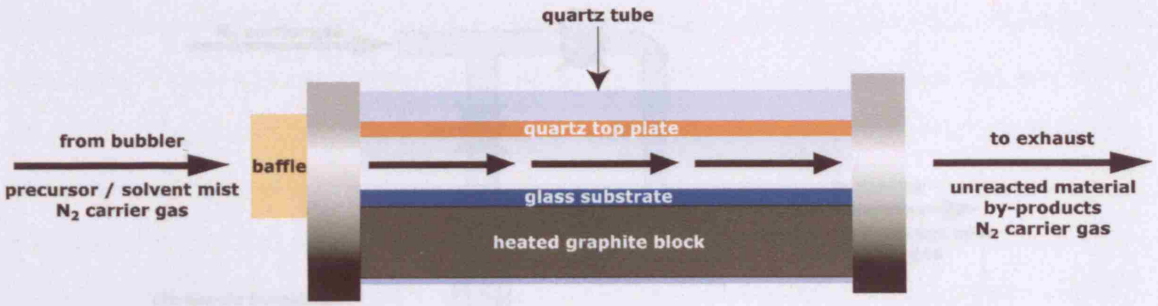


Figure 26. Diagram of a CVD reactor highlighting the main parts; the heated graphite block, glass substrate, quartz top plate, manifold/baffle and the encapsulating CVD reactor and glass quartz tube[165].

For all experiments, both the substrate and top plate were 150 x 45 x 4 mm sheets of $SiO_2$ pre-coated standard float glass. Prior to insertion in the CVD reactor, all glass samples were cleaned using a tissue soaked in water, then with tissue soaked with propan-2-ol. The glass was allowed to dry in air prior to it being mounted in the CVD reactor. The substrate was heated on a carbon block containing a Whatman cartridge heater in a horizontal-bed cold-wall CVD reactor. The temperature of the carbon block was monitored by Pt-Rh thermocouples.

## 2.2 Aerosol Assisted Chemical Vapour Deposition (AACVD)

### 2.2.1 AACVD Equipment Set-up

AACVD makes use of an aerosol within its set up[166]. Here, desired precursor/s (nanoparticle and host matrix mix) were dissolved in the appropriate solvents E.g. toluene, acetone, ethanol, acetonitrile and water. This mix was then transferred to a carefully designed bubbler which was put in place in a Vicks ultrasonic humidifier purchased from Argos (Figure 27). The humidifier generated ultrasonic waves from a piezo-elecric device and this allowed the waves to transfer from the bubbler to the contained precursor mix, ultimately generating a wave pattern on the surface of the mix. When the wave height was sufficient, the wave crests became unstable and formed droplets that were ejected from the surface to generate the aerosol mist[167].

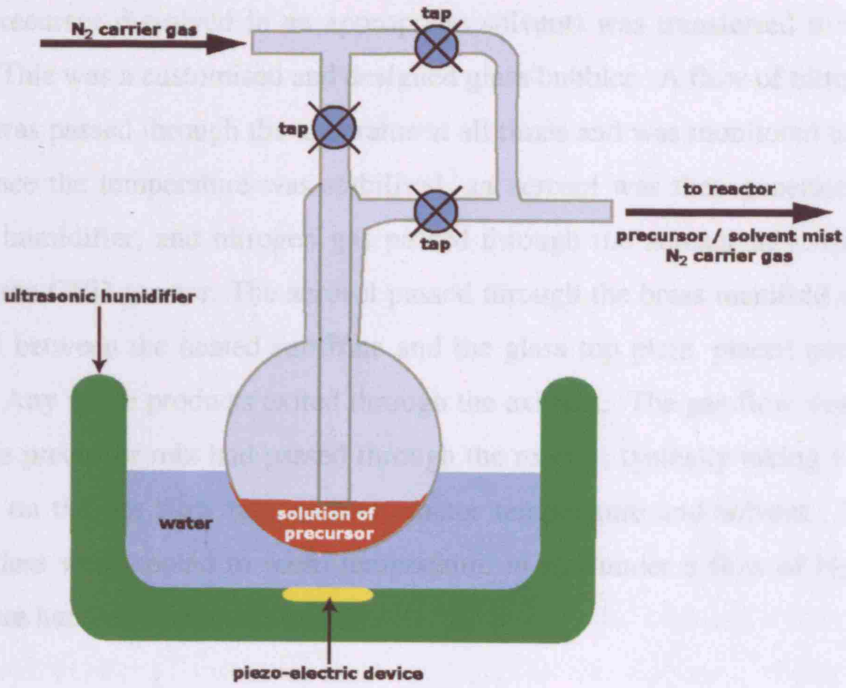


Figure 27. Schematic diagram of the aerosol delivery system showing the connection taps, piezo-electric device and humidifier base[168].

This mist was then carried to the CVD reactor using nitrogen as a carrier gas; nitrogen entered the bubbler flask and was guided to the solution by a series of taps directing the flow. The combined precursor and mist was carried by the nitrogen through a second route in the bubbler flask towards the carbon reactor. The CVD reactor was heated from 400 to 650 °C. This allowed the solvent to evaporate hence leaving the precursor as a vapour. This allows the precursor to be present in the reactor in the gaseous state, but a conventional thermal vaporisation technique has been avoided.

## 2.2.2 AACVD Procedure

All AACVD experiments were carried out on apparatus tailored to this reaction type consisting of a horizontal-bed cold-wall reactor connected to an arrangement of delivery tubing, a bubbler and a humidifier.

A typical deposition experiment proceeded as follows. The precursor mixture (the required precursor dissolved in an appropriate solvent) was transferred to the aerosol chamber. This was a customised and designed glass bubbler. A flow of nitrogen (BOC, 99.99 %) was passed through the apparatus at all times and was monitored using a flow meter. Once the temperature was stabilised, an aerosol was then generated using an ultrasonic humidifier, and nitrogen gas passed through the aerosol mist, directing the aerosol to the CVD reactor. The aerosol passed through the brass manifold and entered the reactor between the heated substrate and the glass top plate, placed parallel to the substrate. Any waste products exited through the exhaust. The gas flow was continued until all the precursor mix had passed through the reactor, typically taking 1 to 2 hours depending on the gas flow rate, carbon reactor temperature and solvent. The coated films on glass were cooled to room temperature *in situ* under a flow of $N_2$, and after cooling were handled and stored in air.

## 2.3 Combined Aerosol Assisted/Atmospheric Pressure Chemical Vapour Depostion Procedure

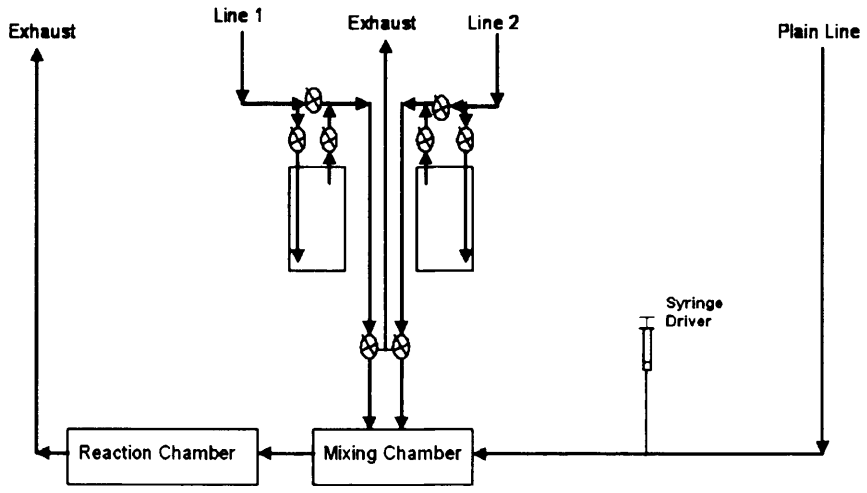


Figure 28. APCVD set up showing all connections and parts[169].

The APCVD set up was somewhat more complex consisting of custom built apparatus with a horizontal-bed cold-wall reactor connected to an arrangement of stainless-steel heated pipes, valves and bubblers. In addition, to allow water or a secondary additive into the system, a syringe driver was attached to the plain-line gas-flow. A schematic of the APCVD rig used is shown in Figure 28. All heaters were regulated by Eurotherm controllers and RS type k thermocouples.

The precursor was transferred into the APCVD bubbler. The nanoparticle solution was added to the glass bubbler. Simultaneous deposition enabled the AACVD process to supply a mist of nanoparticles, whereas the APCVD connection provided a precursor in the gaseous form, Figure 29. These mists/gaseous particles were allowed to mix in the mixing chamber via a concentric tube entrance to the chamber, Figure 30. The combined mist was then directed to the reactor, which enable deposition of nanoparticles incorporated within a host matrix.

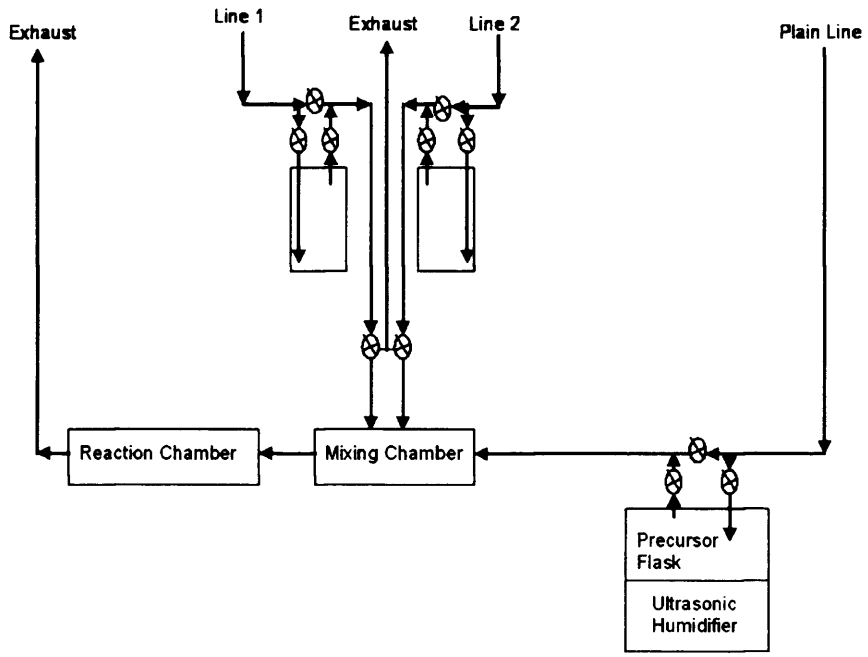


Figure 29. AA/APCVD set up showing all connections and parts[169].

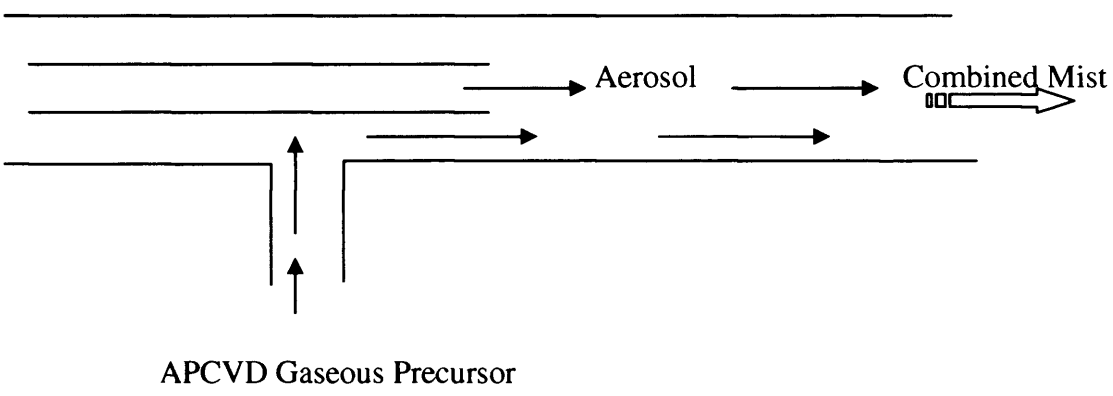


Figure 30. Schematic of the AA/APCVD 2 way valve[170].

Once the temperatures were stabilised, an aerosol was then generated using an ultrasonic humidifier, and nitrogen gas passed through the APCVD bubbler and aerosol mist, directing the aerosol to the CVD reactor. The aerosol passed through the brass manifold and entered the reactor between the heated substrate and the glass top plate, placed parallel to the substrate. Any waste products exited through the exhaust. The gas flow was continued until all the precursor mix had passed through the reactor, typically taking 20 minutes depending on the gas flow rate, carbon reactor temperature and solvent. The coated films on glass were cooled to room temperature *in situ* under a flow of $N_2$, and after cooling were handled and stored in air.

## 2.4 Synthesis of Nanoparticles

A range of different methods were used to synthesise gold and silver nanoparticles, silver nanoshapes and $Fe_2O_3$ nanoparticles. The $WO_3$ nanoparticle precursor and tungsten oxide nanopowder were ordered from Aldrich and the $CeO_2$ nanoparticles were supplied in water by Umicore. These nanoparticles and a host matrix were deposited together mixed within the same aerosol mist, and also as alternating nanoparticle and host matrix oxide layers. The gold, silver and $Fe_2O_3$ nanoparticle along with silver nanoshape synthesis are outlined below:

## 2.4.1 Synthesis of Ag Nanoparticles

Five different silver nanoparticle and nanoshape synthesis methods were used in this research. These are outlined below:

### 2.4.1.1 Sodium Citrate Reduction Synthesis of Ag Nanoparticles in Water[171]

Distilled water (125 mL) was transferred to a beaker. A solution of silver nitrate ($AgNO_3$) in (1 mM, 125 mL) was prepared following standard procedures. This solution was heated to boiling with stirring using a magnetic stirring bar. A 1% solution of sodium citrate was prepared in distilled water and 5 mL was added to the primary solution prepared earlier. The resulting mixture was heated until the solution turned yellow. The solution was then cooled to room temperature and stored in the fridge.

This yielded ~60 nm silver nanoparticles. The size could be altered by adding more or less sodium citrate or using an alternative reducing agent (e.g. sodium borohydride).

### 2.4.1.2 Synthesis of Ag Nanoparticles in Toluene[171]

Distilled water (30 mL) was transferred to a beaker. A solution of 5.0 M $NaNO_3$ (12.749g $NaNO_3$) was then prepared. Thereafter 50 mL of toluene was transferred to a beaker and a solution of 50 mM tetraoctylammonium bromide (TOAB) (1.367 g tetraoctylammonium bromide) prepared. The TOAB solution in toluene was added to the aqueous $NaNO_3$ solution. This was stirred vigorously for one hour to remove $Br^-$ ions from the solution and prevent the formation of AgBr when $AgNO_3$ is added. The organic phase was extracted and set aside and the aqueous phase was discarded. Distilled water (14 mL) was transferred to another beaker and a 30 mM $AgNO_3$ solution prepared (0.0764g $AgNO_3$). A pipette was used to transfer 7.5 mL of 30 mM $AgNO_3$ solution to the organic solution. The resulting mixture was stirred vigorously for 45 minutes. The organic phase was extracted and the aqueous layer was discarded using a separating funnel. The next step was carried out in order to cap the silver nanoparticles;

0.16 mg (0.189 mL) of 1-dodecanethiol was added to the organic solution and the solution was stirred vigorously for 15 minutes. Meanwhile, 0.4 M $NaBH_4$ in water (0.3783 g $NaBH_4$ in 24 mL $H_2O$) was prepared and 6.25 mL added dropwise over a 35 minute period to the solution containing the silver organic layer while stirring vigorously. The resulting mixture was stirred vigorously for 15 hours overnight. The organic layer was extracted and the aqueous layer discarded. The organic layer was washed three times with dilute ethanol. The mixture was allowed to settle and the organic layer was extracted. The nanoparticles were stored in a closed container.

### 2.4.1.3 Synthesis of Ag Nanorods in Water[172]

### a) Preparation of Silver Seed Solution

Sodium citrate dihydrate (0.0594 g) and silver nitrate (0.0425 g) were added to distilled water (10 mL). Ice cold 0.1 M $NaBH_4$, a reducing agent (3.783 g, 25 μL) was injected into the solution while stirring vigoruously. A colour change to light yellow was observed).

### b) Procedure For Nanorod Growth

A 20 mL aqueous solution containing cetyl ammonium bromide (CTAB 3.2 g, 0.1 M) was prepared and heated to 40 °C while stirring. This was to ensure complete dissolution of CTAB. Once fully dissolved, the solution was cooled to room temperature. Two further solutions were prepared: 100 μL of 0.05 M (1.69 g) $AgNO_3$ and 1000 μL of 0.1 M ascorbic acid and were added to the first solution. A varied amount of 1M NaOH was added (0.25, 05 and 1 mL) and within 2 minutes the colour changed to a greenish grey, indicating the formation of silver nanorods.

### 2.4.1.4 Solvent Induced Shape Evolution of PVP Protected Spherical Silver Nanorods[173]

Acetyl nitrate, $AgNO_3$, Poly(N-vinyl-2-pyrrolidone) (PVP) (MW=10,000) were obtained from Aldrich and used without any further purification. Solutions of $AgNO_3$ (77.7 mM) and PVP (40 mM) were separately prepared in 10 mL of pyridine and then mixed well to form a homogeneous mixture. This mixture was then left unstirred in the dark for several days. The solution turned yellow when the PVP and $AgNO_3$ solutions were mixed, indicating the formation of silver nanoparticles. The reaction mixture was monitored by UV-visible spectroscopy to follow the nanoparticle growth progress. Nanotriangles and nanorods could be separated by centrifuging the mixed particle system at 6000 rpm for 10 mins. This allowed the nanorods to settle to the bottom of the container and the solution containing the nanoparticles was discarded and the nanorods were re-dispersed in toluene. TEM imaging was used to capture the final nanorod growth.

### 2.4.1.5 Synthesis of Ag Nanocubes[174]

Distilled water (47.5 mL) was deoxygenated by bubbling with nitrogen gas for 20 min. Aqueous solutions of 30 mM sodium citrate (0.5 mL) and 5 mM silver nitrate (1 mL) were then added. An aliquot of freshly prepared sodium borohydride (50 mM, 0.5 mL) was quickly added to this mixture, followed by the addition of 0.5 mL aqueous solution of PVP (5 mg $mL^{-1}$). The mixture changed to a deep yellow colour after the reaction had proceeded for 30 minutes. Vigorous stirring was maintained during the entire process. The dispersion of silver nanoparticles was then transferred to a 20 mL liquid scintillation glass vial and irradiated for 40 hours with a Halogen lamp equipped with a UV cut off filter. The colour of this dispersion became greenish-blue, indicating the formation of silver nanocubes.

## 2.4.2 Synthesis of Au Nanoparticles[171]

### 2.4.2.1 Synthesis of 2.5 X $10^{-4}$ M Au Nanoparticles (Sodium Citrate Reduction Method)

A solution of 5.0 x $10^{-3}$ M $HAuCl_4$ (0.1699 g in 100 mL distilled water) was prepared and 1 mL was taken and added to another 18 mL of distilled water. A solution of 0.5% sodium citrate (0.25g in 50 mL of $H_2O$) was made. The 19 mL solution of $HAuCl_4$ was heated until it began to boil. Sodium citrate solution (1 mL, 0.5%) was added as soon as this solution began to boil. The resulting mixture was heated until a colour change was evident (pale purple). The solution was then removed from the heating element and stirred until it was cooled to room temperature. To account for loss of water during boiling, the solution was topped up to 20 mL.

### 2.4.2.2 Preparation of Au Nanoparticles in Toluene

A solution of tetraoctyl ammonium bromide in 80 mL of toluene was prepared. This solution was added to an aqueous solution of hydrogen tetrachloroaurate (0.3537 g in 30 mL of distilled water). The resulting mixture was stirred for 10 minutes. The reaction mixture was vigorously stirred whilst adding $NaBH_4$ (0.38 g in 25 mL of $H_2O$) dropwise over a period of 30 min. Care was taken to ensure that organic and aqueous phases were mixed together. This solution was stirred for an additional 20 min. The organic phase was extracted and washed once with diluted $H_2SO_4$, to ensure neutralization and five times with distilled water. The organic layer was dried with $Na_2SO_4$.

## 2.4.3 Synthesis of $Fe_2O_3$ Nanoparticles

### 2.4.3.1 Synthesis of $Fe_2O_3$ Nanoparticles in Water[175]

Distilled water (100 mL) was transferred to a 200 mL flask and NaOH (8 g, 2M) was dissolved to form an aqueous solution. The mixture was stirred for a couple of minutes. Iron (III) sulfate pentahydrate (0.9600 g) and iron sulfate (0.3203 g) were weighed out and dissolved in 20 mL of distilled water. The sulfate and hydroxide mixtures were combined and stirred for one hour to ensure completeness of the reaction. The resulting solution was put in a centrifuge and spun at 3000 rpm. The supernatant was taken out, water added and spun again for another 15 minutes. This was repeated 2 more times. Phosphate buffer solution was added to ensure all the nanoparticles were released from the supernatant.

### 2.4.3.2 Synthesis of $Fe_2O_3$ Nanoparticles in Toluene[176]

A mixture of Dioctyl ether (10 mL, 99%) with 1,2-hexadecanediol (2.5 mmol, 90%) and stabilising ligands which were a mixture of oleic acid (1.5 mmol, 70%) and oleylamine (1.5 mmol, 70%) were prepared. Thereafter, $[Fe(acac)_3]$ (0.5 mmol, 98% purity) was first dissolved in the combined solvent/stabilising ligand mixture and stirred at room temperature for 1 h under argon gas flow. After 1 h, the mixture was then slowly heated to 130 °C and this mild heating changed the solution colour from red to yellow, indicating the formation of $Fe^{3+}$ ions. The subsequent rapid heating to the boiling point of the solvent reduced the $Fe^{3+}$ ions to neutral atoms. During this heating process the solution turned black at around 200°C, indicating the onset of nucleation. The temperature was kept at 260-290°C for 50 min for reflux. After the black colloidal solution was air cooled to room temperature, the nanoparticles were precipitated with ethanol and separated by centrifugation. The precipitates were then re-dispersed in a toluene solution. This purification process was repeated 2-3 times. The resulting nanoparticles dispersion was stable and did not flocculate at ambient temperature after six months.

## 2.5 Characterisation of the Thin Films

All samples were analysed as thin films attached to the glass substrate. This section will explore the methods used to characterise the thin films.

### 2.5.1 Physical Characteristics and Robustness

Scratch tests were carried out with a paper towel, rubber gloves, brass stylus and stainless steel scalpel; each material was used to mark a 3 cm scratch across the film. Solubility tests were achieved by immersion of small pieces of the coated glass in a range of solvents (acetone, methanol and ethanol, water, 2 M NaOH, 2 M HCl and 2M $HNO_3$). Adhesion of the films to the substrate was determined by the Scotch tape test (removal of an X shaped piece of sticking tape). Sheet resistances were determined on a four-point-probe instrument.

### 2.5.2 X-ray Diffraction (XRD)

X-ray analysis of the films was measured on two different machines. The first using glancing angle incidence (1.5°) on a Siemens D5000 machine using primarily mono-chromated Cu $K_{\alpha 1}$ radiation (1.5406 Å). The diffraction patterns were taken over the range $0°<2\theta<70°$. The XRD data enabled the crystal phase composition of the films to be found.

The second machine used for measurements was a Bruker-Axs D8 GADDS diffractometer using Cu $K_{\alpha 1}$ radiation (1.5406 Å). This diffractometer was equipped with a focussed and movable x-y stage to analyse different parts of the film and used glancing angle incidence (1.5°). The diffraction patterns were modelled using the Reitveld refinement method using GSAS programmes and compared to database standards[177].

### 2.5.3 Energy Dispersive X-ray (EDAX) Analysis

Energy dispersive X-ray analysis (EDAX) was used to determine the quantitative amount of the elements in the film. A carbon coated sample was mounted onto an aluminium stub using carbon sticky paper. This was to enhance the conductivity. The sample was analysed on a JEOL 35-CF instrument using ISIS software (Oxford Instruments) and also a Philips XL30 ESEM instrument.

### 2.5.4 Raman Spectroscopy

Raman spectra were acquired using a Renishaw System 1000 Raman Spectrometer with a helium-neon laser source of wavelength 632.8 nm. The system was calibrated against a neon lamp.

### 2.5.5 XPS Measurements

XPS data was analysed using a VG ESCLAB 220i XL instrument using monochromatic Al Kα radiation. Binding energies were referenced to surface elemental carbon 1s peak with binding energy 284.6 eV in order to compensate for the effects of charging. Casa XPS software was used to determine this. Depth profiling was also used to determine variation of composition with layer thickness.

### 2.5.6 Scanning Electron Microscopy (SEM) Imaging

SEM images were captured to determine the morphology of the film surface and the thickness of the films, which was found from the cross-sectional images. The sample preparation was as for EDAX analysis but the films were coated with gold to increase conductivity and produce higher quality images. A JEOL 6301 instrument was the preferred microscope for imaging.

### 2.5.7 Visible/IR Reflectance/Transmittance

Measurements were performed on a Hitachi U4000 spectrophotometer between 240 nm and 2600 nm. A more advanced instrument was also used for some measurements between 300 and 2400 on a HunterLab Ultra Scan Pro instrument and also a Perkin Elmer lambda 950 instrument

### 2.5.8 UV/vis Spectrosopy and Band Gap Measurements

This technique measured the absorption of light in the UV/vis region. UV/vis absorption measurements were obtained on a Thermospectronic Helios α spectrometer between 300-1100 nm.

### 2.5.9 Transmission Electron Microscopy (TEM)

TEM samples were prepared by evaporating a single drop of the sample onto a copper conducting grid. The sample was then allowed to dry for 2 hours, depending on the solvent used. TEM imaging was carried out on a Joel JEM 100CX II instrument.

## 2.6 Functional Properties

### 2.6.1 Photocatalytic Activity Measurements

Photocatalytic activity of the samples was assessed by the destruction of an overlayer of a test organic stearic acid on a 3 cm x 3 cm portion of glass coated with the desired material. The test coated glass was irradiated at 254 nm for 1 h prior to measurement. The stearic acid was applied by dropping 7.5 μL of 0.4 mmol stearic acid onto the glass surface which was spun at 1500 revolutions a minute during the dropping procedure. The infrared spectrum of the stearic acid overlayer was measured over the range 2950 –

2800 $cm^{-1}$. The glass coated with stearic acid was irradiated with 254 nm and also 365 nm radiation provided by BDH germicidal lamps (2 x 8 W). The IR spectrum of the stearic acid was measured after 30 min intervals for up to 2 h and the areas of the bands that were attributed to the C-H stretches were quantified.

### 2.6.2 Photo-Induced Hydrophilicity Determination

Contact angles of selected glass samples were determined by measuring the spread of a 1.0 μL droplet of water. The measurements (mm) were converted to degrees via a spreadsheet package called "Contact". The measurements were taken before and after irradiation with UV (254 and 365 nm) for 1 hour and also after leaving the samples in the dark for 24 hours, followed by exposure to room light for 24 hours to determine the change in wettability. This was also repeated over a number of cycles for comparison with reference materials.

### 2.6.3 Photochromism

The UV spectra of the coating on glass was taken from 300-800 nm and then placed under UV radiation using either 254 or 365 nm ultraviolet light from a lamp consisting of two 8 W Hg vapour tubes. The optical absorption coefficient for 720 nm and 650 nm light was measured before and after irradiation using a Shimadzu UV-2401PC UV-vis spectrometer. The UV-vis spectrum was retaken and the sample was again left for irradiation. This was repeated 6 times at regular 20 minute intervals.

### 2.6.4 Colour Analysis

Colour analysis was performed at 2° viewing angle using D56 artificial daylight, which was also used for haze measurements. The CIELab colour coordinates were calculated from the reflectance/transmission spectra using LBNL Window, which is an industry standard software.

## 2.6.5 Transition Temperature Measurements

The thermochromic transition temperature was determined by measuring the absorption at 4000 $cm^{-1}$ using a Nicholet FT-IR spectrometer. The sample temperature was monitored by an aluminium temperature cell controlled by RS heaters, Eurotherm temperature controllers and k-type thermocouples. The sample temperature was measured by a k-type thermocouple taped to the film surface.

# Chapter 3:

# Deposition of Thin Films of Silver Nanoparticles, Silver Nanoparticles Incorporated into a Titania Host Matrix, Silver Nanorectangle and Silver Nanorod Films by Aerosol Assisted Chemical Vapour Deposition

## 3.1 Introduction

This chapter will report the aerosol assisted chemical vapour deposition (AACVD) of silver nanoparticle and nanoshape films. The silver nanoparticles were synthesised and then embedded into a titania anatase host matrix using the same deposition method in order to impart some useful optical and anti-bacterial[178] properties to the films. Two film growth techniques were used to grow these films, multi-layer sequential deposition and also co-deposition in a single AACVD reaction.

## 3.2 Synthesis and Deposition Parameters

Silver nanoparticles were prepared as per the method discussed in the experimental section (Chapter 2). Spherical silver nanoparticles were synthesised by two different routes, the first method was a sodium citrate reduction in water, and the second a sodium borohydride reduction in toluene. These nanoparticles were then used to successfully deposit thin films incorporating nanoparticles within a host matrix. A number of different methods were used to synthesise nanorods of silver. The first method involved preparation of a seed solution. The solvent induced shape evolution of poly vinyl pyrollidone (PVP) protected silver nanorods was completed. PVP was also used to grow silver nanocubes, this procedure required an additional step involving halogen lamp irradiation. The AACVD and sol-gel synthesis of these silver nanoparticles was completed.

The flow rate and reactor temperature were varied to obtain the optimum conditions for silver nanoparticle film growth, this is summarised in Table 2. Silver nanoparticles

were incorporated into a titania host matrix by two different methods of precursor delivery, the first method involved an alternating layer by layer deposition of silver nanoparticle and titania (1 layer of each) and the second method used simultaneous deposition of the two systems using a single step within the same solvent.

| **Film Number** | **Film Type** | **Host Matrix** | **Deposition in Solvent 50 mL** | **Substrate Temperature/°C** | **Flow Rates/ L min$^{-1}$** |
|---|---|---|---|---|---|
| **1** | Ag nanoparticle | - | Water | 500 | 1 |
| **2** | Ag nanoparticle | - | Toluene | 500 | 1 |
| **3** | Alternating Ag and titania layers | $[Ti(O^iPr)_4]$ (0.56g, 2mmol) | Ag nanoparticles in water, $[Ti(O^iPr)_4]$ in Toluene | 500 | 1 |
| **4** | Alternating Ag and titania layers | $[Ti(O^iPr)_4]$ (0.56 g, 2mmol) | Ag nanoparticles in water, $[Ti(O^iPr)_4]$ in acetone | 500 | 1 |
| **5** | Alternating Ag and titania layers | $[Ti(O^iPr)_4]$ (0.56 g, 2mmol) | Toluene | 500 | 1 |
| **6** | Simultaneous Ag and titania deposition | $[Ti(O^iPr)_4]$ (0.56 g, 2mmol) | Toluene | 500 | 1 |
| **7** | Ag nanorod | - | Water | 450 | 0.5 |
| **8** | Alternating layers of Ag nanorod and titania | $[Ti(O^iPr)_4]$ (0.56 g, 2mmol) | Ag nanorods in water, $[Ti(O^iPr)_4]$ in toluene | 450 | 0.5 |
| **9** | Sol gel deposition of Ag nanorods | - | Water (PVP protected) | - | - |
| **10** | Spray-evaporation of Ag nanocubes | - | Water (PVP protected) | - | - |

Table 2. Films deposited using silver nanoparticles and nanorods

## 3.3 Film Characteristics – Spherical Silver Nanoparticle Thin Films

Aerosol assisted chemical vapour deposition (AACVD) of the silver nanoparticle solutions prepared via a sodium citrate reduction in water, and also by a sodium borohydride reduction in toluene at a substrate temperature of 500 °C and flow rates of 1 $Lmin^{-1}$ enabled silver nanoparticle thin films to be laid on glass substrates. All films types were yellow in colour, stable in air (for over a year), adhesive — they passed the Scotch tape test — and resisted scratching with a tissue, paper, felt and brass. The films showed minimal haze and were semi-transparent to the eye. The films could not be removed by immersion of the films in common solvents, acid and alkali (2M).

### 3.3.1 Elemental Analysis For Nanoparticulate Silver Films

EDAX analysis confirmed that silver was indeed present in the films. The silver nanoparticles were homogeneously dispersed throughout the film (multiple spot analysis and wide area EDAX analysis). EDAX analysis showed that the films, to detection limits, were free from carbon and chlorine contamination. The EDAX spectra below is for a Ag nanoparticle thin film (Figure 31).

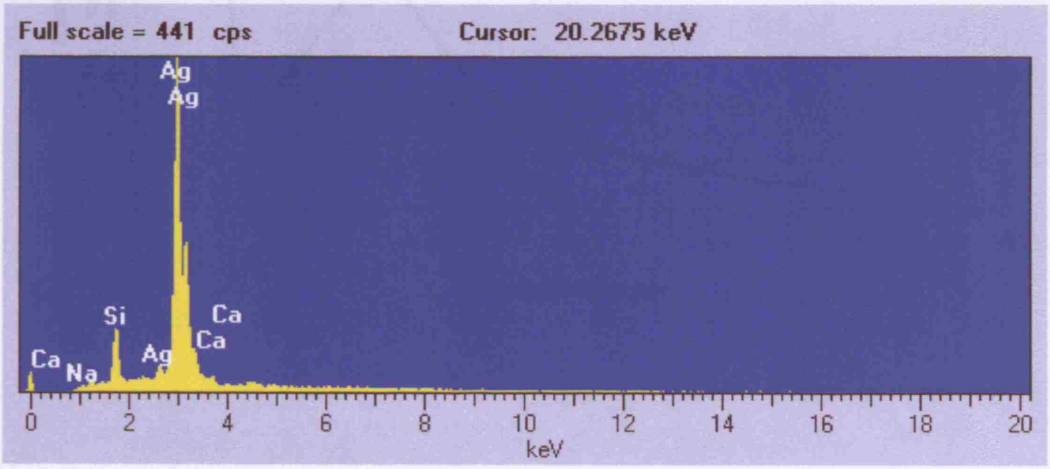


Figure 31. EDAX spectra detecting Ag and elements contained in glass.

UV-visible absorption analysis studies were carried out in order to investigate how the surface plasmon resonance peak changed upon transfer of the silver nanoparticles onto glass as a thin film. The UV-visible absorption spectra for the silver nanoparticles in water is shown in Figure 32A. Here a surface plasmon peak can be seen at 420 nm, this value is comparable to the reference value for silver nanoparticles[179].

Figure 32B shows the UV for an aqueous silver nanoparticle thin film as deposited by AACVD. The spectrum suggests there is a good transferability of the silver across the thin film. However, the surface plasmon resonance peak is shifted to 500 nm and somewhat decreased in intensity. This is most probably due to agglomeration on the substrate or could also mean a change in the nanoparticle size upon deposition onto the glass substrate as TEM imaging gave an original particle size of 18 nm, on the glass substrate the agglomerates were of 50 nm in diameter (Figure 33). This shift is expected, Mie theory predicts a red-shift of the surface plasmon resonance peak with change in particle size. The surface plasmon resonance peaks are also dependant upon concentration- hence a decrease in the intensity of the plasmon peak seen in Figure 32B.

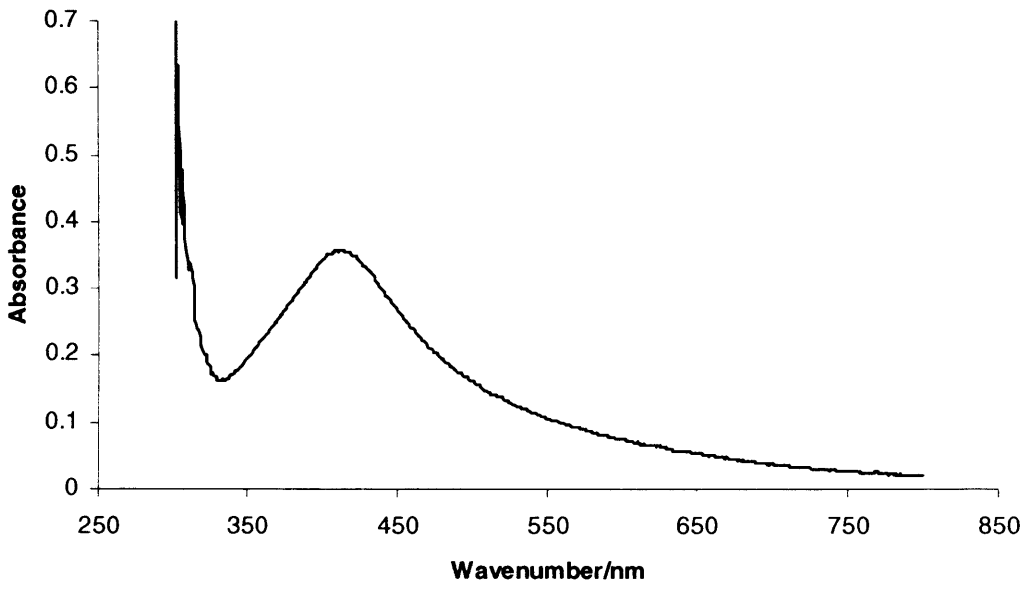


A

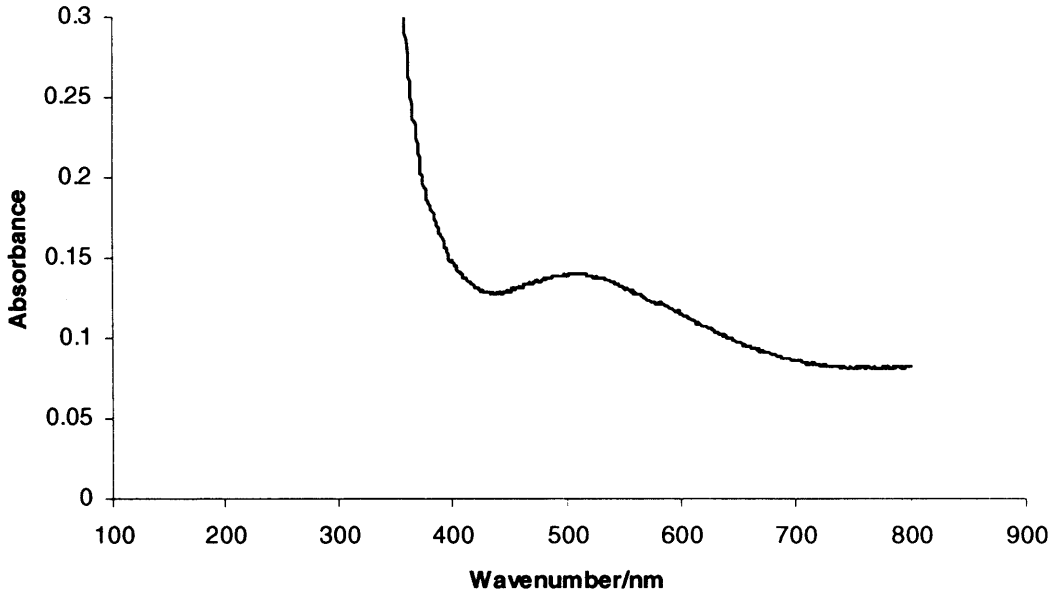


B

Figure 32. Comparison of the UV spectra of A) the initial aqueous silver nanoparticle solution with B) the aqueous silver nanoparticle thin film.

Furthermore X-ray diffraction studies confirmed the presence of silver with reflections at values of 36 and 44°[180].

## 3.3.2 Scanning Electron Microscopy: Growth Morphology For Nanoparticulate Silver Films

Scanning electron microscopy (SEM) showed that the silver nanoparticle films formed with little fusion of the silver particles (Figure 33). Spherical particles of dimension 20 - 50 nm were deposited; TEM imaging showed an original particle size of 18 nm. This shows that the particles synthesised were uniform in shape and transferred to the glass substrate intact retaining their particle shape.

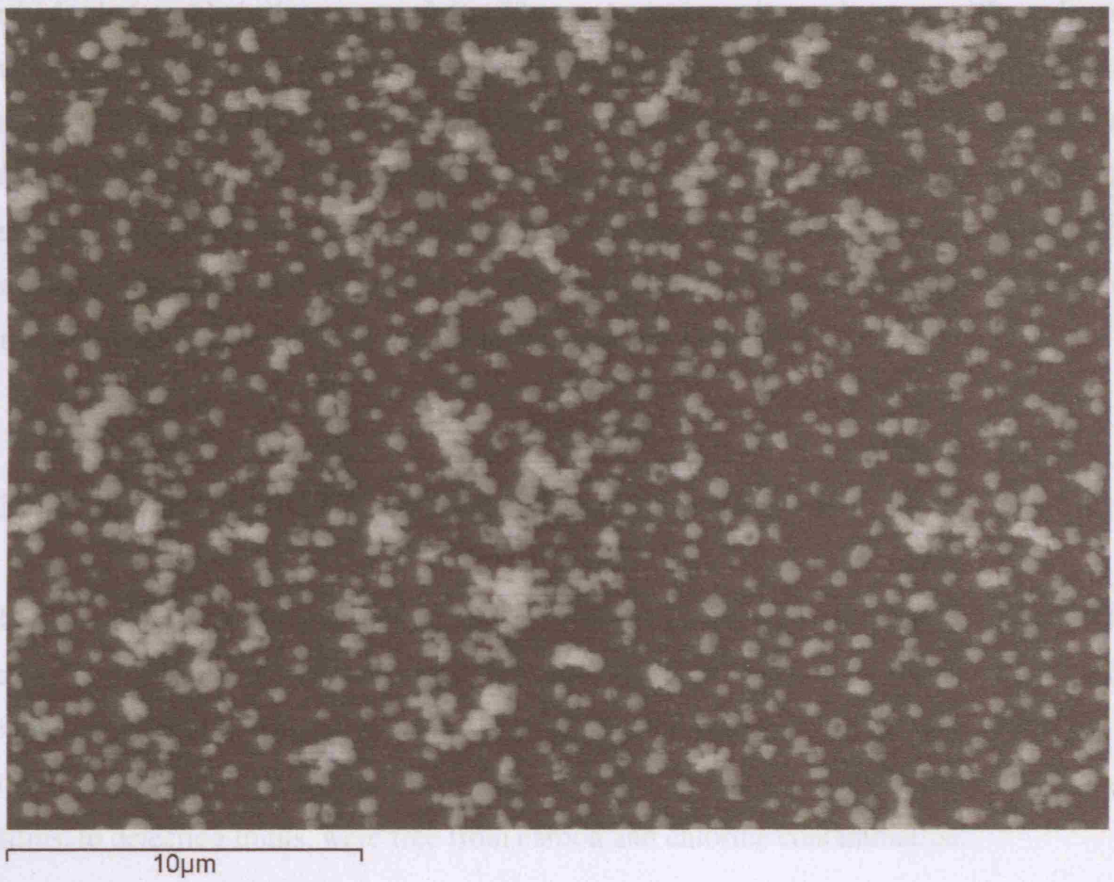


Figure 33. SEM image of a silver nanoparticle film by deposited by AACVD.

## 3.4 Film Characteristics – Silver Nanorod, Nanocube and Nanorectangle Thin Film Deposition

Two different routes to prepare silver nanorods were tested, the first a silver nanoparticle seed initiated growth, and the second a solvent induced shape evolution of PVP protected spherical silver nanorods. The seeded growth successfully formed silver nanorods from the seed Ag nanoparticle solution. This was confirmed by a change in colour of the original seed solution from yellow to the characteristic green-grey colour[181]. The PVP growth gave the solution a yellow/brown colour.

Aerosol assisted chemical vapour deposition (AACVD) of the silver nanorod solution prepared by a seed initiated growth at a substrate temperature of 500 °C and flow rates of 1 $Lmin^{-1}$ enabled silver nanorod thin films to be laid on glass substrates. These films were light green in colour and stable in air (for over a year). A PVP templated silver nanorod precursor formed a yellow thin film at a substrate temperature of 500 °C and a flow rate of 1 $Lmin^{-1}$. Both films types were very adhesive — they passed the Scotch tape test — and resisted scratching with a tissue, paper, felt and brass. The films showed minimal haze and were transparent to the eye. The films could not be removed by immersion of the films in common solvents, acid and alkali (2M).

### 3.4.1 Silver Nanorod Thin Films: Elemental Analysis

EDAX analysis confirmed that silver was present in the films formed from the PVP templated silver nanorod precursor and also from the precursor prepared by seed initiated growth. The silver was homogeneously distributed throughout the film (multiple spot analysis and wide area EDAX analysis). EDAX analysis showed that the films, to detection limits, were free from carbon and chlorine contamination.

UV-vis absorption measurements were completed to investigate the surface plasmon resonance effects of the silver nanorod thin film formation, and the ability to tune this further upon transfer of the silver nanorods to thin films on glass. Metal nanorods are known to show a second surface plasmon resonance peak; changing the nanoparticle shape can extend the peak further into the infra-red to a longer wavelength[182]. Elongation in one dimension causes the plasmon resonance to split into 2 bands. This is due to the oscillation of electrons along the major rod axis in addition to the oscillation perpendicular to this axis[32].

The UV-vis measurement for the aqueous silver nanoparticle seed solution is shown in Figure 34. Here a surface plasmon peak can be seen at 400 nm for the nanoparticle seed solution, this value is comparable to the reference value for silver nanoparticles. Figure 34 also shows the UV for the aqueous nanorod solution. There was a change in the UV surface plasmon resonance peak upon formation of the nanorods from the seed solution,

indicating that silver nanorods had indeed been formed. This was confirmed by TEM imaging which showed rods of dimension 7 by 30 nm. However there was no split in the surface plasmon resonance peak, perhaps due to the broad nature of the surface plasmon leading to a fusion of the two peaks. There was no change in the peak upon change in the host solvent, toluene.

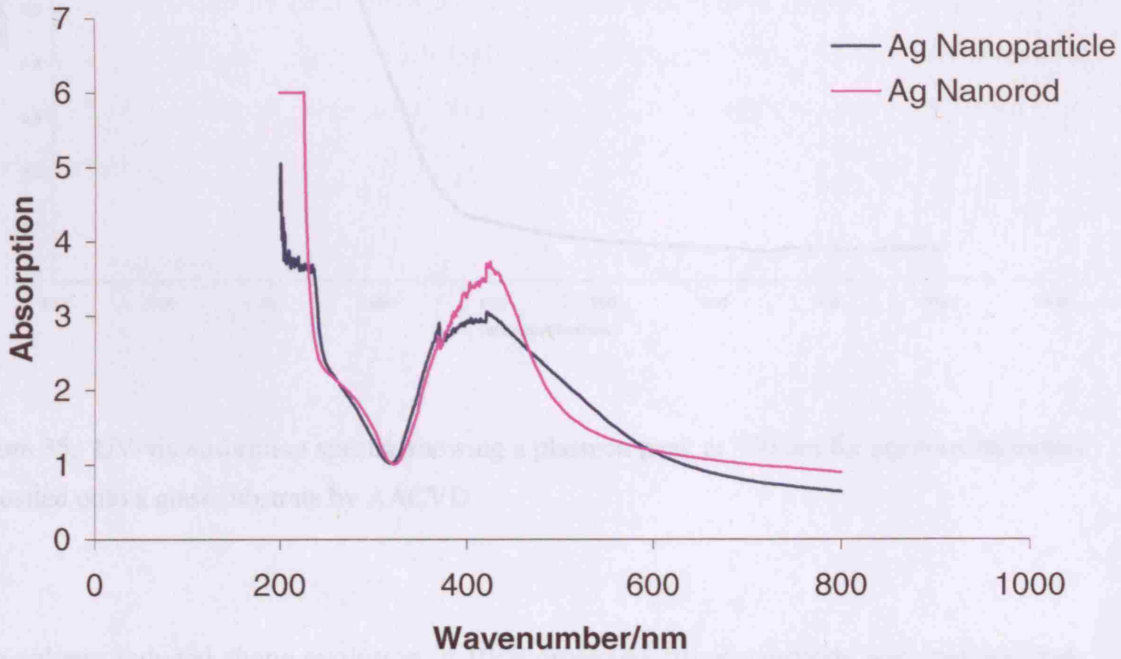


Figure 34. UV-vis absorption spectra showing a change in the plasmon resonance peak for Ag nanorods

The UV-vis absorption spectra for the film formed from aqueous silver nanorods is shown in Figure 35, this spectrum shows a surface plasmon resonance peak representative of silver nanoparticles at 440 nm. There is a shift in the peak position and intensity due to the change in particle shape and size upon transfer to the glass substrate, as confirmed by SEM imaging.

Nanorod thin film prepared from silver nanorods synthesised in toluene did not show any surface plasmon resonance peaks representative of silver. This could be due to the very reflective nature of the thin films or perhaps the formation of silver oxide upon deposition onto the thin film surface.

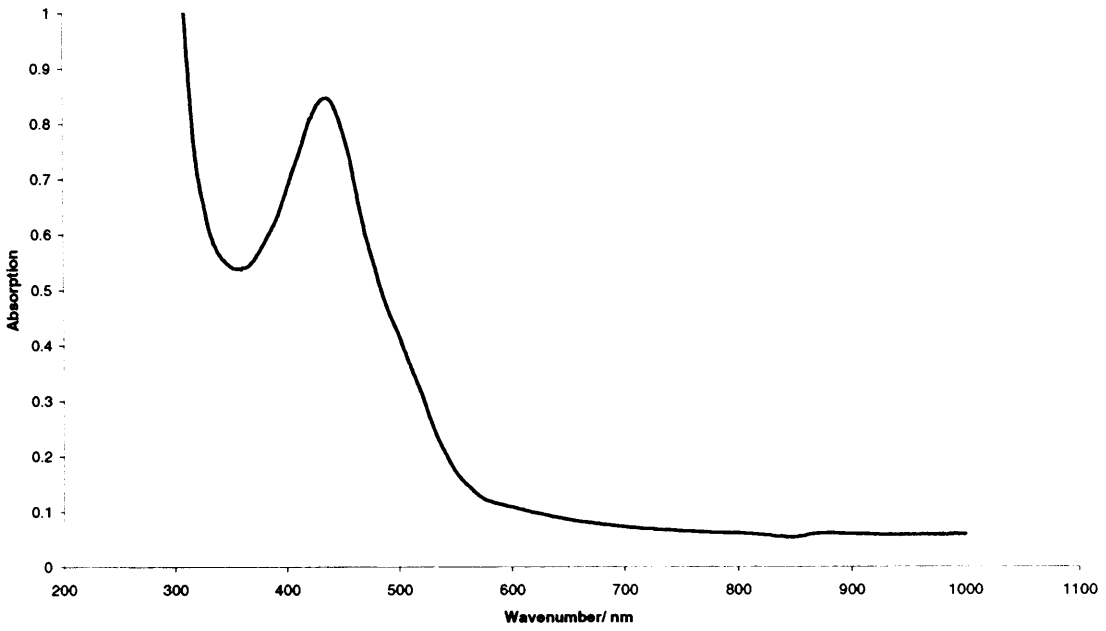


Figure 35. UV-vis absorption spectra showing a plasmon peak at 440 nm for aqueous nanorods deposited onto a glass substrate by AACVD

The solvent induced shape evolution of PVP protected silver nanorods was investigated. The reaction mixture was monitored by UV-visible spectroscopy to follow the nanoparticle growth progress. A clear increase in the plasmon peak intensity with PVP facilitated growth was seen over a 5 hour period.

The solvent induced shape evolution of PVP protected spherical silver nanorods synthesised irregular nanorod shapes. TEM imaging was used to give an idea of the dimension of the rods and capture the final nanorod growth, proving that rods of differing sizes were formed with structured morphology. Thin film deposition of the resulting solution afforded thin films that were very reflective; the silver was not particulate and behaved as the bulk metal. It is thought that this is the reason why no surface plasmon resonance peak was observed in the UV-visible absorption spectra of the thin film. However, as EDAX analysis confirmed the presence of silver in these films, it is fair to say successful transfer of the solution occurred.

### 3.4.2 Scanning Electron Microscopy For Nanoparticulate Silver Films and Their Functional Properties

Scanning electron microscopy (SEM) showed that the silver rods in the micron size regime were deposited as a thin film on glass by aerosol assisted transport (AAT), (Figure 36) from seed initiated growth with cetyl ammonium bromide. The rods are of dimension 1.5 x 0.2 μm. Since TEM imaging confirmed an original nanorod dimension of 20 x 60 nm, growth of these nanorods has occurred, maintaining the basic rod shape upon deposition.

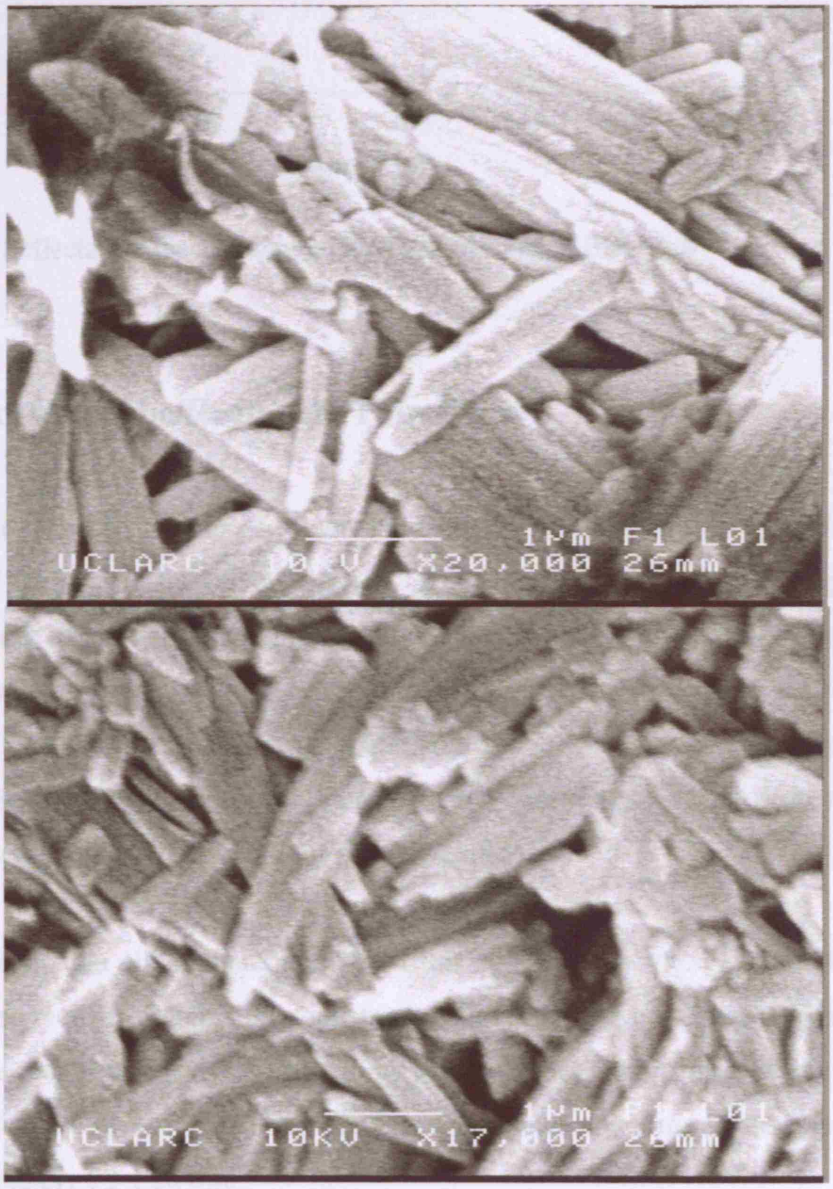


Figure 36. SEM images of micron sized silver rod films on glass deposited by AAT.

Looking at the reflectance/transmittance of the silver nanorod film prepared from PVP protected nanorods, Figure 37, the films reflect at 50 - 70 % in the near infra – red and transmit at 30 - 50 % across the spectrum.

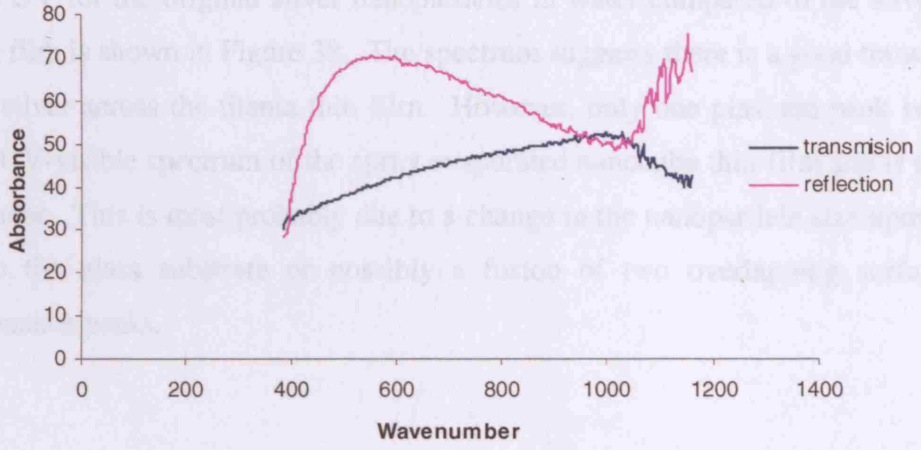


Figure 37. Reflectance/transmittance of PVP grown nanorod thin films

## 3.5 Silver Nanocube/Rectangle Thin Films

The PVP assisted formation of silver nanocubes was successful after irradiation of a solution of PVP protected silver solution for 40 hours with a halogen lamp. Towards the end of the irradiation, the colour of this dispersion became greenish blue, indicating the presence of silver nanocubes. Aerosol assisted chemical vapour deposition (AACVD) of the aqueous silver nanocube solution at a substrate temperatures of 450, 500 and 550 ºC did not deposit an adhesive film with transfer of the nanocubes intact. The films were dusty white in colour and particulate.

In comparison, the silver nanocube thin-films prepared by spray-evaporation coating were grape-green in colour and semi-transparent to the eye. These films passed the Scotch tape test — and resisted scratching with a tissue, paper, felt and pen. The films showed low haze levels (1.04 %). TEM imaging determined the size of the nanocubes as approximately 20 x 20 nm.

UV analysis of the nanocube solution confirmed silver nanocubes with the two surface plasmon resonance peaks at 430 and 680 nm. The second peak is due to the presence of a secondary nanorectangle in the nanocube solution, observed by TEM. Metal nanorods/rectangles in solution are known to display two plasmon resonance peaks[183]. The UV for the original silver nanoparticles in water compared to the silver nanocube thin film is shown in Figure 38. The spectrum suggests there is a good transferability of the silver across the titania thin film. However, only one plasmon peak is present for the UV-visible spectrum of the spray evaporated nanocube thin-film and is significantly broader. This is most probably due to a change in the nanoparticle size upon deposition onto the glass substrate or possibly a fusion of two overlapping surface plasmon resonance peaks.

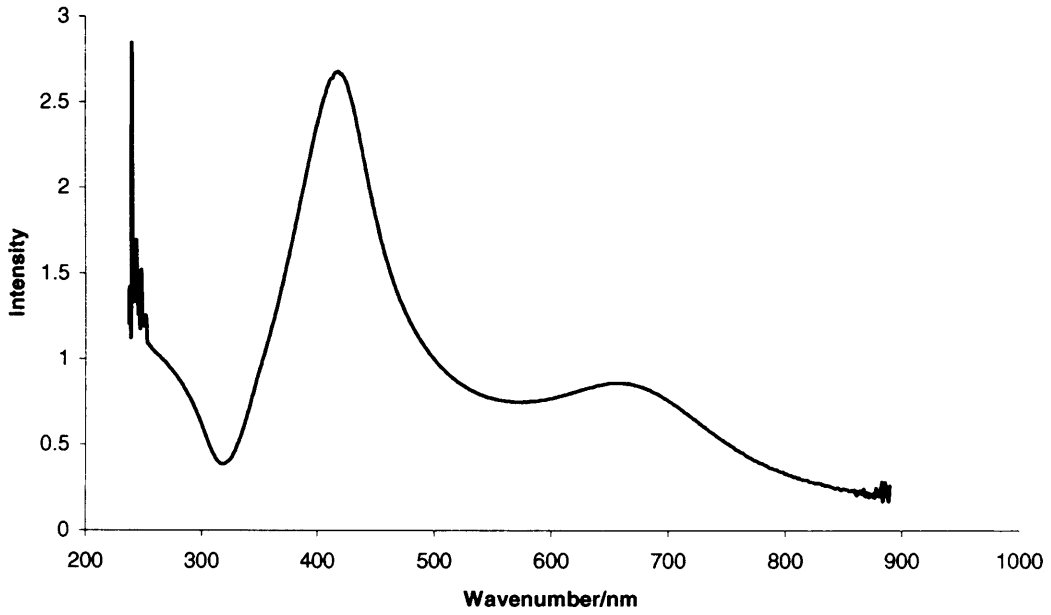


A

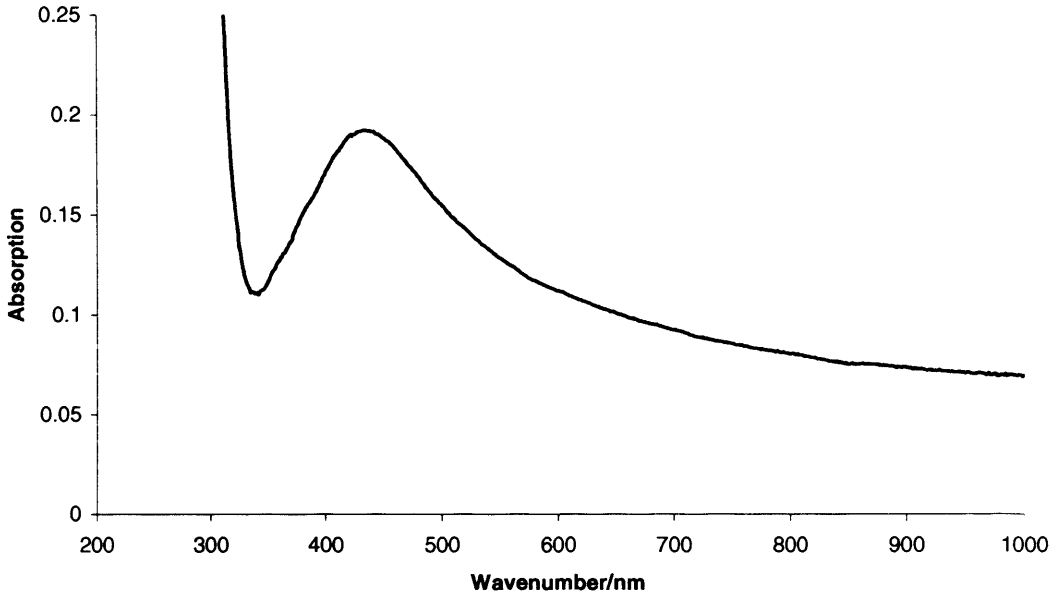


B

Figure 38 A) UV of the aqueous nanocube solution B) UV of the spray-evaporated silver nanocube film

EDAX analysis confirmed that silver was present in the films. The silver nanocubes were homogeneously dispersed throughout the film (multiple spot analysis and wide area EDAX analysis). EDAX analysis showed that the films, to detection limits, were free from carbon and chlorine contamination.

Scanning electron microscopy (SEM) of the films showed silver irregular nanocubes and rectangles (Figure 39). Larger particles were detected of length 300 nm in addition to particles with a length of 50 nm. The size of the original cubes was 20 x 20 nm, as confirmed by TEM imaging. Therefore the cubes have undergone some growth upon deposition yielding rectangular silver particle thin films.


Figure 39. SEM images of three different silver nanocube spray evaporated thin films, prepared at a substrate temperature of 250 °C.

## 3.6 Deposition of Silver Nanoparticle – Titania Thin Films By Aerosol Assisted Chemical Vapour Deposition

### 3.6.1 Film Characteristics and Elemental Analysis

Aerosol assisted chemical vapour deposition (AACVD) of the silver nanoparticle solutions alongside titania was completed at a substrate temperature of 500 °C and flow rates of 1 $Lmin^{-1}$. This enabled silver nanoparticle/titania thin films to be laid on glass substrates. The films were yellow-brown in colour, stable in air (for over a year), adhesive — they passed the Scotch tape test — and resisted scratching with a tissue, paper, felt and brass. The films showed minimal haze and were semi-transparent to the eye. The films could not be removed by immersion of the films in common solvents, acid and alkali (2M).

EDAX analysis confirmed that silver was present in the films. The silver nanoparticles were homogeneously dispersed throughout the titania film (multiple spot analysis and wide area EDAX analysis). EDAX analysis showed that the films, to detection limits, were free from carbon and chlorine contamination. The EDAX spectrum, below is for a Ag nanoparticle/$TiO_2$ composite thin film prepared from the simultaneous deposition of silver nanoparticles and titania in toluene (Figure 40). Here the wide area EDAX analysis gave a Ag : Ti ratio of 1:6. No carbon was detected in all film types. Films types 3, 4 and 5 (Table 2) gave lower Ag nanoparticle counts, the Ag: Ti ratio being 1:9. Additional peaks can be seen in the spectra and these are from breakthrough to the underlying glass.

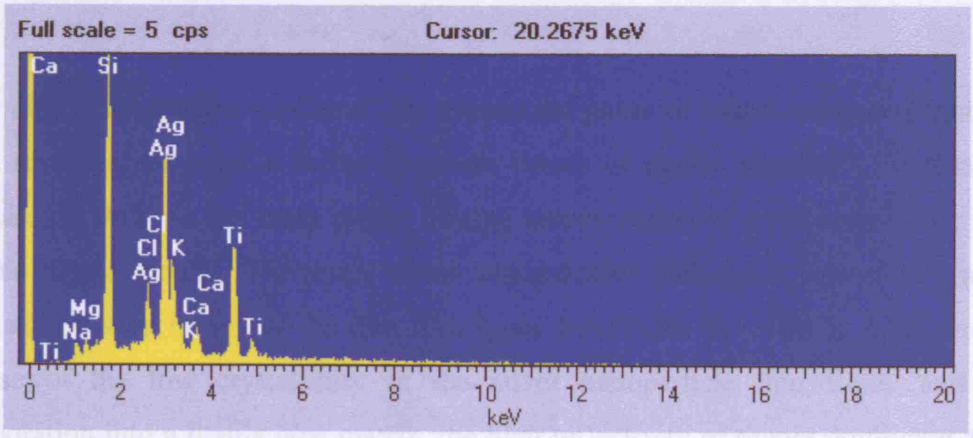


Figure 40. EDAX spectrum detecting Ag, Ti and elements contained in the coating with additional peaks seen due to the breakthrough to the underlying glass.

UV-vis absorption studies were carried out in order to investigate the relation of the surface plasmon resonance peak upon transfer of the silver nanoparticles into a titania host matrix. Figure 41 shows the UV-vis absorption spectrum for the film formed from aqueous silver nanoparticles and titania. Here a shift in the plasmon peak position is also seen to 500 nm from the original silver nanoparticle UV-vis spectrum reported earlier. The nanoparticles enter a material of different refractive index and this leads to a shift in the plasmon resonance peak. Identical behaviour was observed for the silver nanoparticle/titania thin films deposited by an alternating layer-by-layer deposition.

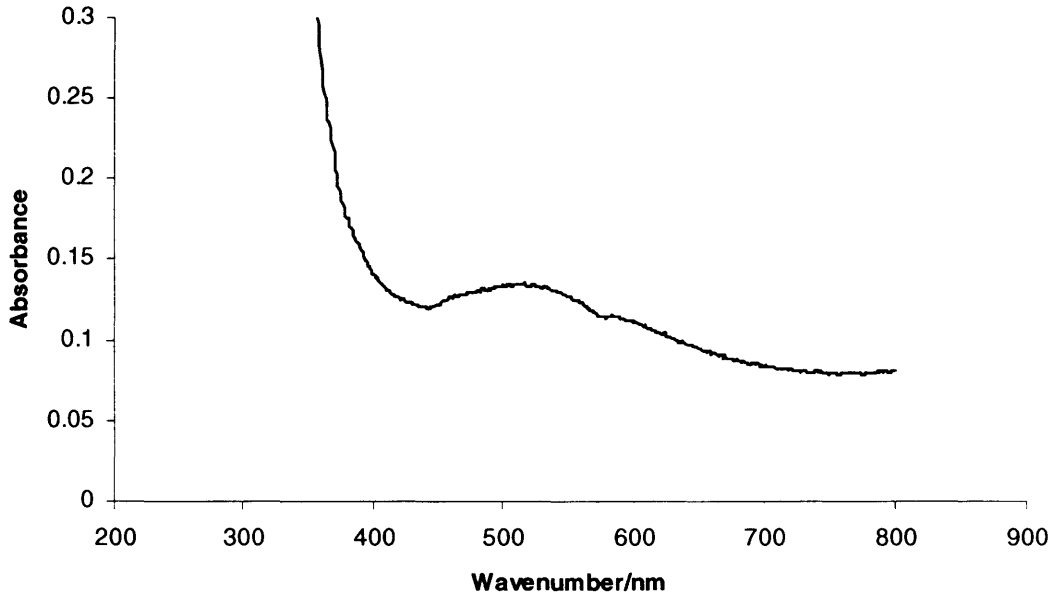


Figure 41. UV spectrum of thin films of aqueous silver nanoparticles incorporated into a host titania matrix.

X-ray diffraction studies confirmed the crystalline phase of titania anatase (Figure 42). Peaks seen are comparable to the literature values of titania anatase[184]. Furthermore there are no shifts in the main peaks, hinting incorporation of a nanoparticulate phase into the titania matrix. However, silver nanoparticles (reference values 36 and 44°) could not be seen in any of the thin film types 1-6 (Table 2). This is most probably because of the low crystallinity of the silver nanoparticle thin films, and upon incorporation into a titania host matrix, the high reflectivity of titania dominates the X-ray diffraction pattern. However, EDAX analysis confirmed the ratio of silver to

titanium in these films as 1:6 and this forms a good basis to comment on the activity of silver influencing any optical and functional properties.

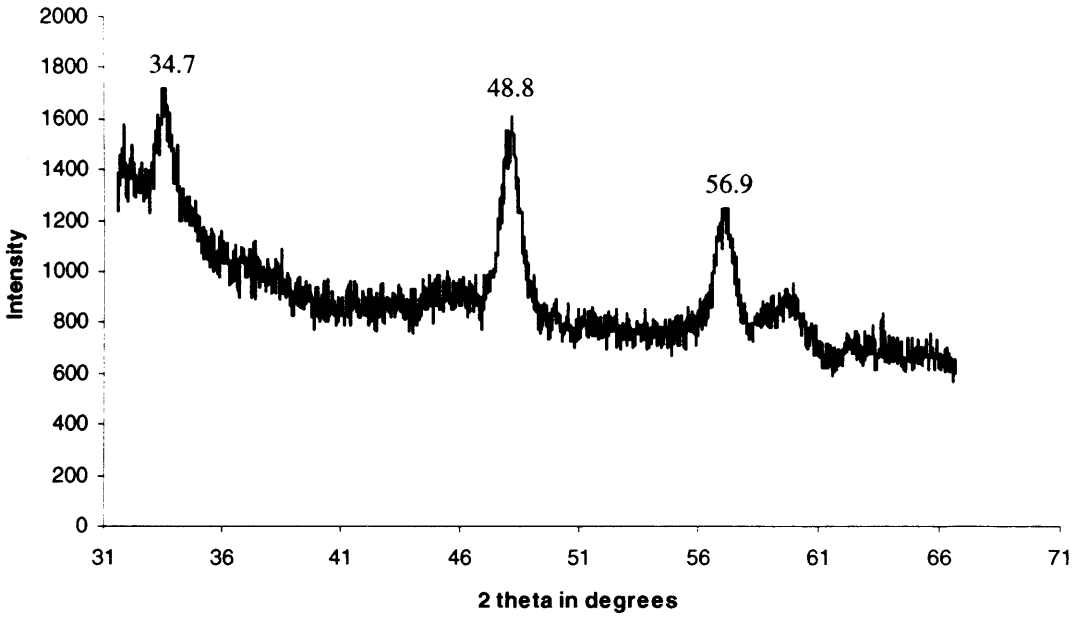


Figure 42. XRD data for an Ag nanoparticle/titania film simultaneously deposited at 500 °C, confirming the anatase phase of titania.

## 3.6.2 Scanning Electron Microscopy: Growth Morphology For Nanoparticulate Silver Films

Scanning electron microscopy (SEM) showed that the silver nanoparticle – titania films formed with island growth morphology (Figure 43). Larger particles were detected of diameter 200 nm in addition to particles of diameter 30 nm. These smaller particles are thought to be silver and the larger particles titania. However this was difficult to confirm due to restrictions in the spatial resolution. In some instances, the Ag nanoparticles were clustered together and a micron in size. Figure 43A shows SEM images of silver nanoparticle and titania films grown by layer-by-layer growth in toluene (film type 3). Figure 43B shows SEM images for silver nanoparticle incorporated titania films using a mixed precursor in toluene (film type 6). The SEM images show particles that are 30-100 nm in diameter, along with nanoparticles of

approximately 10 nm diameter. No evidence is seen for the deposition of thin film layers, growth of initial layers of titania or silver (depending on which layer is deposited first) is thought to have promoted island type growth rather than layer by layer deposition.

A

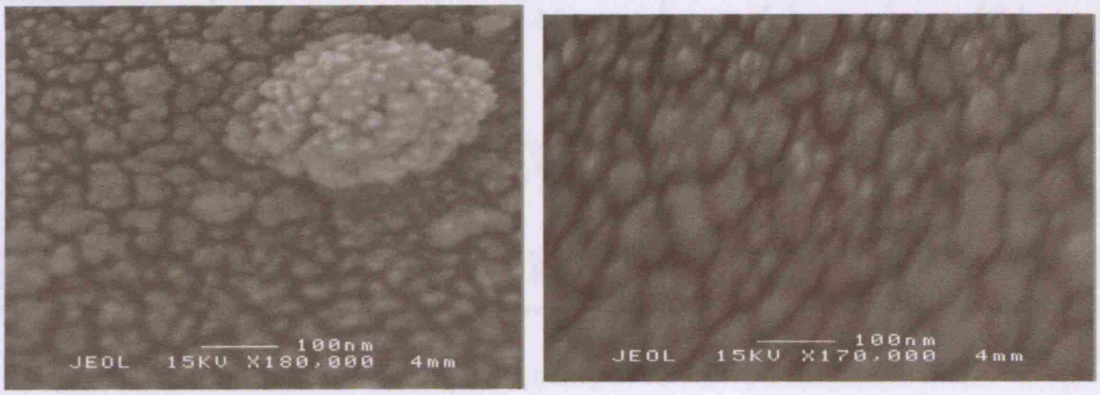


B

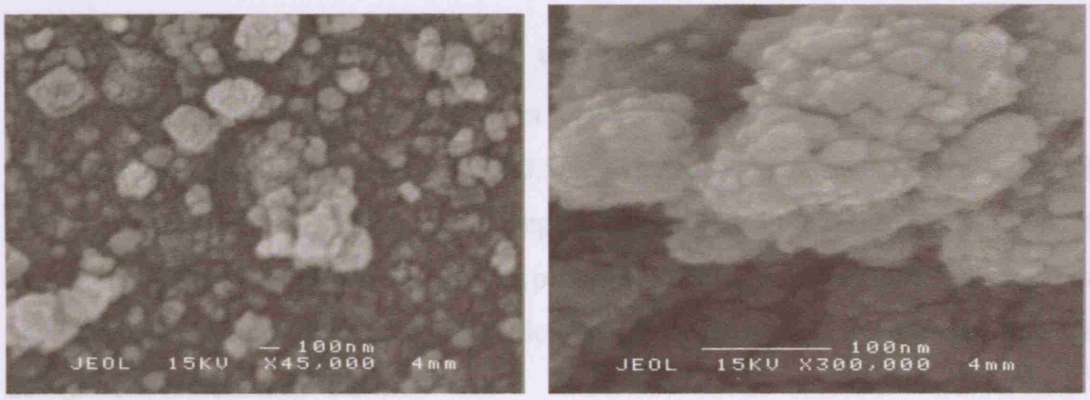


Figure 43. Images of silver nanoparticle incorporated titania films by A) layer growth (film type 3) and B) mixed precursor and nanoparticle solution (film type 6)

### 3.6.3 Functional Analysis For Nanoparticulate Silver Films and Spherical Silver Nanoparticles Embedded in a $TiO_2$ Host Matrix

The silver/titania composite films exhibited photo-induced super-hydrophilicity (Table 3) and were also photocatalytically active (Figure 44). The photo-induced super-hydrophilicity was enhanced compared to a plain titania film and this shows promise as an optical coating[185].

| Film Type | Time /hr<br>0 | 1 | 2 | 24 hrs in the dark |
|---|---|---|---|---|
| Ag/$TiO_2$ layers (water) | 11.6 | 3.7 | 2.9 | 11.8 |
| Ag/$TiO_2$ layers (toluene) | 12.2 | 6.4 | 2.8 | 13.8 |
| Ag/$TiO_2$ (toluene, mixed precursor) | 10.2 | 2.6 | 4.4 | 12.6 |
| Ag/$TiO_2$ (toluene mixed precursor) | 8.4 | 2.4 | 2.4 | 10 |
| $TiO_2$ | 30.2 | 8.6 | 5.4 | 27.9 |

Table. 3 Water contact angle (θ°) data for Ag nanoparticle incorporated titania films.

The initial contact angles for film types 3-6 (Table 2) were 8 - 12° indicating that the surface is hydrophilic. This water contact angle dropped to 2 - 6° upon exposure of the film surface to 254 nm UV radiation for 0.5 hr. This value then increased to the original contact angle prior to irradiation upon keeping the samples in the dark for 24 hrs. These results compare well with the control experiment carried out for titania anatase which gave contact angles of 9° prior to irradiation and 2° upon exposure of the film surface to 254 nm UV radiation for 0.5 hr.

All silver nanoparticle/titania films showed enhanced photocatalytic activity, degradation of stearic acid was much faster than for a titania anatase thin film prepared in the same manner (Figure 44). Silver nanoparticle/titania (film type 6) destroyed a stearic acid overlayer at a rate of 9.4 x $10^{13}$ molecules $cm^{-1}min^{-1}$. In comparison, a control titania anatase thin film destroyed the stearic acid over layer at a rate of 3.2 x $10^{12}$ molecules $cm^{-1}min^{-1}$. This clearly shows an increase in the degradation upon silver nanoparticle incorporation as surface area and crystallinity were constant.

Previously, sol-gel synthesised Ag nanoparticle/anatase thin films have also shown Ag nanoparticles to enhance the photocatalytic activity of titania anatase[186, 187, 188]. Chao *et al*

have completed research in this field[189]. They postulate that the enhanced activity is due to a number of factors, the first a decrease in anatase grain size upon incorporation of the silver nanoparticles allowing the surface area of $TiO_2$ to increase promoting charge transfer in the films. The increase in activity is also due to enhanced electron-hole pair separation including inhibition of their recombination. The silver effectively enhances the charge pair separation efficiency for the titania anatase thin films[190].

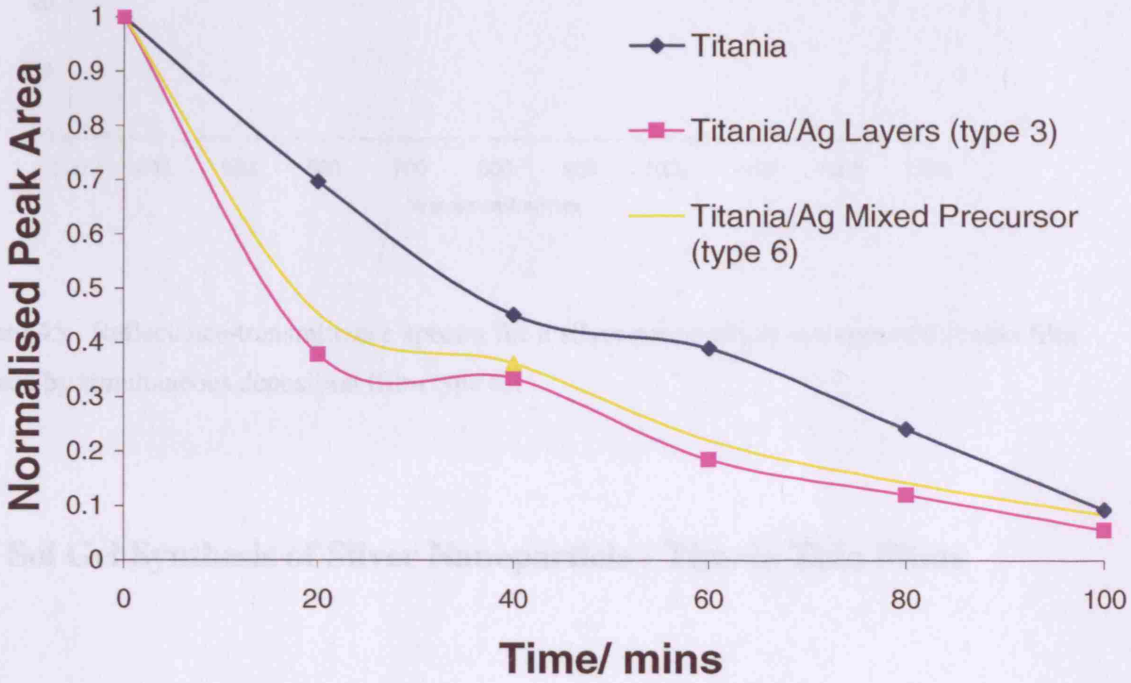


Figure 44. Photocatalytic activity for Ag nanoparticle incorporated titania films deposited in layers (type 3) and also by simultaneous deposition (type 6). A decrease in normalised peak area is seen.

Looking at Figure 45, the reflection/transmittance spectra for film type 6, Ag nanoparticle/titania thin films, the absorption edge is shifted to shorter wavelengths as compared to titania anatase. At room temperature, the films transmit across most of the spectrum from 55 % to 75%. The films reflect in the region of 40 – 50 %.

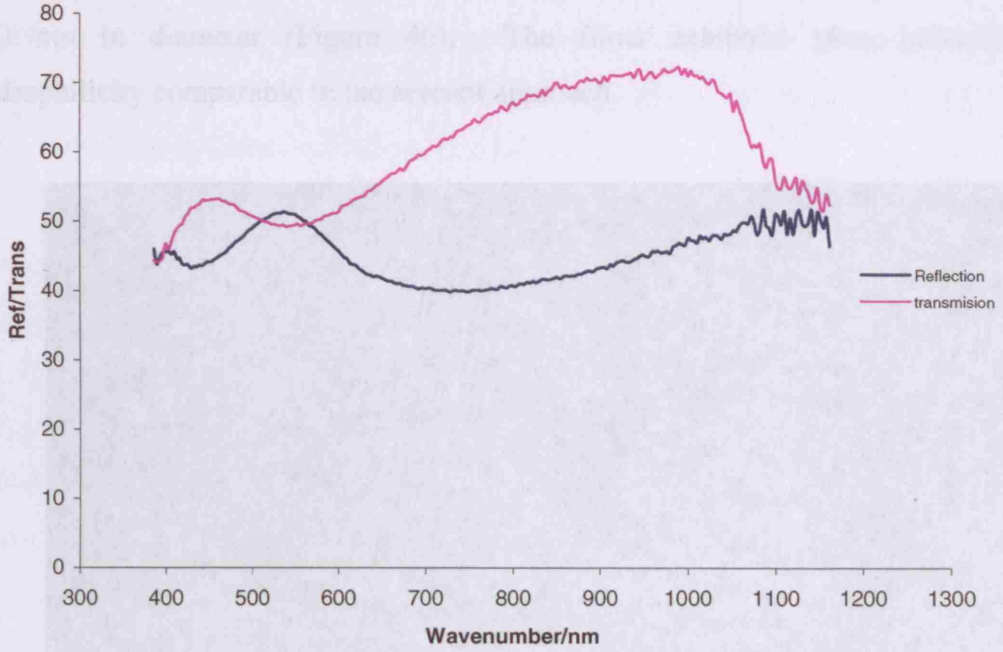


Figure 45. Reflectance-transmittance spectra for a silver nanoparticle incorporated titania film formed by simultaneous deposition (film type 6).

## 3.7 Sol Gel Synthesis of Silver Nanoparticle - Titania Thin Films

To investigate further the potential properties of these precursors, Ag nanoparticles were incorporated into a titania host matrix by the sol-gel process. Initially silver nanoparticles were coated on to the glass slide. Ten coats of the Ag nanoparticle solution were applied using a dip coater at a rate of 2 withdrawals per minute. UV-visible absorption analysis for sol-gel Ag nanoparticle films did not show any surface plasmon resonance peaks. However, EDAX was able to detect Ag. SEM and EDAX clearly confirmed nanoparticles with a diameter of 5 nm. These films did not show any enhanced optical properties over the aerosol assisted CVD approach and transmitted/reflected well across most of the spectrum.

UV for sol-gel titania/Ag nanoparticle films did not show any peaks- this could be due to the reflective nature of the films. However EDAX was able to detect titania and

silver. Particles were detected of diameter 10 nm in addition to larger particles that were 100 nm in diameter (Figure 46). The films exhibited photo-induced super-hydrophilicity comparable to the aerosol approach.

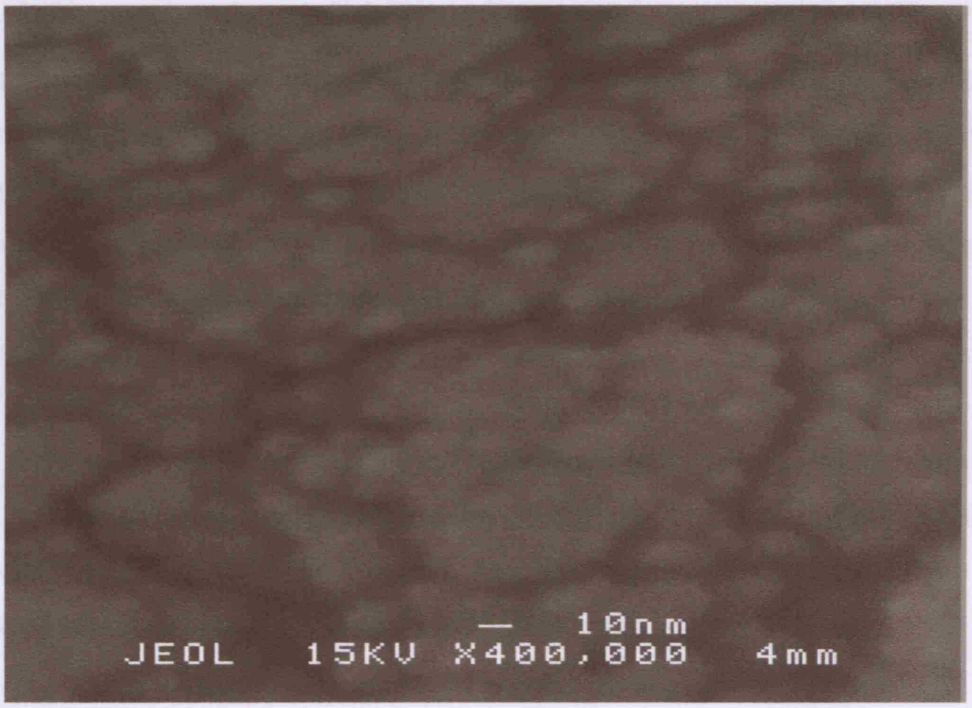


Figure 46. SEM image for a sol gel deposited Ag nanoparticle/titania thin film

The films deposited by the sol gel process did not show any enhanced or different properties to those prepared by AACVD.

## 3.8 Discussion

Sun and Xia have reported the synthesis of monodisperse silver nanocubes (100 nm) by reduction of silver nitrate with ethylene glycol[66]. Here, ethylene glycol is both a reducing agent and solvent and *poly*(vinylpyrrolidone) is used as a capping agent. They showed that the size of the silver nanocrystals can be easily varied by controlling the experimental conditions such as temperature, metal salt concentration, metal/stabiliser ratio, and growth time[66]. Under certain conditions, large quantities of highly symmetric

silver nanocubes with size ranging from 50 to 100 nm can be obtained. Recently, highly mono-disperse myristate capped silver nanoparticles have been reported[68]. However, there are no reports for transfer of these silver nanoshapes onto glass for thin film deposition by chemical vapour deposition.

Aerosol assisted chemical vapour deposition (AACVD) has previously been used to deposit metallic silver coatings from silver carboxylates and silver sulfides from silver thiolates[69,70]. These silver coatings show useful transmission-reflection properties and sulphide films have potential for use in ion insertion batteries or as lubricants[71]. However, the majority of work on silver nanoparticle thin films has been via the sol gel process[72].

Thin films of silver nanoparticles have also been found to exhibit a photovoltaic effect[73]. The study of silver nanoparticles of different size and shape combinations embedded within a silica host matrix has been extensively studied- these films displayed enhanced optical properties such as high transmission[74].

Parkin *et al* have shown that sol-gel deposited thin films of silver nanoparticles incorporated within a host titania matrix significantly enhance the photocatalysis and antimicrobial properties of titania[75]. This result was also obtained in the work reported in this thesis, where the AACVD deposited silver nanoparticle/titania thin films exhibited greater photocatalysis compared to a control titania thin film deposited under the same deposition conditions. Prior to this research, no work has yet been reported on the AACVD of silver nanoparticles and nanoshapes incorporated within a host titania matrix.

He *et al* have studied the effects of silver doping on the microstructure and photocatalytic activity of titania by the sol-gel process[191]. There is a marked increase in the photocatalytic activity of titania upon doping with silver by one order of magnitude. This is due to promotion of charger transfer and greater electron-hole separation in the presence of silver. This work has also been researched by Chao *et al*[192].

Ryu *et al* have researched the effect of silver on the optical properties of titania. They found that these films have high transparency in the range 400-1000 nm[193]. In this

thesis, the silver nanoparticle/titania films transmit across most of the spectrum from 55 % to 75%.

## 3.9 Conclusion

In conclusion, a number of silver nanoparticle thin films on glass were deposited. Two different methods were used to prepare silver nanoparticles, the first method was a sodium citrate reduction in water, and the second a sodium borohydride reduction in toluene. These were used to successfully deposit thin films incorporating nanoparticles within a host matrix by AACVD. Silver nanorods were also formed by preparation of a seed solution followed by nanorod growth. The solvent induced shape evolution of PVP protected silver nanorods was also studied. Silver nanocubes were prepared by PVP addition and halogen lamp irradiation.

Silver nanoparticles in water were successfully deposited as thin films on glass via AACVD. This was repeated with the silver nanoparticles prepared in toluene. These nanoparticles were incorporated within a titania host matrix by two different approaches, the first involved depositing alternating silver and titania layers, and the second approach transferred both as a mixed solution to the substrate. The latter was only applicable to silver nanoparticles prepared in toluene, as the addition of titania into an aqueous solution would result in the hydrolysis of titania. Silver nanorods were prepared using cetyl ammonium bromide as a reducing agent and then deposited as thin films.

The AACVD of silver nanorods formed micron sized rods. In comparison, the spray-evaporation coated silver nanocubes deposited rectangular shapes. These films showed useful optical properties and merit further investigation for use as an optical window coating. Very few reports of the optical properties of silver nanoshape thin films have been published. Tuning the plasmon resonance within the titania host matrix is definitely an extension for future research.

The work completed in this thesis reports on the optical and functional properties of silver nanoparticles thin films. It has been reported here that silver nanoparticles not only enhance the optical properties and give rise to interesting tuneable surface plasmon resonance effects, but also show a marked increase in photocatalytic activity and enhanced photo-induced super-hydrophilicity. This shows potential for applications as window coatings especially in hospitals where there is a greater risk of MRSA contaminations; use of silver nanoparticles as antibacterial window coatings is an attractive option. Furthermore, silver nanoparticles give rise to a light yellow colour which can prove useful for when yellow is the desired window colour.

# Chapter 4:

# Combined Aerosol Assisted – Atmospheric Pressure Chemical Vapour Deposition: Deposition of Au/$TiO_2$Thin Films

## 4. 1 Introduction

A new combined chemical vapour deposition method was developed using simultaneously aerosol assisted and conventional atmospheric pressure chemical vapour deposition. This enabled films of Au nanoparticles within a host titania matrix to be grown from a suspension of synthesised nanoparticulate gold in toluene. This method is based on aerosol assisted chemical vapour deposition, which uses a liquid-gas aerosol to transport soluble precursors to a heated substrate. It was shown that preformed gold nanoparticles could be transported in an aerosol generated ultrasonically, and deposited into a growing film alongside transport of the titania precursor by APCVD. The Au/$TiO_2$ films formed in this process have unusual optical properties, appearing red in reflected light and blue in transmitted light. The Au nanoparticles deposited as nanocubes. The Au nanoparticle/$TiO_2$ thin films were photoactive and super-hydrophilic. These films showed unusual microstructures not obtained by sol-gel or evaporation routes. Furthermore, the high reflectance generated by these films means they have potential for solar control applications[194].

The method and apparatus used to co-deposit these thin films was designed in house and could potentially be incorporated into float glass production lines.

## 4. 2 Experimental Design

### 4.2.1 Gold Nanoparticulate Films

Titanium tetraisopropoxide was obtained from Aldrich and used as supplied (99% purity). Gold nanoparticles were synthesised in both water and toluene, by the methods outlined in the experimental section.

Gold nanoparticles as synthesised above, were used to deposit films at 500 °C and at a $N_2$ carrier-gas flow-rate of 0.5 L $min^{-1}$.

## 4.2.2 Titanium Dioxide- Gold Nanoparticle Composite Films

The titania precursor, 0.56 g of titanium isopropoxide (Aldrich) was transferred into the APCVD bubbler. Gold nanoparticles (5 mL in 20 mL toluene) were placed in the PTFE AACVD bubbler. Simultaneous deposition enabled the AACVD process to supply a mist of toluene containing gold nanoparticles, whereas the APCVD connection provided a titanium isopropoxide mist, Figure 47. These mists were allowed to mix in the mixing chamber by a concentric tube entrance to the chamber, Figure 48. The combined mist was then directed to the reactor, which enabled deposition of gold nanoparticles incorporated within a host matrix.

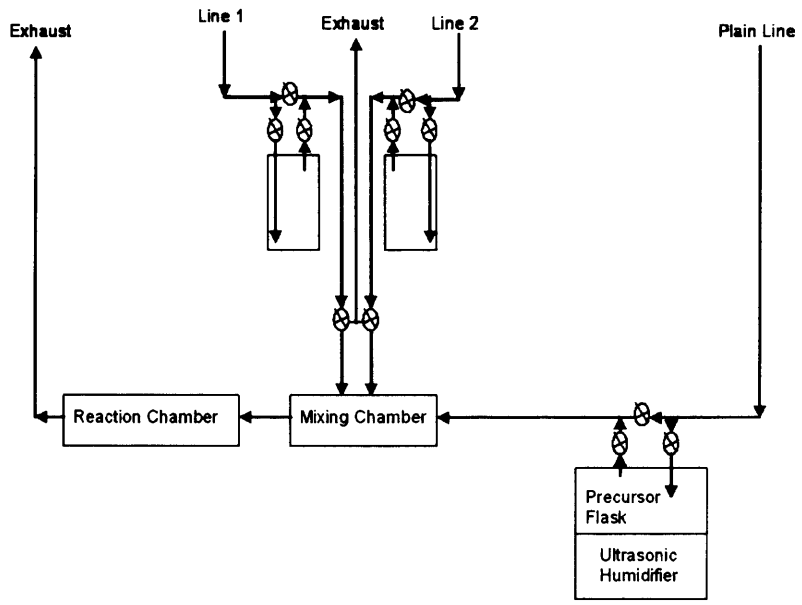


Figure 47. Schematic of the AA/APCVD set-up

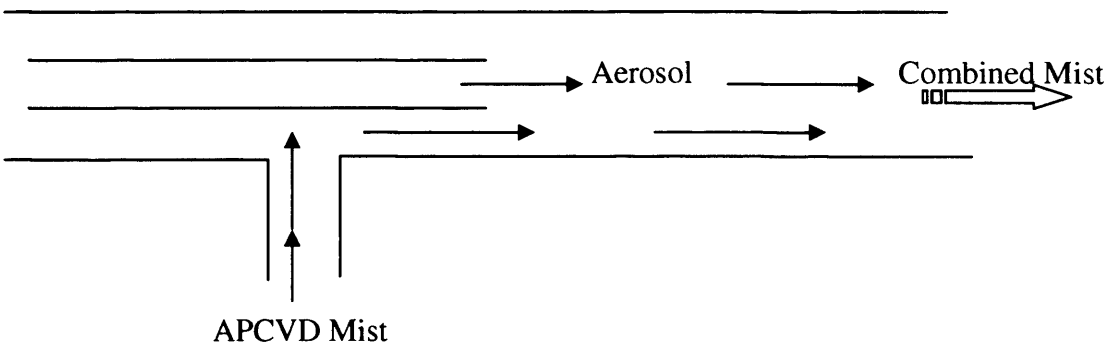


Figure 48). Schematic of the AA/APCVD connection tube.

Above is a schematic of the connection tube at a scale of 1:2. The inner tube is connected to the aerosol apparatus whereas the outer tubing connects to the APCVD mixing chamber. The two streams combine within the connection tube, undergo mixing and then enter the manifold which leads into the CVD cold walled reactor.

## 4. 3 Film Deposition Parameters

Two types of film were deposited: Au nanoparticle thin films on glass and Au nanoparticles embedded in a $TiO_2$ host matrix. The flow rates and volumes of solvent were selected to give the most extensive deposition over the substrate. Deposition of Au and Au/$TiO_2$ thin films on glass were carried out as shown in Table 4.

| Au colloid used/ mmol | Precursor/ mmol | Molar ratio Au:precursor | Solvent/ mL | Aerosol flow rate/ $Lmin^{-1}$ | AP flow rate/ $Lmin^{-1}$ |
|---|---|---|---|---|---|
| 0.5 | None | | Toluene/ 50 | 0.5 | 0.1 |
| 0 | $[Ti(O^iPr)_4]$ / 1 | | Toluene/ 50 | 0.5 | 0.1 |
| 0.5 | $[Ti(O^iPr)_4]$ / 1 | 1:2 | Toluene/ 50 | 0.5 | 0.1 |
| 1 | $[Ti(O^iPr)_4]$ / 1 | 1:1 | Toluene/ 50 | 0.5 | 0.1 |
| 1.5 | $[Ti(O^iPr)_4]$ / 1 | 2:1 | Toluene/ 50 | 0.5 | 0.1 |

Table 4. Parameters used to deposit nanoparticle and nanocomposite thin films

## 4.4 Deposition of Au Nanoparticle Films Using AACVD

### 4.4.1 Film Characteristics and Elemental Analysis of Au Nanoparticle Films Using AACVD

Gold nanoparticle thin films were prepared on glass from the aerosol assisted transport of synthesised nanoparticulate gold. The deposition of gold nanoparticles from gold colloid solutions occurred on both the substrate and the top plate, which is the glass plate that rests 8 mm above the surface of the substrate. The films were uniform and blue in transmitted light and purple with a metallic luster in reflected light. They covered the entire glass substrate. The films passed the Scotch tape test, were adhesive, but could be scratched with both a brass and steel stylus. The films were stored and handled in air with no apparent degradation; however, the films were non-adherent and could be easily removed by slight mechanical abrasion and could be wiped with a tissue, indicating that the gold particles were weakly adsorbed on the glass surface rather than strongly bound to it or absorbed within it.

EDAX and UV-visible absorption spectra confirmed the formation of gold nanoparticles, the surface plasmon resonance peak representative for gold nanoparticles was observed in the UV. The wavelength of the surface plasmon resonance absorption maximum depends on the size and shape of the particles[27]. The UV-visible absorption spectra for the original gold nanoparticles in toluene showed a surface plasmon resonance peak at 550 nm, which is comparable with reference values (Figure 49) [195]. However, the UV-visible absorption spectra for the Au nanoparticle thin film shows the peak is shifted to two merged peaks, one at 550 nm and the other at 600 nm. This is most probably due to the partial clustering of the nanoparticles on the glass substrate[196]. It could also mean a change in the nanoparticle size/shape upon deposition onto the glass substrate. This corresponds well with the SEM images of the thin films, where nanocubes of dimension 20 – 80 nm were seen.

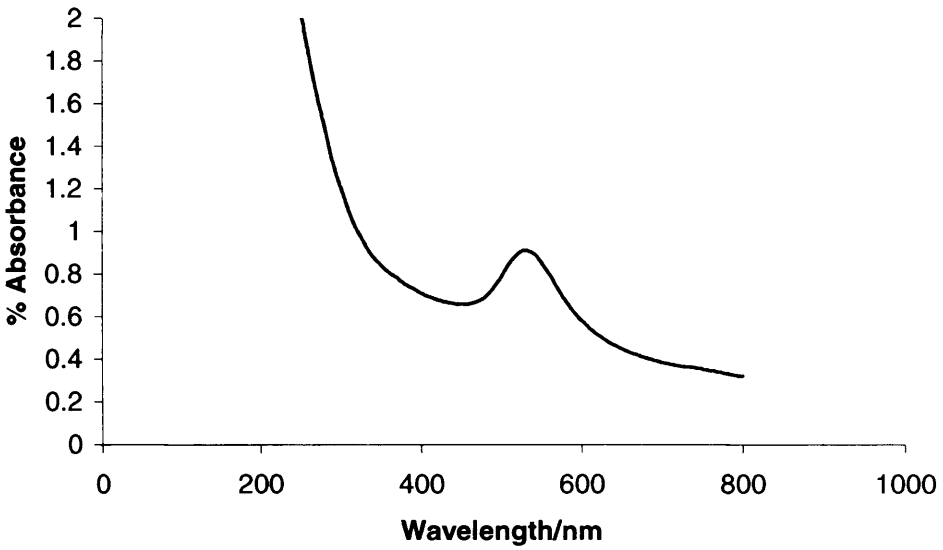


A

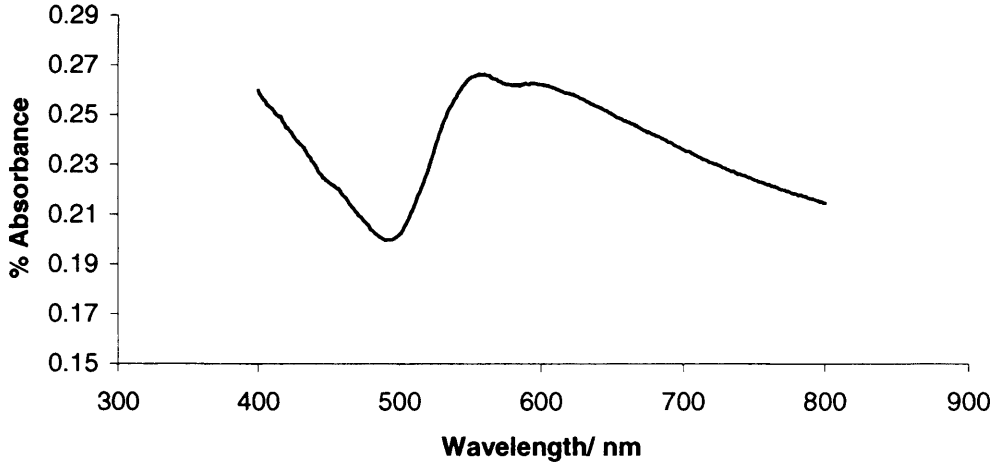


B

Figure 49. UV spectrum of A) the original Au nanoparticle solution and B) the Au nanocube thin film showing surface plasmon resonance peaks at 550 and 600 nm respectively.

Au 4f 7/2 and 5/2 peaks at binding energies of 87.5 and 83.7 eV, respectively, and 4d peaks corresponding to metallic gold, were observed by XPS (Figure 50)[197]. X-ray powder diffraction of the gold nanoparticle films showed that the films indeed contained gold nanoparticles. The X-ray pattern of the thin film indicates that there is no significant preferred orientation of the crystallites on the surface (Figure 51).

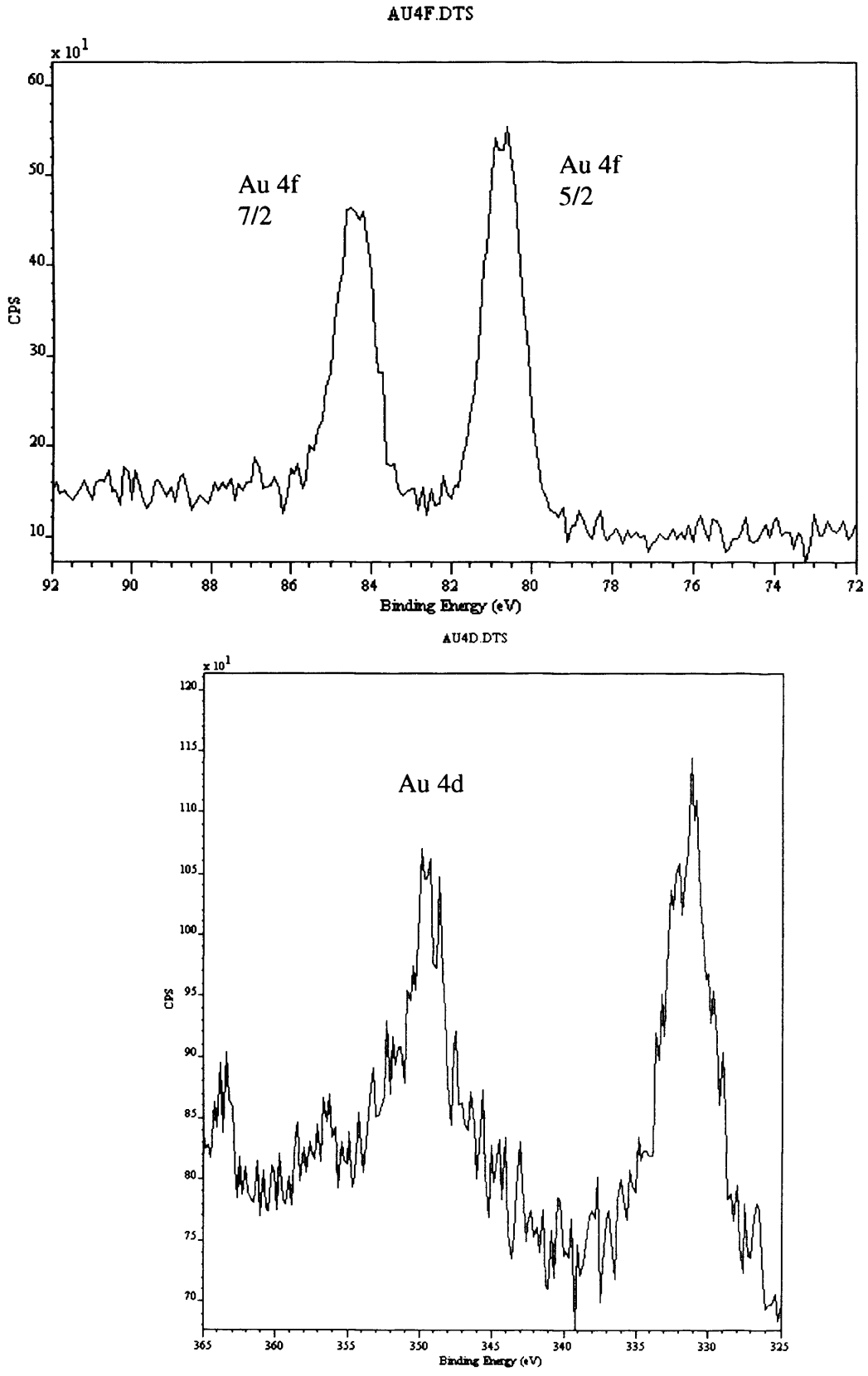


Figure 50. XPS data for the Au nanocube thin film made by aerosol assisted chemical vapour deposition.

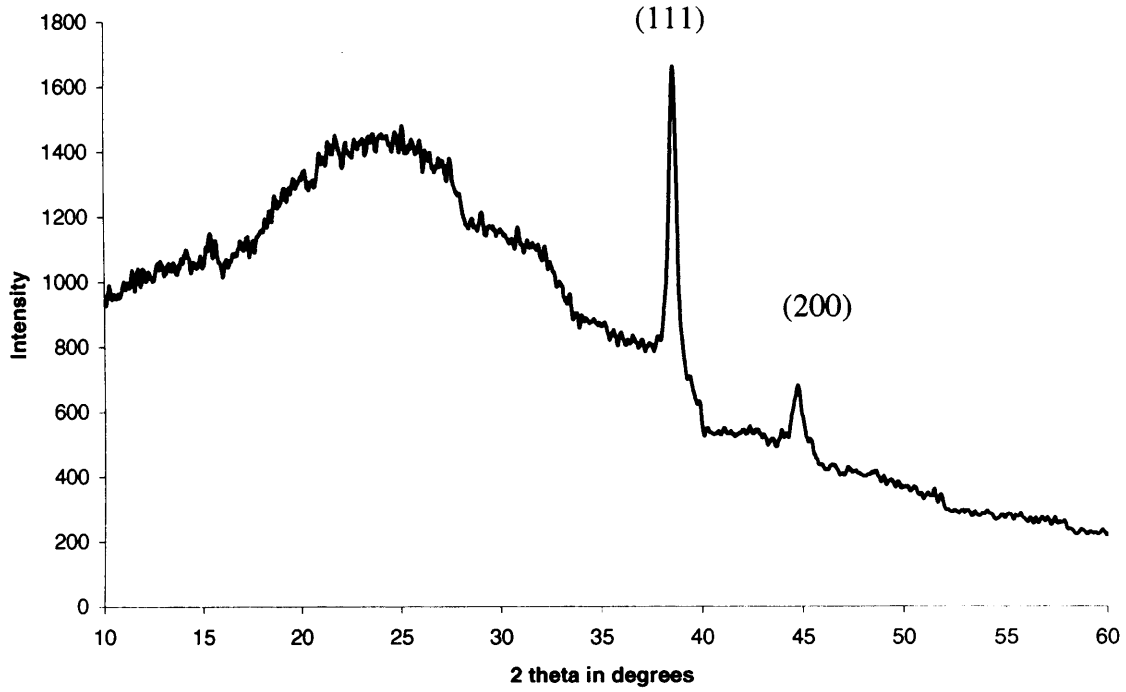


Figure 51. XRD pattern of a gold nanoparticle thin film made by aerosol assisted CVD. An amorphous background is seen.

## 4.4.2 SEM Study of Au Nanoparticle Films Using AACVD

The initial gold nanoparticle solution examined by TEM before the aerosol assisted process showed the solution was made up of spherical particles of dimension 10 – 50 nm (Figure 52A). Scanning electron microscopy of the gold films formed from spherical gold nanoparticles showed a dense continuous film made up of interlocking cubes of approximate size 30-100 nm, Figure 52B. EDAX analysis showed that the films contained only gold. Therefore a change in the particle shape occurs upon deposition onto the glass substrate, perhaps complimented by the new aerosol into APCVD design. Combination of the aerosol and APCVD mists could assist with the formation of nanocubes, or the reactor dynamics associated with the new apparatus. This suggests that certain CVD dynamics favour formation of gold nanocubes as compared to spherical nanoparticle deposition. It is thought that cube formation occurs

either whilst the aerosol mist undergoes transformation to gaseous intermediate species or upon deposition/nucleation on the glass substrate.

A

B

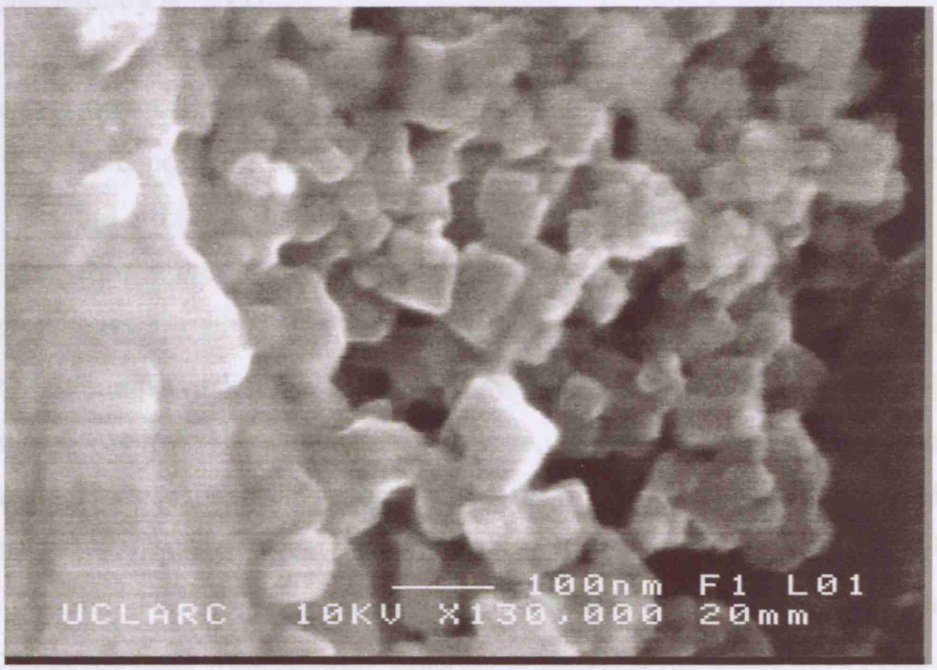


Figure 52. A) TEM image of the original Au nanoparticle solution B) SEM image of an Au nanocube thin film produced by aerosol assisted CVD at 500 °C.

The apparent increase in particle size and change in shape from spherical particles to nanocubes could be due to agglomeration of the particles either in the gas phase or on the substrate surface. No nitrogen or bromine were observed in the XPS spectrum, indicating that atoms from the tetraoctylammonium bromide used in the synthesis, which prevented particle agglomeration in solution, are no longer present, this is also a consideration for the conversion to nanocubes.

## 4.5 Deposition of Au Nanoparticle/$TiO_2$ Films Using AP/AACVD

### 4.5.1 Film Characteristics and Elemental Analysis of Au Nanoparticle/$TiO_2$ Films Using AP/AACVD

Combined aerosol assisted CVD and conventional atmospheric pressure chemical vapour deposition was used to deposit films of gold nanoparticles incorporated within a host titania matrix. Preformed gold nanoparticles were transported in an aerosol generated ultrasonically, and deposited into a growing film alongside transport of the titania precursor by APCVD.

A deposition time of 25 minutes, enabled both the Au nanoparticles and titania host matrix to be co-deposited resulting in a composite film. Titania films were deposited with 1, 2 and 4 mL of a 4.3 mM gold nanoparticle solution, as synthesised by the method described in the Experimental chapter (Table 4). All films were deposited at a substrate temperature of 500 °C. The films differed in thickness throughout the substrate but samples taken for analysis were approximately 4 μm in thickness at a distance of 3 cm from the start of the substrate. Undoped titania films produced by CVD are colourless or pale yellow. The titania films deposited alongside gold nanocubes were purple in colour. The intensity of the purple colour increased with gold particle content. The deposition occurred on both the substrate and the top-plate. All titania composite films were strongly adherent to the glass and could not be removed by a tissue and were undamaged through routine handling. The films could be scratched with a brass stylus and steel scalpel. Optical haze, being the percentage of D56 artificial daylight scattered by the films, was measured to be 0.37%, 0.62% and 0.78% for the

three identical Au nanoparticle - $TiO_2$ film samples. The gold nanoparticles could not be removed by immersion of the film in common solvents and acid and alkali (2M). The gold nanoparticles could not be removed by any physical method that did not also remove the titania coating, indicating that the nanoparticles are strongly bound to the film or firmly contained in it.

The colour of the thin films was quantified using the CIELAB colour co-ordinates which are used to express perceived colour (Figure 53). Two parameters $a^*$ and $b^*$, define colour: positive $a^*$ values correspond to red, negative $a^*$ values to green. Positive $b^*$ values correspond to yellow, negative $b^*$ values correspond to blue. Figure 53 shows the colour of the Au nanocube/$TiO_2$ composite thin films in both transmitted and reflected light. Transmitted light through the film is blue whilst reflected light is red, which is consistent with the visible spectra. The intensity of transmitted colour imparted by the composite film is comparable to commercial body tinted glass, despite the film being 4 orders of magnitude thinner[198]. Because extinction coefficients of gold particles are known to be greater than organic or transition metal dyes[199], these films may be used as coloured coatings. The near symmetric opposite colouration of this films in reflected and transmitted light is unusual.

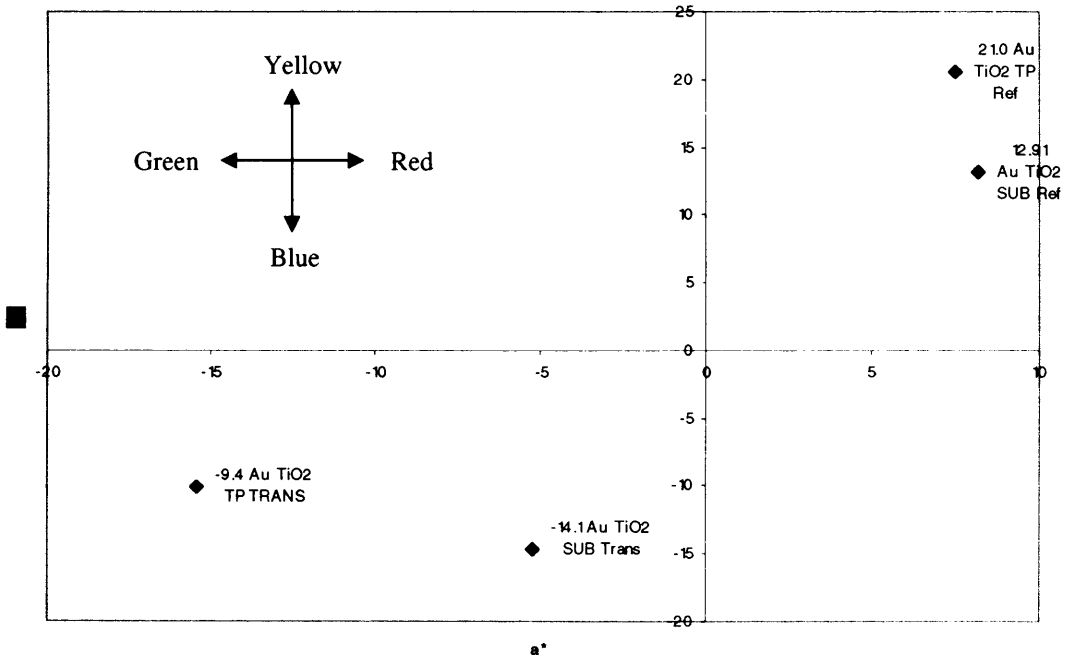


Figure 53. Au nanocube – $TiO_2$ thin film colour quantified using the CIELAB colour co-ordinates. (SUB = substrate and TP = top plate).

UV/vis spectroscopy of the $TiO_2$/Au composite films showed absorption peaks in the region of 590-650 nm, which are assigned to the red shifted and broadened plasmon resonance of gold nanoparticles. The peak broadening could due to the change in shape of the nanoparticles from spheres to cubes. The intensity of the plasmon peak increased and broadened further with increasing gold content. The reflection profile changes significantly with increasing gold concentration. Lower Au nanocube concentrations show a narrow reflection peak, whilst higher gold concentrations show broader, more intense peaks, with tails extending into the near – infra red region. The refractive index of the matrix is also known to influence the surface plasmon resonance. Mie theory[45] and Maxwell Garnett[45] theory both predict a red-shift of the surface plasmon resonance peak with increasing refractive index of the surrounding medium. The refractive index measurement for bulk anatase $TiO_2$ is 2.4[200], hence the presence of the surrounding medium and change in nanoparticle shape is the cause of the red-shift in this case.

X-ray diffraction detected crystalline gold in the composite films (Figure 54). Au peaks can clearly be seen in the XRD pattern at 39 and 45 °. These arise from the (111) and (200) planes in the Au cubic lattice[201]. Few titania peaks were seen in the X-ray diffraction pattern, indicating that the deposited titania matrix had low crystallinity. A strong signal at approximately 24° is expected for anatase titania[202]. The intensity of the Au peaks increased with increasing particle concentration. Low crystallinity in CVD films of titania deposited at 400 °C and below have previously been observed[52]. XRD patterns were recorded along the length of each film at 10 mm intervals. Identical experimental parameters were used to collect diffraction data from each point. The peak intensities and integrated areas of the Au (111) and (200) peaks varied along the substrate. This indicates a change in the Au amount across the substrate. As the film thickness is not constant, the integrated areas of the diffractions peaks cannot be directly related to the concentration of gold within the film. However, the integrated peak area at a given point is related to the total amount of crystalline gold at that point.

The full width at half maximum (FWHM) of the peaks was almost constant along the length of the substrate indicating roughly constant crystallite size. Although there was a slight reduction in the FWHM at higher deposition temperatures, indicating larger

crystallite sizes. The ratio of the integrated area of the (111) to (200) peaks is invariant showing no change in preferred orientation of the crystalline gold phase.

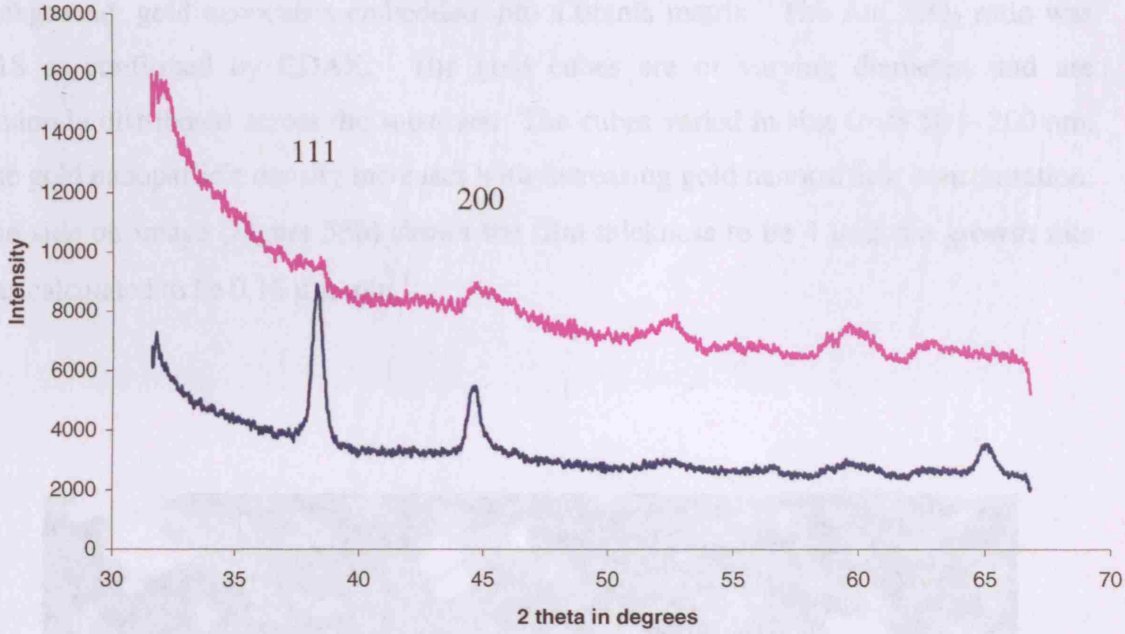


Figure 54. Xray diffraction of Au nanocubes embedded in a $TiO_2$ thin film matrix prepared by AP/AACVD.

XPS confirmed the presence of Au and titania in the composite film. Au 4f 7/2 and 5/2 peaks at binding energies of 84.3 and 88.1 eV were observed, corresponding to Au metal (reference values 84 and 87.6 eV). This shows that the Au nanoparticles do not undergo a chemical reaction during the CVD process. Ti 2p 1/2 and 3/2 binding energies were observed at 459 and 465 eV corresponding to $TiO_2$ (reference values 459 and 464.8 eV)[203]. These correspond well to the literature values for the $Ti^{4+}$ ion in $TiO_2$. The absence of a $Ti^{3+}$ environment indicates that the blue colour of the films is not caused by a partially reduced titanium oxide phase. This suggests that the colour is due to gold nanoparticles.

Further evidence for titania[204] is by Raman analysis where there are also peaks present that indicate the presence of anatase $TiO_2$ at 143, 396 and 612 $cm^{-1}$.

## 4.5.2 A Study of The Growth Morphology and Optical Properties For Au Nanoparticle/$TiO_2$ Films Deposited Using AP/AACVD

The SEM images below (Figure 55a) show bright cubes on a darker textured background: gold nanocubes embedded into a titania matrix. The Au: $TiO_2$ ratio was 1:18 as confirmed by EDAX. The gold cubes are of varying diameter, and are randomly distributed across the substrate. The cubes varied in size from 50 – 200 nm. The gold nanoparticle density increases with increasing gold nanoparticle concentration. The side on image (Figure 55b) shows the film thickness to be 4 μm; the growth rate was calculated to be 0.16 μm $min^{-1}$.

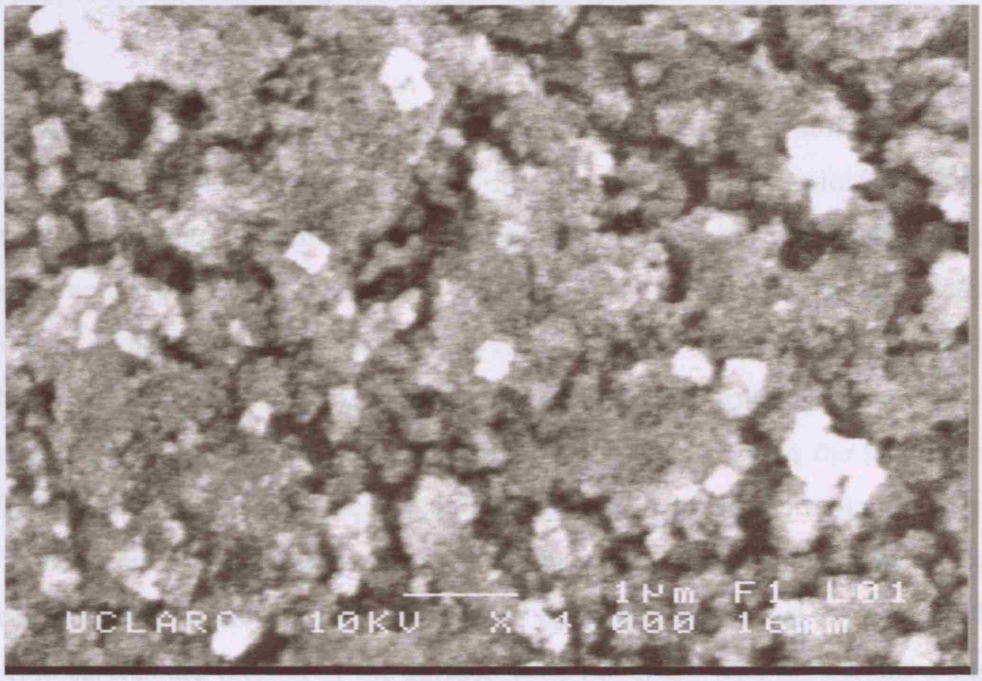


Figure 55a. Nanocubes of Au distributed across the $TiO_2$ thin film matrix prepared by AP/AACVD.

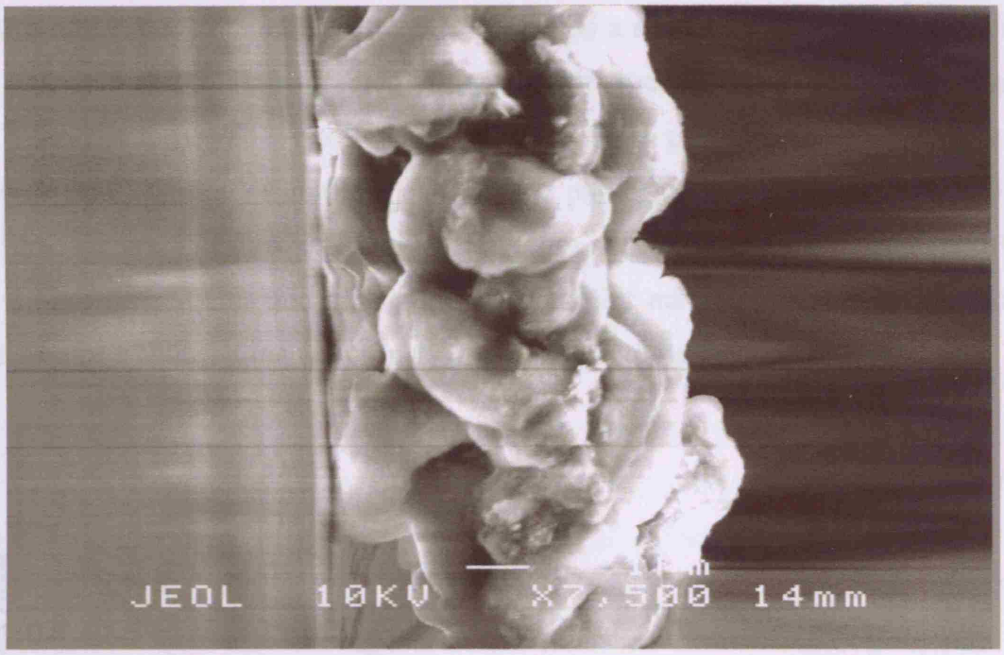


Figure 55b. A side on image of the Au/$TiO_2$ thin film prepared by AP/AACVD.

Surprisingly, the Au nanoparticle/$TiO_2$ thin films deposited using this system display enhanced photocatalytic activity compared to $TiO_2$ thin films deposited via AACVD, Figure 56. The gold/titania compsite films displayed two useful functional properties – they were active photocatalysts and they showed photo-induced super-hydrophilicity. The contact angle for water droplets on the films was low – between 9–16°, indicating that the surface is hydrophilic. This contact angle dropped further to between 3–7° on exposure of the surface for 0.5 h to 254-nm radiation. On keeping the samples in the dark for 24 h the contact angle increased to 10–12°, and on further irradiation decreased again to between 4–5°. The reversible change in contact angle with light/dark storage has been observed before for $TiO_2$ films. The explanation was that in the light Ti(III) hydroxide centres are created at the surface which strongly hydrogen bond water and hence reduce the contact angle. A slower oxidative process reverts the Ti(III) to Ti(IV) with release of water and loss of the hydroxy groups[205]. In the dark formation of Ti(IV) predominates as there is no light to promote Ti(III) formation, and the films become less hydrophilic[206]. This change in contact angle with time was repeated over many light-dark cycles.

The Au nanocube – titania films readily destroyed a stearic acid overlayer and did so with both 254 and 365 nm irradiation, rates of destruction (5.5 x $10^{12}$ molecules $cm^{-1}min^{-1}$ for 254 nm). This rate is comparable to CVD prepared titania[205], and it was found that the addition of gold did enhance the photocatalytic properties of the titania thin film. Figure 55b shows a highly porous film structure. It is common for surfaces with a high surface area and high porosity to exhibit enhanced photoactivity and this could also be a contributing factor in the high photoactivity of these film types.

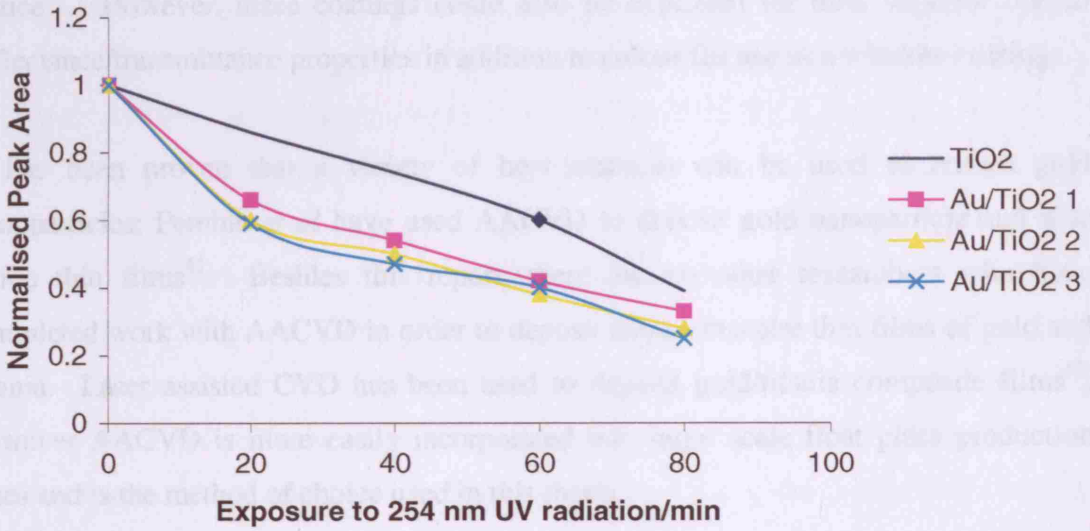


Figure 56. Decrease in normalised stearic acid peak area for a Au nanocube/$TiO_2$ film compared to a $TiO_2$ thin film deposited by AP/AACVD at 500 °C.

Both the titania and Au nanocube/titania thin films were approximately 4 μm in thickness across the entire substrate. Furthermore, the X-ray pattern for the titania film was also found to be amorphous. Therefore the titania thin-film as prepared was a good control measurement for the photocatalysis experiment.

The reflectance/transmittance spectra of Au nanocube - $TiO_2$ thin films were measured in the visible and IR regions. The films did not transmit above 45% across the spectrum, but do reflect above 80% in the near IR.

## 4.6 Discussion: Deposition of Au Nanoparticle and Au Nanoparticle/$TiO_2$ Films Using AP/AACVD

Many researchers have reported the deposition of thin films of gold nanoparticles and some of these thin films have found applications in catalysis and gas sensing[59]. One of the main advantages of these film types is their high conductivity- the films are non-metallic in nature and retain their nanoparticulate nature upon transfer to the thin film. The enhanced electrical conduction is due to activated electron hopping throughout the lattice[39]. However, these coatings could also be exploited for their superior optical reflectance/transmittance properties in addition to colour for use as a window coatings.

It has been proven that a variety of host matrices can be used to embed gold nanoparticles; Pemble *et al* have used AACVD to deposit gold nanoparticle and zinc oxide thin films[61]. Besides this report, there are no other researchers who have completed work with AACVD in order to deposit nanocomposite thin films of gold and titania. Laser assisted CVD has been used to deposit gold/titania composite films[62], however AACVD is more easily incorporated into large scale float glass production lines and is the method of choice used in this thesis.

Gold/silica core shell nanoparticles have been deposited on glass by CVD[207]. These films exhibited a peak in the reflectivity in the infra-red and near infra-red regions. This behaviour was also seen for the Au nanocube/titania thin films deposited here, suggesting that particle interaction does occur between the dispersed gold nanoparticles.

The films prepared in this thesis display enhanced properties- they exhibit a greater photocatalytic activity rate than titania, display interesting surface plasmon resonance effects, show unusual growth morphology and good transmission. Gold nanoparticles enhance photocatalysis by acting as charge separators. Here, the excited electrons transfer from the semiconductor conduction band to that of the metal. This prevents recombination allowing the electrons to reduce adsorbed species.

## 4.7 Conclusion: Deposition of Au Nanoparticle and Au Nanoparticle/$TiO_2$ Films Using AP/AACVD

A new aerosol assisted chemical vapour deposition (AACVD) into atmospheric pressure chemical vapour deposition (APCVD) system was used to deposit films of Au nanoparticles from a suspension of synthesised nanoparticulate gold in toluene and thin films of gold nanoparticles incorporated within a host titania matrix. Titania films were deposited by the APCVD of $[Ti(O^iPr)_4]$ alongside the AACVD of gold nanoparticles. The Au nanoparticle/ $TiO_2$ thin films exhibited photoactivity and photo-induced super-hydrophilicity, further the films showed gold nanocubes incorporated within the titania host matrix. These microstructures could not be obtained by sol-gel or evaporation routes.

Previously gold nanoparticles have been incorporated into a titania host matrix by Parkin *et al*[60]. The concentration of gold in these films could be widely tuned, and the optical properties of these films tailored according to application. Both these films and the films deposited in this study display enhanced optical properties, surface plasmon resonance effects and metal like reflectivity and this has great potential for use as optical window coatings, self cleaning glass and other applications of photocatalysis mentioned in Chapter 1.

A key goal of the future is to extend the range of light used for photodegradation further into the visible region.

# Chapter 5:

# Tungsten Oxide and Tungten Oxide-Titania Thin Films Prepared by Aerosol Assisted Deposition; Use of Preformed Solid Nanoparticles

## 5.1 Introduction

Tungsten oxide nanoparticle thin films were deposited by an aerosol assisted deposition technique (AAD). Here, a suspension of solid nanoparticulate $WO_3$ in toluene was used for the first time in a modification of the aerosol assisted chemical vapour deposition step. Tungsten oxide nanoparticles were also deposited alongside $[Ti(O^iPr)_4]$ by aerosol assisted chemical vapour deposition forming thin films of tungsten oxide/titania composites. The $WO_3$ nanoparticle and $TiO_2$ films exhibited photoactivity and photo-induced super-hydrophilicity and surprisingly, the titania films showed very unusual microstructures. These microstructures could not be obtained by sol-gel or evaporation routes.

This chapter will detail the preparation, morphology and structure study of $WO_3$ nanoparticle and titania films using preformed commercially available solid $WO_3$ as compared to conventional chemical vapour deposition routes. Extensive research has led to the conclusion that many solid phase nanoparticles can be transferred into an adhesive thin film provided that they can be dissolved/suspended in an appropriate carrier solvent. It is thought that in some cases, the nanoparticulates may tune the morphology of the thin film yielding highly unusual microstructures[208].

## 5.2 Method For Film Deposition

### 5.2.1 Aerosol Assisted Deposition Precursors

Solid $WO_3$ nanoparticles and titanium tetra isopropoxide $[Ti(O^iPr)_4]$ were obtained from Aldrich and used as supplied (99% purity). The $WO_3$ nanoparticles (typically 0.2 g)

were sonicated by an ultrasonic bath (2 h) to aid dispersion in toluene (40 ml). This produced a pale yellow coloured solution with some un-dissolved solid. This solution was used as a precursor for aerosol assisted transport to form $WO_3$ films on glass. A similar concentration solution of $WO_3$ in toluene was used to make $WO_3$-$TiO_2$ thin films- except that titanium isopropoxide (0.56 g, 2 mmol) was added to the initial precursor solution.

### 5.2.2 Sol-Gel and Evaporation Coating Studies

Sol-gel synthesis and evaporation coating routes were used to form thin films of $WO_3$ nanoparticles and $TiO_2$/$WO_3$ nanoparticles using the above mentioned precursors. These coatings were heated in a furnace at 550 °C for 1 hour to induce crystallinity. The purpose of these experiments was to explore the differences in microstructure, surface adhesion and durability of the coating compared to those formed by the AACVD route.

## 5.3 Deposition Parameters

A number of different deposition parameters were tested to obtain the optimum conditions for depositing $WO_3$ nanoparticle thin films on glass. These conditions were also applicable to deposition of $WO_3$ nanoparticles within a host titania matrix. All films were synthesised in one step in toluene instead of layer-by-layer growth used in previous chapters. Hence two series of films were deposited as detailed in Table. 5 below along with the optimum deposition conditions for each set deposited. In addition, the effect of increasing the concentration and host solvent for the $WO_3$ nanoparticles was investigated.

| Film Number | Precursors | Solvent 50 mL | Substrate Temperature /°C | Flow Rates/ L $min^{-1}$ |
|---|---|---|---|---|
| 1 | Tungsten oxide 0.05 g, 0.2 mmol | Toluene | 450 | 1 |
| 2 | Tungsten oxide 0.05 g, 0.2 mmol | Water | 450 | 1 |
| 3 | Tungsten oxide 0.05 g, 0.2 mmol | Acetone | 450 | 1 |
| 4 | Tungsten oxide 0.05 g, 0.2 mmol $[Ti(O^iPr)_4]$ (0.56 g, 2 mmol) | Toluene | 450 | 1 |

Table 5. Films deposited using $WO_3$ nanoparticles

## 5.4 Tungsten Oxide Nanoparticle Thin Film Deposition by Aerosol Transport From Solid Nanoparticulate Tungsten Oxide

### 5.4.1 Film Characteristics and Elemental Analysis

Nanoparticulate tungsten oxide thin films were prepared on glass from the aerosol assisted transport of commercial tungsten oxide nanopowder. The films were uniform across the substrate and gave good coverage of the glass substrate. The films were yellow in colour and passed the Scotch tape test. Furthermore the films were adhesive, could not be wiped off with tissue or gloves but could be scratched with both a brass and steel stylus. The film did not dissolve in common solvents, acid (2M) and alkali (2M). Interestingly all of the deposition was on the top substrate plate rather than the heated bottom plate.

The UV-visible spectrum of the film was characteristic of tungsten oxide, a broad absorption band was seen at 500-900 nm indicating that tungsten oxide was indeed deposited[209]. This was also confirmed by wide area EDAX analysis, where tungsten and oxygen environments were seen.

Extensive X-ray powder diffraction studies were carried out and showed that the tungsten oxide films were crystalline (Figure 57) with the fully stoichiometric triclinic-$WO_3$ structure. The diffraction pattern for the initial tungsten oxide powder was studied and matched exactly to the thin film X-ray pattern but hinted slight grain growth occurred upon transfer of the nanoparticles to glass. Reflections seen were comparable to reference values[210].

Reitveld refinement was completed and the indexed cell constants for the starting tungsten oxide nanopowder were calculated to be $a$ = 7.285(1) Å, $b$ = 7.488(1) Å, $c$ = 7.650(1) Å; α = 89.57(3)°, β = 90.18(4)°, γ= 90.81(1)°. In comparison, the indexed cell constants for the thin film were $a$ = 7.321(1) Å, $b$ = 7.525(1) Å, $c$ = 7.683(2) Å; α = 89.58(3)°, β = 90.18(1)°, γ = 90.78(1)°. These values are comparable to triclinic $WO_3$ references values[16] of $a$ = 7.312(1) Å, $b$ = 7.525(1) Å, $c$ = 7.689(1) Å; α = 88.847(3)°, β = 90.192(4)°, γ = 90.94(1)°[211].

Further analysis led to the conclusion that the thin films do not show any indication of significant preferred orientation of the crystallites on the glass substrate. In comparison, this result is different to those obtained for conventional atmospheric pressure CVD and aerosol assisted CVD approaches to tungsten oxide on glass as preferred orientation is seen for these film types in the (0 2 0) direction[212]. The Scherrer Equation (GSAS) was used to calculate the average crystallite sizes. Here, the line broadening determined the dimensions, and the value for the starting tungsten oxide nanopowder was 199 (2) Å and the size for the thin film was 227(2) Å. As the thin film size is slightly larger, it follows that some slight grain growth or selective deposition of the slightly larger grains within the weighted average crystallite size has occurred.

Furthermore, the Raman pattern for the as formed $WO_3$ film is identical to the starting material and is a perfect match for triclinic $WO_3$[213], EDAX analysis showed that the films contained only tungsten and oxygen and elements present in standard glass substrates used in this study.

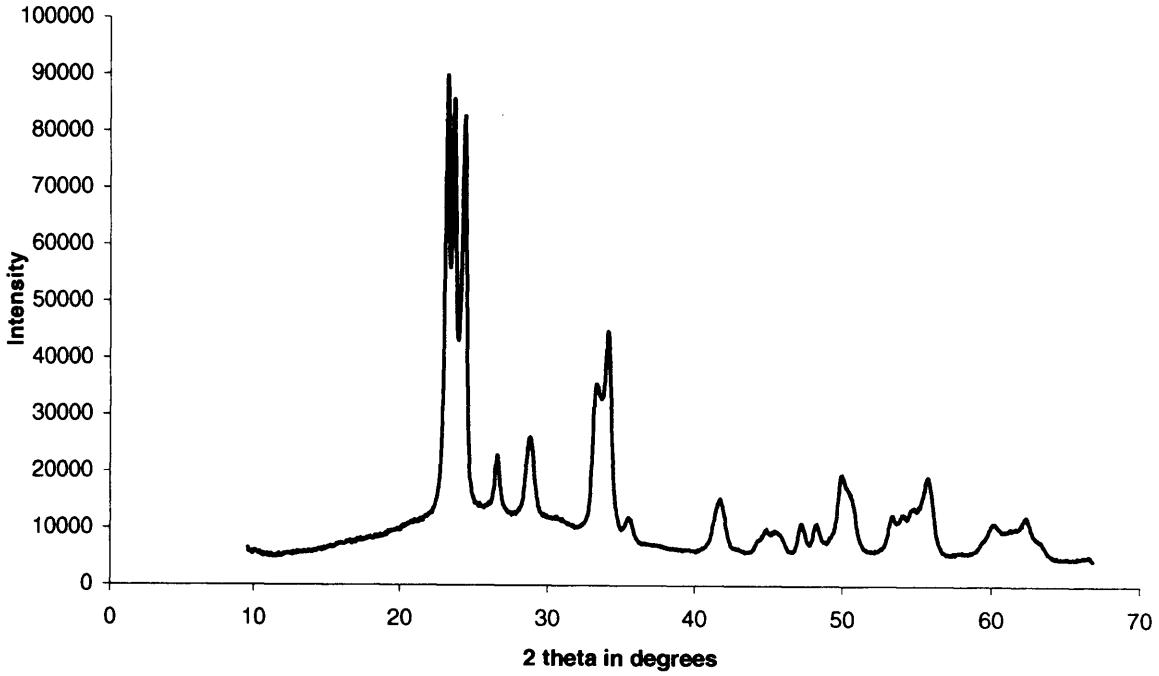


Figure 57. X-ray powder diffraction pattern of the $WO_3$ films formed at 450°C by the aerosol assisted deposition of nanoparticulate $WO_3$ suspended in toluene.

## 5.4.2 Growth Morphology and Functional Characteristics of Tungsten Oxide Nanoparticle Thin Films Synthesised By Aerosol Assisted Transport

Scanning electron microscopy of the tungsten oxide nanoparticle thin films showed a dense continuous film made up of interlocking particles. As seen in Figure 58, there is a particle size ranging from 10 - 60 nm and agglomerates of average dimension 100 - 300 nm. The tungsten oxide nanopowder was examined by TEM prior to being used in the aerosol transfer for film deposition. The TEM images showed that the powder was made up of agglomerates, with some observable $WO_3$ particles of dimension 150 - 200 Å present. This suggests that successful transfer of $WO_3$ nanoparticles to the film has occurred with good transferability.

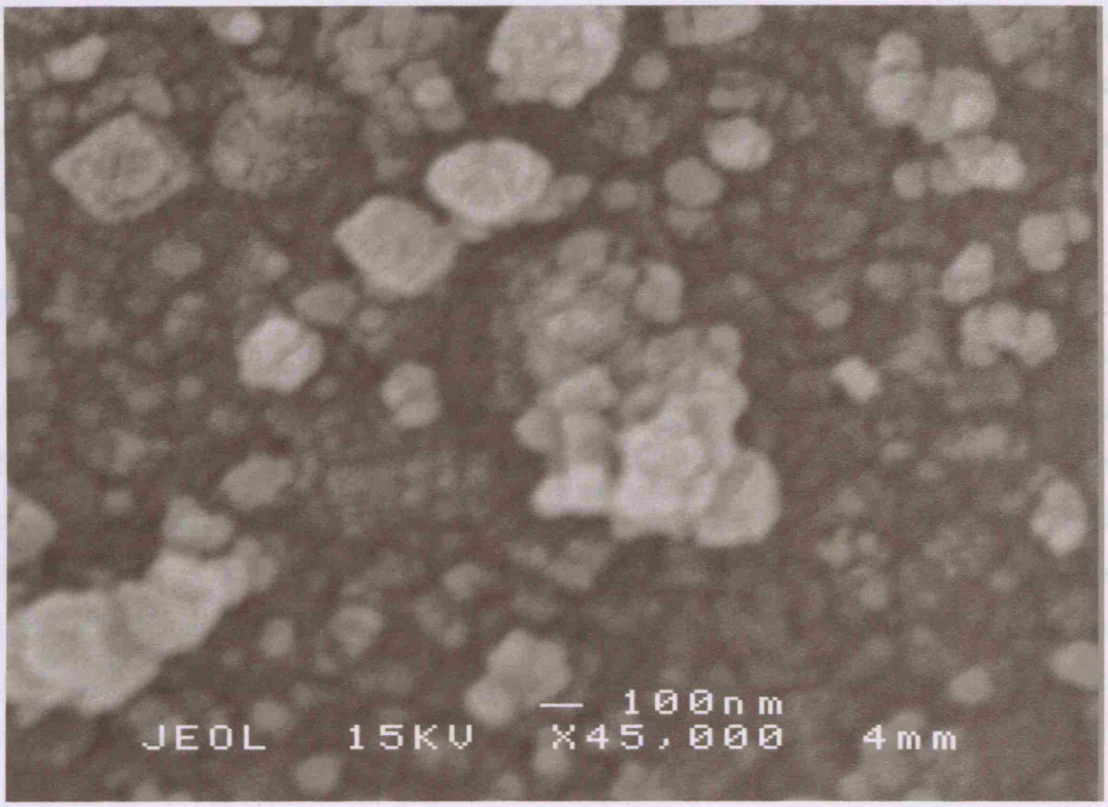


Figure 58. Scanning electron micrograph of the $WO_3$ films formed by the aerosol assisted deposition of nanoparticulate $WO_3$ suspended in toluene at 450 °C.

The tungsten oxide nanoparticle thin films were both active photocatalysts and exhibited photo-induced super-hydrophilicity. The stearic acid degradation rate was 0.1 x $10^{12}$ molecules $cm^{-1}min^{-1}$ for irradiation with 254 nm UV light. The contact angle for water droplets on the tungsten oxide thin films was very low – between 3 - 7° indicating that the surface is very hydrophilic and also porous. This contact angle dropped further to between 0.5- 2° on exposure of the surface for 0.5 h to 254 nm radiation. Keeping the samples in the dark for 24 h caused the contact angle to increase to 7 – 8° and on further irradiation decreased again to between 0.5-2 °. These test were carried out over many light-dark cycles and the super-hydrophilic behaviour was repeatable over many cycles. The very low initial contact angle puts these films in the class of super-hydrophillic films and gives similar measurements to that of titanium dioxide thin films formed from sol-gel or CVD[214]. The very low contact angles for these films are most likely due to the film surface being both partially hydroxylated allowing a greater affinity for hydrogen bonding to water and also contributions from the film's high

porosity as a consequence of the very fine microstructural form of nano-scaled particles. The $WO_3$ films readily destroyed a stearic acid overlayer and did so with both 254 and 365 nm irradiation, rates of destruction were 4 x $10^{12}$ molecules $cm^2min^{-1}$ and similar to previously reported CVD prepared $WO_3$ thin films[110].

It has been shown here that transfer of nanopowder to a thin film on glass can readily occur by aerosol assisted transport. This is the first time that this technique has been used to form thin films of tungsten oxide using a nanopowder based precursor. The films were deposited readily at normal flow rates, temperatures and deposition parameters as used for conventional aerosol assisted chemical vapour deposition. Here, this technique is termed "aerosol assisted" as no chemical reaction occurs as such- the precursor contains the desired tungsten oxide nanoparticles in the required form; the tungsten oxide nanopowder readily formed a suspension in the toluene due to its nanoparticulate nature.

The transfer to the glass was successful- the thin films were composed of nanoparticulates. However some agglomeration to produce a highly interlocked film, which could be due to kinetics in the gas phase or via the mode of deposition occurred. However, the much larger agglomerates seen in the TEM images were not present in the thin film, suggesting that sonication was successful in aiding the dispersion of the nanoparticle powder in the host solvent. Furthermore at the end of the reaction, the solvent and nanopowder were fully carried by the gaseous aerosol mist and no nanopowder was left behind in the reactor flask after the deposition.

Deposition for this film type occurred primarily on the top plate of the reactor suggesting that the thermophoretic effect occurred[215]. This effect is explained by large particles that are unable to diffuse through the stagnant boundary layer caused by a buoyancy effect; faster moving gas particles move away from the hot surface preventing deposition on the substrate and therefore deposition is favoured on the top plate. This occurs because the top-plate is cooler as it is not directly heated making it easier for the smaller particles to penetrate. This can explain why the smaller nanoparticles were incorporated in the film whilst the larger aggregated ones are repelled and exited to the exhaust.

## 5.5 Deposition of Titania Thin Films in The Presence of Tungsten Oxide Nanoparticles

### 5.5.1 Film Characteristics and Elemental Analysis

Aerosol assisted chemical vapour deposition was used to deposit thin films using $[Ti(O^iPr)_4]$ dissolved in toluene in addition to the tungsten oxide nanopowder, as used previously co-deposited in one single step. In this case deposition occurred on both the top plate and the heated substrate. All films produced were pale yellow-beige with rainbow interference fringes seen in reflection due to variations in thickness. All films passed the Scotch tape test and were resistant to scratching by brass scalpel, steel stylus and wiping with a tissue. The films were not dissolved by immersion in common organic solvents and also acid (2M) and alkali (2M).

Wide area EDAX analysis showed that the film was made up of 1 atom% tungsten, with the remaining elements counted including titanium and oxygen. The UV analysis was found to be characteristic of titania anatase.

X-ray diffraction studies on the $TiO_2$ - $WO_3$ nanoparticle thin films was carried out. Figure 59 confirms the titania anatase phase where reflections are seen at 25 (101), 37 (103), 38 (004), 39 (112), 48.5 (200), 54 (105), 56 (211) and 64°. This is comparable to reference values for titania. To investigate the pattern further, in an attempt to find a secondary tungsten oxide match, the pattern was then modelled using Rietveld refinement[216].

Once the lattice and peak profile parameters were refined and preferred orientation taken into account, the anatase phase of $TiO_2$ (*I*41/*amd*, $a$ = 3.7804(3) Å, $c$ = 9.500(2) Å) was assigned. The preferred orientation was modelled using the March-Dollase model[216]. A good match to the recorded data was found when the 110 plane was used as the preferred plane with a March co-efficient of $r$ = 0.542(2), a measure of the sample compression/elongation due to preferred orientation. As the SEM images indicate the crystallites are plate-like (rather than rod-like) then, as the value of $r$ is less

than 1, we can conclude that the crystals are preferentially aligned so that the 110 plane is parallel to the deposition surface[217].

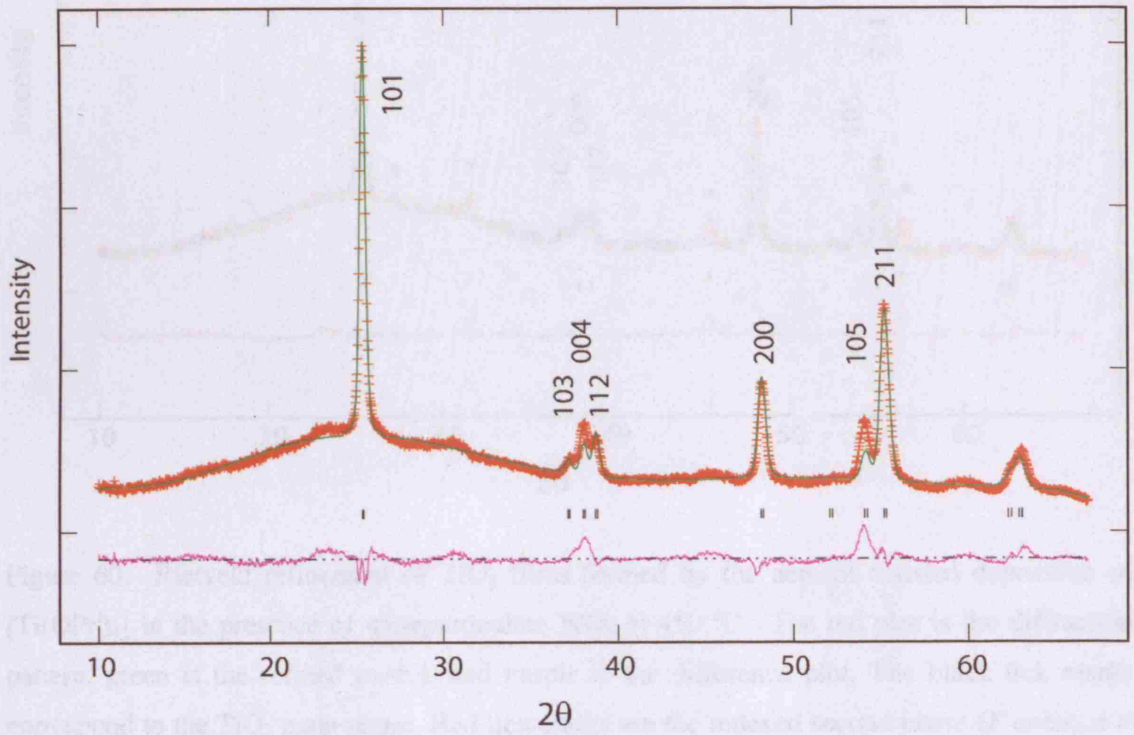


Figure 59. Rietveld refinement of $TiO_2$ films formed by the aerosol assisted deposition of $[Ti(OPr^i)_4]$ in the presence of nanoparticulate $WO_3$ at 450 °C. The red plot is the diffraction pattern, green is the refined model, and purple is the difference plot.

X-ray analysis studies on further areas of the substrate found additional peaks in the pattern for the part of the film that was 5 cm from the reactor inlet (marked with *asterisks* in Figure 60). This secondary phased was indexed and found to be a cubic cell with lattice parameter $a$ = 5.646 Å and systematic absences consistent with face centred symmetry[218]. These peaks were of much lower intensity than those corresponding to $TiO_2$, suggesting that this impurity is present only in small amounts. A search of the inorganic crystal structure database was conducted to identify this phase, but no reasonable match could be found. There is a possibility that the secondary phase is a tungsten oxide derivative, originating from the introduced $WO_3$ nanoparticles.

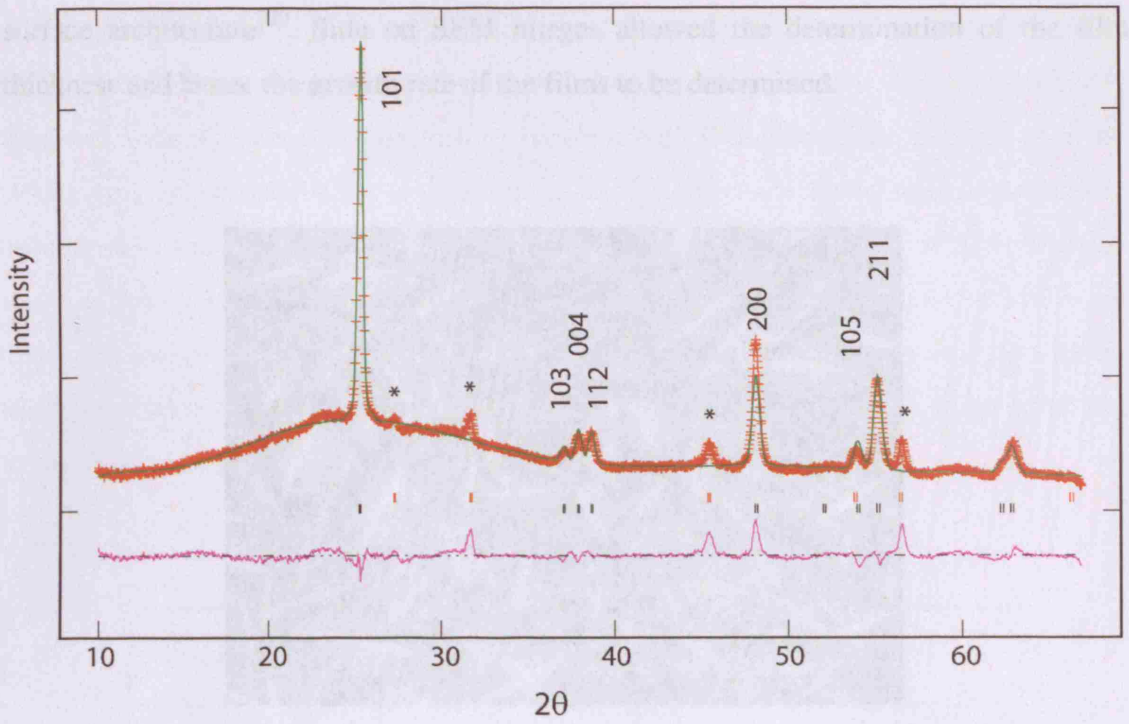


Figure 60. Rietveld refinement of $TiO_2$ films formed by the aerosol assisted deposition of $[Ti(OPr^i)_4]$ in the presence of nanoparticulate $WO_3$ at 450 °C. The red plot is the diffraction pattern, green is the refined model, and purple is the difference plot. The black tick marks correspond to the $TiO_2$ main phase. Red tick marks are the indexed second phase (*F* cubic, $a$ = 5.646 Å).

The Raman patterns for the titania films showed the expected bands for anatase with bands at 143, 396, 515 and 612 $cm^{-1}$, no evidence was seen for any tungsten oxide phase at any part of the deposited film.

## 5.5.2 Growth Morphology and Functional Properties of Tungsten Oxide Nanoparticle - Titania Thin Films

SEM imaging showed interesting morphologies; a needle and pine style texture oriented perpendicular to the substrate of dimension ca 500 nm by 10 nm and underlying plates, Figure 61. This structure was repeated over 5 thin film substrates and has not been seen before for titania anatase thin films[219]. Hence as all other factors were the same, the presence of the tungsten nanoparticles seems to be the most likely cause of this unique

surface architecture[220]. Side on SEM images allowed the determination of the film thickness and hence the growth rate of the films to be determined.

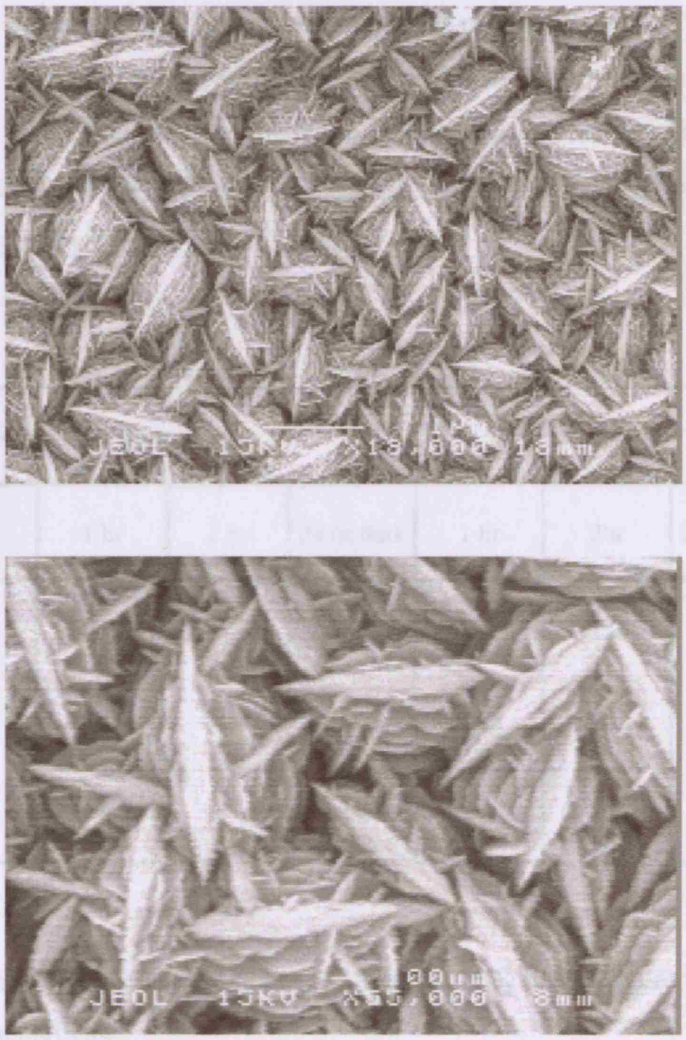


Figure 61. Scanning electron micrographs of the $TiO_2$ films formed by the aerosol assisted deposition of $[Ti(O^iPr)_4]$ in the presence of $WO_3$ nanopowder at 450 °C.

The film thickness of the film formed from titanium isopropoxide and tungsten oxide nanopowder was determined by side on SEM imaging and found to be 7 - 10 μm depending on the film sample analysed. From the deposition times, the growth rate was calculated to be 3.5 - 10 μm per hour.

All titania thin films formed in the presence of tungsten oxide nanoparticles were very hydrophilic as formed. Typical initial water droplet contact angles were around 5-10°, this is considerably smaller than that found for a typical titania coating formed by CVD which gave initial water contact angles of ca 30°[221]. The very low contact angles can be explained by the microstructure seen from the SEM measurements. The film thickness and porosity are also known to contribute to this effect. Upon irradiation with 254 nm light, the contact angles decreased further to 0-2° and upon leaving the samples in the dark, the contact angles regained their original values of 5-10°; the films exhibited photo-induced super-hydrophilicity (Table 6).

| Film Number | Exposure to UV light 254 nm | | | | | | |
|---|---|---|---|---|---|---|---|
| | 0 hr | 1 hr | 2 hr | 24 hr dark | 1 hr | 2hr | 24 hr dark |
| 1 | 12.3 | 3.2 | 1.4 | 6.8 | 1.8 | 1.3 | 9.6 |
| 2 | 2 | 0.49 | 7.3 | 8 | 0.88 | 0.88 | 3.2 |
| 3 | 4.14 | 0.88 | 1.2 | 2.3 | 1.1 | 1.1 | 4.76 |

Table 6. Variation of water contact angles with time for $TiO_2$ films prepared in the presence of tungsten oxide nanoparticles.

It was concluded that the unusual microstructure was responsible for the very low contact angles that were not otherwise obtained via the APCVD, AACVD or sol-gel routes[110]. As discussed in Chapter 1, low contact angles have high commercial value for self-cleaning applications for example on windows.

The films were also photo-catalytically active showing enhanced rates of destruction of the stearic acid over-layer with both 254 and 365 nm UV radiation. On exposure to 254-nm light, half of the stearic acid coating was removed in 1.2 h. This gives a destruction rate of $4 \times 10^{12}$ molecules $cm^2min^{-1}$ (Figure 62A). Using 365 nm UV light

inevitably gave a longer destruction time of 2.2 h for the same amount of stearic acid (Figure 62B). The results were comparable to previously reported Sol-gel and CVD prepared titania[222].

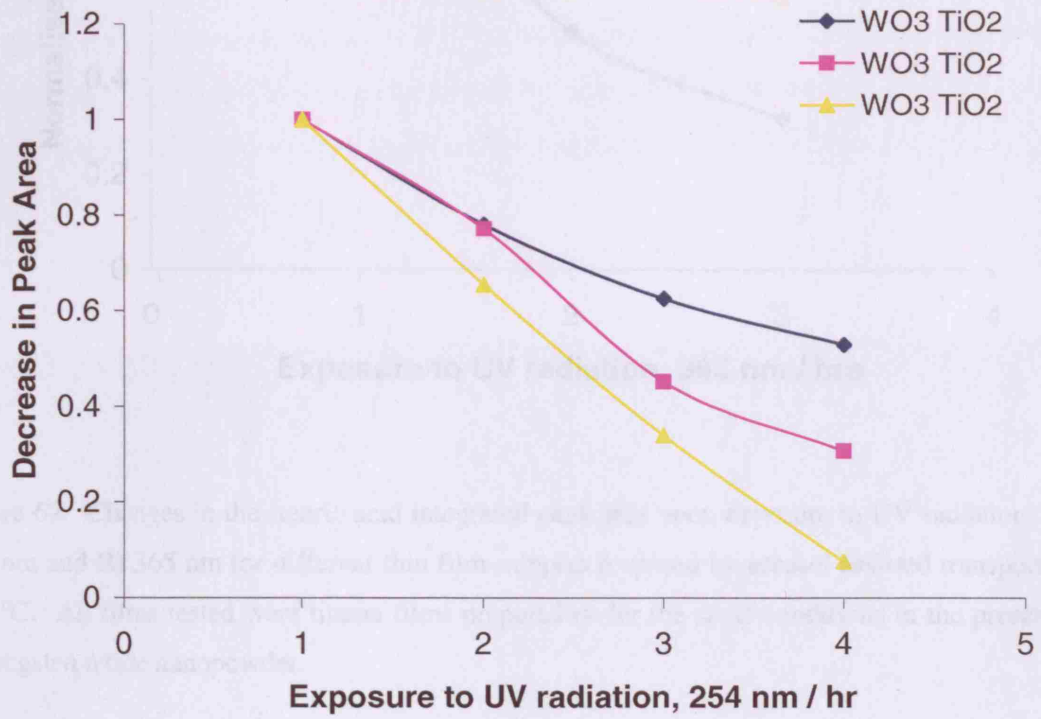


A

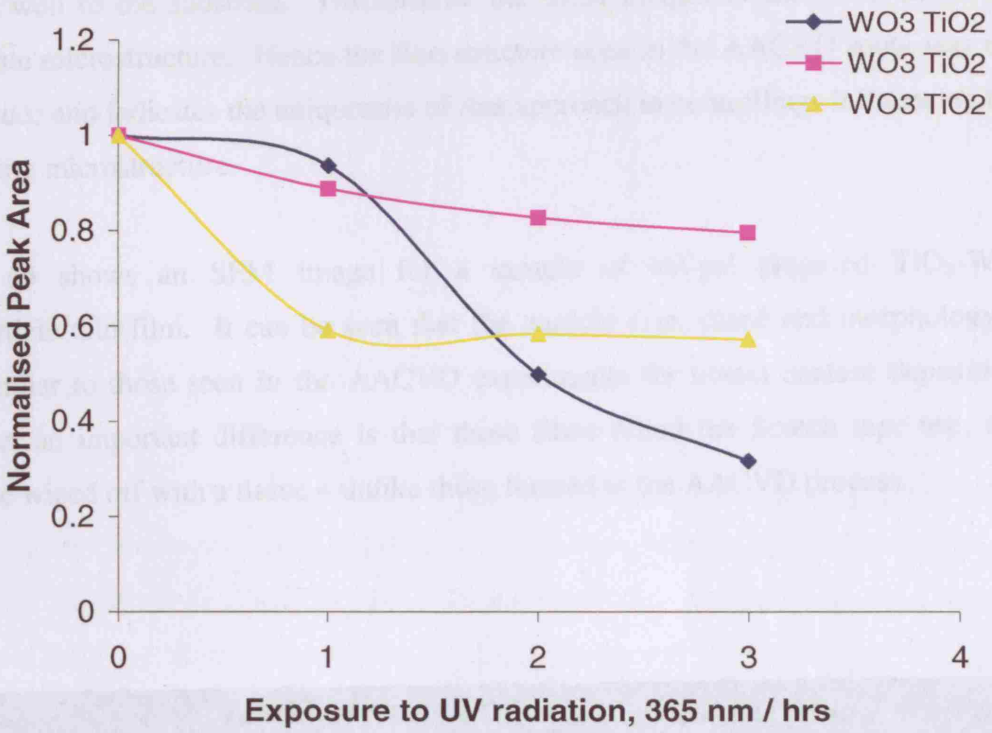


B

Figure 62. Changes in the stearic acid integrated peak area upon exposure to UV radiation: A) 254 nm and B) 365 nm for different thin film samples prepared by aerosol assisted transport at 450 °C. All films tested were titania films prepared under the same conditions in the presence of tungsten oxide nanopowder.

The nanoparticle incorporation at 1 % did not show effective photochromism. However, these films show promise as an optical coating because they are unique and display important properties namely interesting growth morphology, photocatalysis and photoinduced superhydrophilicity.

## 5.6 Sol Gel Synthesis of Tungsten Oxide – Titania Thin Films

As a comparison to the films formed by AACVD the same $WO_3$ nanoparticulate-$[Ti(O^iPr)_4]$ precursor solution was used to make sol-gel dip-coated films. The reason for this study was to see whether the unusual microstructure found in section 5.5.2 would be found in the identical film type. Sol-gel studies enabled the formation of a non-adhesive, white, powdery film. This was unlike those formed by AACVD that

adhered well to the substrate. Furthermore the SEM images of the films showed a particulate microstructure. Hence the fine structure seen in the AACVD route was not in evidence and indicates the uniqueness of that approach in controlling- influencing the underlying microstructure.

Figure 63 shows an SEM image for a sample of sol-gel prepared $TiO_2$-$WO_3$ nanoparticle thin film. It can be seen that the particle size, shape and morphology is very similar to those seen in the AACVD experiments for titania anatase deposition. However an important difference is that these films failed the Scotch tape test, and could be wiped off with a tissue – unlike those formed in the AACVD process.

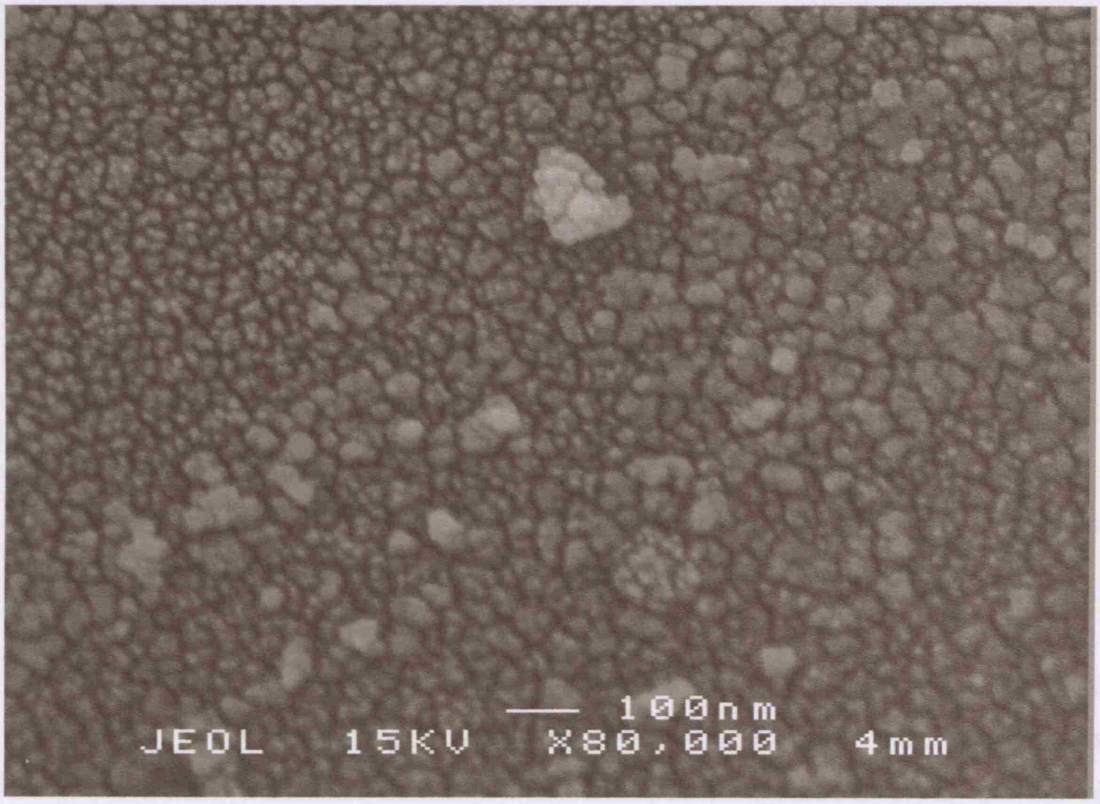


Figure 63. SEM of a $WO_3/TiO_2$ film formed by the sol-gel process. The film was calcined at 550 °C.

Haze measurements were taken on all samples and the average specular reflectance haze was on average 2%. This is greater than that of commercial windows that have haze values of 0.2%[6].

## 5.7 Discussion

The reasoning for the interesting morphology induced by the tungsten oxide nanoparticles has not been concluded here. It is known that in its absence, titania thin films are continuous and show no peculiar growth effects. Tungsten has been detected at approximately 1 atom % across the substrate and greater accumulations of tungsten were not found. Small amounts of tungsten may have entered the titania lattice as a solid solution but X-ray diffraction studies showed no evidence for this. However, the additional secondary cubic phase seen in the X-ray diffraction pattern suggest that the tungsten oxide could be inducing a structurally directing role. The phase is present at only 1 atom% and although few peaks are seen, it does match a cubic cell.

Previously, it has been reported that CVD prepared $WO_3$ films deposited under a deficiency of oxygen are blue rather than yellow[105]. A valence charge transfer mechanism is responsible for the blue colour, this is a polaron transition; hopping of electrons between neighbouring metal ions of different oxidation states[106, 107]. In this thesis, the tungsten oxide nanoparticle thin films were yellow rather than blue.

Tungsten oxide has been used for applications as electrochromic window coatings for many years. Ramana *et al* have studied the phase transitions in $WO_3$ thin films by pulsed-laser deposition[223]. Many other thin film processes such as PVD and sol-gel techniques have been used to deposit tungsten oxide composite thin films[109]. Parkin *et al* have shown gold nanoparticles within a host thin film tungsten oxide matrix significantly enhance the photochromism, photocatalysis and optical properties[110].

He *et al* have studied the effects of gold nanoparticles on the electrochromism of $WO_3$ by vacuum evaporation[224]. Badilescu *et al* have looked at nanostructured $WO_3$ thin

films by the sol-gel process[225]. These films gave a spherical nanoparticle morphology. In the work reported in this thesis, a unique needle growth morphology was seen. There have been no reports to date on the deposition of tungsten oxide nanoparticle thin films alongside a host matrix by aerosol assisted CVD. Furthermore, the use of commercially available tungsten oxide nanopowder or semiconductor nanopowders, have not been reported as aerosol assisted CVD precursors. Hence the method reported here has made use of an involatile nanoscaled solid precursor to deposit thin films. The films displayed enhanced photocatalysis, photo-induced super-hydrophilicity and unique growth morphology.

## 5.8 Conclusion

This chapter explored the use of solid nanoparticulate starting materials as precursors for the formation of thin films. This process has not been termed CVD as such as no overriding chemical reaction seems to have occurred, the initial material and final material were very similar by XRD, with the exception to some possible grain growth. Aerosol assisted deposition (AAD) was used to deposit $WO_3$ nanoparticle thin films from commercially available tungsten oxide nanopowder. This generated thin films with reasonable growth rates of 3 - 7 μm $hour^{-1}$ and conformal coverage of the substrate. Hence this growth process has potential to form thin films of material from involatile nanoscaled solid precursor and so a molecular volatile precursor is not required. Another benefit is that the nanopowder used did not require the use of charged or ligand stabilized materials and capping groups E.g. thiols. Furthermore, all films were very adhesive and super-hydrophilic. Titania films formed in the presence of $WO_3$ nanoparticles showed unique morphology in addition to exhibiting photocatalysis and photo-induced super-hydrophilicity. The initial water contact angles of these films are considerably lower than that seen for $TiO_2$ films prepared in the absence of nanoparticles and is attributed to the highly porous microstructure.

Hence by using a commercial solid nanoparticulate powder it has been proven that nanoparticulate adherent thin films can be synthesised, and that the presence of these nanoparticles can affect the surface morphology of titanium dioxide.

# Chapter 6:

# Cerium Dioxide, Cerium Dioxide – Titanium Dioxide Composite and Cerium Dioxide – Gold Composite Thin Films on Glass Prepared by Aerosol Assisted Chemical Vapour Deposition

## 6.1 Introduction

Four series of thin films were deposited on glass by aerosol assisted chemical vapour deposition- cerium dioxide, cerium dioxide - titanium dioxide composites and cerium dioxide-gold nanoparticle composites. The films were analysed by a range of techniques as described in Chapter 2. Pure $CeO_2$ films, two phase $CeO_2$/titania films, films containing pure gold nanoparticles made in toluene, and in water, and two phase cerium oxide ($CeO_2$) and gold nanoparticle films (prepared in toluene for one series and water for the next) were synthesised. The AACVD prepared films all showed a variety of functional properties such as photocatalysis and super-hydrophilicity, $CeO_2$ nanoparticle thin films displayed photocatalysis and photo-induced hydrophilicity at a level comparable to titania. The approach adopted here showed that as made nanoparticles can be transported by an aerosol in an aerosol assisted transport (AAT) process and that the films formed were composed of essentially the same nanoparticles that went into the initial solvent.

## 6.2 Method For Film Deposition - Aerosol Assisted Deposition Procedure

Cerium dioxide nanoparticles were obtained commercially, (Umicore Research) suspended in water and were 12 +/-1 nm in diameter. Gold nanoparticles were synthesised in both water and toluene, by the methods outlined in Chapter 2.

### 6.2.1 Cerium Dioxide Nanoparticulate Films

$CeO_2$ nanoparticulate films were deposited at 500 °C and at a $N_2$ carrier-gas flow-rate of 0.5 L $min^{-1}$.

### 6.2.2 Titanium Dioxide – Cerium Dioxide Composite Films

The titania precursor was prepared by dissolving 0.56 g of titanium isopropoxide (Aldrich) in toluene (50 ml). Layer by layer deposition growth was used to form composite titania anatase-ceria thin films on glass. The AACVD process initially formed a titania film. Thereafter, the cerium dioxide nanoparticles in water were transferred to the PTFE chamber and then deposition continued to form a layer of $CeO_2$ on top of the existing titania layer. The process was repeated up to three times for each precursor to form multiple layers of titania dioxide and cerium oxide nanoparticles.

### 6.2.3 Gold - Cerium Dioxide Composite Nanoparticulate Films

The Turkevich method was used to yield fairly uniform size gold colloids with diameter of 15-20 nm. Preparation of gold nanoparticles in toluene yielded a highly concentrated gold colloidal suspension with particle diameter in the range of 5-10 nm. These could be suspended in both polar and non-polar solvents.

A similar process to that used to make $TiO_2/CeO_2$ films was adopted to make composite $Au/CeO_2$ nanoparticles films by using alternate precursor solutions, in turn and forming a film by a layer-by-layer method.

A single mixed precursor solution was also used for making heterogenous $CeO_2$ and Au nanoparticle films in water, and the film was deposited in one step.

## 6.3 Deposition Parameters

A number of different deposition parameters were tested to obtain the optimum conditions for depositing $CeO_2$ nanoparticle thin films on glass. These conditions were

also used to incorporate $CeO_2$ nanoparticles within a host titania matrix. $CeO_2$, $CeO_2$/aqueous Au nanoparticle films were synthesised in one step in water whilst $CeO_2/TiO_2$ and $CeO_2$/organic Au nanoparticle films were deposited by layer-by-layer growth reported in previous chapters. Hence four series of films were deposited as detailed below in Table 7 along with the optimum deposition conditions for each set deposited. In addition, the effect of increasing the concentration of $CeO_2$ nanoparticles was investigated. The variation in the host solvent on the films formed was also tested.

| Film Number | Precursors | Solvent 50 mL | Substrate Temperature /°C | Flow Rates/ L $min^{-1}$ |
|---|---|---|---|---|
| 1 | Cerium dioxide | Water | 500 | 0.5 |
| 2 | Cerium dioxide [$Ti(O^iPr)_4$] (0.56 g, 2mmol) | Water | 500 | 0.5 |
| 3 | Cerium dioxide Gold nanoparticles | Water | 500 | 0.5 |
| 4 | Cerium Dioxide Gold nanoparticles | Water/toluene | 500 | 0.5 |

Table 7. Films deposited using $CeO_2$ nanoparticles.

## 6.4 Cerium Dioxide Nanoparticle Thin Film Deposition by Aerosol Chemical Vapour Deposition From Aqueous Nanoparticulate Cerium Dioxide

### 6.4.1 Film Characteristics and Elemental Analysis

Cerium dioxide ($CeO_2$) thin films were successfully deposited on glass substrates via aerosol assisted chemical vapour deposition. The most extensive deposition across the substrate occurred at a temperature of 500°C. The films were transparent but had a slight white hue. The edges of the coated glass showed some rainbow-like interference effects. The films were adhesive and passed the Scotch tape test, but could be scratched with a brass stylus and stainless steel scalpel. All films were insoluble in water and

common organic solvents (methanol, ethanol, acetone), but they did dissolve/disperse in both acid (HCl, 2 M) and alkali (NaOH, 2 M). The films showed no change in optical properties on storage in air for 6 months.

Spot EDAX analysis was carried out as described in Chapter 2. These data confirmed that $CeO_2$ was present in the films with a cerium to oxygen ratio of exactly 1:2. Spot analysis on all particles yielded similar results, which suggests a homogeneous distribution of $CeO_2$ on the surface of the film. Some breakthrough to the underlying glass was seen from the EDX analysis, this was quantified for based on an uncoated glass standard and subtracted to get an accurate quantification. There was therefore a good transferability from the precursor to the substrate.

The UV- visible spectrum was taken of both the original aqueous cerium dioxide nanoparticulate solution and the thin films. Both spectra were similar and a common band edge was seen at ca 380 nm- corresponding to a band gap of 3.2 eV. This correlates well with both cerium dioxide nanoparticles (> 10 nm size) and bulk materials that have a band gap of ca 3.2 eV (Figure 64)[226].

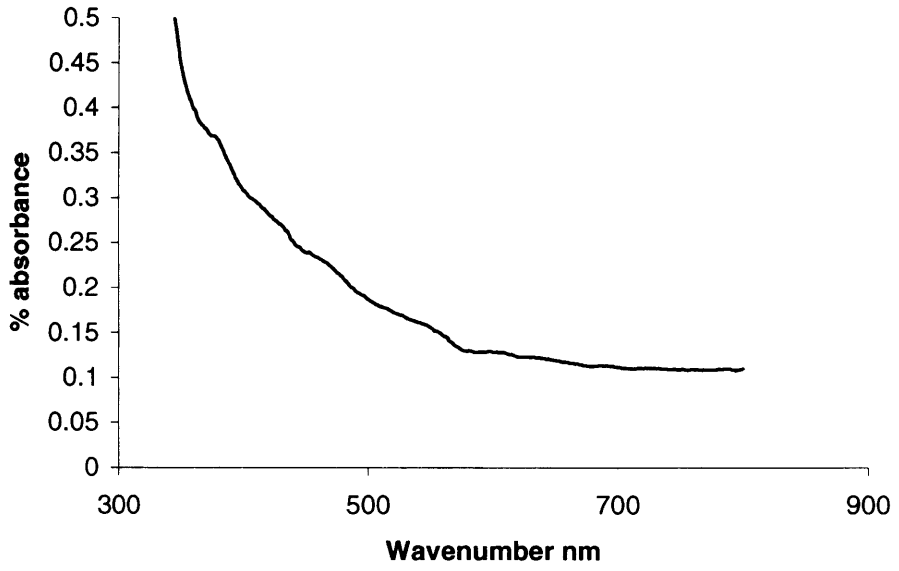


Figure 64. UV-vis spectrum of a $CeO_2$ thin film prepared by AACVD at 500 °C showing a band edge at 380 nm corresponding to a band gap of 3.2 eV.

Glancing angle X-ray diffraction confirmed the $CeO_2$ phase with distinct reflections seen for the cerium oxide. These are comparable with reference values[227]. There is no change in the width of the peaks at half-height compared to the starting material, indicating that the nanoparticle phase does not change the crystallinity of the film. From the line broadening of the peaks, crystallite sizes of ca 12 nm were calculated and it was found that cubic $CeO_2$ was present with lattice constant 5.39(2) Å, this compares well with bulk $CeO_2$ which has $a$ = 5.41 Å[228].

Raman studies were completed on several ceria thin-film samples and analysis did not show any bands for the $CeO_2$ nanoparticulate films. This is as expected because $CeO_2$ is cubic, and cubic structures often do not undergo detectable Raman scattering[229]. No additional bands due to a hydroxide phase or carbon (graphitic or other contamination) were noted.

### 6.4.2 Film Growth Morphology and Functional Tests

SEM imaging confirmed that nanoparticles of dimension 12-15 nm were uniformly distributed across the sample surface with no change in the shape, size and organisation on the glass substrate, Figure 65. These particles seem to stack on top of each other to form a continuous film with coalescence of some nanoparticles occurring. TEM imaging confirmed that the original $CeO_2$ nanoparticles used in the experiment solution were approximately 12 nm. This shows that the $CeO_2$ nanoparticles successfully transferred via the aerosol to the glass substrate and were incorporated to form a thin film, with little or no agglomeration. More importantly, the original particle size is maintained upon transfer to the substrate. This process also compares favourably with the XRD results, which show from line broadening crystallite sizes of ca 12 nm. SEM imaging enabled the film thickness and hence the growth rates to be determined by taking side on images of the ceria thin film sample. The film thickness was found to be around 500 nm for a 1 hr deposition.

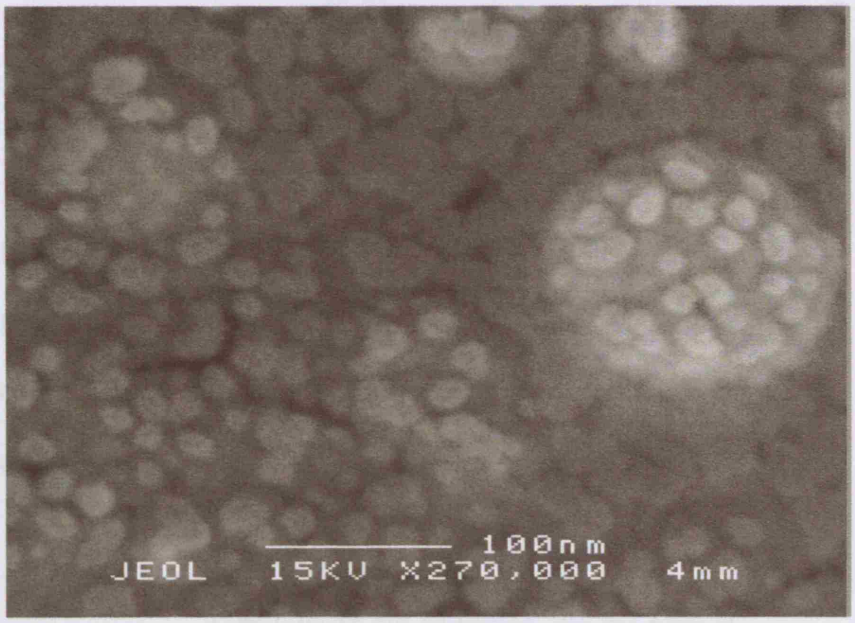


Figure 65. SEM image of a $CeO_2$ nanoparticle film on glass prepared by AACVD at 500 ºC. A particle size of 12-15 nm is seen.

Photocatalytic activity was determined by a stearic acid test. The photocatalytic response of the ceria thin films is shown in Figure 66. The rate of destruction of stearic acid was found to be ($1.8 \times 10^{12}$ molecules $cm^{-1}min^{-1}$ for 254 nm). This rate is comparable to CVD prepared titania[178]; all the $CeO_2$ samples prepared were photocatalytically active comparable to a titania film of the same thickness as suggested via the photodegradation of stearic acid. There are only a few reports on the photoactivity in aqueous solutions of $CeO_2$. On the other hand, cerium oxide thin films have been shown to be largely inactive in destroying methylene blue[230]. The high photoactivity of nanocrystalline cerium oxide films formed in this study was surprising because nanoparticulate cerium oxide has been marked as a non-photoactive treatment for wood[197]; "cerium oxide shows a very fast recombination of charge carriers before they can migrate to the surface (because of crystal defects, oxide-reduction reaction), so, there is no further creation of free radicals." However in this thesis, these films were photoactive and displayed photo-induced hydrophilicity. This could be a consequence of the very small particle size of the cerium dioxide particles. The mechanism by which photocatalysis occurs in ceria is different to titania. Instead, the formation/annihilation of oxygen vacancies in redox processes occurs on the surface of ceria samples and is considered to play a crucial role in many oxidation reactions[231].

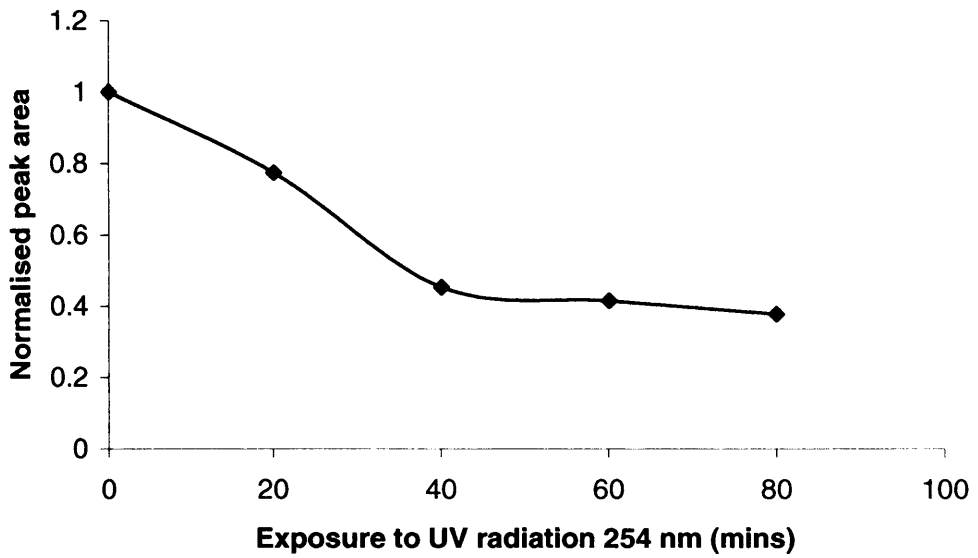


Figure 66. Change in normalised stearic acid peak area for a $CeO_2$ thin film prepared by AACVD at 500 °C (254 nm).

Water droplet contact angle measurements were taken as described in Chapter 2 and all ceria thin films samples exhibited photo-induced super-hydrophilicity. The initial water contact angles for nanoparticulate cerium oxide films on glass were around 70° prior to irradiation, this reduced to 15° on exposure to 254 nm radiation for 1 hour and decreased further to 5° after 24 hours exposure to room light. Leaving the films in the dark for 24 hours lead to film water contact angles increasing to 64° (Table 8).

Water contact angles of less than 5° are often observed for pure anatase films. The proposed mechanism for the lowering of contact angles for a titania film involves the formation of a reduced Ti(III)-O-H terminated surface that can readily hydrogen bond to water. On storage in the dark, in air, the films slowly reoxidise to a Ti(IV)-oxo terminated surface that is not as hydrophilic – and hence the contact angle increases[231]. It is possible that a similar situation could occur here with formation of a Ce(III)-O-H surface[232]. It has been reported that a sol-gel prepared $CeO_2$ thin film did not show any photo-induced super-hydrophilicity and maintained a contact angle of 20° even after irradiation for 1 h[233]. The films studied here show very different behaviour in regard to the contact angles. This is hard to explain- although the cerium oxide films reported here are nanoparticulate in nature. The $CeO_2$ nanoparticulate films were made on six

separate occasions in this study and all showed the same trends in contact angle- with marked photo-induced hydrophilicity that diminished on storage of the films in the dark. Although it is widely reported that photoactivity and photo-induced hydrophilicity both occur at any one time, and if a sample is photoactive, it is also very likely to be super-hydrophilic.

| | Exposure to 365 UV radiation | | | |
|---|---|---|---|---|
| | 0hr | 1hr | 2hr | dark |
| $CeO_2$ | 35 | 13.4 | 9.8 | 23.7 |
| $CeO_2/TiO_2$ | 8.4 | 7 | 4.9 | 12.5 |

Table 8. Water contact angles measurements for a ceria thin film and also a ceria titania composite thin film.

At room temperature, the UV-Visible/near infra-red reflectance-transmittance measurements showed that the films transmit across most of the visible spectrum (ca 40%) but do not reflect to a large extent at any wavelength.

## 6.5 Cerium Dioxide Nanoparticle/Titania Thin Film Deposition by Aerosol Assisted Chemical Vapour Deposition From Aqueous Nanoparticulate Cerium Dioxide and Titanium Isopropoxide

### 6.5.1 Film Characteristics and Elemental Analysis

Cerium dioxide nanoparticles were successfully incorporated into a $TiO_2$ host matrix by the AACVD of titanium isopropoxide and ceria nanoparticles at 500 °C. This was done via a layer-by-layer growth of thin films on glass. Initially, a layer of $TiO_2$ was deposited by conventional single source AACVD using $[Ti(O^iPr)_4]$, the reactor source

was switched and a layer of $CeO_2$ nanoparticles deposited. A further set of films was deposited by making a $TiO_2$ layer followed by a $CeO_2$ layer a further $TiO_2$ and a final $CeO_2$ layer. A final set of films was made in this system however the deposition sequence was in reverse- $CeO_2$ followed by $TiO_2$ followed by $CeO_2$ followed by $TiO_2$. The reason for the multiple depositions was that there was a precursor solubility mismatch; the $CeO_2$ nanoparticles are suspended in water, whereas $[Ti(O^iPr)_4]$ hydrolyses in aqueous solutions.

The films formed from the reaction of titanium isopropoxide and water at 500 °C were milky white in colour with a rainbow interference effect due to a variation in film thickness. The films were semi-transparent and passed the Scotch tape test but could be scratched with a steel scalpel. The films did not dissolve in dilute acid and alkali and were insoluble in water and common organic solvents (methanol, ethanol, acetone). All samples prepared had a uniform composition and thickness across the central portion (ca 3-4 cm) of the substrate. The films showed no change in optical properties on storage in air for 6 months.

Glancing angle X-ray diffraction confirmed both the $CeO_2$ and anatase $TiO_2$ phases. However there is some overlap of the $CeO_2$ and $TiO_2$ peaks but these values are comparable with reference values nevertheless. The X-ray data confirms that there is no shift in the main peaks, indicating that a composite film has been formed with the $CeO_2$ nanoparticles embedded within a host matrix. However, there is a decrease in the width of some of the titania peaks at half height- compared with a pure $TiO_2$ film made with the same precursor set, probably as a consequence of the longer periods of heating involved in laying down multiple layers of the composite film.

Both the UV-visible absorption spectra for the original solution and the $CeO_2$ thin films were comparable. Raman analysis was performed and showed the expected bands for anatase titania at 143, 396, 515 and 612 $cm^{-1}$. There is no shift in the peak positions, this is also consistent with the incorporation of $CeO_2$ within a host matrix.

Spot EDAX analysis showed that cerium, oxygen and titania were present in the films- with some slight inconsistencies (Figure 67). Wide-area EDAX showed that the $CeO_2$ to titania ratio was 1:13. This was reproducible across the substrate. The elemental

analysis gave results that were comparable to the concentration of $CeO_2$ and $TiO_2$ used, therefore there was a good transferability from the precursor to the substrate.

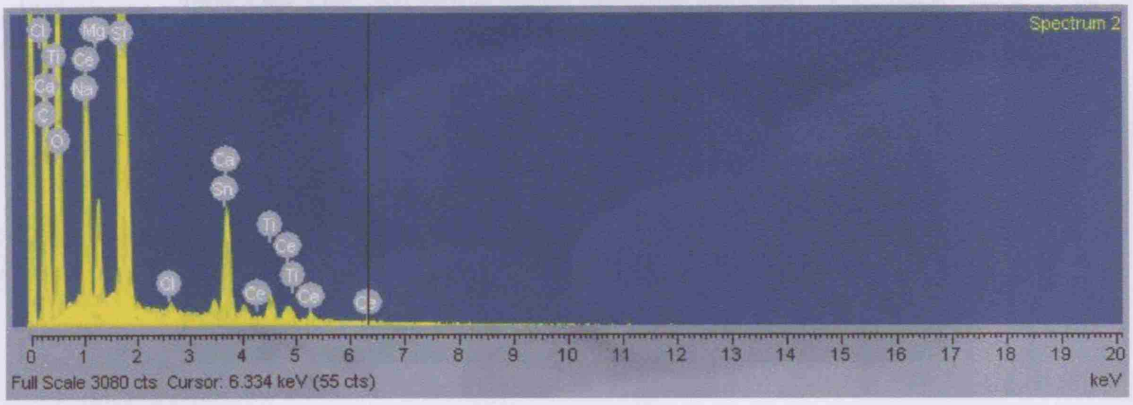


Figure 67. EDAX analysis data for a $CeO_2$/titania composite thin film prepared by AACVD at 500 °C. (The presence of tin is due to breakthrough to the coated tin layer on glass, present due to the float glass process, where the glass is passed over molten tin).

## 6.5.2 Thin Film Growth Morphology and Functional Properties

As seen in the SEM images of $CeO_2$ nanoparticle/$TiO_2$ thin films, a more compact background is observed, along with nanoparticles approximately 10 nm in diameter (Figure 68). The brighter particles are likely to be ceria nanoparticles and are comparable to the nanoparticle size in the original aqueous solution- there is no agglomeration of the $CeO_2$ upon incorporation into a $TiO_2$ host matrix. This was reproducible across the sample surface, with even distribution of $CeO_2$ within the $TiO_2$ host matrix. From side on SEM images, the film thickness was found to be 800 nm, giving a growth rate of 800 nm $hr^{-1}$. Depositing multiple layers did not give a "layered" structure, rather changing the number of layers repeatedly yielded $CeO_2$ nanoparticles incorporated within a titania host matrix. Adding additional layers increased the thickness of the films.

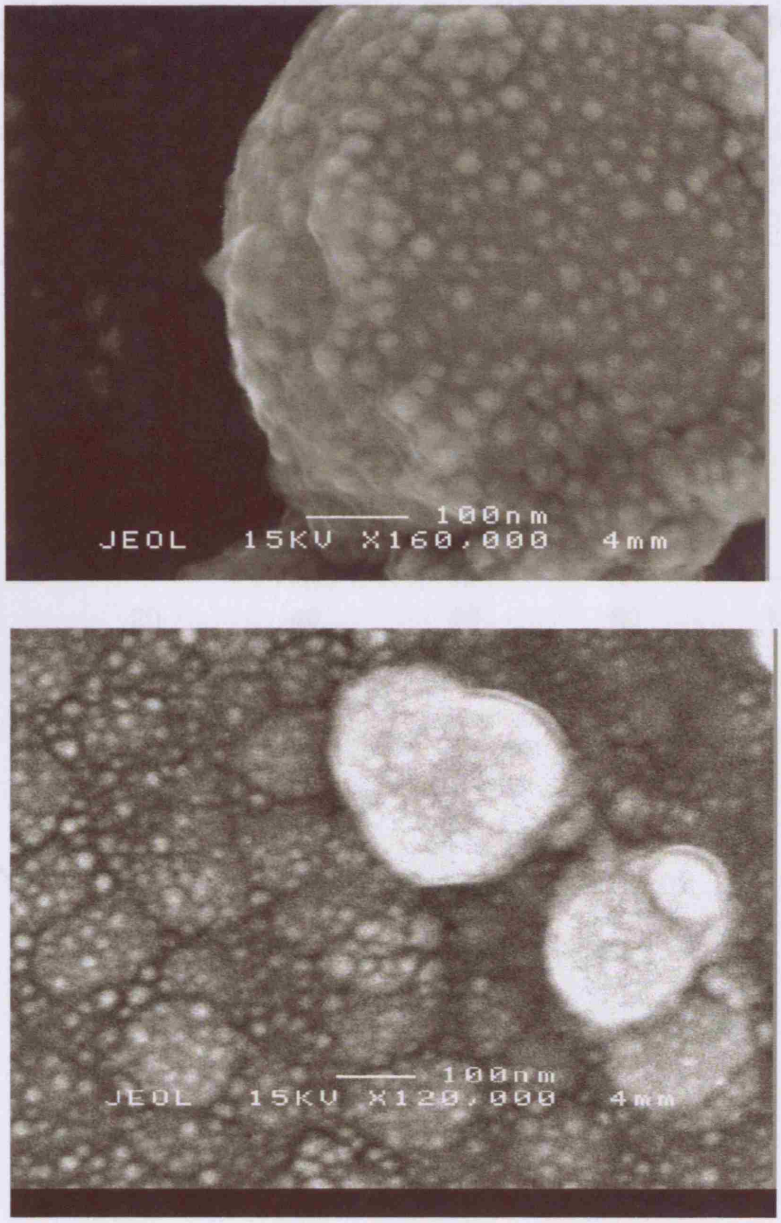


Figure 68. SEM images showing a compact background with nanoparticles of approximate diameter 10 nm along with larger ovals 100 nm wide.

All samples prepared were photocatalytically active and exhibited photo-induced super-hydrophilicity as suggested by the stearic acid test and contact angle measurements. The photocatalysis of the composite $CeO_2$-$TiO_2$ films was found to be at a level comparable to titania alone- the decrease in the normalised C-H peak area for $CeO_2$ incorporated $TiO_2$ samples occurred at virtually the same rate as that for a titania sample, a destruction rate of $4.2 \times 10^{12}$ molecules $cm^2min^{-1}$ for 254 nm UV light was calculated. Therefore the addition of $CeO_2$ into the $TiO_2$ host matrix did not detectably

enhance the photocatalytic activity of the titania thin film. Figure 69 shows the degradation rate is much faster for 254 nm light as compared to 365 nm.

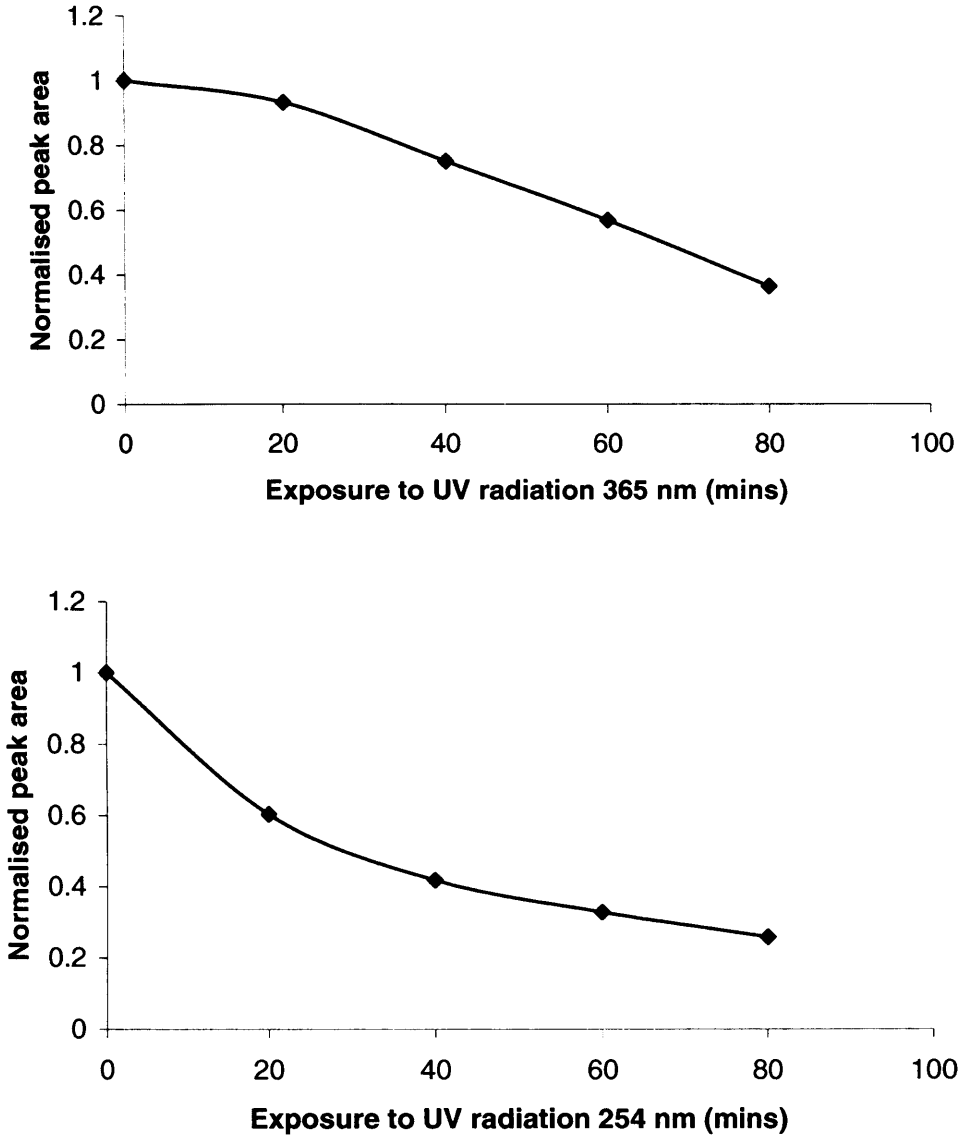


Figure 69. Decrease in stearic acid C-H peak area for a ceria-titania film prepared by AACVD at 500 °C upon radiation with UV light.

Previous studies have shown that incorporation of a $CeO_2$ phase into $TiO_2$ enhances the photocatalysis capability of titania- however this was for reactions in water[234]. The substantially enhanced activity was attributed to stabilised charge separation and the potential of $Ce^{4+}/Ce^{3+}$ couple being more positive than that of $H^+/H$, which makes the electrons of the conduction band ($TiO_2$) more easily transferable to $Ce^{4+}/Ce^{3+}$ than $H^+/H$[235].

The initial water contact angles for $CeO_2$-$TiO_2$ films were ca 55° prior to irradiation with UV light, this reduced to 12° on exposure to 254 nm radiation for 1 hour and decreased further to 2° after 24 hours continuous exposure to room-light. Leaving the films in the dark for 24 hours lead to film water contact angles of 49°. This result is comparable to the low contact angles exhibited by titania alone.

At room temperature, the reflectance-transmittance measurements showed that the films transmit across the visible spectrum but do not reflect to a large extent at any wavelength. The films did show marked specular reflectance associated with haze.

In conclusion, introducing nanoparticulate $CeO_2$ into a $TiO_2$ host matrix did not enhance the photocatalytic activity of the titania thin films, or the photo-induced super-hydrophilicity properties.

## 6.6 Cerium Dioxide Nanoparticle/Gold Nanoparticle Thin Film Deposition by Aerosol Assisted Transport From Aqueous Nanoparticulate Cerium Dioxide and Synthesised Gold Nanoparticles

### 6.6.1 Preparation of Gold Nanoparticle Thin Films By AACVD

Thin films of gold nanoparticles were deposited by aerosol assisted transport at glass substrate temperatures of 500°C from solutions containing gold nanoparticles. This work was completed using an AACVD set up, whereas the gold nanoparticle films deposited in Chapter 4 were using an AA/APCVD set up. Two sets of films were grown- one where the initial gold nanoparticles were suspended in water and the other where they were suspended in toluene. Both sets of films were transparent and purple. The films passed the Scotch tape test but could be scratched with a brass scalpel and they did dissolve in organic solvents, acid and alkali.

UV-visible analysis of the original aqueous and organic gold nanoparticle solutions was carried out (Figure 70). A surface plasmon resonance band as expected for gold was

seen at 520 nm in both solutions. However, for the gold nanoparticle films, a strong plasmon resonance was seen at ca. 540 nm (Figure 71). This plasmon peak was at a slightly longer wavelength than in the initial nanoparticulate suspension (520 nm)- indicating perhaps some growth within the nanoparticle during the deposition or a shift in the dielectric constant of the media.

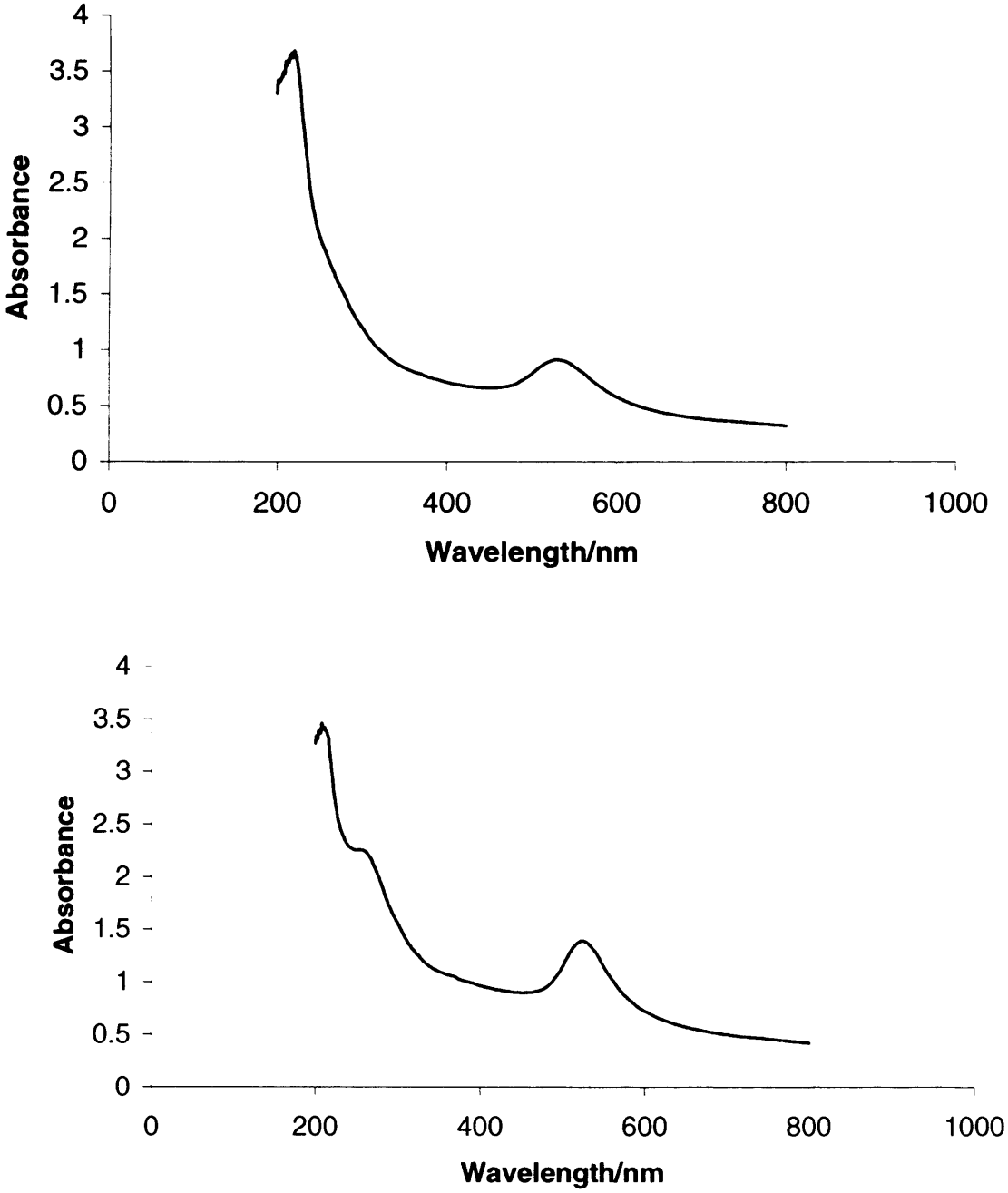


Figure 70. UV-vis absorption spectra for gold nanoparticle solutions in toluene and water respectively.

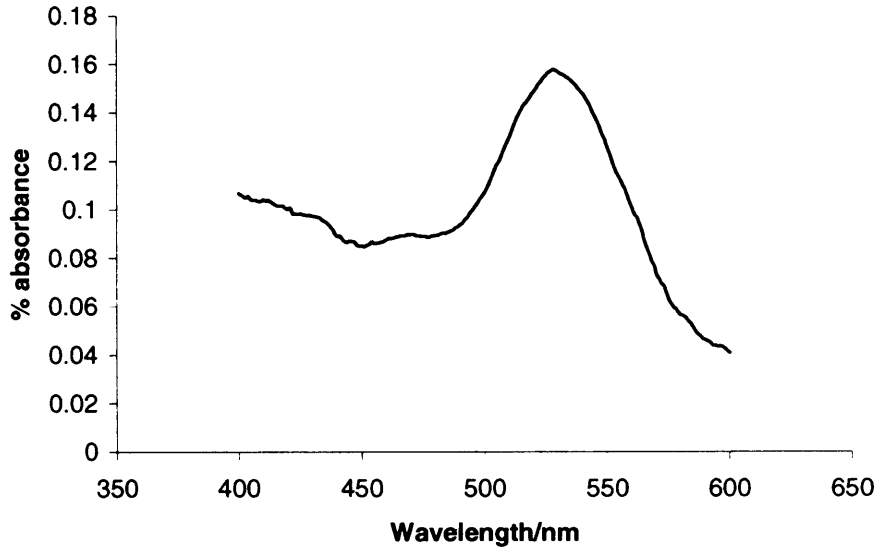


Figure 71. UV-vis absorption spectrum for a gold nanoparticle thin film deposited by aerosol assisted CVD at 500 °C in toluene.

The presence of gold nanoparticles was confirmed by spot EDAX analysis and XPS. TEM imaging of the original nanoparticle solutions was also carried out and the nanoparticles in toluene were found to be larger than those prepared in water. The Au nanoparticles in water were 8 nm whereas the gold nanoparticles in toluene were found to be approximately 15 nm. SEM imaging showed that both sets of these gold particles agglomerated on the glass substrate formed particles of size 15 – 60 nm, and did not deposit as the original particles.

## 6.6.2 Preparation of Ceria/Gold Nanoparticle Thin Films By AACVD

### 6.6.2.1 Ceria/Gold Nanoparticle Thin Film Characteristics and Elemental Analysis

Two different preparations of Au nanoparticles were used, nanoparticles synthesised in water and also in toluene. The Au nanoparticles formed in water were added to the cerium oxide nanoparticles in water resulting in a single aqueous mixture of Au and

$CeO_2$ nanoparticles. This allowed a ceria/gold nanoparticle thin-film to be deposited in a single step. The second method involving gold nanoparticles suspended in toluene and the cerium oxide nanoparticles in water utilised sequential depositions of titania followed by gold.

All films prepared were milky white with a purple hue. The films did not pass the Scotch tape test and could be scratched with a scalpel. The films dissolved in alkali (NaOH, 2 M) but were insoluble in water and common organic solvents (methanol, ethanol, acetone). All samples prepared had a uniform composition across the substrate. The films showed no change in optical properties on storage in air for 8 months.

Both the UV- visible spectrum for the original Au and $CeO_2$ solution and the Au-$CeO_2$ thin films were comparable- in that a gold plasmon resonance was observed for the gold at ca 520 nm and the cerium oxide band edge at 380 nm. This indicates a good transfer of $CeO_2$ and Au to the glass substrate and that the species can be co-deposited and that they do not chemically combine.

Glancing angle X-ray diffraction confirmed both the $CeO_2$ and Au nanoparticle phases, Figure 72. Distinct reflections can be seen for both the cerium oxide and gold. The peaks for gold are at 39.8° and 44.5°. Ceria peaks are seen at 28.9, 47.8, 56.5 and 64.8°. These are comparable with reference values[236]. The X-ray data confirm that there is no shift in the main peaks, indicating that a nanoparticle composite film has been formed. There is a no change in the width of the peaks at half height, indicating that the presence of another nanoparticle does not change the crystallinity of the film. The amorphous background seen in Figure 72 is due to breakthrough to the underlying glass.

The Raman analysis did not show any peak for $CeO_2$ as the structure for $CeO_2$ is cubic, but XRD analysis confirmed both the gold nanoparticle and the cerium oxide phase.

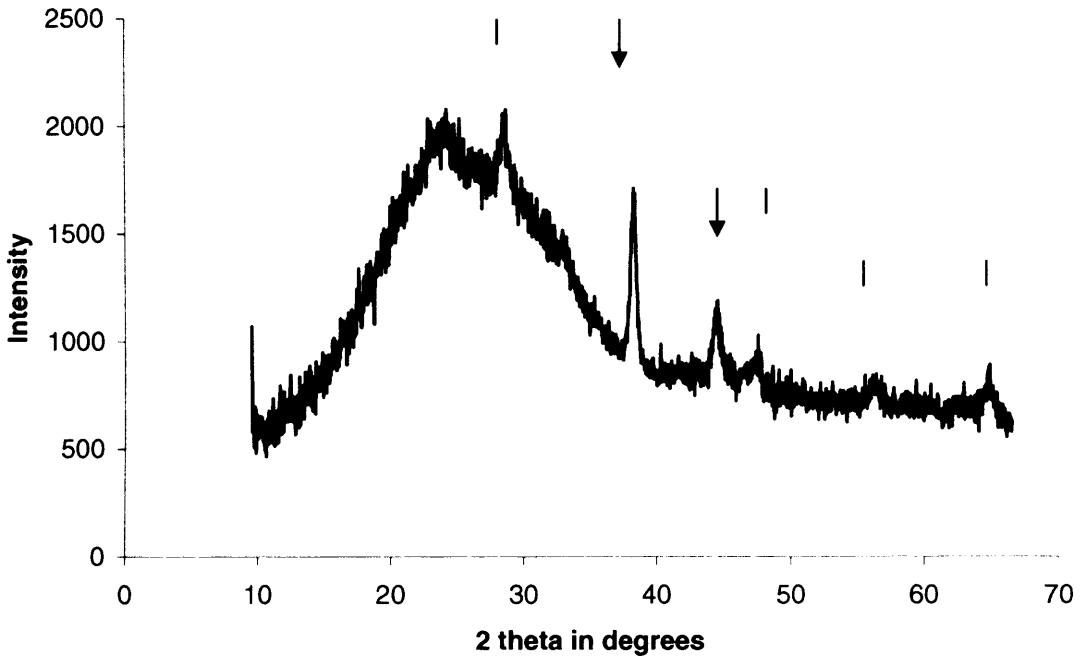


Figure 72. XRD pattern confirming the cerium dioxide and gold nanoparticle phase in a film of nanoparticulate $CeO_2$/Au. The film was deposited by aerosol assisted CVD at 500 °C.

↓ Au and | = $CeO_2$.

XPS confirmed the presence of gold and ceria in the film. Figure 73 Shows the Ce Auger peaks, the Ce 3d, Au 4f and Au 4d. Au 4f 7/2 and 5/2 peaks were seen at binding energies of 87.5 and 83.7 eV respectively, and 4d peaks corresponding to metallic gold[170].

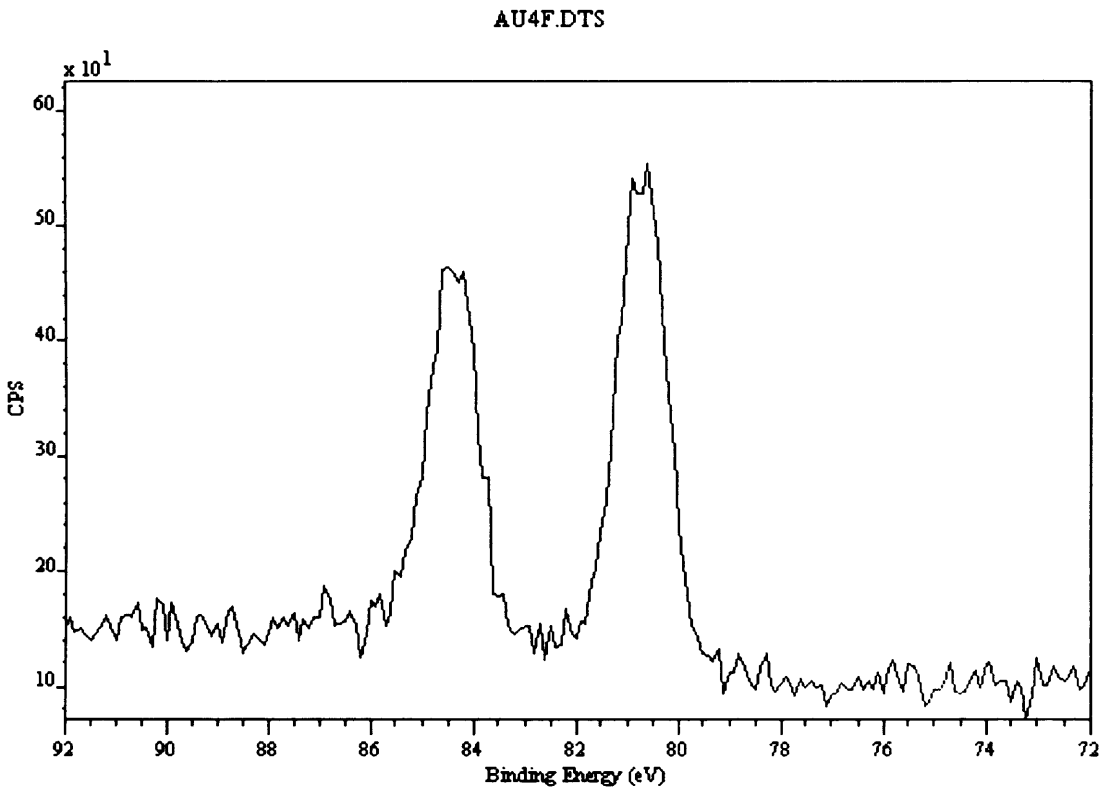
AU4F.DTS
x 10^1
60
50
40
30
20
10
CPS
92
90
88
86
84
82
80
78
76
74
72
Binding Energy (eV)

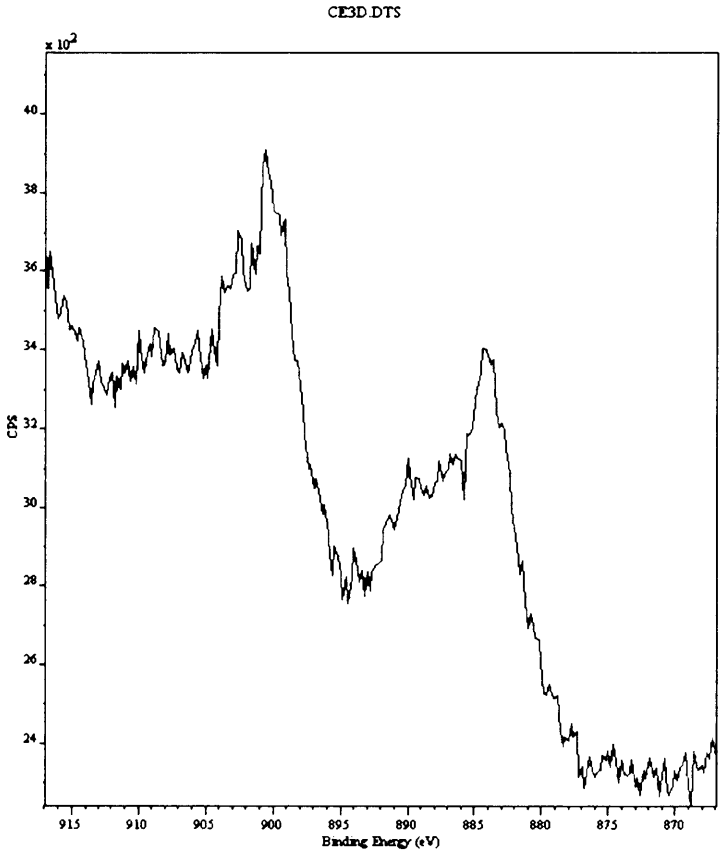
CE3D.DTS
x 10^2
40
38
36
34
32
30
28
26
24
CPS
915
910
905
900
895
890
885
880
875
870
Binding Energy (eV)

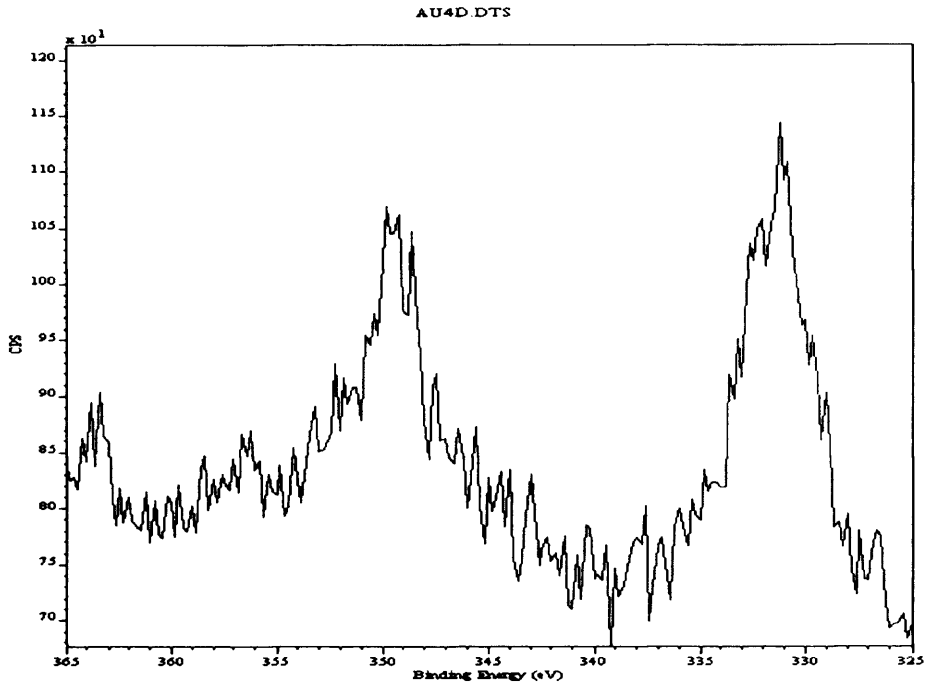


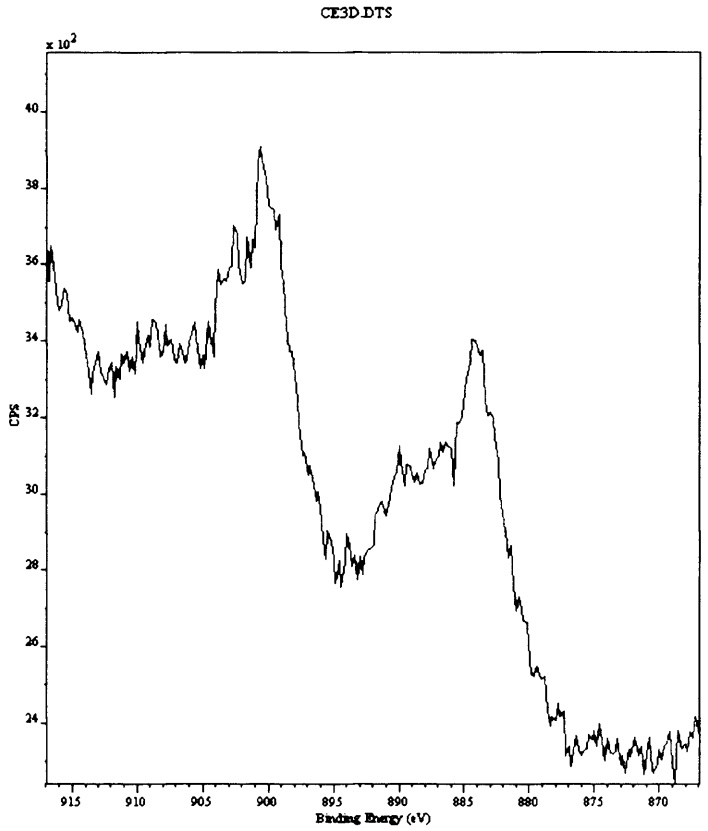


Figure 73. XPS analysis for a ceria/gold nanoparticle thin film deposited by aerosol assisted CVD at 500 °C.

In general it was found that when Au is coated on top of $CeO_2$, a greater atom% Au is found, whereas if $CeO_2$ is deposited onto Au, the atom% for Ce is higher. This is not surprising as XPS is a surface sensitive technique sampling the top 1-10 monolayers. Spot EDAX analysis showed that the smaller particles, 10 nm in size contained Au in greater quantity, and the larger particles, 50 nm or so contained greater amounts of Ce (Figure 74).

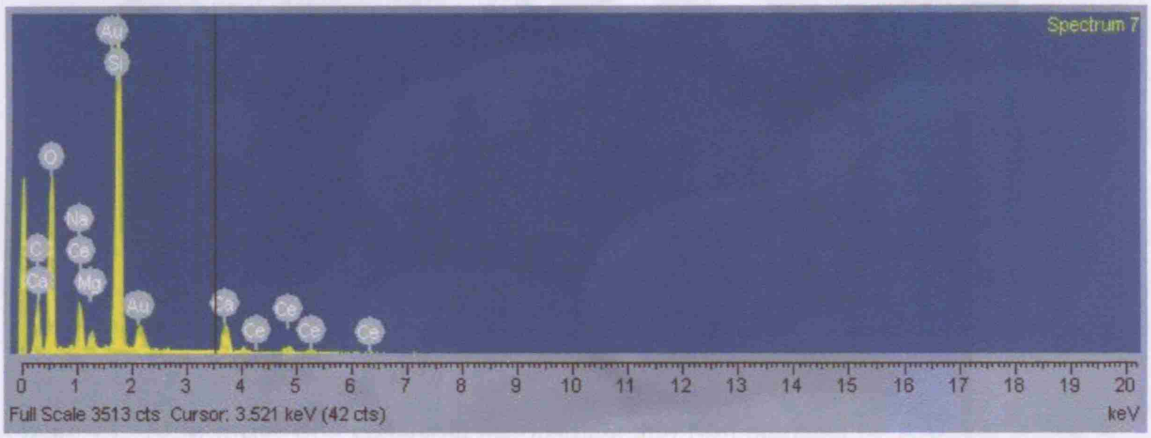


Figure 74. EDAX analysis for a ceria/gold nanoparticle thin film prepared by AACVD at 500 °C confirming Ce and Au.

### 6.6.2.2 Ceria/Gold Nanoparticle Thin Film Growth Morphology and Functional Properties

SEM images of $CeO_2$/Au nanoparticle films show smaller nanoparticles of dimension 15 nm together with larger particles of diameter 40 nm, Figure 75. Spot EDAX analysis showed that these smaller particles contained larger amounts of gold, and that the larger ones contained more ceria. Additional SEM images of Au/$CeO_2$ nanoparticle films show smaller particles with an approximate diameter of 20 nm along particles with a 10 nm diameter, Figure 76. All elemental analyses confirm that a composite ceria/gold nanoparticle thin film has been deposited, hence there is good transfer from the precursor solutions.

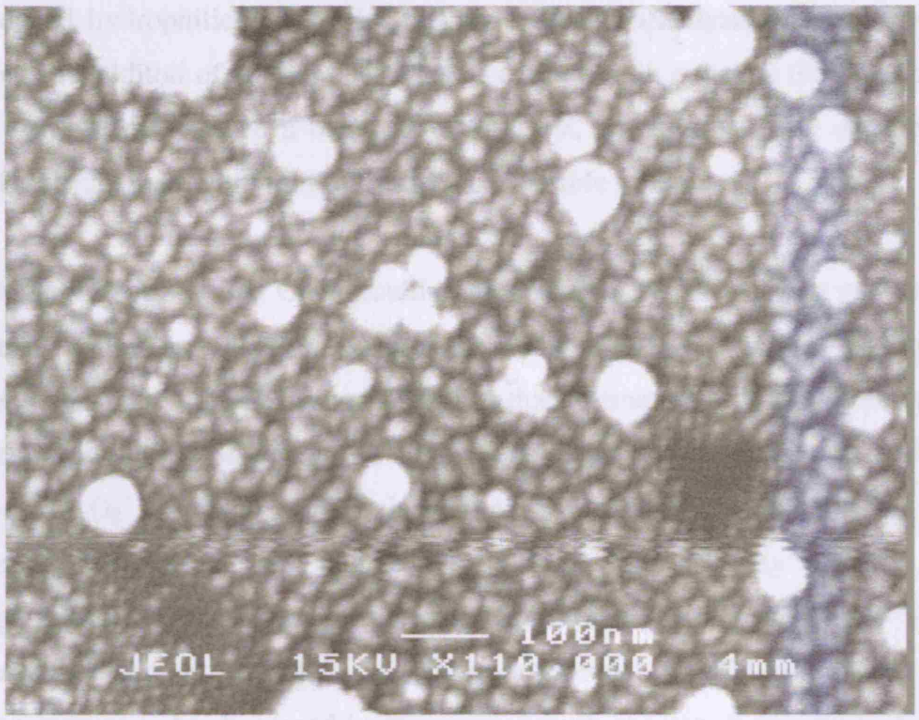


Figure 75. SEM image of a ceria/gold nanoparticle thin film prepared by AACVD at 500 °C. The film contained smaller gold nanoparticles and larger ceria nanoparticles.

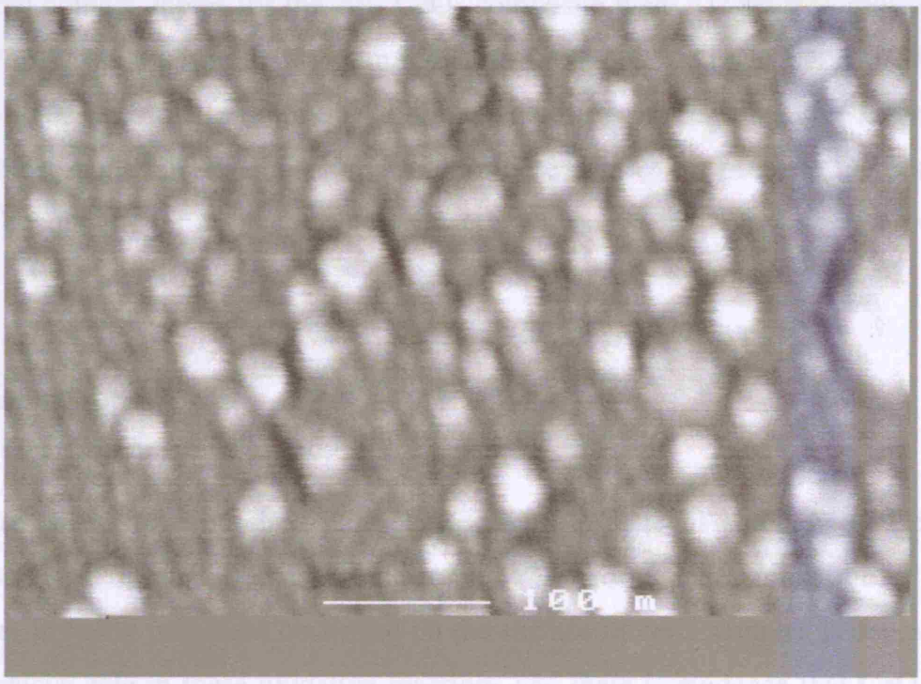

Figure 76. SEM image of a gold/ceria nanoparticle thin film prepared by AACVD at 500 °C. This film contained two different nanoparticle sizes.

The Au/$CeO_2$ nanoparticulate films were photocatalytically active and also exhibited photo-induced hydrophilicity. Again, the level of photocatalysis was comparable to titania, but the additon of Au nanoparticles to ceria did not enhance the photocatalytic ability. These films showed a bandgap of 2.94 eV, and consequently can be photo-activated by irradiation with light in the near UV-visible range.

These properties suggest that $CeO_2$ could be potentially used as a photocatalyst for the oxidation of pollutants. It has been proven that photocatalytic activity in $CeO_2$ thin films occurs through a different mechanism to that in titania[237]. An EPR study of the $CeO_2$ nanofilms shows that upon UV illumination in the presence of oxygen the formation of $O_2^-$ and other radicals which are derived from the trapping of photogenerated electrons are induced[237]. These species play a role in the photodegradation process, although the lower width of the band gap interval implies a lower oxidative potential of the holes photo-produced on $CeO_2$ compared to those formed on anatase. As discussed in the previous sub-chapter, it is proposed that the main effect of UV photo-activation of $CeO_2$ could be to favour the formation of surface oxygen vacancies.

The initial contact angles for the Au- $CeO_2$ composite were 41° prior to radiation, this reduced to 8° on exposure to 254 nm radiation for 1 hour and decreased further to 4° after 24 hours exposure to room light. Leaving the films in the dark for 24 hours lead to film contact angles of 45°. This shows that these films have promise for use as anti misting coatings.

## 6.7 Discussion

There are only a few reports on the photoactivity in aqueous solutions of $CeO_2$, and consequently additional studies are desirable. The formation/annihilation of oxygen vacancies in redox processes occurring on the surface of ceria samples is considered to play a crucial role in these oxidative reactions and there is evidence that $CeO_2$ can be used as a photocatalyst for the oxidation of pollutants[238]. This thesis reported photocatalytic activity for ceria thin films at a level comparable to titania.

Previous studies have shown that incorporation of a $CeO_2$ phase into $TiO_2$ enhances the photocatalysis capability of titania[239]. The substantially enhanced activity is attributed to titania-anatase and the potential of $Ce^{4+}/Ce^{3+}$ couple being more positive than that of $H^+/H$, which makes the electrons of the conduction band ($TiO_2$) more easily transferable to $Ce^{4+}/Ce^{3+}$ than $H^+/H$.

Intensive research has been completed on the optical properties of ceria, in particular absorbance, reflectance and transmittance. More work has yet to be completed on the influence of nanostructures on properties such as grain-boundaries, defects, oxygen vacancies, crystallite size and how these affect the optical properties of the ceria thin films[91].

$CeO_2$ thin-films have previously been deposited by several techniques including magnetron sputtering and sol-gel processing. More work is yet to be completed on the influence of nanostructure on properties such as grain boundaries, defects, oxygen vacancies, crystallite size and how these affect the optical properties of ceria thin films[240, 241]. The films deposited in this thesis did not give rise to any extra ordinary growth morphologies: the original spherical nanoparticle shape was maintained upon transfer to the glass substrate. Deposition of the ceria nanoparticles into a titania host matrix also deposited similar growth.

In particular, researchers are interested in utilising enhanced optical properties for use in electrochromic appliances. Electrochromic materials change their optical properties in response to an electrical signal. Thin films of ceria have been deposited by physical vapour deposition methods in order to aid this study. This process allows films of high quality to be grown. Researchers are currently analysing ceria thin films properties and relating these to the deposition parameters and electrochromic behaviour[60].

A range of other ceria thin films have been deposited, and these include $CeO_2$ thin films deposited on Ni metal[93], on $Al_2O_3$ (1-102) and $TiO_2$ (001) single crystal substrates by MOCVD[94]. Ceria had also been deposited electrochemically on $ZrO_2$ and $Al_2O_3$ thin films formed on stainless steel[95] and sapphire by molecular beam epitaxy[96]. Physical vapour deposition of ceria onto ITO coated glass, Si wafers and fused silica has also

produced films of the desired quality[97]. There are no reports on the AACVD of ceria nanoparticles or their subsequent incorporation into a titania host matrix.

Krogman *et al* have investigated the optical properties of ceria thin films, here they tune the thickness and refractive index of the films in order to shift the minimum wavelength to the preferred value[242]. They found that the films showed a very high transmission of 97 %. In the work reported in this thesis, the ceria thin films exhibited a transmission of 40-60 %. However, Krogman *et al* were able to tune the refractive index and thickness to yield the maximum transmission.

In this research, generally, there was a very good transfer of nanoparticles to the substrate, with no change in size or shape upon incorporation into a host matrix. The films yield desirable colours and display photocatalysis and good contact angle data, which is useful for solar control and anti misting coatings.

## 6.8 Conclusion

Thin films of $CeO_2$ nanoparticles were successfully deposited and thereafter $CeO_2$ nanoparticles were incorporated into a titania host matrix. These films showed no enhancement in the photocatalytic activity as compared to titania. Thin films of Au nanoparticles were formed from solutions made in water and toluene via aerosol assisted chemical vapour deposition. Thin films of gold and ceria nanoparticles were deposited via AACVD from both toluene and water solutions. These thin films show potential as photocatalysts but through a different mechanism to titania.

In the $TiO_2/CeO_2$ deposition it was proven that preformed nanoparticles from solution can be embedded into a host matrix thin film by using a conventional CVD precursor. This technique is different to those currently used to form nanoparticulate thin films and will have widespread applicability to a range of thin films. Furthermore the nanoparticulate cerium oxide thin films show marked photo-induced super-hydrophilicity and good photocatalytic performance for the destruction of a stearic acid over-layer. Therefore $CeO_2$ shows promise both as a photocatalyst and for use in solar

control window coatings and merits further investigation and is a very promising material for the future. Moreover, its high refractive index and excellent transmission in the visible and infrared regions will allow its application as successful window coatings[243]. Furthermore ceria is mechanically stable i.e. adhesive and stable against mechanical abrasion, chemical attack and high temperatures[244, 245].

# Chapter 7: Deposition of Iron Oxide Nanoparticle Thin Films and Iron Oxide – Titania Composite Thin Films on Glass Prepared by Aerosol Assisted Chemical Vapour Deposition.

## 7.1 Introduction

Aerosol assisted chemical vapour deposition (AACVD) was used to deposit 4 series of thin films on glass. Two different methods were used to prepare iron oxide nanoparticles, the first method was a chemical reduction in water, and the second method made use of stabilising ligands which were a mixture of oleic acid and oleylamine. Both the aqueous and organic iron oxide nanoparticles were transferred onto glass to deposit a nanoparticulate thin film. These were used to successfully deposit thin films incorporating nanoparticles within a host matrix. The aqueous iron oxide nanoparticles were incorporated within a titania host matrix by a different approach which involved depositing alternating iron oxide and titania layers.

Thin films of $Fe_2O_3$ nanoparticles attract interest due to their technological and fundamental importance. They are commonly used in information storage, magnetic resonance imaging contrast agents, superparamagnetism, and macroscopic quantum tunnelling associated with size quantization and electronic quantum confinement effects[246, 247, 248,249].

In this study, research was conducted on the properties of $Fe_2O_3$ nanoparticles transferred to a thin film on a glass substrate by aerosol assisted chemical vapour deposition (AACVD) and thereafter deposition of thin films of $Fe_2O_3$ nanoparticles incorporated into a host $TiO_2$ matrix was completed.

This chapter describes the preparation and characterisation of iron oxide nanoparticle incorporated thin-films on glass prepared from the aerosol assisted chemical vapour deposition of titanium isopropoxide and iron oxide nanoparticles (3 nm and 11 nm sizes). It was also possible to dope iron oxide nanoparticles into the titania host matrix.

The incorporated nanoparticles do not enhance the optical properties or show an increase in the photocatalytic activity. However the photo-induced super-hydrophilicity is very much enhanced compared to titania.

## 7.2 Method For Film Deposition - Aerosol Assisted Deposition Procedure

Iron oxide ($Fe_2O_3$) nanoparticles in water were synthesised by a chemical reduction experiment and organic capped $Fe_2O_3$ nanoparticles were made as described in the methods outlined in Chapter 2. The aqueous nanoparticles were 9-14 nm in diameter whereas the organic capped nanoparticles were 1-5 nm wide.

### 7.2.1 Iron Oxide Nanoparticulate Films

Iron oxide nanoparticles (5 mL) were transferred to the aerosol bubbler, and thin-films were deposited at 500 °C and at a $N_2$ carrier-gas flow-rate of 0.5 L $min^{-1}$.

### 7.2.2 Titanium Dioxide – Iron Oxide Composite Films

The titania precursor was prepared by dissolving 0.56 g of titanium isopropoxide (Aldrich) in toluene (50 ml), and an AACVD experiment conducted. For the incorporation of nanoparticles, 5 mL of either the iron oxide nanoparticles (0.5 mmol) in water or toluene (50 mL) solution was used for the run.

Layer by layer deposition growth was used to form composite titania anatase-iron oxide thin films on glass. The AACVD process initially formed a titania film. Thereafter, the iron oxide nanoparticles in water were transferred to the PTFE chamber and then deposition continued to form a layer of iron oxide on top of the existing titania layer. The process was repeated up to three times for each precursor to form multiple layers of titania dioxide and iron oxide nanoparticles.

Additionally a single mixed precursor solution was used for making composite iron oxide and titania thin films in toluene, and the film was deposited in one step.

## 7.3 Deposition Parameters

A number of different deposition parameters were tested to obtain the optimum conditions for growing nanoparticle thin films of $Fe_2O_3$ on glass. The flow rate and reactor temperature were varied for iron oxide nanoparticle film growth. These iron oxide nanoparticles were then incorporated into a titania host matrix by two different methods of precursor delivery, the first method involved an alternating layer by layer deposition of iron oxide nanoparticle (in aqueous solution) and titania and the second method used simultaneous deposition of titanium isopropoxide and $Fe_2O_3$ organic capped nanoparticles in a single step within the same solvent. This is summarised in Table 9.

| Film Number | Precursors | Solvent 50 mL | Substrate Temperature/ °C | Flow Rates/ L $min^{-1}$ |
|---|---|---|---|---|
| 1 | Aqueous $Fe_2O_3$ nanoparticles 0.5mmol | Water | 450 | 1 |
| 2 | $Fe_2O_3$ nanoparticles 0.5mmol | Toluene | 450 | 1 |
| 3 | Aqueous $Fe_2O_3$ nanoparticles 0.5mmol $[Ti(O^iPr)_4]$ 0.56 g, 2mmol | Layer by layer deposition of aqueous nanoparticles and titania in toluene | 450 | 1 |
| 4 | Organic $Fe_2O_3$ nanoparticles 0.5mmol $[Ti(O^iPr)_4]$ 0.56 g, 2mmol | Simultaneous deposition of nanoparticles and titania in toluene | 450 | 1 |

Table 9. Deposition parameters for $Fe_2O_3$ nanoparticle and composite $Fe_2O_3$ nanoparticle/titania films.

## 7.4 Preparation of $Fe_2O_3$ Nanoparticle Thin Films by Aerosol Assisted Chemical Vapour Deposition From Synthesised Nanoparticulate Iron Oxide

### 7.4.1 Elemental Analysis of Thin Films on Glass

Iron oxide nanoparticle thin films were prepared on glass from the aerosol assisted transport of synthesised aqueous iron oxide nanoparticles and also iron oxide nanoparticles in toluene. The films were uniform and pale yellow/orange in colour. They covered the glass substrate. The iron oxide nanoparticle films made from aqueous nanoparticles did not pass the Scotch tape test, were particulate, and could be wiped off with a tissue. However, the films deposited from organic capped iron oxide nanoparticles in toluene were adhesive, passed the Scotch tape test but could be scratched with both a brass and steel stylus. Interestingly all of the deposition was on the top plate rather than the heated bottom plate. The films were not too hazy, with haze measurements ranging from 1.2- 3%. However for commercial usage, it is desirable for the haze to be less than 0.1 %.

Wide area EDAX analysis confirmed the presence of Fe within the film for both toluene based and aqueous film types. Furthermore, spot EDAX analysis carried out at regular intervals across the sample confirmed that the iron was distributed homogeneously across the substrate. UV-visible analysis for both films types showed strong peaks at 300 nm. This is as expected for $Fe_2O_3$ nanoparticles, where very strong absorptions at wavelengths of 290 nm are often seen with a shoulder at 380 nm[250].

X-ray powder diffraction of the $Fe_2O_3$ nanoparticle films did not give rise to any reflections and the glass background was present. Few peaks were seen in the X-ray diffraction pattern, indicating that the deposited films have low crystallinity. It is sometimes normal for nanoparticle thin films on glass to show only an amorphous background pattern due to a small crystallite size of some nanoparticle thin films. The difference in peak width is related to particle size, and a larger particle size gives rise to narrower peaks. The particle diameter can be derived through the Scherrer equation[251].

## 7.4.2 Growth Morphology

The initial aqueous and organic capped iron oxide nanoparticle solutions were examined by TEM as described in the Experimental, Chapter 2. TEM images for aqueous nanoparticles were examined and uniform nanoparticles of size 11 nm could be seen. There was an excellent particle size distribution, with 83 % of nanoparticles in the sample areas examined having a particle diameter of 11 nm (Figure 77A). Similarly, 81% of the organic capped $Fe_2O_3$ nanoparticles were 3 nm in diameter (Figure 77B).

A

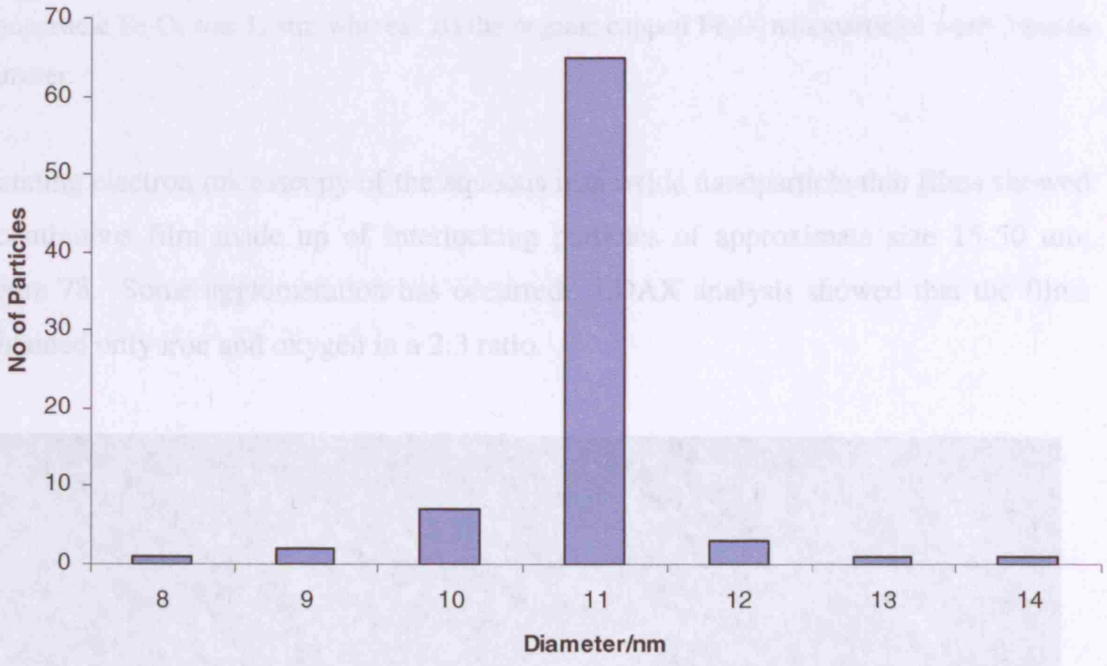

B

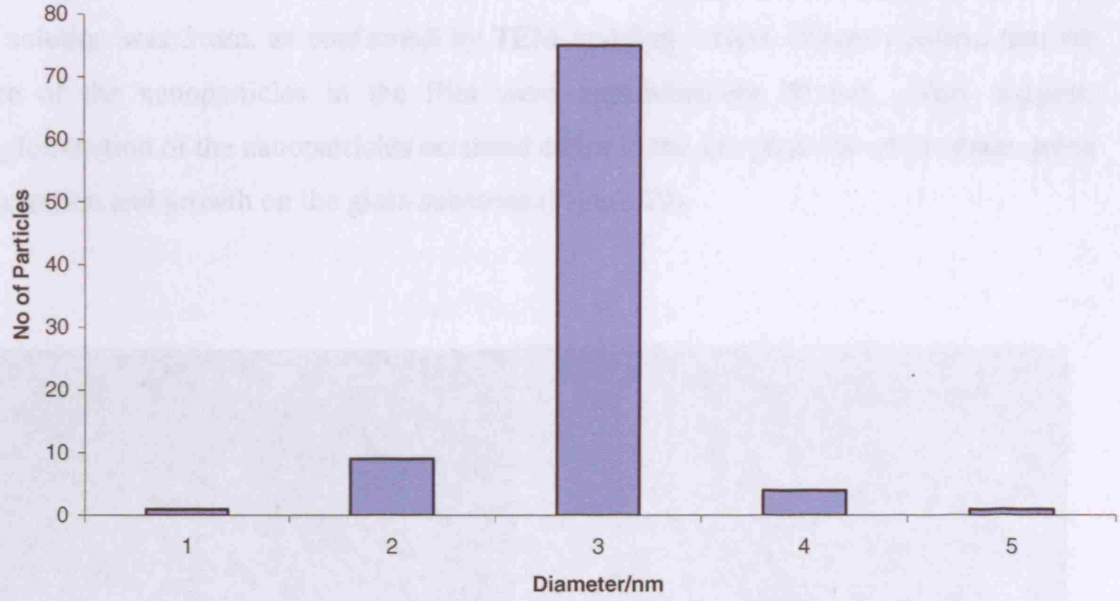


Figure 77. Size distribution graphs for $Fe_2O_3$ nanoparticles confirming that A) aqueous nanoparticle $Fe_2O_3$ was 11 nm whereas B) the organic capped $Fe_2O_3$ nanoparticles were 3 nm in diameter.

Scanning electron microscopy of the aqueous iron oxide nanoparticle thin films showed a continuous film made up of interlocking particles of approximate size 15-50 nm, Figure 78. Some agglomeration has occurred. EDAX analysis showed that the films contained only iron and oxygen in a 2:3 ratio.

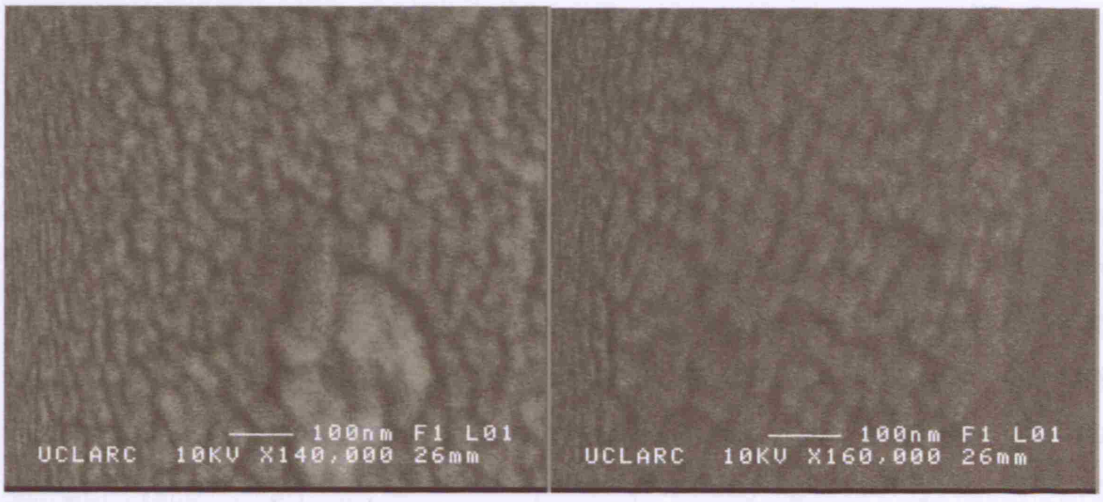


Figure 78. SEM images of $Fe_2O_3$ nanoparticle thin films made by AACVD at 450 °C from an aqueous solution.

In comparison, the iron oxide nanoparticle thin films deposited from toluene were a darker yellow in colour and much more adhesive. The original size of the nanoparticles in solution was 3 nm, as confirmed by TEM imaging. SEM images confirm that the size of the nanoparticles in the film were approximately 20 nm. This suggests agglomeration of the nanoparticles occurred either in the gas phase or whilst undergoing nucleation and growth on the glass substrate (Figure 79).

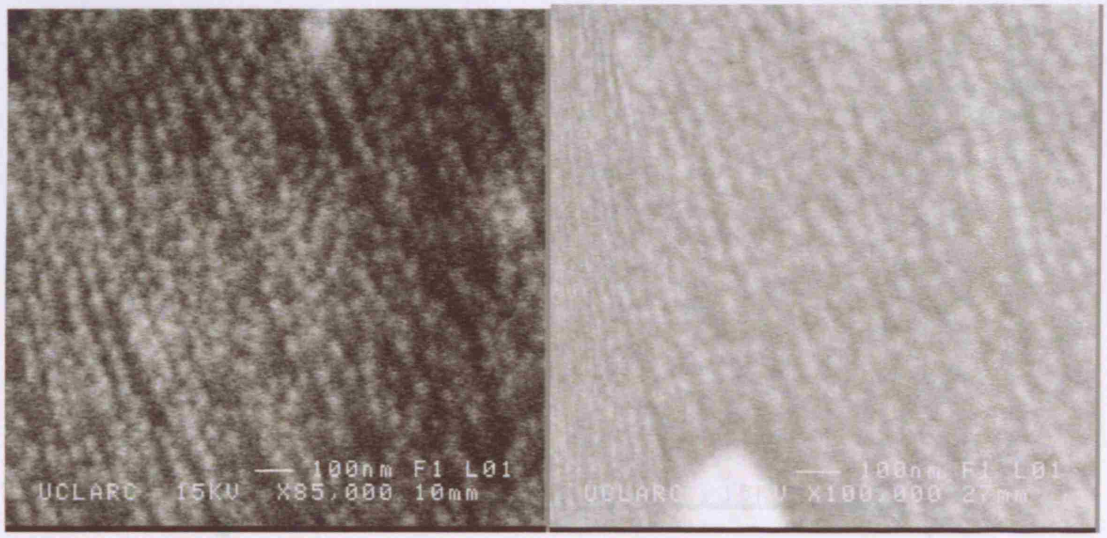


Figure 79. SEM images of $Fe_2O_3$ nanoparticle thin films made from dispersions of capped iron oxide nanoparticles in toluene at 450 °C.

## 7.4.3 Film Functional Properties

The contact angle for water droplets on the iron oxide nanoparticle thin films was very low – between 3 – 7° indicating that the surface is very hydrophilic and also porous. This contact angle dropped further to between 1- 2° on exposure of the surface to 254 nm radiation for 0.5 h. On keeping the samples in the dark for 24 h the contact angle increased to 6 – 7° and on further irradiation decreased again to between 2°. This change in contact angle with time was repeated over many light dark cycles. The very low initial contact angle puts these films in the class of super-hydrophillic films and gives similar measurements to that of titanium dioxide thin films formed from sol-gel or

CVD. The contact angle is probably a consequence of the surface being both partially hydroxylated and hence able to hydrogen bond effectively to the water, and having high porosity engendered by having a very fine microstructural form of nano-scaled particles.

Figure 80 shows the reflectance/transmittance properties for an oleic acid/oleyl amine capped iron nanoparticle thin film. These films reflected at 27 % in the UV and at 15 % in the near infra-red. The films transmitted well from 60 – 77% across the spectrum. This is as expected for nanoparticulate thin films. The Swanepoel method was used to determine the film thickness; 465 nm was calculated.

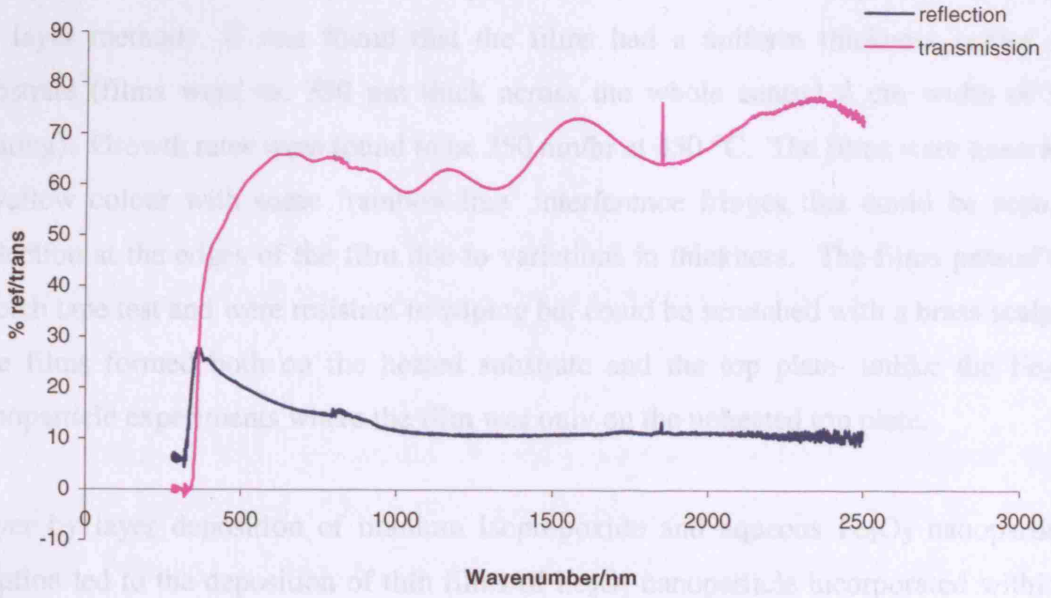


Figure 80. Reflectance/transmittance properties for a $Fe_2O_3$ nanoparticle thin film made from iron oxide nanoparticles capped with oleyl amine and oleic acid at 450 °C.

The aerosol transport method provides a ready means of forming thin-films from a relatively involatile precursor. The film that is formed is on the top-plate of the reactor and is composed of only relatively small nanoparticulates that formed islands rather than agglomerated particles. This shows potential for applications making use of magnetic properties of iron oxide thin film and also for anti-misting optical coatings.

## 7.5 Preparation of Iron Oxide Nanoparticle Films Incorporated In a Titania Host Matrix

### 7.5.1 Elemental Analysis of Iron Oxide Nanoparticle/Titania Composite Thin Films on Glass

Aerosol assisted chemical vapour deposition of iron oxide nanoparticles/anatase titania was accomplished from $[Ti(O^iPr)_4]$ dissolved in toluene at 450 °C. Iron oxide nanoparticles were added to the initial precursor solution and also deposited by a layer by layer method. It was found that the films had a uniform thickness across the substrate (films were ca. 350 nm thick across the whole central 4 cm width of the coating). Growth rates were found to be 350 nm/hr at 450 °C. The films were generally a yellow colour with some 'rainbow-like' interference fringes that could be seen in reflection at the edges of the film due to variations in thickness. The films passed the Scotch tape test and were resistant to wiping but could be scratched with a brass scalpel. The films formed both on the heated substrate and the top plate- unlike the $Fe_2O_3$ nanoparticle experiments where the film was only on the unheated top plate.

Layer by layer deposition of titanium isopropoxide and aqueous $Fe_2O_3$ nanoparticle solution led to the deposition of thin films of $Fe_2O_3$ nanoparticle incorporated within a $TiO_2$ host matrix with similar characteristics to the organic capped iron nanoparticle/titania thin films. The XRD, Raman and EDAX analysis all confirmed the incorporation of the iron oxide nanoparticles into titania. Wide area EDAX analysis showed that the film was made up of titanium, iron, and oxygen.

Figure 81 shows the UV-visible absorption spectra for organic capped iron oxide nanoparticle/titania thin films. Here, a strong interference pattern is clearly seen. UV analysis for all films types showed a shoulder at 390 nm. This is expected for iron oxide nanoparticle thin films on glass. Notice that the strong peak at 300 nm seen for the iron nanoparticle thin films, is no longer present in the UV spectra. This is most likely due to the incorporation of the nanoparticles into the titania host matrix. The Swanepoel method was used to calculate a film thickness of 1250 nm.

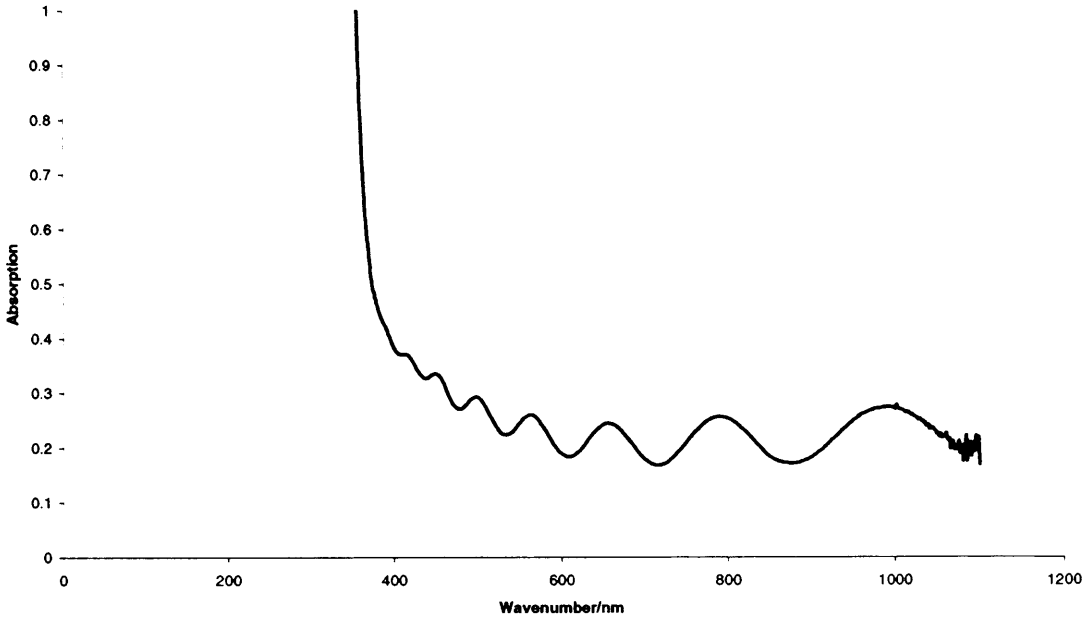


Figure 81. UV-visible absorption spectrum analysis of a titania/$Fe_2O_3$ nanoparticle thin films made from oleyl amine and oleic acid capped iron oxide nanoparticles at 450 °C.

The thin films of $TiO_2$ deposited with $Fe_2O_3$ nanoparticles were investigated using powder X-ray diffraction. The pattern was found to be well matched by the anatase phase of $TiO_2$ and $\gamma$-$Fe_2O_3$ maghemite. A strong signal at approximately 24° is expected for titania anatase. The expected signals for Iron oxide ($\gamma$-$Fe_2O_3$ maghemite) were also seen. Figure 82 shows the labelled iron oxide nanoparticle and titania phases[250]. Some of the iron oxide nanoparticle peaks overlapped with the titania reflections. These iron oxide nanoparticle reflections were generally of much lower intensity than those corresponding to $TiO_2$, suggesting that the iron oxide nanoparticles were present only in small amounts. The full width at half maximum (FWHM) of the peaks was almost constant along the length of the substrate indicating roughly constant crystallite size. Although there was a slight reduction in the FWHM at higher deposition temperatures, indicating larger crystallite sizes. An X-ray diffraction pattern was seen here due to a larger $Fe_2O_3$ crystallite size.

A

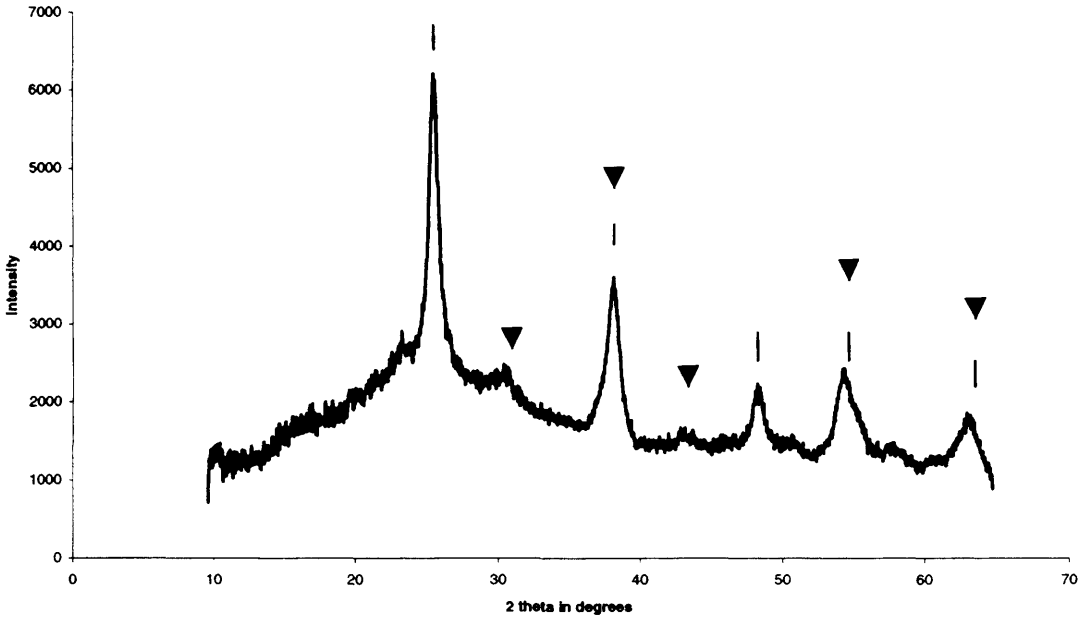


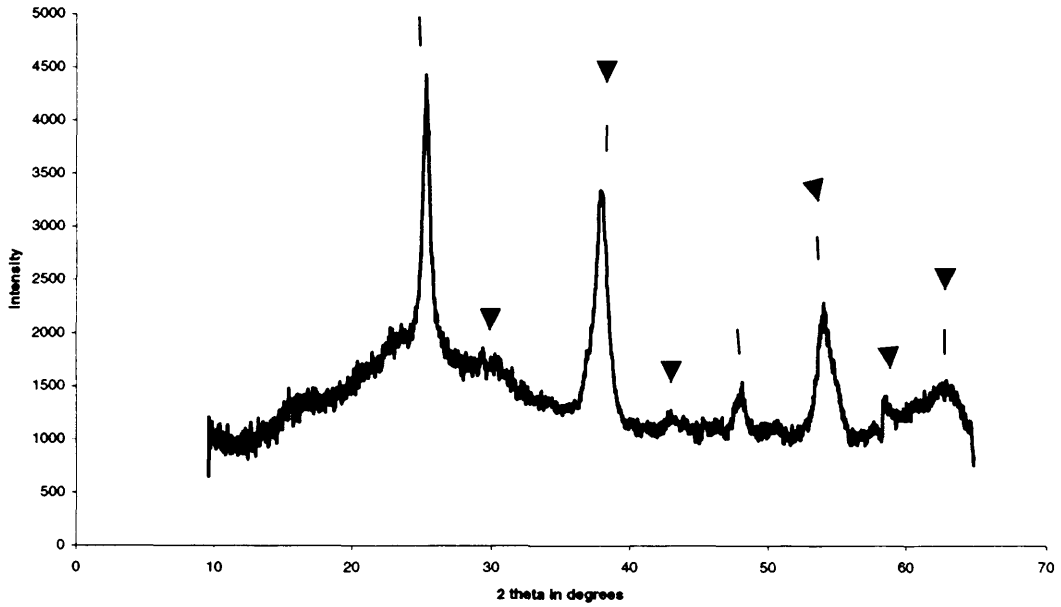


B

Figure 82. XRD spectra for A) a titania/$Fe_2O_3$ nanoparticle thin films made from iron oxide nanoparticles capped with oleyl amine and oleic acid, and $[Ti(O^iPr)_4]$ at 450 °C B) a titania/$Fe_2O_3$ nanoparticle thin films made from aqueous iron oxide nanoparticles and $[Ti(O^iPr)_4]$ at 450 °C. Note that the lines correspond to titania reflections whereas the triangles are iron oxide nanoparticle reflections.

The Raman patterns for the titania films showed the expected bands[251] for anatase with bands at 143, 396, 515 and 612 $cm^{-1}$, no evidence was seen for any iron oxide phase at

any part of the deposited film. However, wide area EDAX analysis confirmed the presence of Fe and Ti on the glass. The Fe : Ti ratio was 1 : 13. This compares well with the original precursors used for deposition. Furthermore, spot EDAX analysis carried out at regular intervals across the sample confirmed that the iron was distributed homogeneously across the substrate.

### 7.5.2 Growth Morphology of Iron Oxide Nanoparticle/Titania Composite Thin Films on Glass

SEM imaging showed a dense spherical ball shape morphology with smaller nanocircles scattered across the substrate (Figure 83) – the balls were of an average diameter of ca. 200 nm and the smaller nanoparticles of $Fe_2O_3$ approximately 15 nm in diameter – use of $Fe_2O_3$ nanoparticles affects the growth and composition of the thin film. Previous work on titania by AACVD and APCVD on glass has always formed a smooth continuous film[19]. Side on SEM images allowed the determination of the film thickness and hence the growth rate of the films. It was found that the film thickness was 350 nm depending on the film sample analysed. The growth rate was calculated to be 350 nm per hour.

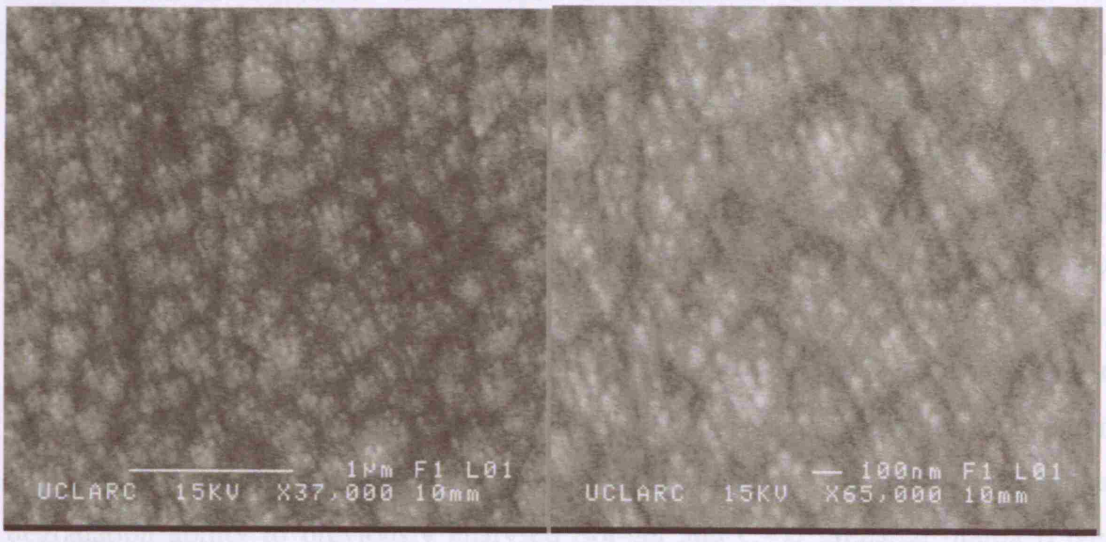


Figure 83. SEM images showing the compact morphology of $Fe_2O_3$ nanoparticles incorporated within a titania host matrix. The films were grown by AACVD at 450 °C.

### 7.5.3 A Sol Gel Study on $Fe_2O_3/TiO_2$ Composite Films

As a comparison to the films formed by AACVD the same $Fe_2O_3$ nanoparticulate-$[Ti(O^iPr)_4]$ precursor solution was used to make sol-gel dip-coated films. The reason for this study was to see whether the microstructure would follow in films made from the same precursor solution – but processed in a different way. By using the sol-gel process a non-adhesive, yellow film resulted. This was unlike those formed by AACVD that adhered well to the substrate. The SEM of the films showed a particulate microstructure. Hence the compact morphology seen in the AACVD route was not in evidence and indicates the uniqueness of that approach in controlling- influencing the film morphology.

### 7.5.4 Functional Properties of Iron Oxide Nanoparticle/Titania Composite Thin Films on Glass

The iron oxide titania films exhibited photo-induced super-hydrophilicity. Typical initial water droplet contact angles were around 40°. The contact angles for the water droplets went down from 18° to 3.4° upon UV irradiation (254 nm, 1 hr). This went down further to 0.2° after further irradiation for one hour. However, when kept in the dark (24 hr) the contact angles returned to 19.7° (Table 10). The initial contact angles are comparable to that found for a typical titania coating formed by CVD which gave initial water contact angles of ca 50°[41]. However, these films were more super-hydrophilic compared to titania and can be included in the unique class of super-hydrophilic coatings. This difference in contact angle can be attributed to the presence of $Fe_2O_3$ nanoparticles in the titania host matrix as seen from the SEM measurements. The films were also photo-catalytically active showing ready destruction of a stearic acid over-layer with both 254 and 365 nm radiation and were comparable in photo-degradation ability to previously analysed Sol-gel and CVD prepared titania (Figure 84)[252] the rate of destruction was 0.69 x $10^{12}$ molecules $cm^{-1}min^{-1}$ for 254 nm UV light).

| Film | 0 hr | 1 hr | 3 hr | 24 hr Dark |
|---|---|---|---|---|
| $TiO_2$ | 53.7 | 25.7 | 17.5 | 46.2 |
| $Fe_2O_3$ / $TiO_2$ Organic capped | 18.3 | 3.4 | 2.1 | 19.7 |
| $Fe_2O_3$ / $TiO_2$ Aqueous | 12.7 | 1.6 | 0.2 | 9.9 |

Table 10. Changes in water contact angles upon irradiation with UV light (254 nm) for iron oxide nanoparticle/titania thin films.

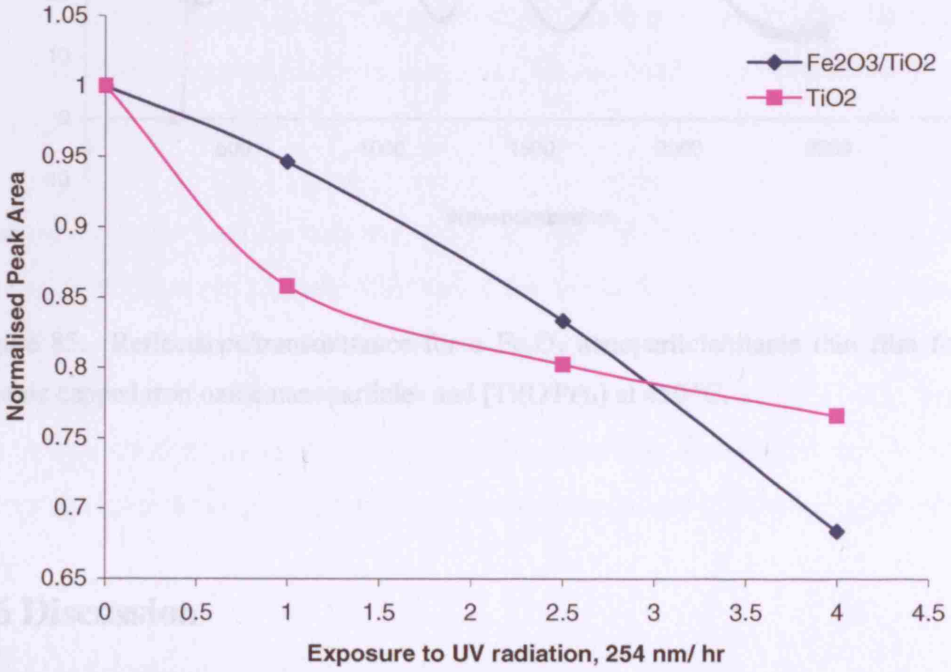


Figure 84. The rate of destruction of a stearic acid over layer in response to 254 nm UV light by a $Fe_2O_3$ nanoparticle/titania thin films formed from organic capped iron oxide nanoparticles and $[Ti(O^iPr)_4]$, deposited by AACVD at 450 °C.

Figure 85 shows the reflectance/transmittance properties for a capped iron nanoparticle thin film. These films reflected at 20 - 30 % across the spectrum showing a strong interference pattern. The films transmitted well from 65 – 75% across the spectrum. This is as expected for nanoparticulate thin films. The Swanepoel method was used to determine the film thickness of the thin film and was found to be 1300 nm.

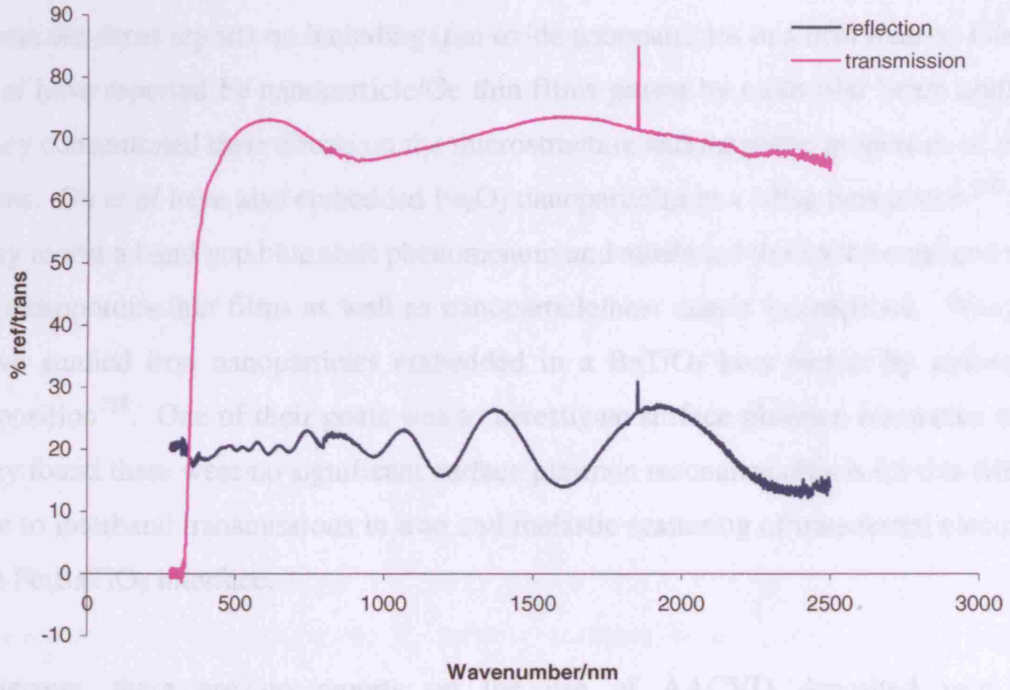


Figure 85. Reflectance/transmittance for a $Fe_2O_3$ nanoparticle/titania thin film formed from organic capped iron oxide nanoparticles and $[Ti(O^iPr)_4]$ at 450 °C.

## 7.6 Discussion

The use of iron oxide nanoparticles is an attractive industrial option due to the enhanced magnetic, electronic and optical properties exhibited by iron oxide at the nanoscale[253]. Previously, Wang *et al* have used the sol-gel process to synthesis $Fe_2O_3$ thin films and recently gold nanoparticles have been embedded in an iron oxide host matrix in order to enhance the optical properties of iron oxide[254]. Here, they concentrated on

functionalising the coated gold. These films gave interesting plasmon resonance effects in addition to the enhanced magnetic properties experienced by iron oxide. There are many reports in the literature for iron oxide thin films embedded with gold nanoparticles. Hida *et al* have also completed this research by sol-gel deposition. Here, they have concentrated on the electrochemical properties rather than optical and functional properties studied in this thesis[255].

There are some reports on including iron oxide nanoparticles in a host matrix- Goswami *et al* have reported Fe nanoparticle/Ge thin films grown by molecular beam epitaxy[256]. They concentrated their efforts on the microstructure and magnetic properties of the thin films. Gu *et al* have also embedded $Fe_2O_3$ nanoparticles in a silica host matrix[257]. Here they report a band gap blue shift phenomenum and attributed this to the confined effects of mesoporous thin films as well as nanoparticle/host matrix interactions. Wang *et al* have studied iron nanoparticles embedded in a $BaTiO_3$ host matrix by pulsed laser deposition[258]. One of their goals was to investigate surface plasmon resonance effects; they found there were no significant surface plasmon resonance effects for this film type due to interband transmissions in iron and inelastic scattering of transferred electrons at the Fe:$BaTiO_3$ interface.

However, there are no reports on the use of AACVD deposited iron oxide nanoparticle/titania composite thin films for applications as optical window coatings. The films reported in this thesis showed enhanced photo-induced super-hydrophilicity compared to the literature reported titania thin films deposited by CVD. Furthermore, the iron oxide nanoparticle/titania composite thin films transmitted well from 65 – 75% across the spectrum and also imparted a yellow tint to the titanium dioxide host matrix.

## 7.7 Conclusion

Aerosol assisted deposition (AAD) was used to deposit $Fe_2O_3$ nanoparticle thin films from a solid nanoscaled precursor. This was a convenient method for applying thin films to glass as it provides reasonable growth rates (350 nm $hour^{-1}$) and conformal coverage of the substrate. The films were adhesive and were very super-hydrophillic.

Titania films formed in the presence of $Fe_2O_3$ nanoparticles form nanoparticulate and "oval" base microstuctures and exhibited two key functional properties, photocatalysis and photo-induced super-hydrophilicity. The initial water contact angles of these films are lower than that seen for $TiO_2$ films prepared in the absence of nanoparticles and is attributed to the presence of $Fe_2O_3$ nanoparticles. The contact angle is probably a consequence of the surface being both partially hydroxylated and hence able to hydrogen bond effectively to the water, and having high porosity engendered by having a very fine microstructural form of nano-scaled particles.

The film that is formed is on the top plate of the reactor and is composed of only relatively small nanoparticulates that formed islands rather than agglomerated particles. This shows potential for applications making use of magnetic properties of iron oxide thin films and also for anti-misting optical coatings.

In general, thin film technology studies reported in the literature have mainly made use of the magnetic properties of iron oxide. There are no reports on the aerosol assisted chemical vapour deposition of iron oxide/titania nanoparticles. As seen from this study, iron oxide nanoparticle/titania thin films gave some interesting properties such as very low contact angles, photocatalytic activity comparable to titania, and a transparent yellow colour with minimal haze.

# Chapter 8: Thin Film Deposition of Gold Nanoparticles into a Vanadium Dioxide Host Matrix By Aerosol Assisted Chemical Vapour Deposition.

## 8.1 Introduction

Gold nanoparticles were incorporated into a $VO_2$ host matrix by aerosol assisted chemical vapour deposition. Varying amounts of auric acid and vanadium acetate in methanol were tested in order to change the gold density in the $VO_2$ host matrix. It was found that a 1 : 2 ratio of auric acid to vanadium acetate deposited thin films of gold nanoparticles within a $VO_2$ host matrix with the highest incorporation of gold nanoparticles. The methods used to characterise the optical and functional properties of these films are as described in Chapter 2.

This work was completed in order to test the effects of the addition of gold nanoparticles to the vanadium dioxide matrix and to investigate any enhancements in optical, colour and photocatalytic properties. It is possible that the gold nanoparticles would allow greater control of the tuning of the vanadium dioxide host matrix properties and perhaps allow the transition temperature of the $VO_2$ film to be modified by the doping effects of the gold nanoparticles. Auric acid was the precursor of choice as it decomposes at 80°C according to the following reaction:

$$HAuCl_4 \rightarrow Au + HCl + {}^3/_2Cl_2$$

The decomposition of a molecule to form a desired solid product with only gaseous by-products is desirable for a CVD precursor. The low decomposition temperature, solubility in a variety of solvents and low volatility make $HAuCl_4$ suitable for AACVD.

This chapter details the aerosol assisted chemical vapour deposition of vanadium dioxide films with nanoparticulate gold particles and their optical switching properties. Previously, gold nanoparticles embedded in a vanadium dioxide host matrix thin films have been made by sol-gel synthesis; metallic gold has been doped into the vanadium

dioxide host matrix by the sol-gel process and this resulted in a reduction in the thermochromic temperature to 49 °C[259]. This chapter builds upon this study by Beitelle *et al* to investigate the effects of gold nanoparticles on the thermochromic switch, growth morphology, reflectance/transmittance properties, photocatalysis and superhydrophilicity[260]. Moreover this work will make use of an aerosol assisted chemical vapour deposition process which has the potential for direct incorporation into float glass production lines[8].

## 8.2 Method For Film Deposition – AACVD Procedure Used For Deposition of Gold Nanoparticle Vanadium Dioxide Composite Films

Hydrogen tetrachloroaurate ($HAuCl_4$), also known as chloroauric acid was obtained from Aldrich Chemical Company as a trihydrate ($HAuCl_4.3H_2O$, 99.999%) and used as received. Vanadium acetate was also used as received from Aldrich (99.5 % purity). Different ratios of vanadium acetate (0.6 – 7.2 mmol) to auric acid (0.01 – 1.2 mmol) were tested in methanol (50 mL) in a single precursor mix.

All AACVD experiments were performed on a custom built apparatus consisting of a horizontal-bed cold-wall reactor connected to an arrangement of delivery tubing, a bubbler and a humidifier- full details of the reactor have been explained previously. The optimum deposition for gold nanoparticle/vanadium dioxide films was 1.2 mmol of auric acid and 0.6 mmol vanadium acetyl acetonate in methanol (50 mL). This mixture was transferred to the aerosol assisted CVD bubbler and a composite gold nanoparticle/vanadium dioxide film was deposited in a single step at substrate temperatures of 450 °C and a flow rate of 1.5 $Lmin^{-1}$.

## 8.3 Deposition Parameters

A number of different deposition parameters were tested to obtain the optimum conditions for depositing composite $VO_2$ and Au nanoparticle thin films on glass. The flow rate and reactor temperature were varied to obtain the optimum conditions for both

gold nanoparticle and host matrix film growth. Composite Au nanoparticle/$VO_2$ thin films were synthesized in one step using the above mentioned precursors. The deposition parameters and reaction conditions are summarised in Table 11.

| Au precursor used/ mmol | $VO_2$ precursor/mmol | Molar ratio Au : $VO_2$ | Flow rate/ $Lmin^{-1}$ | Au atom % | $T_c$ / °C |
|---|---|---|---|---|---|
| Auric acid/ 0.02 | $[VO(acac)_2]$/ 7.2 | 1 : 360 | 1.5 | 0.1 | 50 |
| Auric acid/ 0.26 | $[VO(acac)_2]$/ 7.2 | 1 : 27.7 | 1.5 | 1.75 | 46 |
| Auric acid/ 0.29 | $[VO(acac)_2]$/ 0.36 | 1 : 1.24 | 1.5 | 9 | 44 |
| Auric acid/ 0.59 | $[VO(acac)_2]$/ 2.4 | 1 : 4 | 1.5 | 18 | 45 |
| Auric acid/ 1.2 | $[VO(acac)_2]$/ 0.6 | 1 : 0.5 | 1.5 | 25 | 33 |

Table 11. Parameters used to deposit gold nanoparticle and vanadium dioxide thin films by AACVD.

## 8.4 Deposition of Gold Nanoparticle $VO_2$ Composite Thin Films On Glass By Aerosol Assisted Chemical Vapour Deposition

### 8.4.1 Film Characteristics and Elemental Analysis

The AACVD reaction of vanadium acetyl acetonate and auric acid at substrate temperatures of 450 °C deposited composite Au nanoparticle–$VO_2$ films. It was found with all samples that the films had a uniform composition and colour across the substrate. The films were different shades of violet/purple/red (depending on the thickness of the thin films) (Figure 86), passed the Scotch tape test, were not removed by a tissue or felt but were scratched with both brass and steel. All films were insoluble in water and common organic solvents (methanol, ethanol, acetone), both acid (HCl, 2

M) and alkali (NaOH, 2 M). The films showed no change in optical properties on storage in air for 3 months.

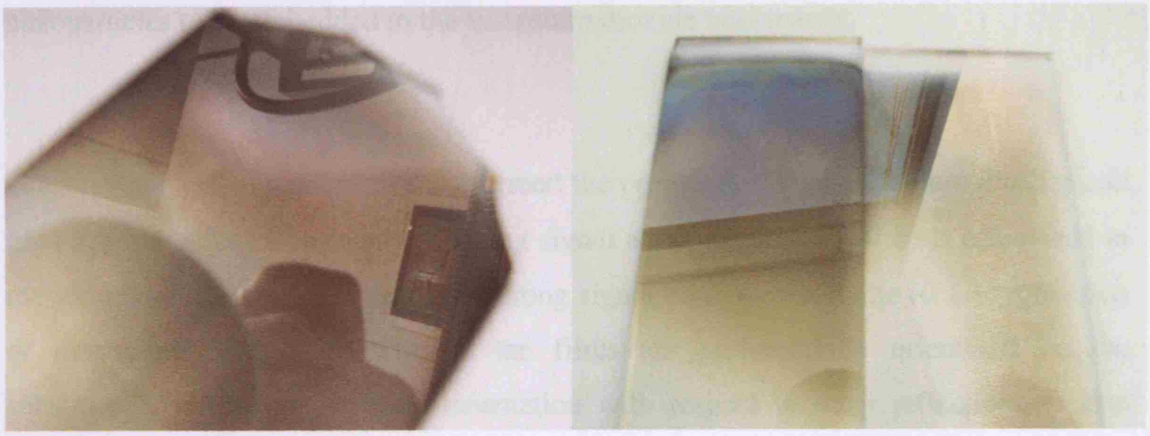

Figure 86. Photographs of the gold nanoparticle/vanadium dioxide thin films on glass prepared by AACVD.

Spot EDAX analysis (wavelength dispersive detector) showed that the sample particles contained only vanadium, gold and oxygen in varying ratios across the length of the substrate and top plate. As confirmed by EDAX, it was found that 0.6 mmol of vanadium acetate was the optimum for gold nanoparticle incorporation. Auric acid (0.02 mmol) and vanadium acetate (7.2 mmol) incorporated 0.1 atom% gold nanoparticles into the $VO_2$ host matrix whereas 0.26 mmol auric acid and 7.2 mmol vanadium acetate incorporated 1.75 atom% gold, as confirmed by EDAX analysis. Auric acid (0.29 mmol) and vanadium acetate (0.36 mmol) incorporated 9 atom% gold. Changing the amount of both the vanadium acetate precursor and auric acid to 2.4 and 0.59 mmol respectively enabled a much higher amount of gold nanoparticle incorporation into the $VO_2$ host matrix. The top plate for this series contained 18 atom% Au whereas the substrate contained a smaller amount ranging from 8 – 13 atom%. Lowering the amount of vanadium acetate precursor to 0.6 mmol and increasing the auric acid amount to 1.2 mmol deposited a $VO_2$ film with 25 atom% Au. Notably carbon was not detected by EDAX (less than 1 atom%). Taking into consideration the complicated reaction kinetics and film adsorption steps, generally increasing the auric acid molar amount led to an increase in the gold content of the film.

This gold nanoparticle content was increased further by lowering the amount of vanadium acetate used in the starting solution. It is thought that by lowering the vanadium acetate precursor, CVD kinetics allow a decrease in the number of vanadium acetate to vanadium dioxide reactions, thus allowing a pathway for the gold nanoparticles to be embedded in the vanadium dioxide host matrix.

Glancing angle X-ray diffraction confirmed the presence of both vanadium dioxide and gold nanoparticles. Commonly, a strong signal at approximately 27.8° is often seen in the vanadium dioxide XRD data, this strong signal corresponds to the (0 1 1) reflection of monoclinic $VO_2$, and indicates the films are preferentially orientated on the substrate[261]. However preferred orientation with respect to other reflections is also known. These values were comparable with the reference values for vanadium dioxide[262]. The X-ray data confirm that a composite film is formed and furthermore no shift in the main diffraction peaks of $VO_2$ is seen, consistent with a composite rather than a solid solution.

The presence of cubic metallic gold in all $VO_2$ thin films was also confirmed by diffraction peaks at 39 and 44.5°, these reflections arise from the (111) and (200) planes of the Au cubic lattice ($a$ = 4.07 Å). The FWHM of the Au peaks were constant along the length of each substrate, indicating roughly constant crystallite size.

At the two different ends of the same sample, the gold nanoparticle and vanadium dioxide amounts do not vary to any great extent, the gold nanoparticles are approximately evenly distributed across the glass substrate.

The X-ray diffraction pattern of the top plate for the 1 atom% Au doped $VO_2$ thin films showed preferred orientation at 34, 37, 53 and 60°. The Au peaks can be seen at 40.5 and 45° (Figure 87).

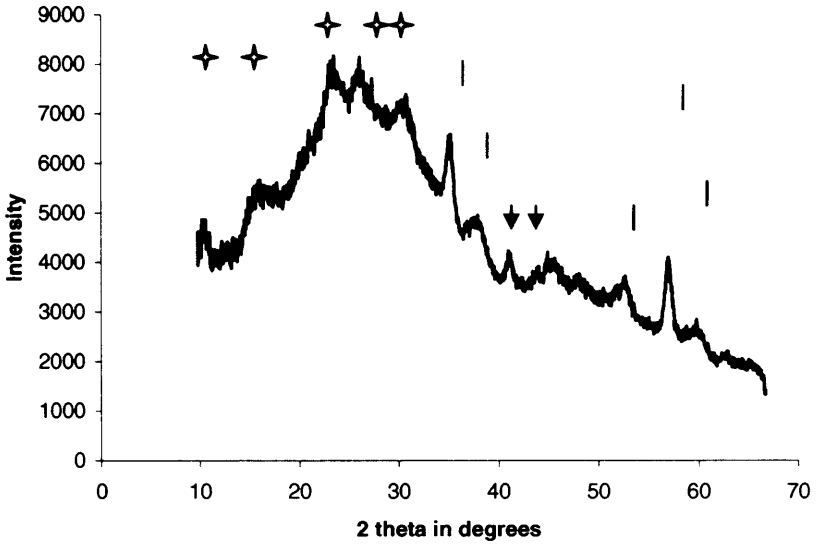


Figure 87. X-ray diffraction pattern for a 1 atom% gold nanoparticle/$VO_2$ film prepared by the AACVD of auric acid and vanadium acetate at 450 °C. ↓ = Au and | = $VO_2$. Peaks marked with a ✧ are from the detector. An amorphous background is seen due to breakthrough to the underlying glass.

For 1.75 atom% Au-doped films, recorded at room temperature, the XRD pattern confirm the formation of $VO_2$ with a (211) and (220) preferred orientation (Figure 88). The reflections marked with a line on the XRD pattern confirm the presence of the $VO_2$ phase whereas small reflections at 41 and 45°, correspond to metallic gold. Additional peaks at 23 and 24° are due to vanadium oxide contamination. However this secondary phase was difficult to conclude due to the contamination reflections spanning a number of vanadium oxide phases.

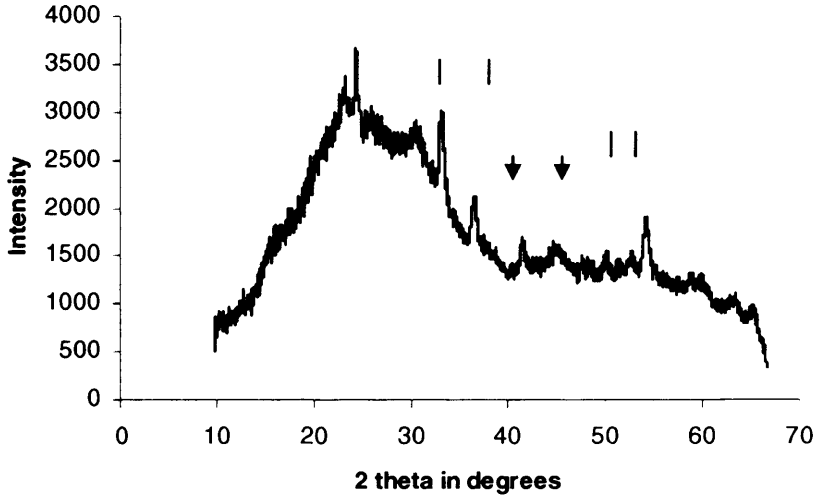


Figure 88. X-ray diffraction pattern for a 1.75 atom% gold nanoparticle/$VO_2$ film prepared by the AACVD of auric acid and vanadium acetate at 450 °C. ↓ = Au and | = $VO_2$.

An increased amount of Au nanoparticle incorporation is seen by the sharper peaks for gold at 39 and 45° in Figure 89, this is due to the greater crystallinity of the thin film. The $VO_2$ peaks are represented by the line markers.

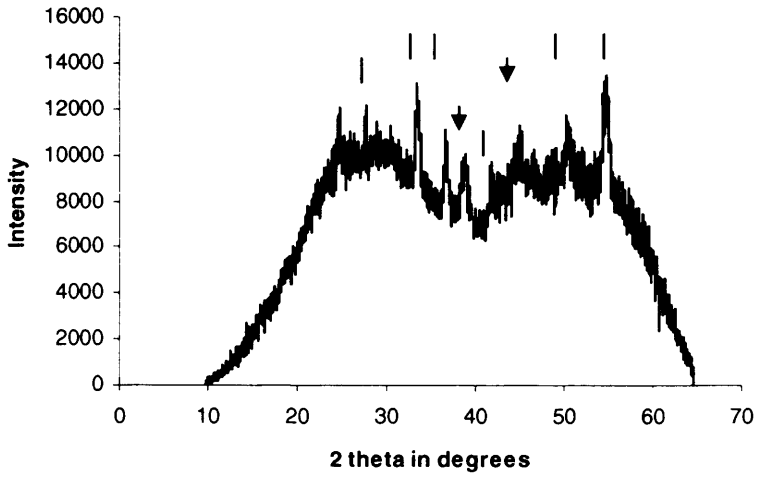


Figure 89. X-ray diffraction pattern for a 9 atom% gold nanoparticle/$VO_2$ film prepared by the AACVD of auric acid and vanadium acetate at 450 °C. ↓ = Au and | = $VO_2$.

An Au content of 18% in the $VO_2$ matrix gives a distinct XRD pattern for Au metal (Figure 90). Intense peaks for Au nanoparticles are observed at 39 and 44.5°. Figure 90A represents a part of the film where only Au is detected with no vanadium oxide phase suggesting that phase segregation has occurred here. This was 3 cm from the start of the films. Figure 90 B and C show weaker peaks at 33, 37 and 54° corresponding to the preferentially orientated $VO_2$, diffraction taken at 1 cm and 6 cm along the substrate from the inlet.

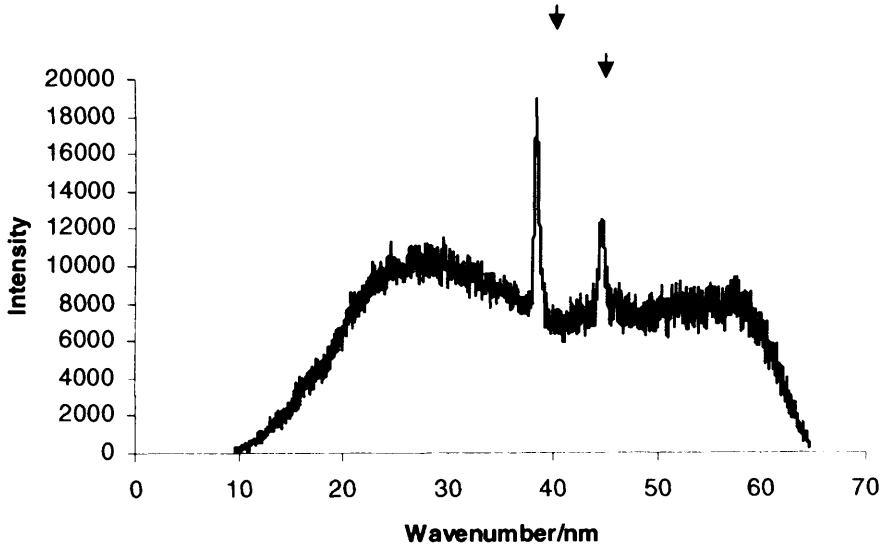


A

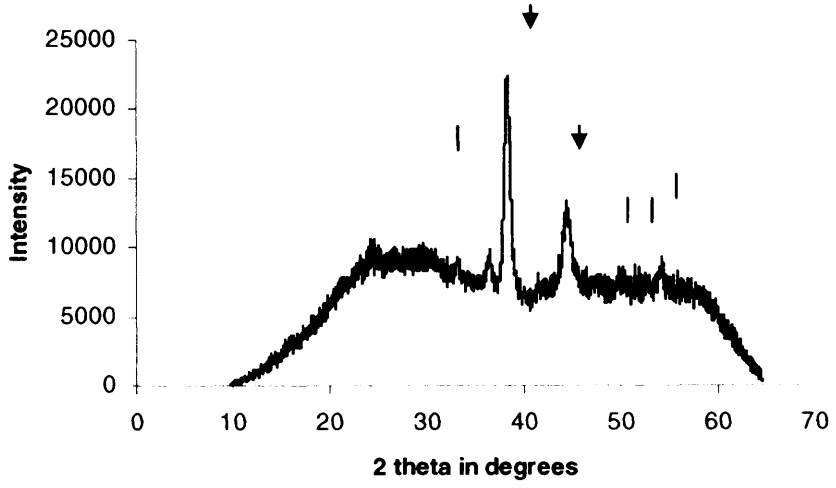


B

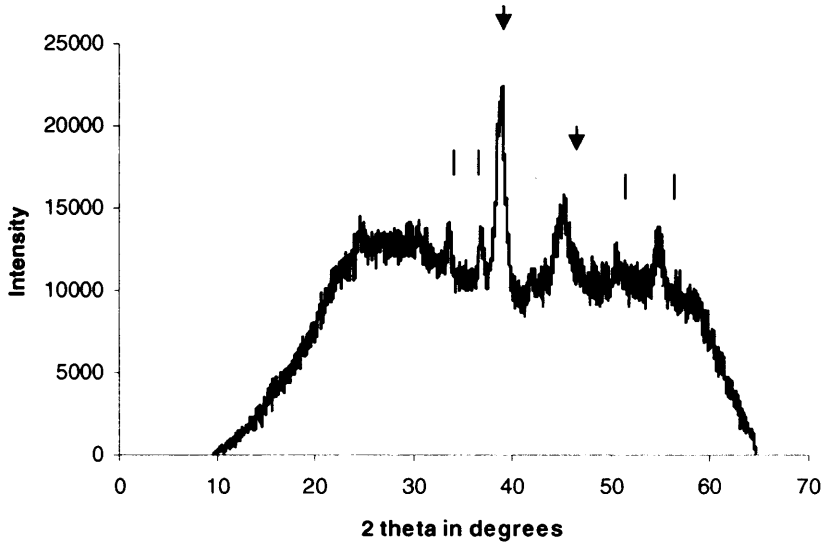


C

Figure 90. X-ray diffraction pattern for a 18 atom% gold nanoparticles/$VO_2$ film prepared by the AACVD of auric acid and vanadium acetate at 450 °C. ↓ = Au and | = $VO_2$.
A) 3 cm, B) 1 cm and C) 6 cm along the start of the substrate.

The nanoparticulate gold phase was also confirmed by UV analysis- the surface plasmon peak reference for gold is ~ 500 nm. UV analysis showed an increase in the surface plasmon resonance band intensity with increasing gold nanoparticle amounts- this correlates well with the EDAX analysis. Furthermore there is a shift in the surface plasmon resonance upon incorporation into the $VO_2$ host matrix. This is often the case when nanoparticles enter a material of different refractive index[263]. The refractive index for gold is 0.57[264] and for $VO_2$ 1.65[265], hence the gold nanoparticles enter a medium of higher refractive index and this is a contributing factor to the red shift.

Typical Raman spectra obtained for the 1 atom% $Au/VO_2$ composite film are shown in Figure 91. These match the literature spectra of Barreca *et al*[266,267], to within ± 2 $cm^{-1}$. All Raman bands for monoclinic vanadium(IV) oxide could be assigned to an *Ag* mode, except the band at 261 $cm^{-1}$ with has been assigned to a *Bg* mode and the band at 143 $cm^{-1}$ which was not assigned. The Raman bands at 595 and 612 $cm^{-1}$ were likely to result from stretching modes of the V-O-V bridging bonds, while the other Raman bands could be attributed to bending motions of the vanadium-oxygen bonds. The room temperature 25 – 35 °C spectra of Au nanoparticle/$VO_2$ films were those typical of the monoclinic phase of vanadium(IV) oxide, the 65 °C spectrum, a temperature just below

the transition temperature, showed all bands greatly reduced in intensity. When the temperature was increased to 75 ºC, which is above the transition temperature, all bands due to the monoclinic phase of vanadium(IV) oxide disappeared.

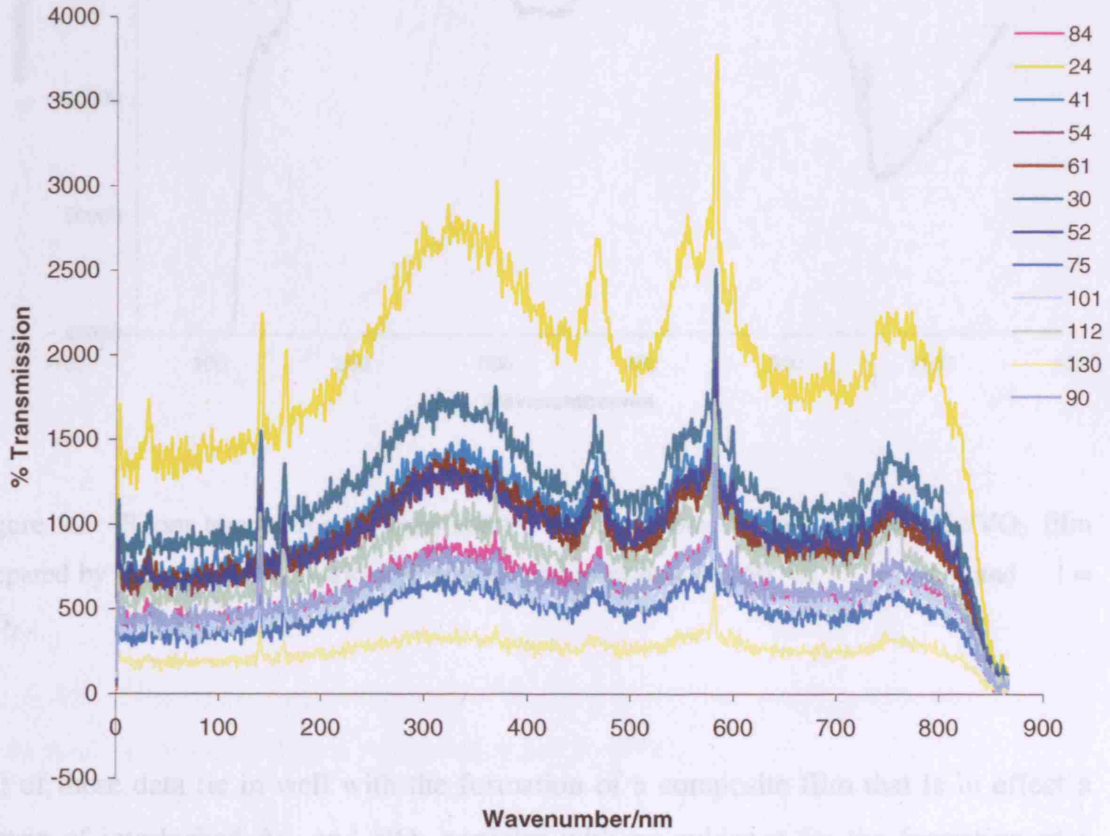


Figure 91. Raman spectra of a 1% atom gold nanoparticle/$VO_2$ film at temperatures ranging from 20 –130 ˚C. This is as expected for $VO_2$, where at temperatures above 70 ˚C the Raman bands collapse and broaden corresponding to the $VO_2$ tetragonal phase.

The Raman spectrum for a 9 atom% Au/$VO_2$ composite film is shown in Figure 92. These match the literature spectra and showed bands at 143, 193, 218, 259, 306, 388 and 499 $cm^{-1}$. The bands at 799 and 918 were attributed to $V_6O_{13}$[267].

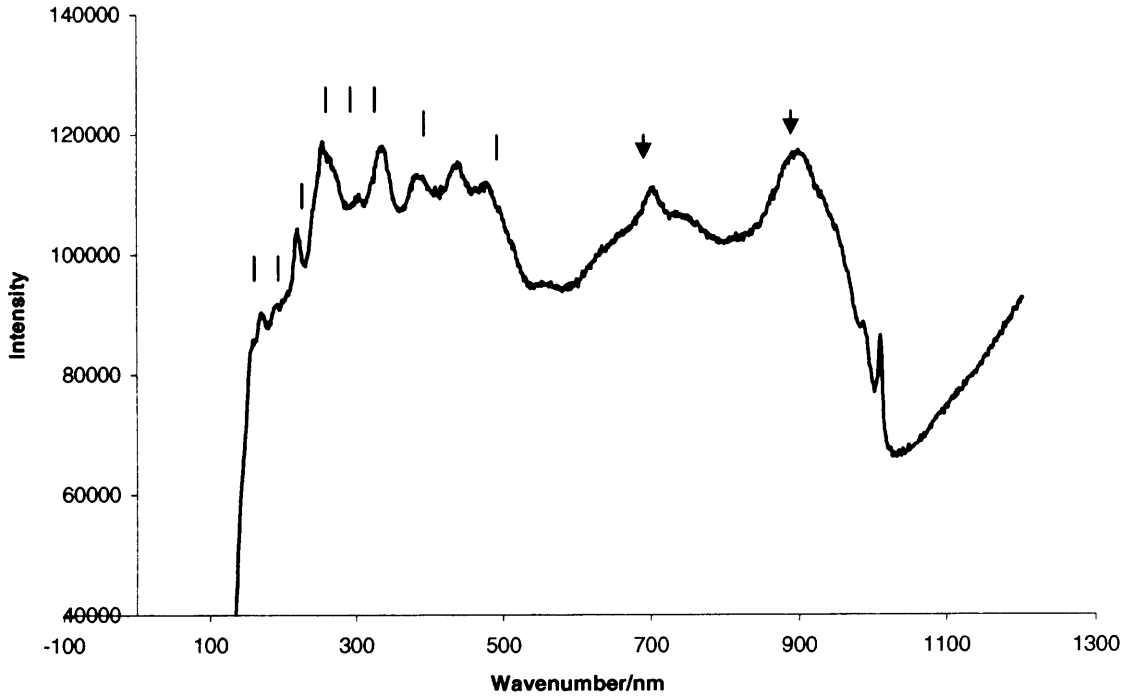


Figure 92. Room temperature Raman spectra for a 9 atom % gold nanoparticle/$VO_2$ film prepared by the AACVD of auric acid and vanadium acetate at 450 °C. ▼ = $V_6O_{13}$ and | = $VO_2$ .

All of these data tie in well with the formation of a composite film that is in effect a matrix of interlocked Au, and $VO_2$ particles with no evidence for the formation of a solid solution of $Au_xV_yO_2$.

## 8.4.2 Film Functional Properties

One characteristic property of vanadium(IV) oxide that makes it a useful material for an intelligent window coating is the increase in infrared reflectance and decrease in infrared transmittance when the material transforms into the high temperature phase. This was investigated by transmission-reflection spectroscopy. The transmittance-reflectance spectra of a vanadium(IV) oxide thin film containing 1.75 atom % Au

nanoparticles at room temperature and 70 °C are shown in Figure 93. At room temperature, the film showed a crossing in the reflectance and transmittance plots.

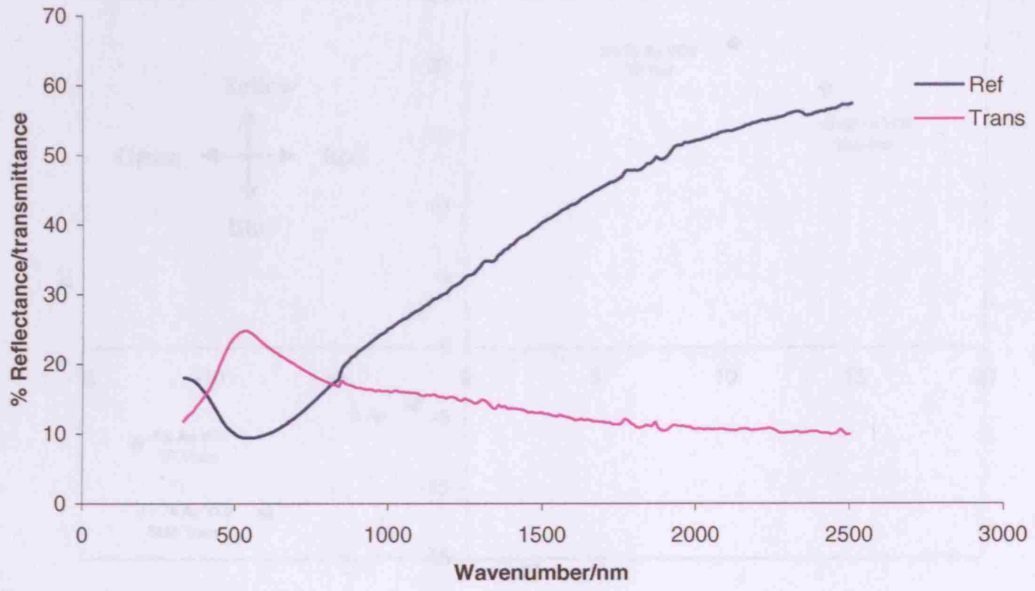


Figure 93) Reflectance/transmittance of a 1.75 atom % gold nanoparticles/$VO_2$ film prepared by the AACVD of auric acid and vanadium acetate at 450 °C.

These films also showed an increase in infrared reflectance and decrease in infrared transmittance when the material transforms into the high temperature phase. At room temperature, the film showed heat mirror behaviour- these films show a reversal in transmission/reflection in the near infra-red. At temperatures above 70 °C, all films showed an increase in the reflectivity and decrease in the transmission- this is as expected for thermochromic coatings and also confirms that vanadium dioxide is present. Furthermore, colour quantification for these film showed enhanced results as compared to nanoparticulate gold thin films (Figure 94). The colour of the thin films was quantified using the CIELAB colour co-ordinates. Two parameters $a^*$ and $b^*$, define colour: positive $a^*$ values correspond to red, negative $a^*$ values to green. Positive $b^*$ values correspond to yellow, negative $b^*$ values correspond to blue. Figure 94 shows the colour of the Au nanocube/$VO_2$ composite thin films in both transmitted

and reflected light. The near symmetric opposite colouration of this films in reflected and transmitted light is unusual.

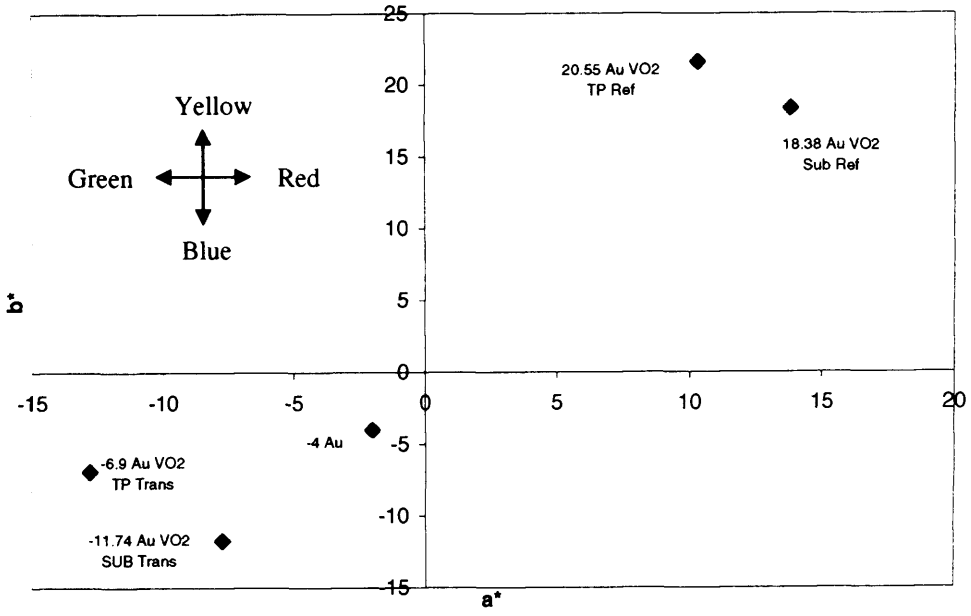


Figure 94. Colour quantification for a 9 atom % Au nanoparticle/$VO_2$ composite film on glass prepared by the AACVD of auric acid and vanadium acetate at 450 °C.

A small amount of Au (1 atom%) improved the thermochromic behaviour of the $VO_2$ films; the transition temperature decreased to 50 °C; a contribution to this reduction could also be from strain introduced within the matrix. This compares well with sol-gel prepared Au doped $VO_2$ thin films where the transition temperature decreases to 61 °C for 0.25 atom% Au[268]. It appears that increasing the Au content decreases the $VO_2$ transition temperature further to approximately 39 °C (Figure 95).

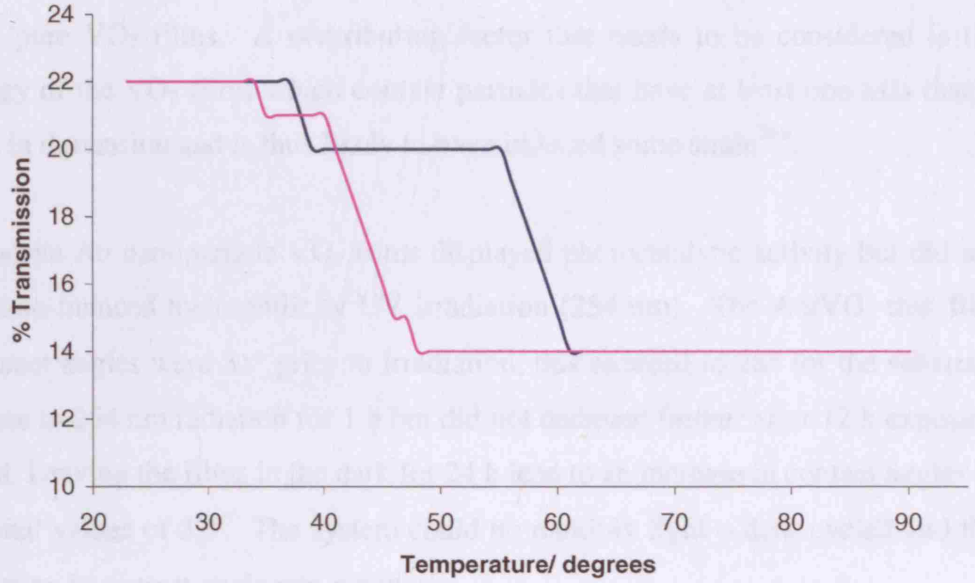


A

B

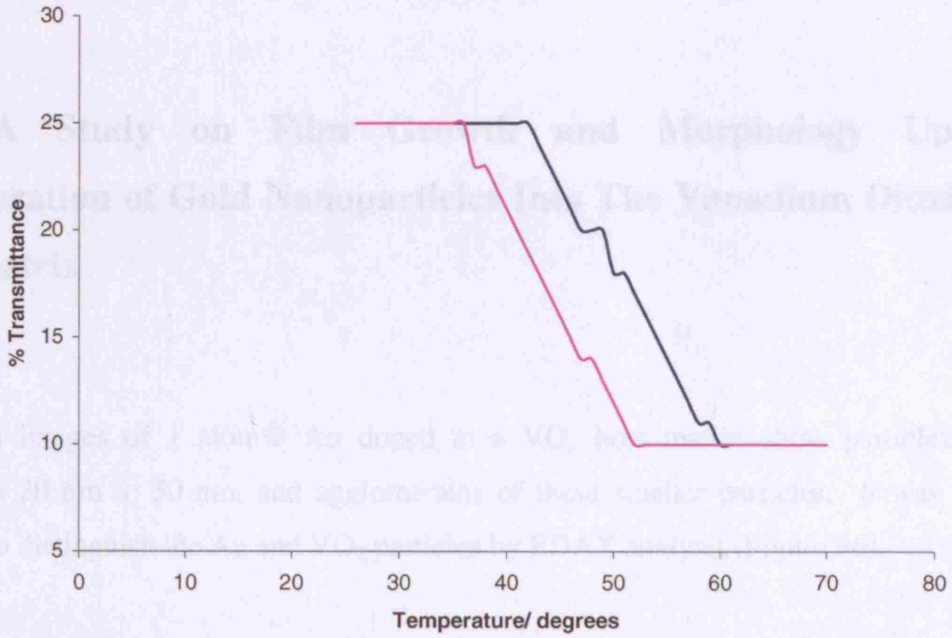


Figure 95. Thermochromic transition temperature measurements (2.5 μm) for A) 1 atom % Au/$VO_2$ and B) 25 atom % Au/$VO_2$ composite films. A decrease in the thermochromic switch is seen with increasing gold nanoparticle content.

There is a clear decrease in switching temperature for the $Au/VO_2$ composites compared to that of pure $VO_2$ films. A contributing factor that needs to be considered is the morphology of the $VO_2$ films which contain particles that have at least one axis that is ca. 50 nm in dimension and is thus likely to have induced some strain[269].

The composite Au nanoparticle $VO_2$ films displayed photocatalytic activity but did not exhibit photo-induced hydrophilicity UV irradiation (254 nm). The $Au/VO_2$ thin film initial contact angles were 31° prior to irradiation, this reduced to 28° for the substrate on exposure to 254 nm radiation for 1 h but did not decrease further after 12 h exposure to sunlight. Leaving the films in the dark for 24 h lead to an increase in contact angles to their original values of 32°. The system could be multiply light – dark cycled and the same variation in contact angle was noted.

The photocatalytic results did not show the films as active photocatalysts and this is as expected for vanadium dioxide.

### 8.4.3 A Study on Film Growth and Morphology Upon Incorporation of Gold Nanoparticles Into The Vanadium Dioxide Host Matrix

The SEM images of 1 atom% Au doped in a $VO_2$ host matrix show particles of dimension 20 nm to 50 nm, and agglomerates of these smaller particles. It was not possible to distinguish the Au and $VO_2$ particles by EDAX analysis (Figure 96).

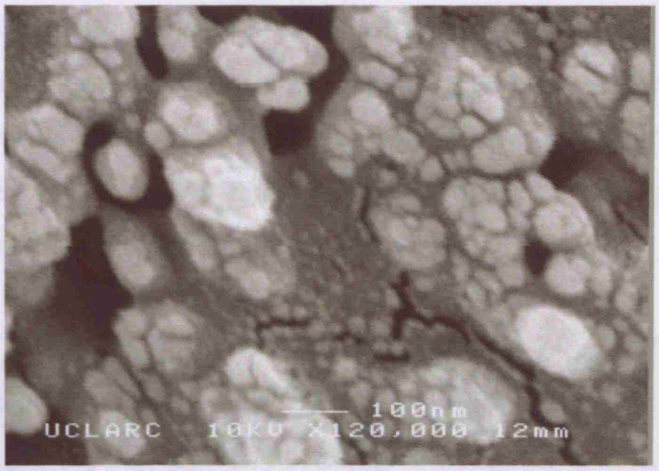


Figure 96. SEM image of a Au nanoparticle/$VO_2$ composite thin film containing 1 atom % Au prepared by the AACVD of auric acid and vanadium acetate at 450 °C.

Interestingly, the SEM images of 1.75 atom% Au doped in a $VO_2$ host matrix showed cubes of approximate dimension 300 nm by 300 nm in addition to smaller particles and agglomerates of varying size. Spot EDAX analysis confirmed that the cubes contained a greater proportion of Au compared to the bulk analysis (Figure 97).

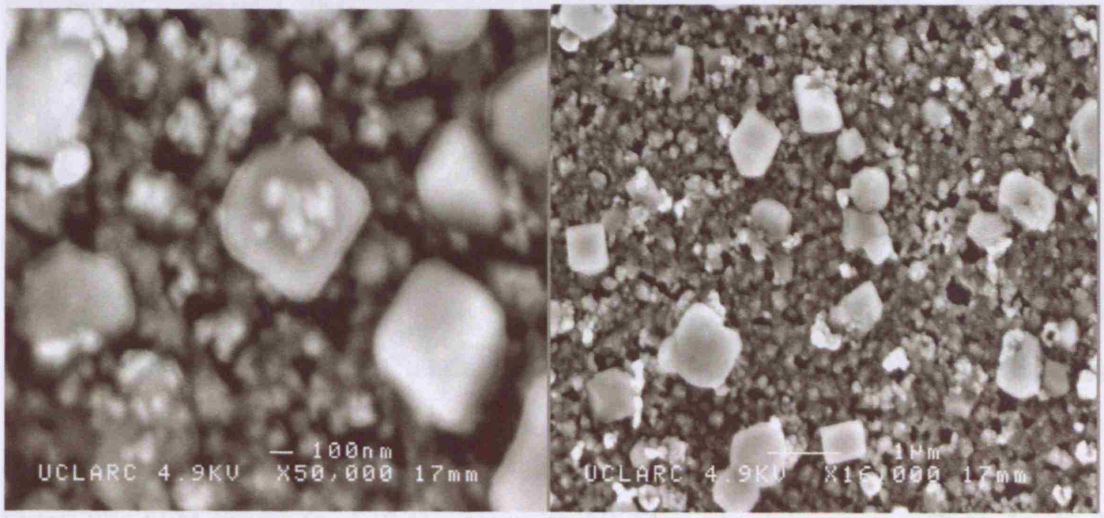


Figure 97. SEM images of a Au nanoparticle/$VO_2$ composite thin film containing 1.75 atom % Au prepared by the AACVD of auric acid and vanadium acetate at 450 °C.

Increasing the Au content to 9 Atom%, the film deposited on the substrate rounded cubes of dimension 300 nm by 300 nm, and the top plate deposited more defined cubes of the same dimension alongside plates less than 100nm wide (Figure 98). Sharper more defined cubes are present on the top plate and this could be due to a number of factors- such as reaction kinetics to facilitate cube growth.

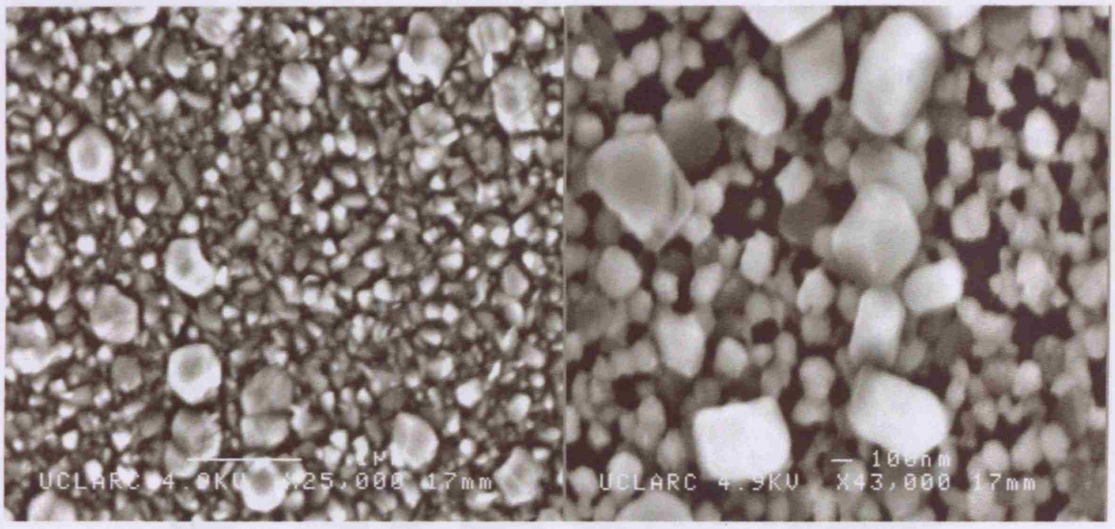


A B

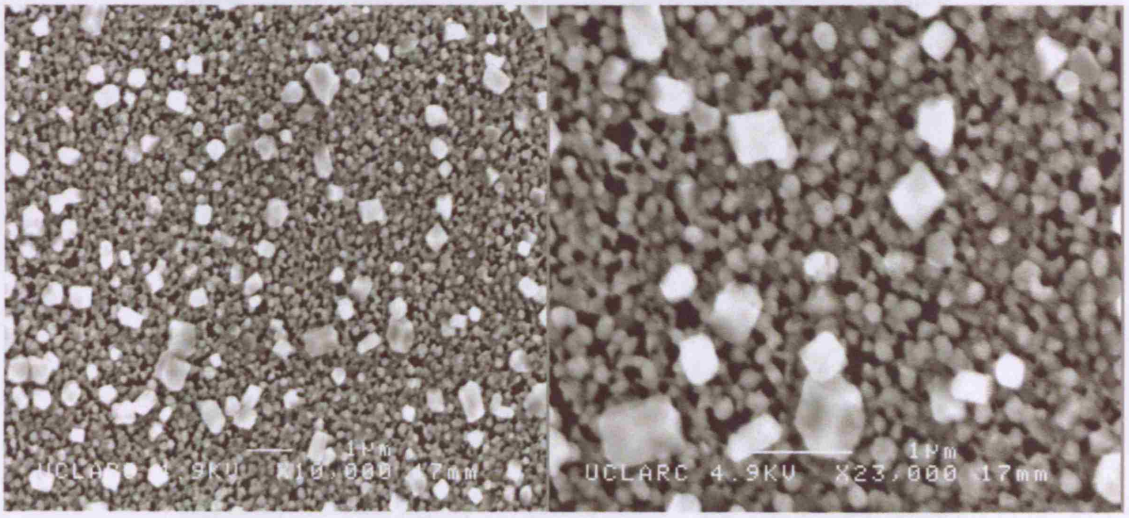


C D

Figure 98. SEM images for $Au/VO_2$ composite thin films containing 9 atom % Au for A) the substrate and B), C) and D) for the top plate. These films were prepared by the AACVD of auric acid and vanadium acetate at 450 °C.

Increasing the Au dopant amount further led to greater deposition on the top plate (18 %) compared to 6 – 13 % on the substrate. This difference in Au dopant amount gives a difference in the two surface morphologies – the top plate deposits rods of dimension 150 by 30 nm that contained both gold and vanadium in a 18:82 ratio. The substrates deposited "cauliflower" type florets of varying dimensions along with larger cubes 1 micron wide (Figure 99).

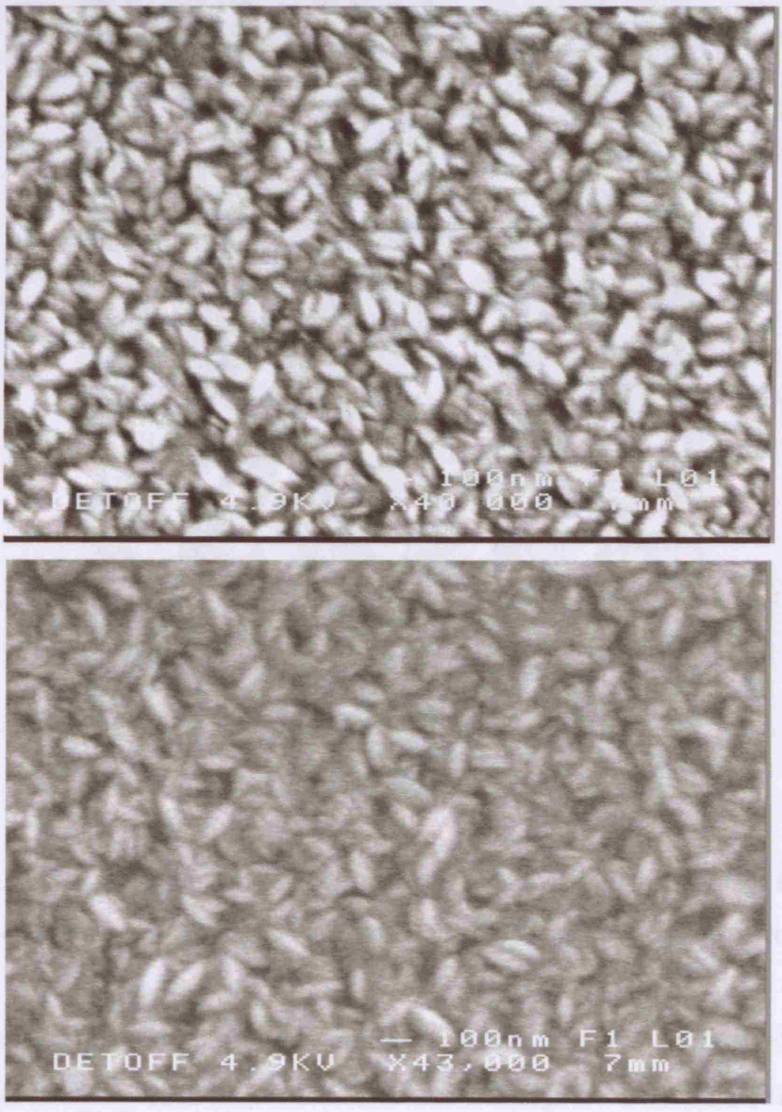


Figure 99A). SEM images of the top plate for a $Au/VO_2$ film containing 18 atom % Au and also $VO_2$ made from the AACVD reaction of auric acid and vanadium acetate at 450 °C.

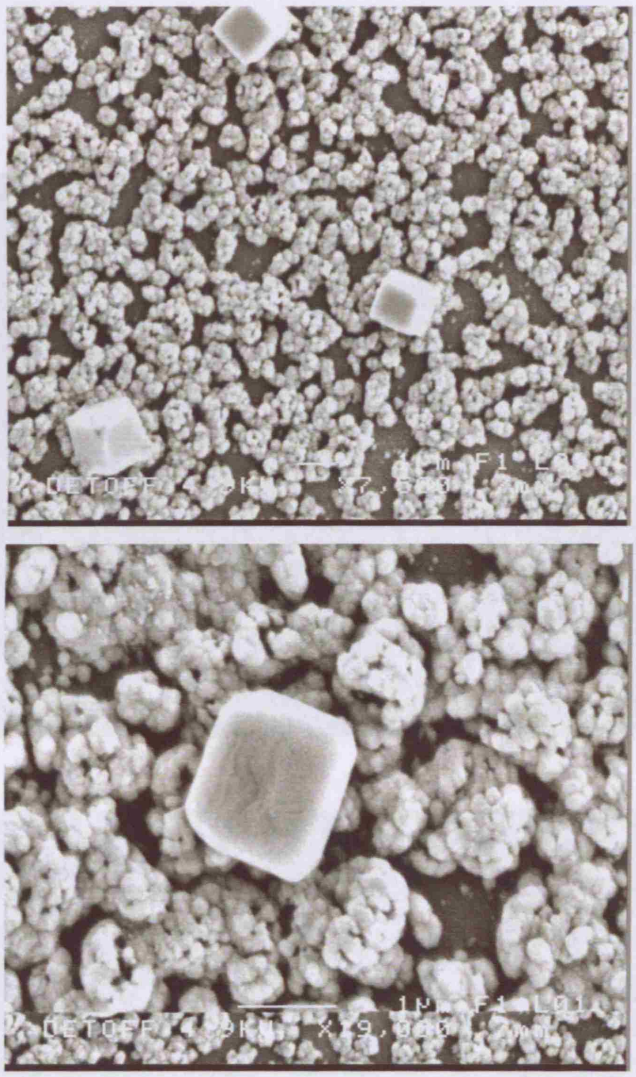

Figure 99B) SEM images of the substrate for a $Au/VO_2$ thin film containing 6 – 13 atom % Au. A change in growth morphology is seen here with the gold adopting a cubic structure.

Increasing the Au dopant amount to 25 atom%, changes the growth morphology further- there is a preference for rod/wire formation as the Au dopant amount increases. The top plate contains wires of dimension 5 nm by 400 nm in addition to much smaller nanoparticles and plate/agglomerates of varying dimension (Figure 100 A). No cubes were seen across the sample and substrate.

The SEM images for the substrate show two different rod sizes - 75 by 200 nm and also 100 by 10 nm. These are found deposited on coalesced island of varying size (Figure 100 B).

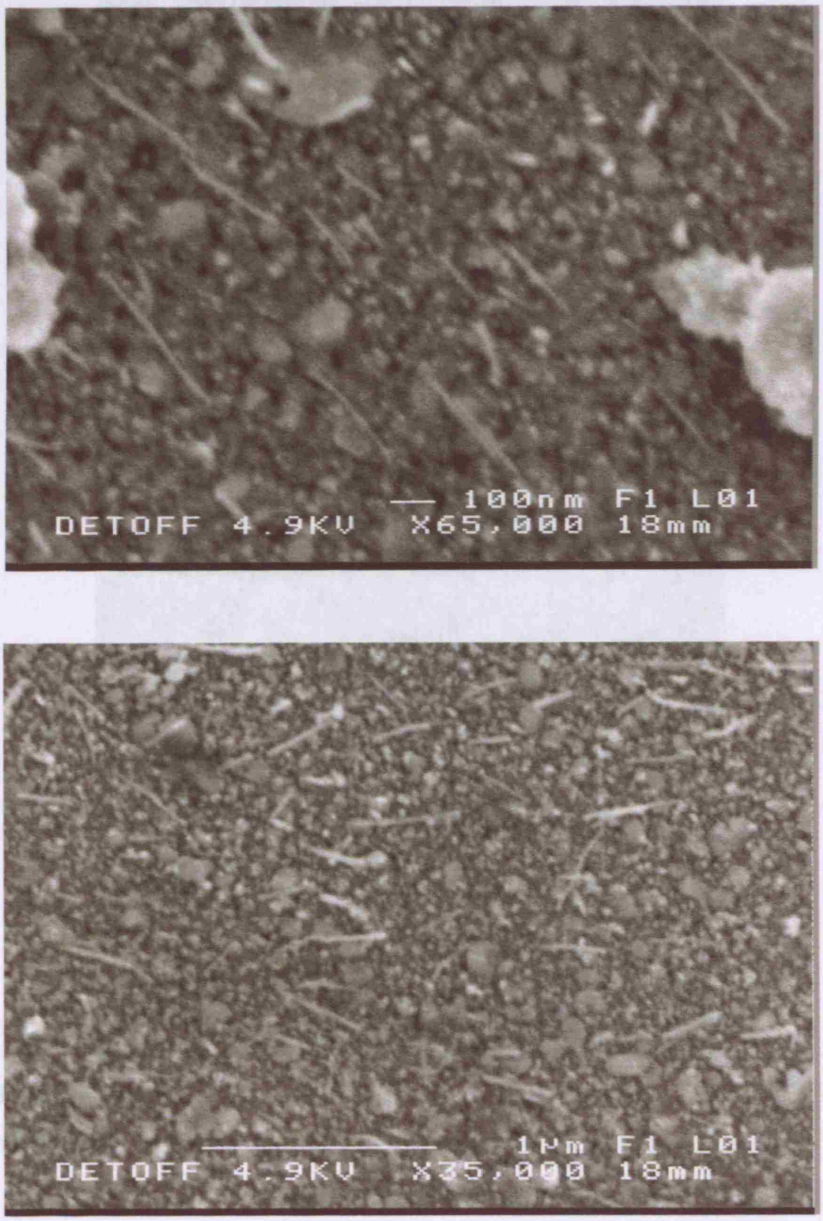


Figure 100 A) SEM images of the top plate for a $Au/VO_2$ thin film containing 25 atom % Au made from the AACVD reaction of auric acid and vanadium acetate at 450 ºC.

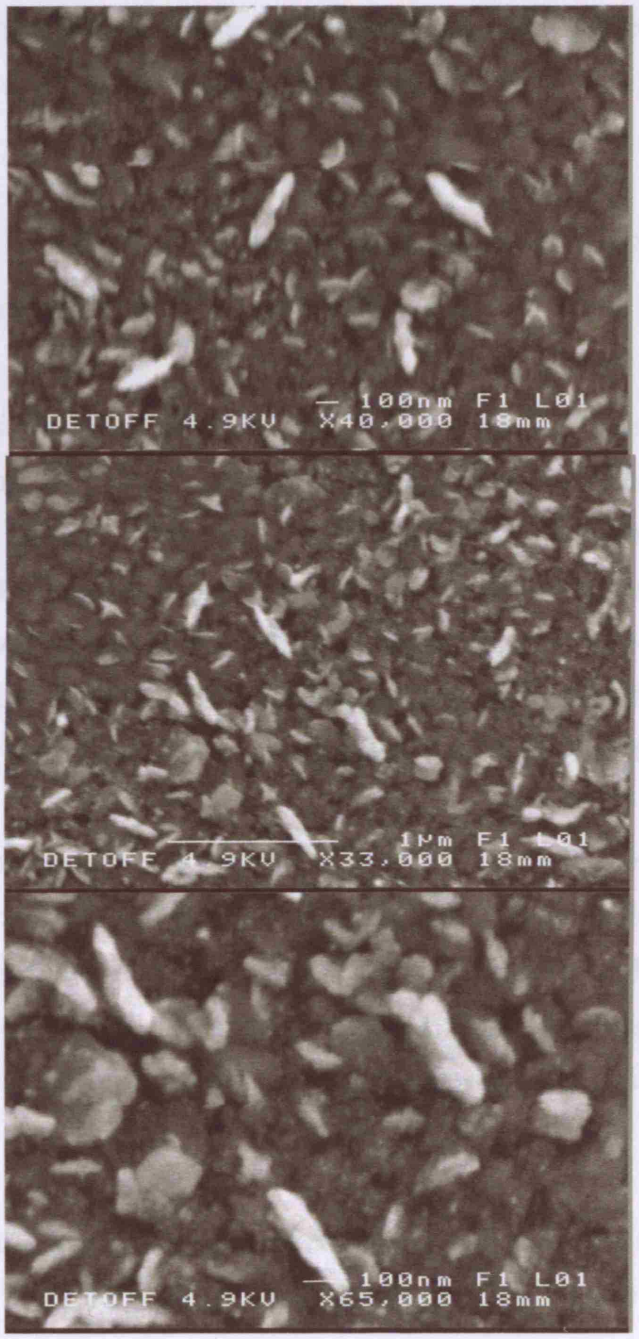


Figure 100 B) SEM images of the substrate for a $Au/VO_2$ thin film containing 25 atom % Au made from the AACVD reaction of auric acid and vanadium acetate at 450 °C.

The presence of gold nanocubes in the matrix instead of spherical nanoparticles is an unexpected result- this means that certain reaction conditions facilitate the growth of gold nanocubes. This could be the reaction kinetics, combination of the gold and vanadium dioxide mists or how easily the gold nanoparticles are able to deposit onto the glass. It seems that there is either a gas phase particle growth step, or surface modification resulting in the formation of nanocubes. The thermophoretic effect, which

is the effect of a temperature gradient, causes the particles to move from a hot surface to a colder one, could also be contributing to this change.

## 8.5 Discussion : Effect of Gold Nanoparticle Incorporation In A Vanadium Dioxide Host Thin Film Matrix

The sol-gel process[150,151] and physical vapour deposition[150,151] have previously been used to prepare doped $VO_2$ films. Metal doped vanadium dioxide films prepared by sol-gel methods result in solid solutions ($Ti_xV_yO_2$) as opposed to composite films ($TiO_2$ - $VO_2$). The entire first row of transition metals have been investigated as dopants into $VO_2$, and are known to alter $T_c$ depending on factors such as size and charge of the dopant ion or changes in electron carrier density on doping[152]. The thickness of the thin films has also been shown to influence the thermochromic transition temperatures[153].

Doped $M_xVO_2$ films (M = $W^{6+}$, $Nb^{5+}$, $Ti^{4+}$, $Cr^{3+}$ or $Al^{3+}$) have been readily prepared by Beteille *et al* by mixing a vanadium alkoxide and a metal salt in an alcoholic solution[154]. The switching temperature decreases when the film is doped with high valent cations ($W^{6+}$) and increases with low valent cations ($Al^{3+}$, $Cr^{3+}$). Interestingly, $T_c$ reduces for low Ti-dopant concentration (5 atom%) and increases for high Ti-dopant levels (20 atom%).

Gold doped $VO_2$ thin films have been successfully synthesised via the sol-gel process by Cavanna *et al*[158]. A solid solution ($Au_xV_yO_2$) resulted and it was found that at 0.25 atom% Au, the transition temperature reduced to 61°C, and for 0.5 atom% Au, the transition temperature lowered further to 57°C. The greatest decrease in the transition temperature was for 1.25 atom% Au, where $T_c$ was found to be 49°C. Similar results were also obtained in this thesis, where in general, an increase in the gold nanoparticle content decreased the transition temperature further.

In comparison to the sol-gel process, it has been found by Parkin *et al* that the APCVD reaction of $VCl_4$ and water yields thin films of a range of vanadium oxides on glass substrates[160]. These include $VO_2$, $VO_x$ (x = 2 – 2.5), $V_6O_{13}$ and $V_2O_5$. In an extension

to their research, Parkin and co-workers investigated thin films of tungsten doped vanadium (IV) dioxide on glass substrates via the APCVD of vanadium (IV) chloride, tungsten (VI) ethoxide and water at 550-650°C[115]. It was found that tungsten doping caused a decrease in the thermochromic phase transition temperature comparable to sol-gel studies. A maximum tungsten loading of approximately 5 atom% could be obtained using the tungsten ethoxide precursor. A tungsten loading of 3 atom% lead to a $T_c$ value of 5°C. Although gold nanoparticles only reduced the transition temperature to 33°C in this research, this change is noteworthy.

The improvement in the colour of the vanadium oxide host matrix by the gold nanoparticles has important industrial potential. Additionally, aerosol assisted chemical vapour deposition was used to deposit these thin films, and this technique is easily incorporated into float glass production lines. These films show a reduction in the thermochromic transition temperature, interesting optical properties and growth morphology; the films have excellent potential for future applications as window coatings and warrant further research in this class of coatings.

## 8.6 Conclusion : Effect of Gold Nanoparticle Incorporation In A Vanadium Dioxide Host Thin Film Matrix

Composite Au nanoparticle/$VO_2$ thin films were successfully deposited on glass by aerosol assisted CVD. Gold nanoparticles were incorporated into a $VO_2$ host matrix by aerosol assisted chemical vapour deposition forming composite gold nanoparticle/vanadium dioxide thin films. The purpose of this study was limited to the preparation of Au nanoparticle - $VO_2$ thin films and the influence of varying the Au/V molar ratio upon the optical switching properties. It was found that 0.6 mmol of vanadium acetate was the optimum for gold nanoparticle incorporation. 0.02 mmol of auric acid incorporated 0.1 atom% gold nanoparticles into the $VO_2$ host matrix whereas 1.2 mmol of auric acid incorporated 25 atom% gold, as confirmed by EDAX analysis.

This research shows that it is possible to deposit composite gold nanoparticle and vanadium dioxide thin films by aerosol assisted chemical vapour deposition with good

transfer of the initial precursors to the glass substrate. Interestingly, gold nanocubes were embedded into the matrix instead of nanoparticles- this means that certain reaction conditions facilitate the growth of gold nanocubes. This could be the reaction kinetics, combination of the gold and vanadium dioxide mists or how easily the gold nanoparticles are able to deposit onto the glass.

The transition temperature for these films was found to be 33 °C (25 atom %) and 55 °C (1 atom %), compared to 61 °C for sol gel prepared Au-$VO_2$ thin films. A reduction to 61 °C by 1 atom % gold could mean a very small incorporation of gold into the vanadium dioxide lattice. Increasing the gold nanoparticle amounts decreased the transition temperature substantially. Interestingly, increasing the gold dopant amount altered the growth morphology of the thin films from agglomerates at low gold incorporation, to cubes from 1.75-13 atom % and rod/wire growth at 18 – 25 atom% Au. The $T_c$ was found to be 55 °C for the lowest Au dopant amount and 33 °C for 25 atom %. The films produced in this study were composite mixtures of Au nanoparticles and $VO_2$ rather than a solid solution $Au_xV_yO_2$. In comparison, solid-solutions are readily formed from a sol–gel approach.

The composite films formed in this study show enhanced optical properties and a thermochromic switch. The photocatalysis for a Au/$VO_2$ thin film is not comparable to a CVD prepared anatase $TiO_2$ thin film. The reduction in thermochromic switching temperature observed for the films is a result of induced strain and dopant nanoparticulate gold. The reduction of 37 °C from pure $VO_2$ is noteworthy and somewhat larger than that seen for pure $VO_2$ formed by CVD (where a reduction of ca. 10 °C is common[270]). Furthermore, the hysteresis width of the transition is significantly lowered in the films formed in this study.

The colour of vanadium dioxide needs to be considered, since undoped $VO_2$ is dark brown, and this colour if not desirable for window coating applications. There are very few reports in the literature on improving the colour of $VO_2$. In this work, all films were different shades of violet/purple/red (due to a surface plasmon resonance effect, depending on the thickness of the thin films). This colour has scope for developing window coatings.

# Chapter 9: Thin Film Deposition of Gold Nanoparticles into a Vanadium Dioxide/Titania Composite Host Matrix By Aerosol Assisted Chemical Vapour Deposition.

## 9.1 Introduction

This chapter reports on the incorporation of gold nanoparticles into a $VO_2$/$TiO_2$ composite host matrix by aerosol assisted chemical vapour deposition. Vanadium dioxide has been researched extensively for application as an optical window coating due to its ability to undergo a reversible thermally induced metal-semiconductor phase transition associated with a first order crystallographic transition at 68 °C[271, 272]. This results in enhanced optical properties useful in climates where a large fluctuation in temperature occurs. Vanadium dioxide thin films have previously been deposited by a range of different techniques ranging from chemical vapour deposition to sputtering, sol-gel synthesis and physical vapour deposition[151, 8, 273].

More work still needs to be completed in tuning the colour of vanadium dioxide thin films. Thin films of vanadium dioxide are a generally a dark brown colour- this is undesirable for applications as optical window coatings. Previously, many attempts have been made using doping effects, which also have the advantage of reducing the thermochromic transition temperature further. In this research, gold nanoparticles were doped into a vanadium dioxide/titania host matrix in order to decrease the transition temperature further, enhance the optical properties and also improve the coating colour. Aerosol assisted chemical vapour deposition was used to deposit both the nanoparticles and the vanadium dioxide/titania host matrix. Both methods are new and novel and have not been reported in the literature; vanadium dioxide was first deposited using AACVD by Parkin *et al*[274] and there are no reports on doping a vanadium dioxide host matrix with nanoparticles by this method. Previously, metallic gold has been doped into the vanadium dioxide host matrix by the sol gel process and this resulted in a reduction in the thermochromic temperature to 49 °C[275].

In this chapter, the aerosol assisted chemical vapour deposition of $TiO_2$/$VO_2$ composite thin films with embedded nanoparticulate Au particles and their optical switching properties are reported. The aim in particular was to assess whether or not the varying amounts of gold density in the $TiO_2$/$VO_2$ host matrix altered the film colour, optical properties and thermochromic switching properties of the host matrix. Varying amounts of auric acid and vanadium acetate in methanol and titanium isopropoxide in toluene were tested as starting materials. The optical properties of these films were analysed by UV and reflectance/transmittance analysis and characterized as per the experimental section in Chapter 2.

## 9.2 Method For Film Deposition – AACVD Procedure

Hydrogen tetracholroaurate ($HAuCl_4$), also known as chloroauric acid was obtained from Aldrich Chemical Company as a trihydrate ($HAuCl_4.3H_2O$, 99.99%) and used as received. Vanadium acetate (0.05 - 0.6 g) and titanium isopropoxide (0.56 g) were also used as received from Aldrich.

All AACVD experiments were performed on a custom built apparatus consisting of a horizontal-bed cold-wall reactor connected to an arrangement of delivery tubing, a bubbler and a humidifier- full details of the reactor have been explained previously in Chapter 2.

### 9.2.1 Vanadium Dioxide - Titania Composite Films

Titanium isopropoxide (0.56 g) and vanadium acetyl acetonate (0.2 g) were added to methanol (50 mL). The mixture was transferred to the aerosol assisted CVD bubbler and a composite $TiO_2$–$VO_2$ film was deposited in a single step at substrate temperatures of 450 °C and a $N_2$ carrier gas flow rate of 1.5 $Lmin^{-1}$. The molar ratio between the two precursors was 1:1.

### 9.2.2 Gold Nanoparticle/Vanadium Dioxide/Titania Composite Films

A variety of precursor combinations were tried in a number of solvents. It was found that the best deposition was by layer deposition of $VO_2$ with Au nanoparticles in a one single layer and a second additional layer comprising of titania anatase. Vanadium acetate (0.2 g) and auric acid (0.45 g) were suspended in 50 mL of methanol. The mixture was transferred to the glass bubbler and an AACVD run was carried out. Thereafter titanium isopropoxide (0.56 g) in toluene (50 mL) was used to deposit an additional layer. The titania layer was deposited both beneath and over a $VO_2$/Au nanoparticle layer in two separate experiments.

## 9.3 Deposition Parameters

A number of different deposition parameters were tested to obtain the optimum conditions for depositing composite $VO_2$/$TiO_2$ and also Au nanoparticle/$VO_2$/$TiO_2$ thin films on glass. The flow rate and reactor temperature were varied to obtain the optimum conditions for both gold nanoparticle and host matrix film growth. Composite $VO_2$/$TiO_2$ thin films were synthesized in one step using the above mentioned precursors whereas the Au nanoparticle/$VO_2$/$TiO_2$ composite thin films were synthesized using layer by layer deposition. This is summarised in Table 12.

| Au precursor in methanol/ mmol | Precursor | Molar ratio Au:precursor | Solvent/ mL | Au $N_2$ flow rate/ $Lmin^{-1}$ | $TiO_2$ $N_2$ flow rate/ $Lmin^{-1}$ |
|---|---|---|---|---|---|
| 0 | $[Ti(O^iPr)_4]$ $[VO(acac)_2]$ | - | Toluene/ 50 | 1.5 | 1.5 |
| 0 | $[Ti(O^iPr)_4]$ $[VO(acac)_2]$ | - | Toluene/ 50 | 1.5 | 1.5 |
| Auric acid/1 | $[Ti(O^iPr)_4]$ $[VO(acac)_2]$ | 1:2 | Toluene/ 50 Methanol/50 | 1.5 | 1.5 |
| Auric acid/1 | $[Ti(O^iPr)_4]$ $[VO(acac)_2]$ | 1:2 | Toluene/ 50 Methanol/50 | 1.5 | 1.5 |

Table 12. Parameters used to deposit gold nanoparticle and vanadium dioxide/titania composite thin films by AACVD.

## 9.4 Deposition of $VO_2/TiO_2$ Composite Thin Films On Glass By Aerosol Assisted Chemical Vapour Deposition

### 9.4.1 Film Characteristics and Elemental Analysis

The AACVD reaction of titanium isopropoxide, and vanadium acetyl acetonate (in methanol, 50 mL) at a substrate temperature of 450 °C deposited composite $TiO_2$–$VO_2$ films. The molar ratio between the two precursors was 1:1. It was found with all samples that the films had a uniform colour across the substrate. The films were different shades of brown (depending on the thickness of the thin films), passed the Scotch tape test, were not removed by a tissue or felt but were scratched with both brass and steel. All films were insoluble in water and common organic solvents (methanol, ethanol, acetone), both acid (HCl, 2 M) and alkali (NaOH, 2 M). The films showed no change in optical properties on storage in air for 3 months.

Glancing angle X-ray diffraction confirmed the presence of both crystalline anatase $TiO_2$ and $VO_2$ in the composite films as shown in Figure 101. A strong signal at approximately 27.8° can be seen in the XRD data, this strong signal corresponds to the (0 1 1) reflection of monoclinic $VO_2$, and indicates the films are preferentially orientated on the substrate[276,277]. The reflections at 24 (1 0 1), 37 (1 0 3), 38 (0 0 4), 39 (1 1 2), 48 (2 0 0), 54 (1 0 5), 56 (2 1 1) and 64° are as expected for the anatase phase of titania. The X-ray data confirms that a composite film is formed and furthermore no shift in the main (0 1 1) diffraction peak of $VO_2$ is seen indicating that very little if any titanium is actually present within the $VO_2$ lattice as a solid solution.

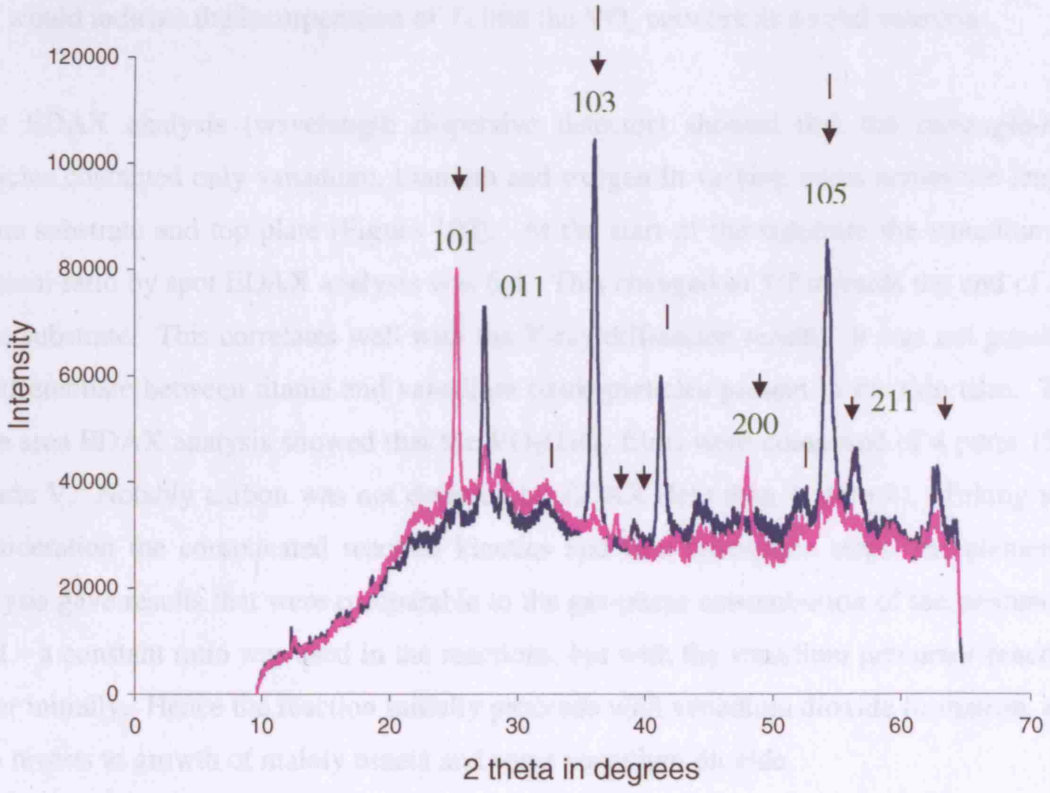


Figure 101. XRD showing varying amounts of $VO_2$ and $TiO_2$ anatase at two ends of an aerosol assisted CVD grown thin film (blue pattern corresponds to the start of the sample and the pink pattern the end). Arrows correspond to $TiO_2$ and lines to $VO_2$.

At the two different ends of the same sample, the titania and vanadium dioxide amounts vary – at the start of the sample (blue pattern), there is a much greater intensity of $VO_2$, whereas at the end of the substrate (pink pattern), the titania reflections are of higher intensity.

Raman spectroscopy of the films showed a pattern consistent with that for a composite film and showed the expected bands for both anatase $TiO_2$ and monoclinic $VO_2$. Bands for $VO_2$ were seen at 144, 190, 315, 389, 498 and 611 $cm^{-1}$. These are comparable to reference values identified by Parker[278] and Aronov[279]. No bands due to $VO_2(B)$, the metastable form of $VO_2$ were observed[280]. There are also peaks present that indicate the presence of anatase $TiO_2$ at 143, 396 and 612 $cm^{-1}$. Furthermore, there are no shifts in the Raman peaks that would indicate the incorporation of Ti into the $VO_2$ network as a solid solution.

Spot EDAX analysis (wavelength dispersive detector) showed that the rectangle-like particles contained only vanadium, titanium and oxygen in varying ratios across the length of the substrate and top plate (Figure 102). At the start of the substrate the vanadium to titanium ratio by spot EDAX analysis was 6:4. This changed to 3:7 towards the end of the glass substrate. This correlates well with the X-ray diffraction results. It was not possible to differentiate between titania and vanadium oxide particles present in the thin film. The wide area EDAX analysis showed that the $VO_2/TiO_2$ films were composed of 4 parts Ti to 6 parts V. Notably carbon was not detected by EDAX (less than 1 atom%). Taking into consideration the complicated reaction kinetics and film adsorption steps, the elemental analysis gave results that were comparable to the gas-phase concentration of the precursors used – a constant ratio was used in the reactions, but with the vanadium precursor reacting faster initially. Hence the reaction initially proceeds with vanadium dioxide formation, and then reverts to growth of mainly titania and some vanadium dioxide.

XPS analysis confirmed the presence of $VO_2$ and titania in the film (Figure 103). Vanadium 2p binding energies were observed at 513.6 eV corresponding to $VO_2$ and titanium 2p 1/2 and 3/2 binding energies were observed at 457.1 and 465.4 eV corresponding to $TiO_2$. The $TiO_2$ : $VO_2$ ratio was 4:6, correlating well with the ratios

confirmed by EDAX. These results tie in well with the literature values for titania anatase and vanadium dioxide[281].

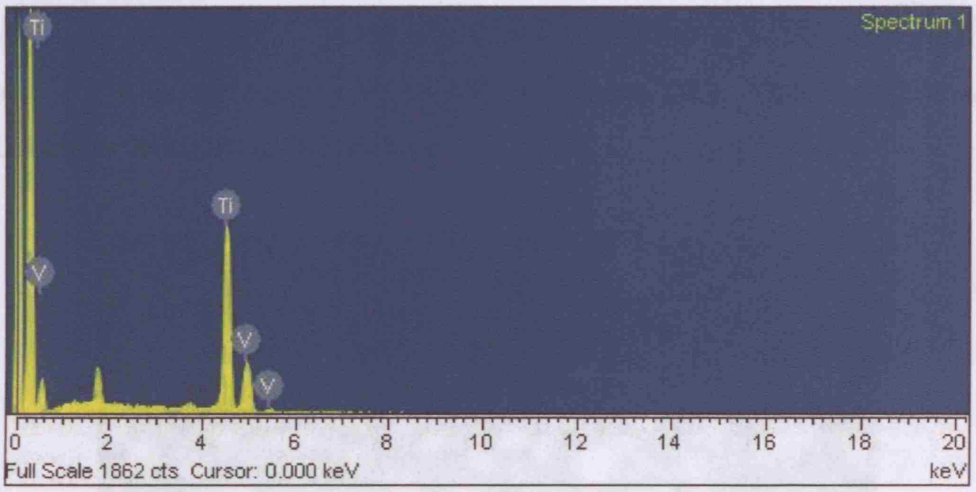


Figure 102. EDAX analysis of a $VO_2$/$TiO_2$ composite film prepared by the AACVD reaction of titanium isopropoxide and vanadium acetate at 450 °C.

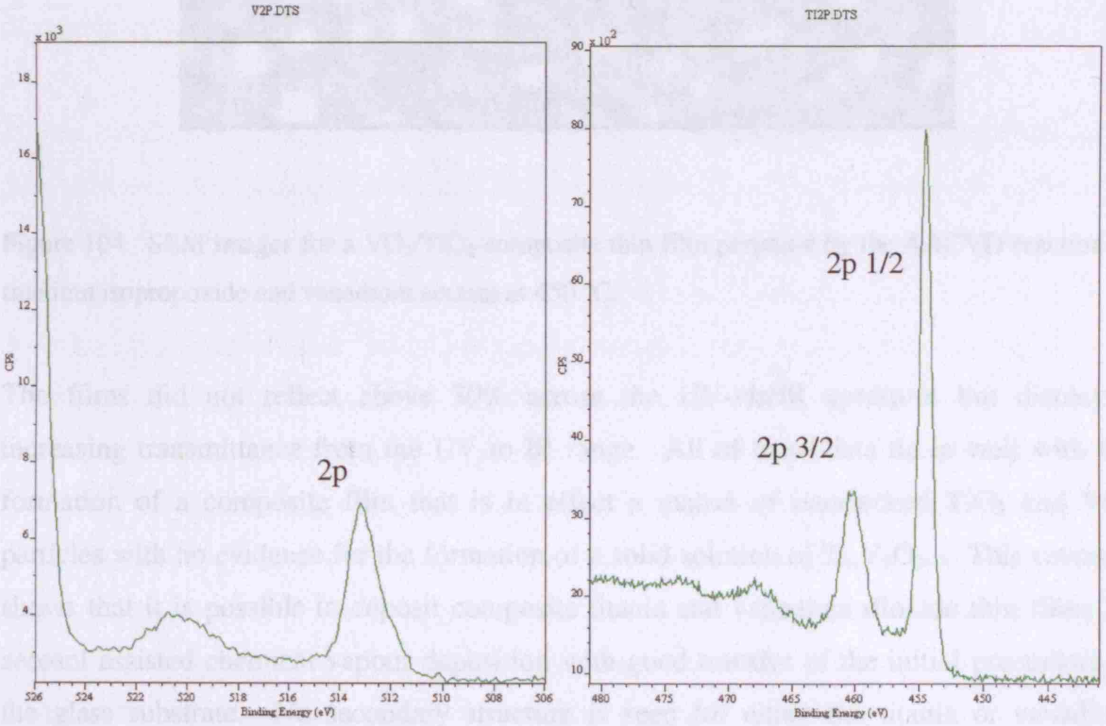


Figure 103. XPS data for a $VO_2$/$TiO_2$ composite film prepared by the AACVD reaction of titanium isopropoxide and vanadium acetate at 450 °C.

## 9.4.2 Film Growth Morphology and Functional Properties

SEM imaging confirmed that the vanadium dioxide/titania composite films are composed of one major type of particle – rectangular with a size of ca. 30 to 100 nm for thin films deposited at a substrate temperature of 450 °C (Figure 104). Side on SEM analysis indicated a growth rate of ca. 180 nm $hour^{-1}$.

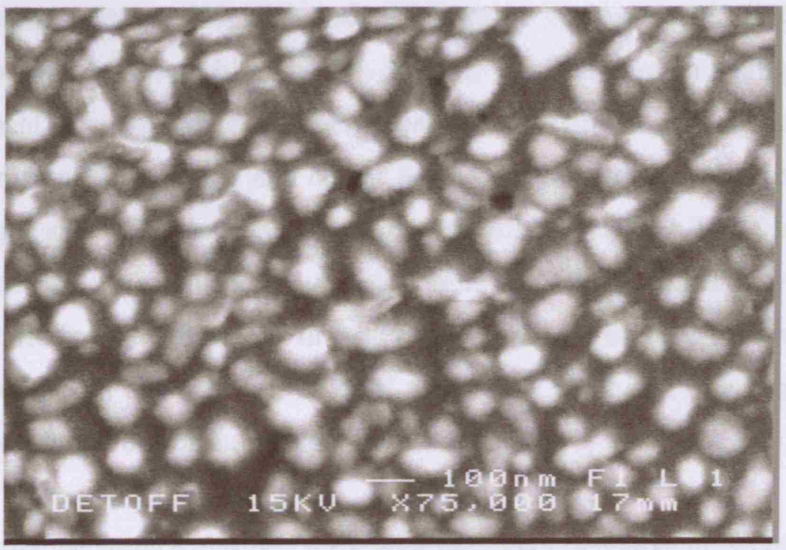


Figure 104. SEM images for a $VO_2$/$TiO_2$ composite thin film prepared by the AACVD reaction of titanium isopropoxide and vanadium acetate at 450 °C.

The films did not reflect above 30% across the UV-vis/IR spectrum but displayed increasing transmittance from the UV to IR range. All of these data tie in well with the formation of a composite film that is in effect a matrix of interlocked $TiO_2$ and $VO_2$ particles with no evidence for the formation of a solid solution of $Ti_xV_yO_2$. This research shows that it is possible to deposit composite titania and vanadium dioxide thin films by aerosol assisted chemical vapour deposition with good transfer of the initial precursors to the glass substrate. No secondary structure is seen for either the titania or vanadium dioxide.

## 9.5 Deposition of Au Nanoparticle/$VO_2$/$TiO_2$ Composite Thin Films On Glass By Aerosol Assisted Chemical Vapour Deposition

### 9.5.1 Film Characteristics and Elemental Analysis

The AACVD reaction of titanium isopropoxide, auric acid and vanadium acetyl acetonate at a substrate temperature of 450 °C deposited composite Au nanoparticle/$TiO_2$–$VO_2$ films. Deposition was by layer deposition of $VO_2$ with Au nanoparticles in a single layer and a second additional layer comprising of titania anatase. It was found with all samples that the films had a uniform composition and colour across the substrate. The films were blue in transmitted light and red with a metallic luster in reflected light. The films passed the Scotch tape test, were not removed by a tissue or felt but were scratched with both brass and steel. All films were insoluble in water and common organic solvents (methanol, ethanol, acetone), both acid (HCl, 2 M) and alkali (NaOH, 2 M). The films showed no change in optical properties on storage in air for 3 months.

Figure 105 shows the surface plasmon resonance band representative of Au nanoparticles at 540 nm from film formed on the top plate. The surface plasmon resonance peak was seen at 650 nm for the substrate. This difference in surface plasmon resonance peak suggests a different gold nanoparticle size/shape on the top plate and substrate. This corresponds well with the SEM images where "worm" like morphology is seen on the substrate, compared to the top plate where more ordered rectangle shapes are present. This could indicate a change in the gold nanoparticle morphology and hence the shift in the peak position[282] and as a red shift is seen here, the cause is likely to be an increase in particle size and the elongated shape. The refractive index of the matrix is also known to influence the surface plasmon resonance. Mie theory and Maxwell Garnett theory both predict a red-shift of the surface plasmon resonance peak with increasing refractive index of the surrounding medium[282]. The refractive index measurement for bulk anatase $TiO_2$ is 2.4, hence the presence of the surrounding medium is also a contributing factor in this case[283].

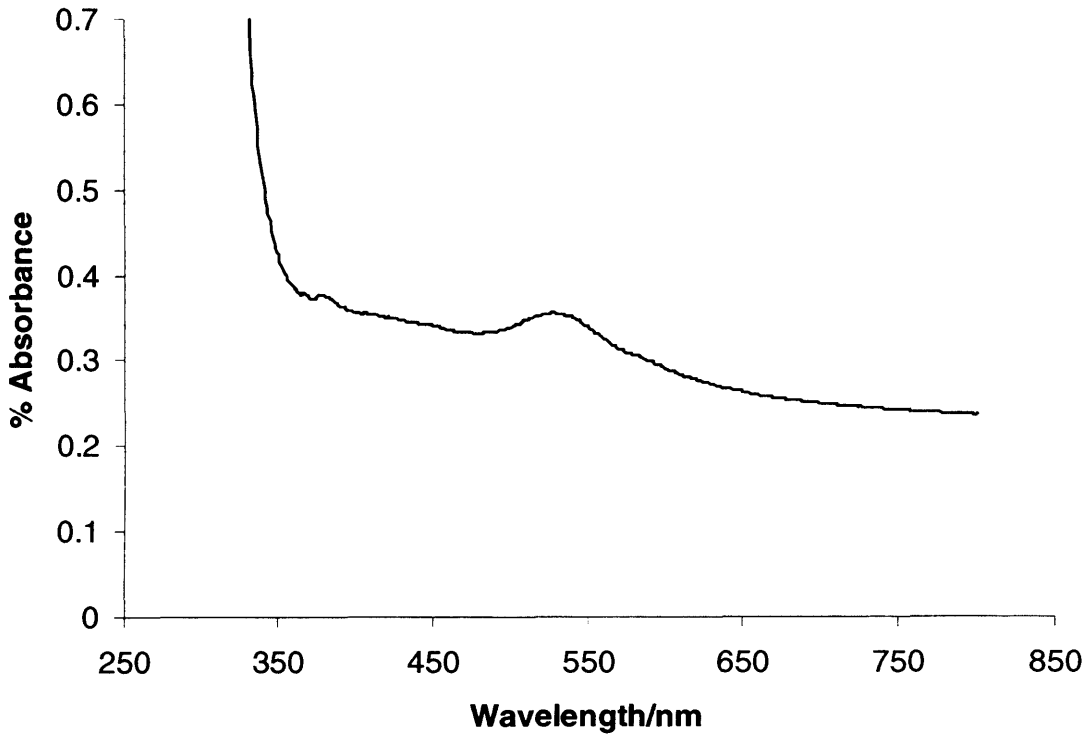


Figure 105. The UV spectrum of a $Au/VO_2/TiO_2$ thin film. The surface plasmon resonance band for gold is seen at 540 nm. Note that this value is for the top plate.

The colour was quantified using the CIELAB colour coordinates, which are commonly used to express perceived colour and are an industry standard (Figure 106). Two parameters $a^*$ and $b^*$, define colour: positive $a^*$ values correspond to red, negative $a^*$ values to green. Positive $b^*$ values correspond to yellow, negative $b^*$ values correspond to blue. Figure 106 shows the colour of the $Au/VO_2/TiO_2$ composite thin films in both transmitted and reflected light. Transmitted light is blue whilst reflected light is red, which is consistent with the visible spectra. The intensity of transmitted colour imparted by the composite film is comparable to commercial body tinted glass, despite the film being 4 orders of magnitude thinner. Extinction coefficients of gold particles are known to be greater than organic or transition metal dyes, therefore these films may be used as coloured coatings[284]. The near symmetric opposite colouration of this films in reflected and transmitted light is a feature for nanoparticulate films[285].

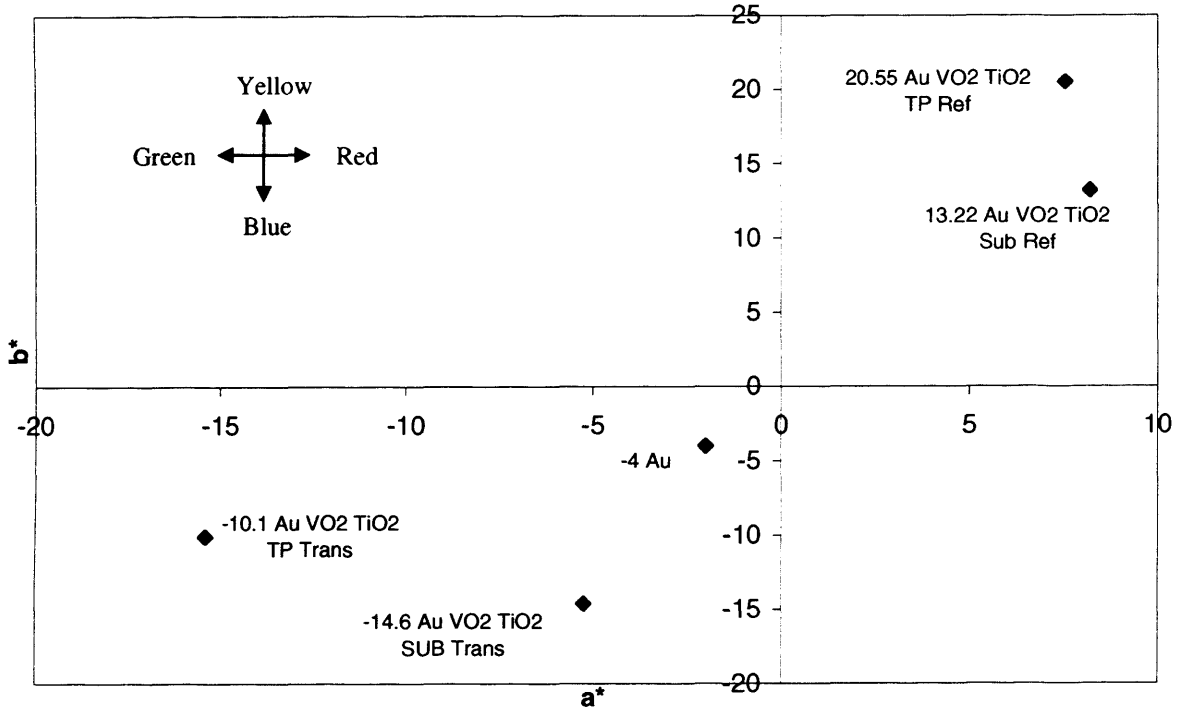


Figure 106. Colour quantification data for the top plate (TP) and substrate (SUB) of Au nanoparticle incorporated $VO_2/TiO_2$ composite thin films on glass prepared by the AACVD reaction of auric acid, titanium isopropoxide and vanadium acetate at 450 °C.

EDAX (wavelength dispersive detector) analysis showed that these particles contained only gold, vanadium, titanium and oxygen in varying ratios across the length of the substrate and top plate (Figure 107). At the start of the substrate the gold to vanadium to titanium ratio was 3:5:2. This changed to 5:4:1 towards the middle and then changed to 4:4:2 towards the end of the substrate. It was not possible to differentiate between titania and vanadium oxide particles but the wide area EDAX analysis showed that the films were composed of 5 parts Au, 2 parts Ti and 3 parts V. Notably carbon was not detected by EDAX (less than 1 atom%). The elemental analysis gave results that were different to the gas-phase concentration of the precursors used – the initial Au:V:Ti ratio was 1:2:2 in the reactions. Notably deposition of gold dominates within the matrix, with titania deposition least

favourable. This could be because the titania precursor undergoes a gas phase reaction and exits through the exhaust- white powder was seen along the exhaust piping system. Spot analysis on all the rectangle particles and aggregated particles from all films yielded similar results and this suggests a trend in the distribution of the $Au/TiO_2/VO_2$ on the surface of the film.

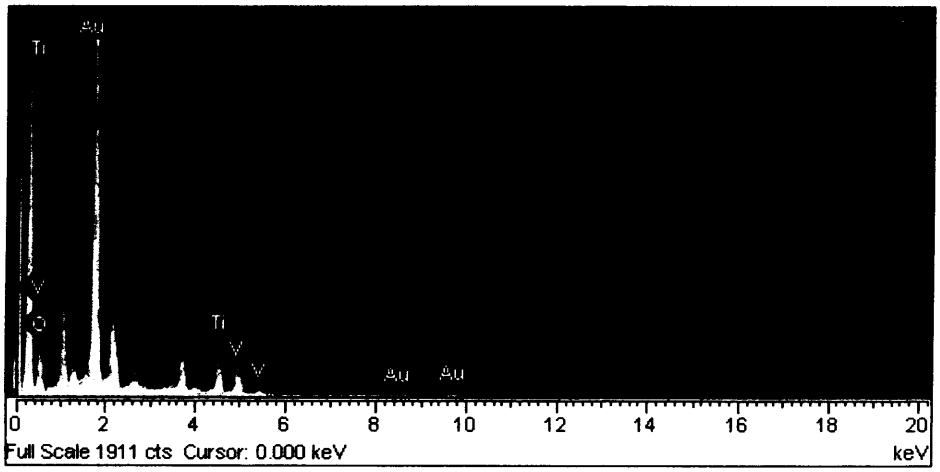


Figure 107. EDAX spectrum of a $Au/VO_2/TiO_2$ film prepared by the AACVD reaction of auric acid, titanium isopropoxide and vanadium acetate at 450 °C.

Glancing angle X-ray diffraction confirmed the presence of cubic metallic gold in all anatase $TiO_2$ and $VO_2$ composite films as shown in Figure 108. Diffraction peaks at 39 and 44.5° were observed which arise from the (111) and (200) planes of the Au cubic lattice (a = 4.07 Å[286]). No crystalline $TiO_2/VO_2$ peaks were observed indicating that the crystallinity of the matrix is low. The FWHM of the Au peaks were almost constant along the length of the substrate, indicating roughly constant crystallite size.

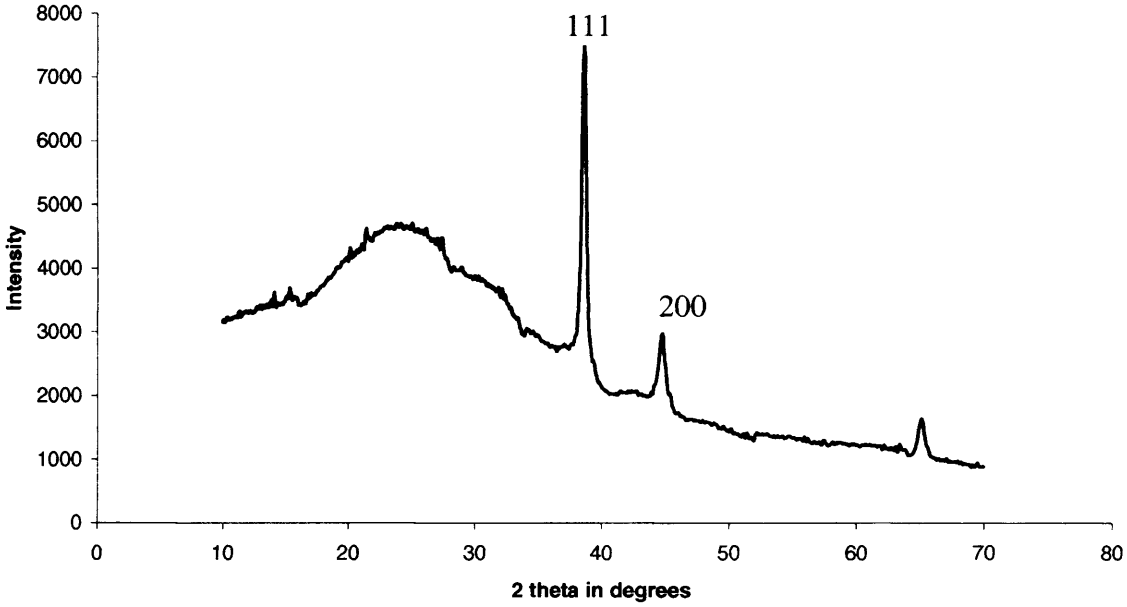


Figure 108. XRD of a Au nanoparticle/$VO_2$/$TiO_2$ composite film prepared by AACVD of auric acid, titanium ispropoxide and vanadium acetate showing the peaks for gold at 39 and 44.5°. The absence of $TiO_2$ and $VO_2$ peaks is due to the low crystallinity of the thin films.

Raman spectroscopy of the films showed a pattern consistent with that for a composite film and showed the expected bands for both anatase $TiO_2$ and monoclinic $VO_2$. The monoclinic $VO_2$ Raman phase was seen with bands at 389, 498 and 611 $cm^{-1}$. These are comparable to reference values. As with the previous chapters, no bands due to $VO_2$(B), the metastable form of $VO_2$ were observed[287]. There are also peaks present that indicate the presence of anatase $TiO_2$ at 396 and 612 $cm^{-1}$. There are no shifts in the Raman peaks that would indicate the incorporation of Ti into the $VO_2$ network as in a solid solution.

All of these data tie in well with the formation of a composite film that is in effect a matrix of interlocked Au, $TiO_2$ and $VO_2$ particles with no evidence for the formation of a solid solution of $Ti_xV_yO_2$ or Au $Ti_xV_yO_2$. Moreover XPS confirmed the presence of Au, $VO_2$ and $TiO_2$ in the film (Figure 109). V 2p binding energies were observed as 513.6 eV corresponding to $VO_2$ and Ti 2p 1/2 and 3/2 binding energies were observed at 457.4 and 465.3 eV corresponding to $TiO_2$. These corresponded well to literature values for the $Ti^{4+}$

ion in $TiO_2$[287]. The absence of a $Ti^{3+}$ environment indicates that the blue colour of the films is not caused by a partially reduced titanium oxide phase, suggesting that the colour is caused by nano-scale gold particles. Au 4f 7/2 and 5/2 peaks at binding energies of 87.5 and 83.7 eV, respectively, corresponding to metallic gold, were observed. The Au:$TiO_2$:$VO_2$ ration was 5:2:3, also confirmed by EDAX. All values were comparable to literature binding energy reference values[287].

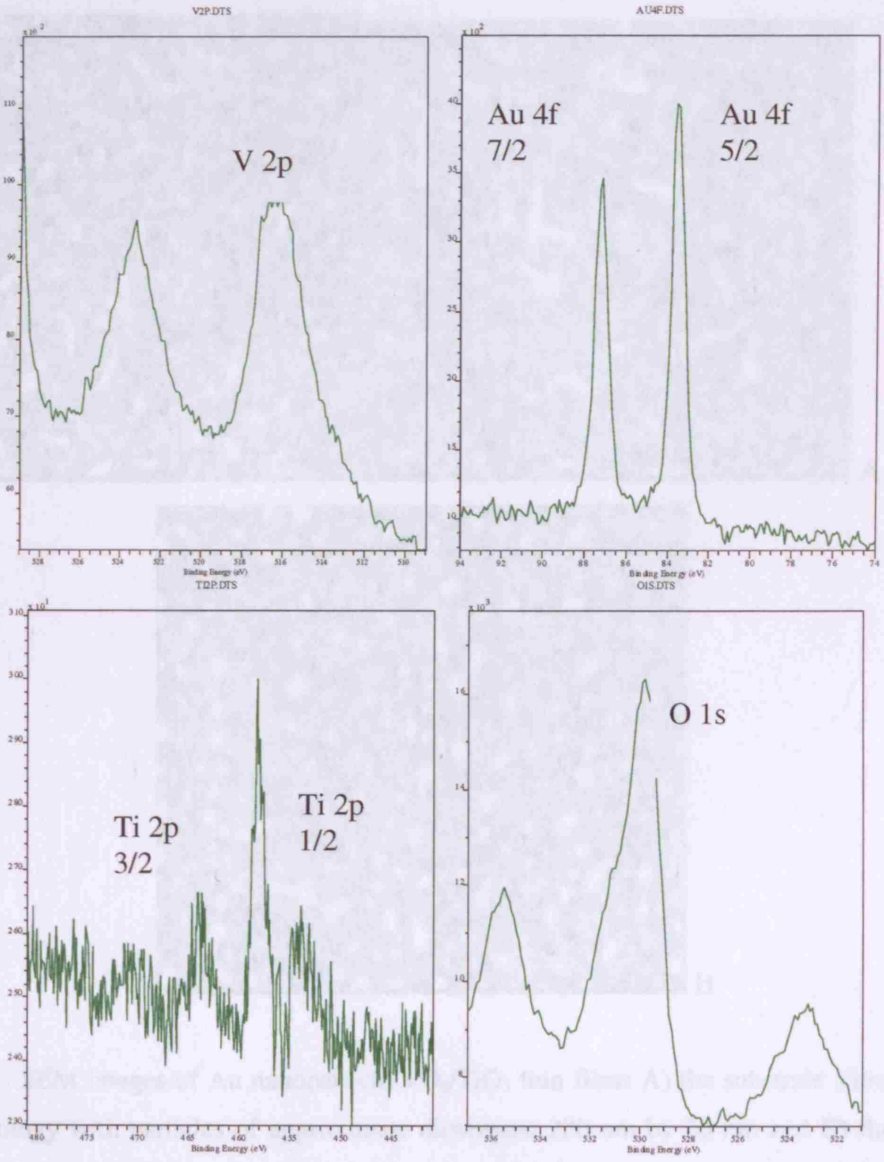


Figure 109. XPS data for Au nanoparticle $TiO_2$/$VO_2$ thin films prepared by the AACVD reaction of auric acid, titanium isopropoxide and vanadium acetate at 450 °C.

## 9.5.2 Film Growth Morphology and Functional Properties

SEM imaging confirmed that the films of Au/$TiO_2$/$VO_2$ are composed of two distinct type of particles – 'worm' like particles of dimension 30 nm by 200 nm and fused islands of average dimension 50 nm by 50 nm (Figure 110). The Au was mapped to the brighter spots.

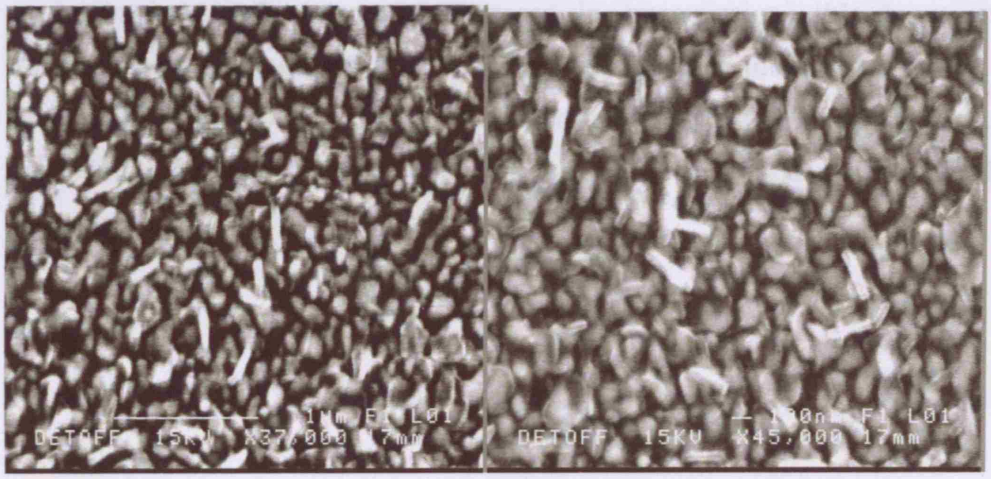


A

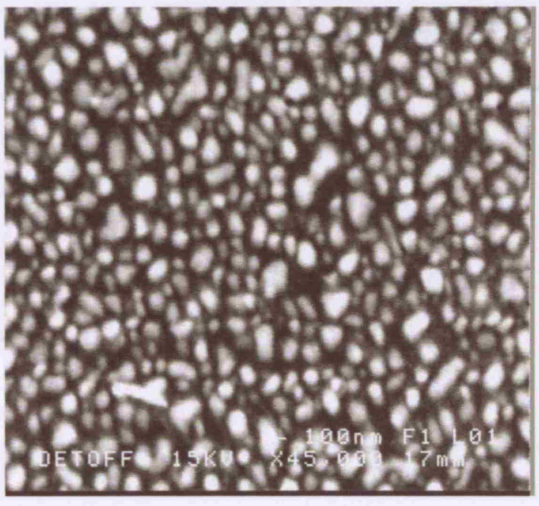


B

Figure 110. SEM images of Au nanoparticle/$VO_2$/$TiO_2$ thin films A) the substrate showing worm like morphology with particles of approximate dimension 200 nm by 20 nm and B) the top plate showed more ordered particles ranging from 40 nm – 100 nm in diameter.

One characteristic property of vanadium(IV) dioxide that makes it a useful material for intelligent window coatings is the increase in infrared reflectance and decrease in infrared transmittance when the material transforms into the high temperature phase[288]. This was investigated by transmission-reflection spectroscopy. The transmittance-reflectance spectra of Au nanoparticles/vanadium dioxide/titania composite thin films at room temperature and 70 ºC are shown in Figure 111. At room temperature, the film showed a reversal in transmission/reflection at the near infra-red. At temperatures above 70 ºC, all films showed an increase in reflectivity and decrease in transmission- this is as expected for thermochromic coatings and also confirms that vanadium dioxide is present. More work needs to be carried out on increasing the transmission of these films types further as the transmission ranges from 15 - 70 % and normally a transmission of greater than 60 % is desirable.

A

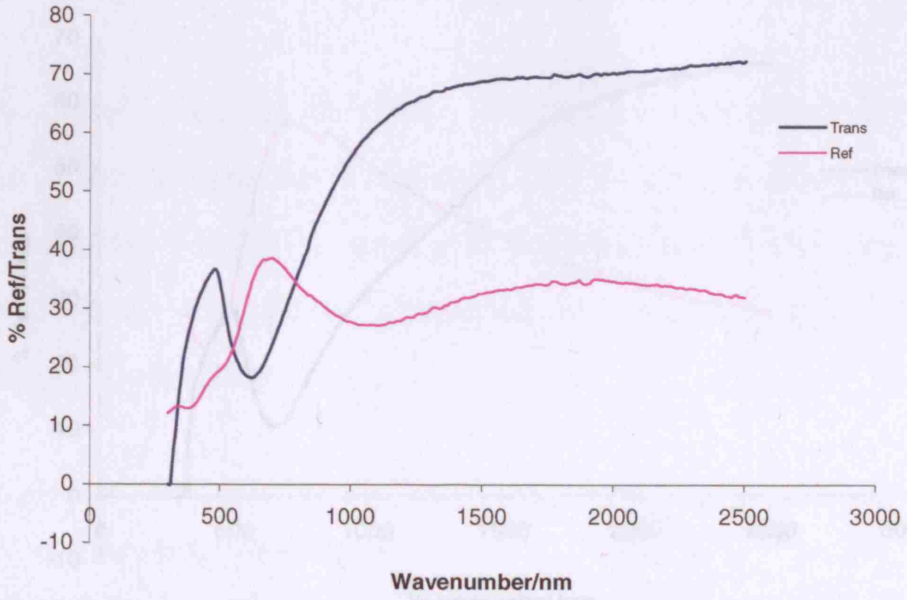

B

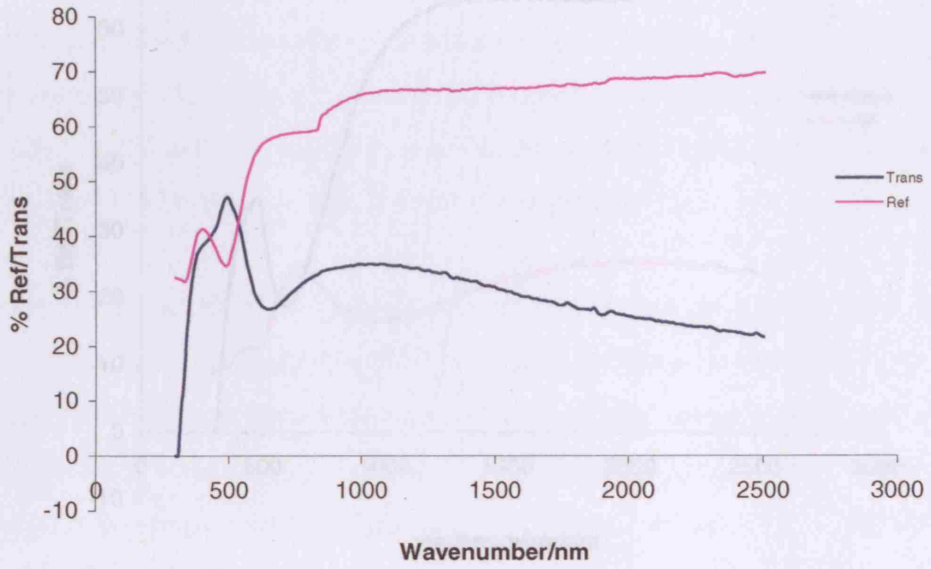
80
70
60
50
40
30
20
10
0
-10
% Ref/Trans
0
500
1000
1500
2000
2500
3000
Wavenumber/nm
Trans
Ref

C

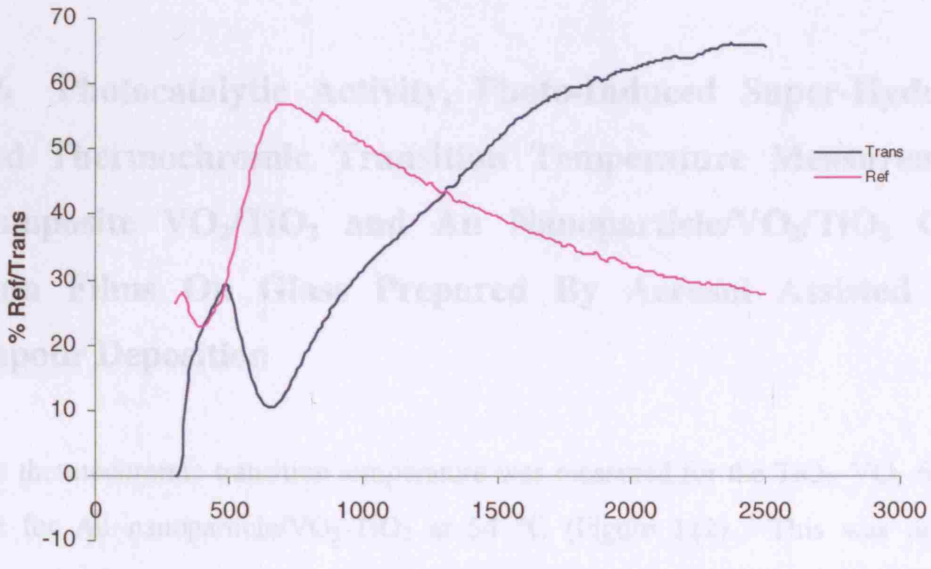
70
60
50
40
30
20
10
0
-10
% Ref/Trans
0
500
1000
1500
2000
2500
3000
Wavenumber/nm
Trans
Ref

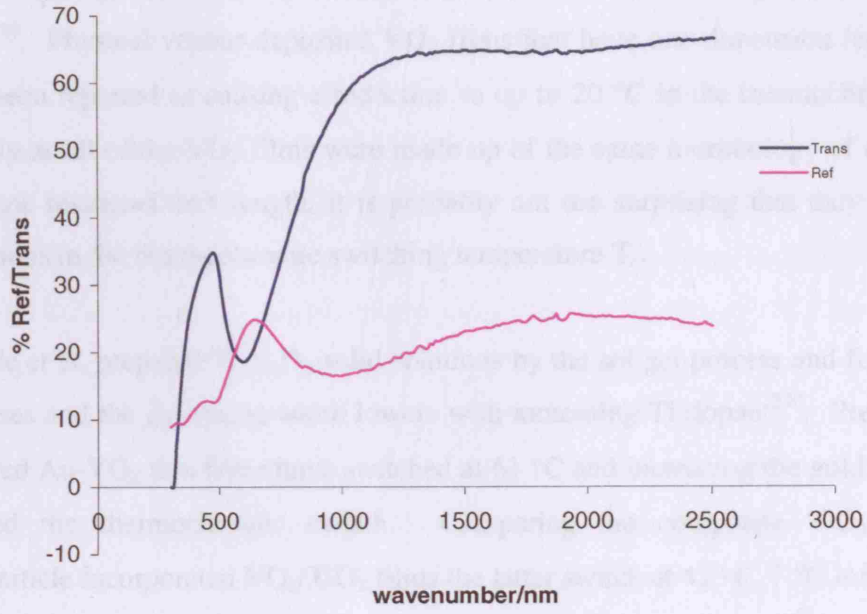


D

Figure 111. Reflectance-transmittance data for Au nanoparticle/$VO_2$/$TiO_2$ composite thin films for A) substrate 24 °C B) substrate 70 °C C) top plate 70 °C and D) top plate at 24 °C.

## 9.6 Photocatalytic Activity, Photo-Induced Super-Hydrophilicity and Thermochromic Transition Temperature Measurements For Composite $VO_2$/$TiO_2$ and Au Nanoparticle/$VO_2$/$TiO_2$ Composite Thin Films On Glass Prepared By Aerosol Assisted Chemical Vapour Deposition

The thermochromic transition temperature was measured for the $TiO_2$–$VO_2$ films at 47 °C and for Au nanoparticle/$VO_2$-$TiO_2$ at 54 °C (Figure 112). This was determined by measuring the transmission through the film at a fixed wavelength of 2.5 μm. The thermochromic switching temperatures did not alter with reaction conditions such as flow rate or substrate temperature. There is a clear decrease in switching temperature from that of pure $VO_2$ films and is most probably related to the morphology of the $VO_2$ films which

all have one axis that is ca. 50 nm in dimension and this is likely to have induced some strain[289]. Physical vapour deposited $VO_2$ films that have one dimension less than 300 nm have been reported as causing a reduction in up to 20 °C in the thermochromic switch[289]. Notably as all of the $VO_2$ films were made up of the same morphology of crystallite, with the same restricted axis length, it is probably not too surprising that they all had similar reductions in the thermochromic switching temperature $T_c$.

Beteille et al, prepared $Ti_xV_yO_2$ solid solutions by the sol gel process and found that the $T_c$ increases and the hysteresis width lowers with increasing Ti dopant[270]. Previously sol-gel prepared Au-$VO_2$ thin films have switched at 61 °C and increasing the gold content further reduced the thermochromic switch. Comparing the composite $TiO_2$/$VO_2$ and Au nanoparticle incorporated $VO_2$/$TiO_2$ films the latter switch at 47 °C, 7 °C lower than for the Au/$VO_2$-$TiO_2$ thin films.

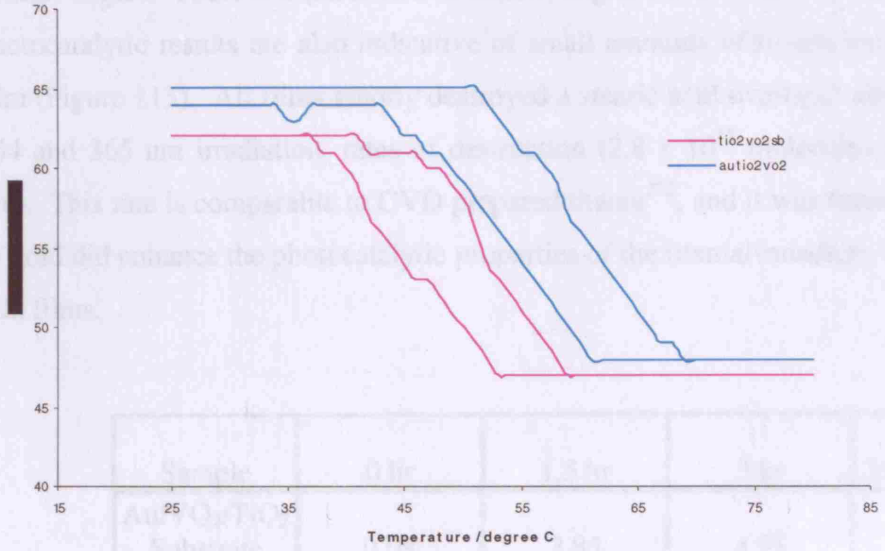


Figure 112. The thermochromic transition temperature for a $TiO_2$–$VO_2$ film at 47 °C and for a Au nanoparticle/$VO_2$-$TiO_2$ film at 54 °C. This was measured at 4000 $cm^{-1}$.

The composite $TiO_2$–$VO_2$ films displayed photocatalytic activity but did not exhibit photo-induced hydrophilicity. This result is unusual since these two effects normally occur simultaneously, and it is sometimes possible for materials to display zero photocatalysis

and enhanced photo-induced hydrophilicity, but the reverse is not common. However, the $Au/VO_2$-$TiO_2$ thin films were both photocatalytically active and also super-hydrophilic upon UV irradiation (254 nm) (Table 12). The $VO_2$-$TiO_2$ thin film initial contact angles for water droplets were 72-80° and did not change with UV irradiation for 5 hours. The $Au/VO_2$-$TiO_2$ thin film initial contact angles were 9° prior to irradiation, this reduced to 7° for the substrate on exposure to 254 nm radiation for 1 h and decreased further to values of 5° after 12 h exposure to sunlight. Leaving the films in the dark for 24 h lead to an increase in contact angles to their original values of 8.9°. The system could be multiply light – dark cycled and the same variation in contact angle was noted. The variations in contact angle are readily explained by the $TiO_2$ component of the films. Anatase is an excellent photocatalyst that also exhibits photo-induced superhydrophilicity[271] and water contact angles of less than 5° are often observed for pure anatase films. The composite films formed contain ca. 20-30% $TiO_2$ that is sufficient to allow part of the surface to show low contact angles. There is a difference in contact angles for the $Au/VO_2$-$TiO_2$ thin films. The photocatalytic results are also indicative of small amounts of titania incorporated into the film (Figure 113). All films readily destroyed a stearic acid overlayer and did so with both 254 and 365 nm irradiation, rates of destruction (2.8 x $10^{12}$ molecules $cm^{-1}min^{-1}$ for 254 nm). This rate is comparable to CVD prepared titania[272], and it was found that the addition of gold did enhance the photocatalytic properties of the titania/vanadium dioxide composite thin films.

| Sample | 0 hr | 1.5 hr | 3 hr | 24 hrs dark |
|---|---|---|---|---|
| $Au/VO_2/TiO_2$ Substrate | 9.08 | 7.85 | 4.95 | 8.9 |
| $Au/VO_2/TiO_2$ Top plate | 11.45 | 8.43 | 7.85 | 11.3 |
| $VO_2/TiO_2$ Substrate | 72.91 | 72.91 | 72.91 | 72.91 |
| $VO_2/TiO_2$ Top plate | 80.02 | 80.02 | 80.02 | 80.02 |

Table 13. Contact angle data for Au nanoparticle/$VO_2$-$TiO_2$ films and composite $TiO_2$–$VO_2$ films.

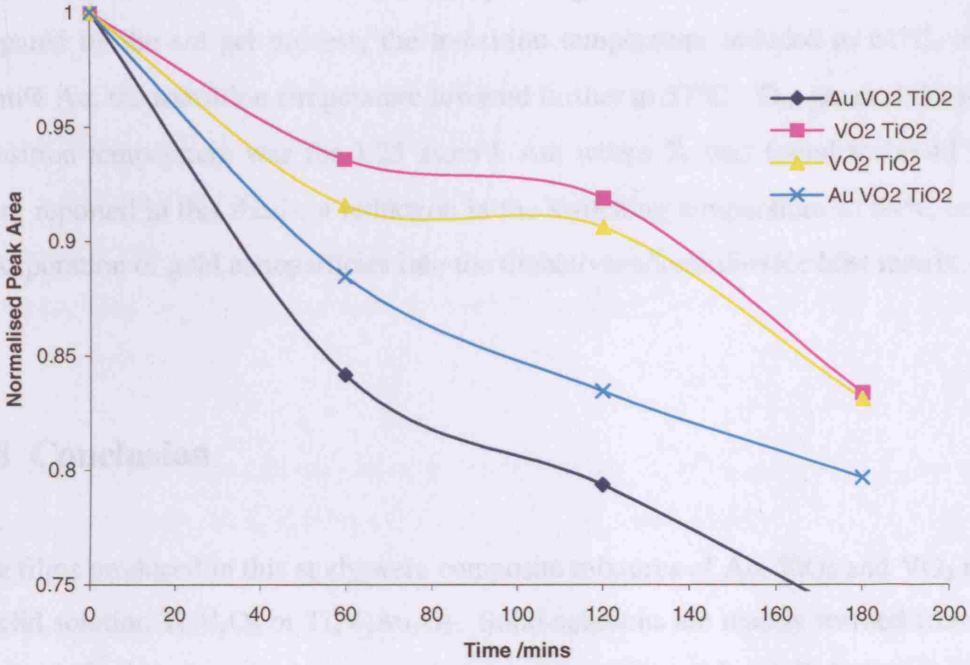


Figure 113. Normalised change in the C-H stretching frequency of a layer of stearic acid in response to irradiation with UV light (254 nm).

## 9.7 Discussion

Previously, Beteille *et al* have attempted the sol-gel synthesis of $TiO_2$ doped vanadium dioxide films[155]. $V_{1-x}Ti_xO_2$ thin films were deposited from $V^V$ and $Ti^{IV}$ alkoxide solutions. The thermal behaviour of sol-gel deposited $V_{1-x}Ti_xO_2$ was studied in the composition range $0 \leq x \leq 0.2$. It was found that at higher titanium levels, the film became less conducting and reflective in the infrared region. They concluded that the transition temperature increased beyond a Ti dopant level of 2 atom%. As a comparison, in this thesis, composite films are formed rather than a solid solution. At 40 % titania and 60 % $VO_2$ a transition temperature of 47 °C is seen rather than an increase in the thermochromic switching temperature.

Cavanna *et al*[158] have found that on incorporating 0.25 atom% Au in a titania host matrix prepared by the sol gel process, the transition temperature reduced to 61°C, and for 0.5 atom% Au, the transition temperature lowered further to 57°C. The greatest decrease in the transition temperature was for 1.25 atom% Au, where $T_c$ was found to be 49°C. In the work reported in this thesis, a reduction in the switching temperature to 54°C occurs upon incorporation of gold nanoparticles into the titania/vanadium dioxide host matrix.

## 9.8 Conclusion

The films produced in this study were composite mixtures of Au, $TiO_2$ and $VO_2$ rather than a solid solution $Ti_xV_yO_2$ or $Ti_xV_yAu_zO_2$. Solid-solutions are readily formed from a sol–gel approach furthermore, the heat treatments used in making sol–gel $Ti_xV_yO_2$ are comparable to the temperatures used in this CVD reaction (albeit for a longer duration). The most likely determining factor in the formation of composite films is reaction kinetics.

The composite films formed in this study show photocatalysis, hydrophilicity and a thermochromic switch. The photocatalysis for a $VO_2$/$TiO_2$ thin film is less than a pure CVD prepared anatase $TiO_2$ thin film – about 40% of the activity. This level of activity scales exactly with the titania content of the film. Although this photoactivity is relatively low it is still sufficient for self-cleaning action. It should be noted that gold nanoparticles significantly enhanced the photo catalytic activity of composite vanadium dioxide/titania thin films. The reduction in water contact angle of the Au nanoparticle/$TiO_2$/$VO_2$ thin films when exposed to sunlight are as expected for a CVD prepared anatase film. The reduction in thermochromic switching temperature observed for the films is a result of induced strain. The reduction of 23 °C from pure $VO_2$ is noteworthy and somewhat larger than that seen for pure $VO_2$ formed by CVD (where a reduction of ca. 10 °C is common). Furthermore, the hysteresis width of the transition is significantly lowered in the films formed in this study. It is possible that the co-location of titania particles within the $VO_2$ matrix improves marginally the thermochromic performance.

In comparison to the Au/$VO_2$ thin films prepared in Chapter 8, that did not show any photocatalytic activity, the Au/$VO_2$/$TiO_2$ were photocatalytically active at a rate comparable to a CVD prepared anatase $TiO_2$ thin film. The Au/$VO_2$ films in Chapter 9 did show a greater reduction in thermochromic switching temperature compare to the films deposited in this chapter- in Chapter 8, the reduction of 37 °C from pure $VO_2$ is noteworthy and somewhat larger than that seen for pure $VO_2$ formed by CVD (where a reduction of ca. 10 °C is common[270]).

The films deposited in this chapter improve the colour of $VO_2$, undoped $VO_2$ is dark brown, and this colour if not desirable for window coating applications. In this work, all films were different shades of violet/purple/red (depending on the thickness of the thin films). This colour has scope for developing window coatings.

In conclusion, the composite $TiO_2$–$VO_2$ and Au nanoparticle/$TiO_2$/$VO_2$ films were deposited via the AACVD reaction of vanadium acetate, titanium isopropoxide and auric acid. The composite films formed show four useful functional properties – improved colour, photocatalysis, photo induced superhydrophilicity and some significant reduction in thermochromic switching temperature, 47 °C. It also shows that composite films of this kind do not interfere with the functionality of each individual component and that solid solutions are not formed.

# Chapter 10: Deposition of ZnO, Au Nanoparticle/ZnO, ZnO Nanoparticle and ZnO Nanoparticle/$TiO_2$ Composite Thin Films By Aerosol Assisted Chemical Vapour Deposition.

## 10.1 Introduction

Zinc oxide is an important thin-film material that is used in a wide range of applications such as varistor technology and sensing[112]. Researchers have made use of its semiconducting, photocatalytic and electronic properties[114]. Furthermore, the transparent nature of zinc oxide thin films is an attractive property for thin film devices[116]. Previously, thin films of zinc oxide have been commonly deposited by sputtering, spray pyrolysis and metal-organic chemical vapour deposition[120]. The sol-gel process has also been considered but its use has been hindered because of the insolubility of zinc alkoxide precursors. An alternative route for sol-gel thin film deposition makes use of concentrated zinc colloids prepared from zinc acetate in ethanol[113].

No work, to our knowledge, has yet been published on the aerosol assisted chemical vapour deposition of zinc oxide thin-film matrices incorporating nanoparticles. This chapter will focus on the aerosol assisted chemical vapour deposition of zinc oxide thin films from zinc acetate dissolved in methanol. This route also enabled films of Au nanoparticles within a host zinc oxide matrix to be grown from a solution of auric acid and zinc acetate. In addition ZnO nanopowder was transferred on to glass, depositing a thin-film and also subsequently incorporated within a $TiO_2$ host matrix. This was completed to impart the useful properties exhibited by zinc oxide nanoparticles to a titania host matrix and to fine tune properties already known for titania, in particular to improve the optical, photocatalytic and photo induced super hydrophilicity of the titania thin films. Furthermore, this work is an extension

to Chapter 5 on tungsten oxide nanopowder precursors- one of the key aims was to develop a new and novel method for transferring semiconductor nanoparticles using solid nanoparticulate starting materials as precursors for the formation of adhesive thin films.

## 10.2 Experimental Design

All AACVD experiments were performed on a custom built apparatus consisting of a horizontal-bed cold-wall reactor connected to an arrangement of delivery tubing, a bubbler and a humidifier- full details of the reactor have been described previously in the Experimental chapter. All chemicals (titanium isopropoxide, auric acid, zinc acetate, zinc oxide nanopowder, iron zinc oxide nanopowder) were purchased and used as prepared from Aldrich.

### 10.2.1 Zinc Oxide Thin Films Deposited By AACVD

Zinc oxide films were grown by suspending zinc acetate (0.2g, 7.3 mmol) in methanol (50 mL). This mixture was transferred to the aerosol bubbler and thin films were deposited at substrate temperatures of 425 °C and carrier gas flow rates of 1.5 L $min^{-1}$.

### 10.2.2 Zinc Oxide – Gold Nanoparticle Composite Films

Auric acid (0.05 g, 1 mmol) and zinc acetate (0.2 g, 7.3 mmol) were added to methanol (50 mL). This mixture was transferred to the aerosol bubbler and thin films were deposited at temperatures of 425 °C and flow rates of 1.5 L $min^{-1}$.

### 10.2.3 Zinc Oxide Nanoparticle Thin Films

Zinc oxide nanopowder (0.2 g, 5 mmol) was added to methanol (50 mL). This mixture was transferred to the aerosol bubbler and thin films were deposited at substrate temperatures of 425 °C and carrier gas flow rates of 1.5 L $min^{-1}$.

### 10.2.4 Zinc Oxide Nanoparticle/Titania Composite Thin Films

Zinc oxide nanopowder (5 mmol) and titanium isopropoxide (1 mmol) were added to methanol (50 mL). This mixture was transferred to the aerosol bubbler and thin films were deposited at temperatures of 450 °C and flow rates of 1.5 L $min^{-1}$.

## 10.3 Deposition Parameters

Deposition of ZnO and Au/ZnO thin films on glass were carried out as shown in Table 14. Five types of film were deposited: ZnO thin films on glass and Au nanoparticles embedded in a ZnO host matrix; In addition ZnO nanopowder was transferred onto glass, depositing a thin-film and also subsequently incorporated within a $TiO_2$ host matrix by aerosol assisted chemical vapour deposition. The flow rates and volumes of solvent were selected to give the most extensive deposition over the substrate.

| Precursor (nano-particle)/ mmol | Precursor 2/ mmol | Molar ratio precursors | Solvent/ mL | Aerosol flow rate/ $Lmin^{-1}$ |
|---|---|---|---|---|
| - | $[Zn(acac)_2]$/ 7.3 | - | Methanol/50 | 1.5 |
| $[Au(acac)_2]$/ 1 | $[Zn(acac)_2]$/ 7.3 | 1:7.3 | Methanol/50 | 1.5 |
| ZnO nanopowder/ 5 | - | - | Methanol/50 | 1.5 |
| ZnO nanopowder/ 5 | $[Ti(O^iPr)_4]$/ 1 | 5:1 | Methanol/50 | 1.5 |

Table 14. Parameters used to deposit nanoparticle and nanocomposite thin films on glass by AACVD.

## 10.4 Deposition of Zinc Oxide Films Using AACVD

Zinc oxide thin films were prepared on glass from the aerosol assisted CVD of $[Zn(acac)_2]$ (0.2 g, 7.3 mmol) in methanol. The deposition of zinc oxide occurred with a deposition time of 65 minutes, on both the substrate and the top plate, which is the glass plate that rests 8 mm above the surface of the substrate. The films deposited on both the top plate and substrate were transparent (80%) and exhibited interference patterns due to a variation in the thickness of the films. The films passed the Scotch tape test, were adhesive and could be scratched with both a brass and steel stylus. The films were stored and handled in air with no apparent degradation. All films were deposited at a substrate temperature of 425 °C. The films differed in thickness throughout the substrate but samples taken for analysis were approximately 2 μm in thickness. The film could not be removed by immersion of the film in common solvents and acid and alkali (2M).

X-ray diffraction detected crystalline zinc oxide (Figure 114). Zinc Oxide peaks can be clearly seen in the X-ray pattern. Highly crystalline ZnO films which also gave strong signals in the X-ray diffraction pattern. The results obtained for ZnO thin films deposited here by AACVD were in good agreement with the reference values which are 33 (100), 34.5 (002), 36.5 (101), 47.5 (102), 56.5, 63 (103), 67 (112) and 73° [290]. The cell constants were calculated and found to be $a$ = 3.239 and $b$ = 5.201 Å. These values are comparable to the reported reference values in the literature.

Furthermore, Raman analysis showed bands at 331, 380, 437, 521 and 576 $cm^{-1}$. Reference values[235] are 332, 380, 437, 522, 533 and 579 $cm^{-1}$. These compare well to the Raman values obtained for the ZnO thin films and to aid this further, UV analysis was also representative of a zinc oxide thin film (Figure 115) [290].

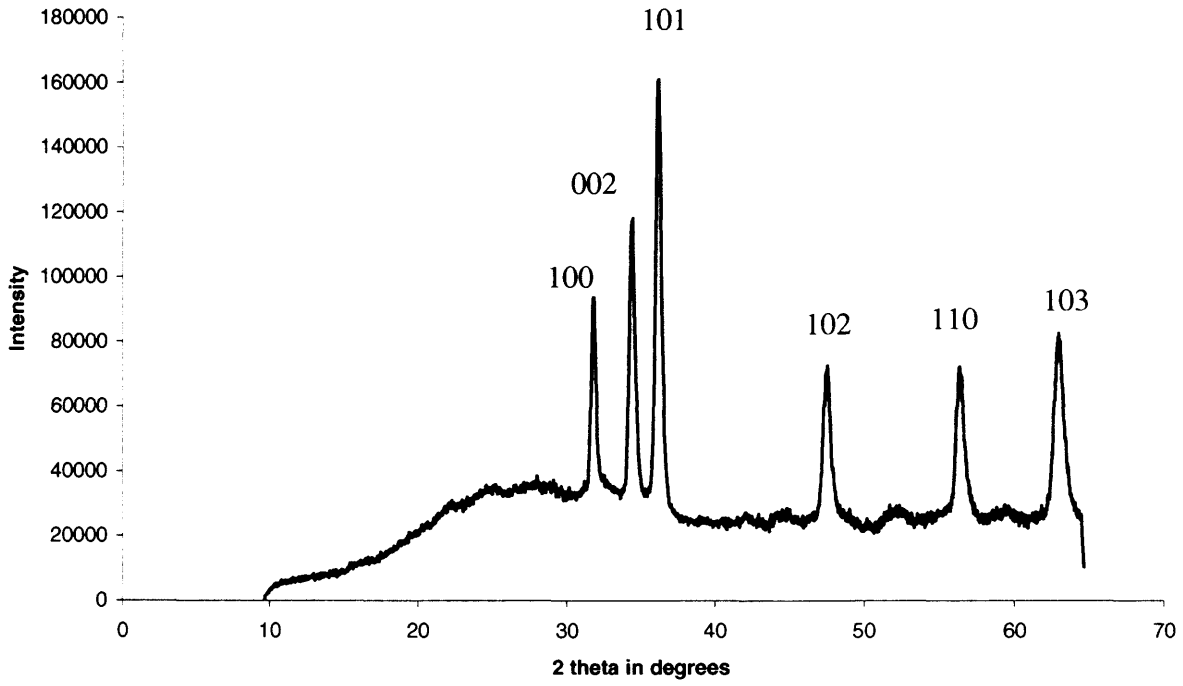


Figure 114. XRD pattern for a ZnO thin film formed on glass from the AACVD reaction of zinc acetate at 450 °C showing no preferred orientation.

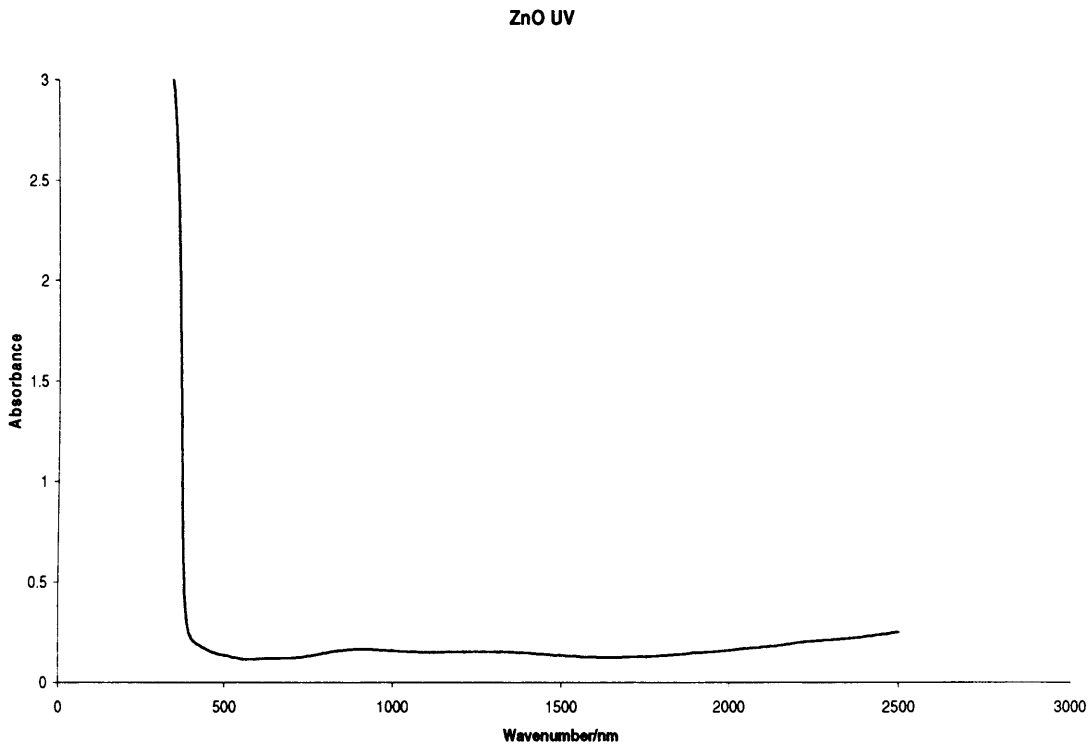


Figure 115. UV-vis spectrum for a ZnO thin film deposited by aerosol assisted chemical vapour deposition at 450 °C.

Spot EDAX analysis confirmed the presence of zinc in the thin films. No carbon was detected. There were consistent results for all data acquired across the substrate suggesting a uniform distribution. SEM images (Figure 116) shows a spiraling island growth morphology with an agglomeration of many particles of dimension 15 nm. This suggests that the ZnO particles have a greater affinity for the substrate than other ZnO nanoparticles.

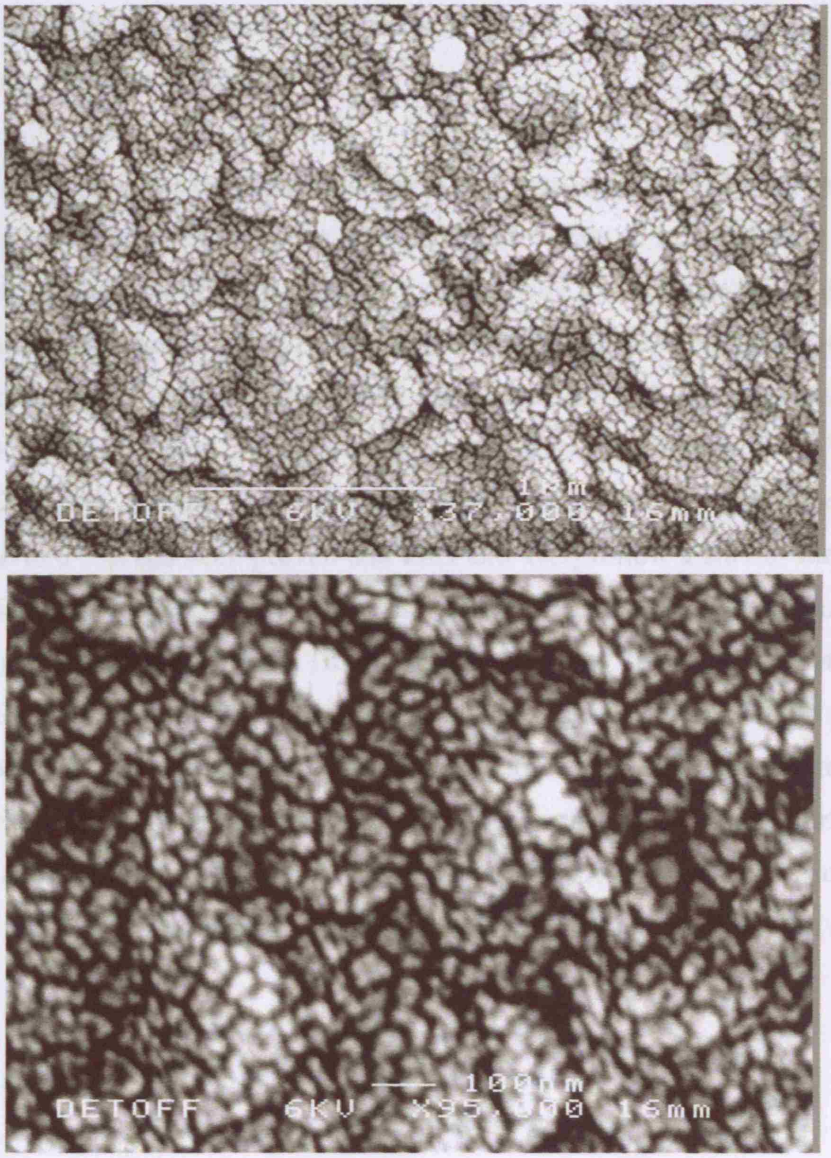


Figure 116. SEM images showing two different ZnO thin films deposited under the same conditions by AACVD using [$Zn(acac)_2$] at 450 °C.

The ZnO thin-films synthesized in this study displayed enhanced photocatalytic activity[122]. These films displayed two useful functional properties – they were active photocatalysts and they showed photoinduced superhydrophilicity. The zinc oxide films readily destroyed a stearic acid overlayer and did so with both 254 and 365 nm irradiation, the rate of

destruction was 1.8 x $10^{12}$ molecules $cm^{-1}min^{-1}$ for 254 nm UV light. This rate is comparable to CVD prepared titania[122].

The contact angle for water droplets on the films was low – between 18–26°, indicating that the surface is hydrophilic. This contact angle dropped further to between 3–7° on exposure of the surface for 0.5 h to 254 nm radiation. On keeping the samples in the dark for 24 h the contact angle increased to 10–12°, and on further irradiation decreased again to between 4–5°. In comparison, a control experiment was carried out with titania anatase deposited by AACVD. Initial contact angles were 6-7° and decreased further to 1-3° upon UV irradiation (254 nm). Storage of the titania thin films in the dark led to an increase in the contact angle to 6°. It has been proven that ZnO and $TiO_2$ follow a similar mechanism for the photo-induced hydrophilicity[123]. This is mainly because despite different structures, ZnO (hexagonal wurtzite) and $TiO_2$ (tetragonal) are both photosensitive oxide semiconductors. Irradiation of titania and zinc oxide generates electron/hole pairs, which can either recombine or undergo complex redox reactions at the surface. Some holes can also react with oxygen in the lattice and this results in the generation of surface oxygen vacancies. Alongside these reactions, electrons can also react with lattice metal ions to reduce $Zn^{2+}$ and $Ti^{4+}$ to $Zn^{+}$ and $Ti^{3+}$ respectively[291,292]. This is represented in equations 1-5.

$ZnO\ (TiO_2) + 2h\upsilon \rightarrow 2h^+ + 2e^-$ (1)

$O^{2-} + h^+ \rightarrow O_l^-$ (surface trapped hole) (2)

$O_l^- + h^+ \rightarrow 1/2O_2 + 0$ (oxygen vacancy) (3)

$Zn^{2+}\ (Ti^{4+}) + e^- \rightarrow Zn_s^+ + (Ti_s^{3+})$ (surface trapped electron) (4)

$Zn_s^+ + (Ti_s^{3+}) + O_2 \rightarrow Zn_s^{2+} + (Ti_s^{4+}) + O_2^-$ (5) reaction of surface trapped electrons with oxygen molecules

Water molecules are then able to coordinate into the oxygen vacancies which results in the hydrophilic nature of the material. This confirms why contacts angles of 1 – 3° were seen for the zinc oxide films deposited here. Previously, values less than 10° have been reported for ZnO thin film contact angles and contacts for ZnO films without irradiation are as high as109° [123]. The films deposited here give rise to much lower initial contact angles. This could be due to the nanoparticulate nature of the films deposited in this research.

## 10.5 Deposition of Zinc Oxide Host Thin Films Incorporating Gold Nanoparticles Using AACVD

A deposition time of 65 minutes, enabled both the Au nanoparticles and zinc oxide host matrix to be co-deposited and also laid down in a layer by layer fashion resulting in a composite film. Zinc oxide films were deposited with [$Zn(acac)_2$] (7.3 mmol) and auric acid (1 mmol) in methanol (50 mL) and were prepared on glass by aerosol assisted CVD (Table 14). All films were deposited at a substrate temperature of 425 °C. The first system studied was a thin-film with an initial layer of Au nanoparticles followed by a ZnO over layer, and the second system deposited ZnO first followed by an Au nanoparticle layer. The final system looked at the co-deposition of ZnO and Au nanoparticles from methanol. The gold nanoparticles could not be removed by any physical method that did not also remove the zinc oxide from the film, indicating that the nanoparticles were strongly bound to the film or firmly contained in it. The films passed the Scotch tape test, were adhesive, but could be scratched with both a brass and steel stylus. The films were stored and handled in air with no apparent degradation. The films differed in thickness throughout the substrate but samples taken for analysis were approximately 1 μm in thickness. The film could not be removed by immersion of the film in common solvents and acid and alkali (2M). The Au nanoparticle/ZnO composite thin films, despite being transparent, showed a fusion of green, yellow and purple/blue interference colours.

X-ray diffraction studies confirmed that both Au nanoparticles and ZnO were present in all films. Highly crystalline ZnO films were deposited with no preferred orientation and matched the reference values. Au peaks can clearly be seen in the XRD below at 39 and 45° (Figure 117). These arise from the (111) and (200) planes in the Au cubic lattice[201]. The figure is for data collected from a composite thin film where the first layer is gold, and the top layer zinc oxide. The intensity of the Au peaks increased with increasing particle concentration. XRD patterns were recorded along the length of each film at 10 mm intervals. Identical experimental parameters were used to collect diffraction data from each point. The peak intensities and integrated areas of the Au (111) and (200) peaks varied across the substrate. This indicates a change in the Au concentration across the substrate. As the film thickness is not constant, the integrated areas of the diffractions peaks cannot be directly related to the concentration of gold within the film. However, the integrated peak area at a given point is related to the total amount of crystalline gold at that point.

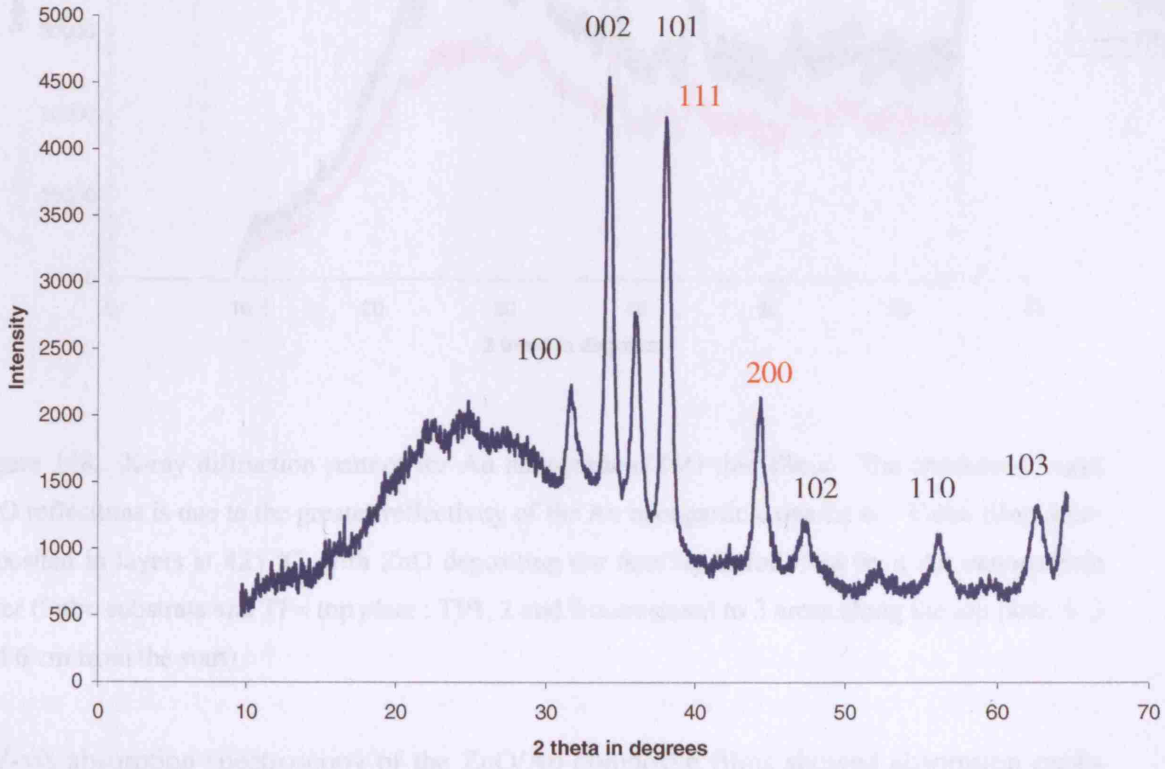


Figure 117. X-ray diffraction pattern for a layered Au nanoparticle/ZnO thin film deposited by AACVD using auric acid and $[Zn(acac)_2]$ at 425 °C. Note that the first deposited layer here is Au nanoparticles, and the top layer is ZnO. The Au miller indices are labelled in red.

The peaks for Au can be clearly seen at 39 and 44 ° for gold in addition to all the crystalline ZnO peaks. Interestingly, in Figure 120, a layer of ZnO is deposited followed by an Au nanoparticle layer on top, and these films do not show the main reference peaks for zinc oxide. Gold nanoparticle peaks are seen at 39 and 40 ° (Figure 118). As EDAX detected zinc oxide in these films with a gold : zinc oxide ratio of 6 : 4, this is most likely due to the greater reflectivity of the Au nanoparticle over layer.

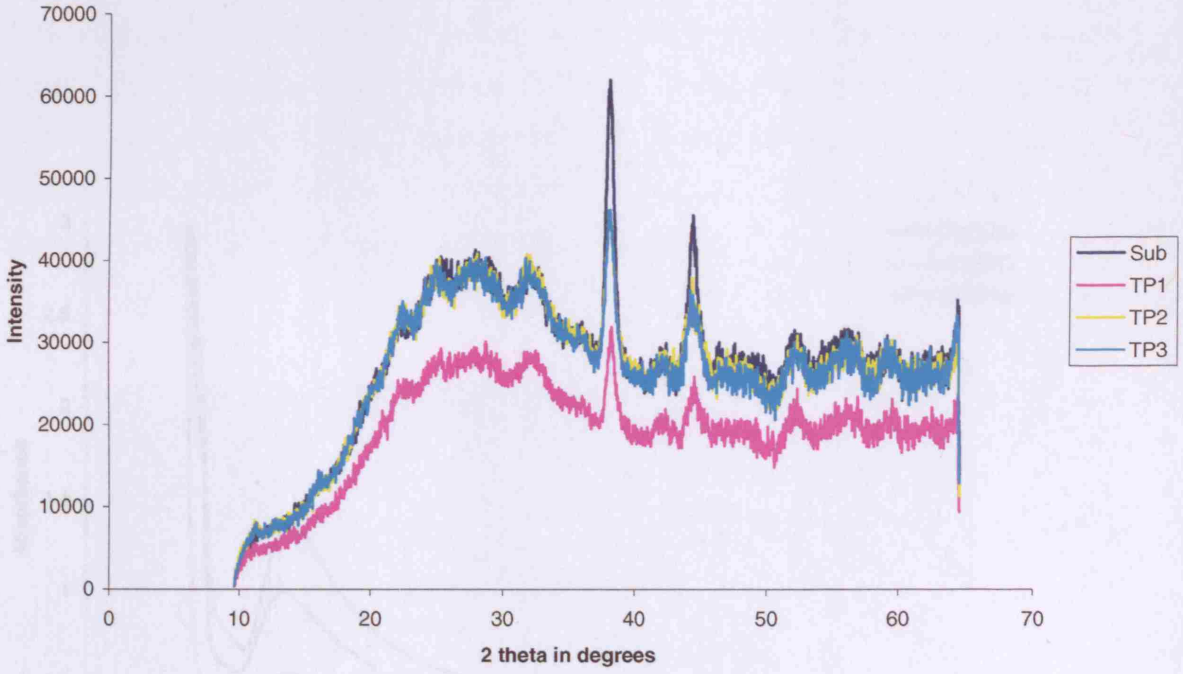


Figure 118. X-ray diffraction pattern for Au nanoparticle/ZnO thin films. The absence of most ZnO reflections is due to the greater reflectivity of the Au nanoparticle overlayer. These films were deposited in layers at 425 °C, with ZnO depositing the first layer, followed by a Au nanoparticle layer (Sub= substrate and TP= top plate : TP1, 2 and 3 correspond to 3 areas along the top plate 1, 3 and 6 cm from the start).

UV-vis absorption spectroscopy of the ZnO/Au composite films showed absorption peaks in the region of 600-950 nm which were assigned to the red shifted and broadened plasmon resonance of gold nanoparticles (Figure 119). Lower Au nanoparticle concentrations show a narrow reflection peak, whilst higher gold concentrations show broader, more intense

peaks, with tails extending into the near – infra red region. The peak broadening is most likely due to the change in refractive index upon incorporation into the host ZnO matrix and also due to particle size effects. The refractive index of the matrix is also known to influence the surface plasmon resonance[45]. It is known that a red-shift of the surface plasmon resonance peak occurs with increasing refractive index of the surrounding medium occurs[45]. The refractive index measurement for bulk anatase ZnO is 1.98 and for Au 0.47. Therefore the higher refractive index of the surrounding medium, along with change in the nanoparticle size are the cause of the red-shift in this case.

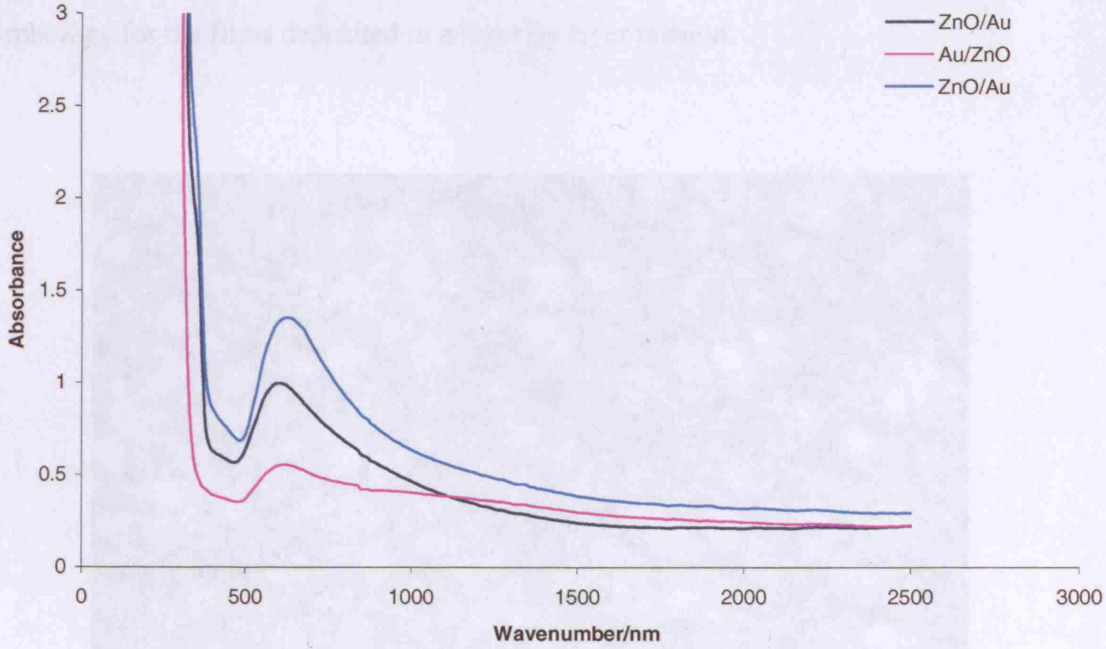


Figure 119. UV-vis absorption spectra showing a red-shift in the surface plasmon resonance for Au nanoparticle-ZnO films. ZnO/Au = Au nanoparticle layer beneath a ZnO layer and Au/ZnO = ZnO layer beneath a Au nanoparticle layer.

Spot EDAX analysis confirmed the presence of zinc and gold in the thin films. The wide area ratio of Au : Zn was 6 : 4 and no carbon was detected. This was representative of the entire sample. SEM images (Figure 120) show a cauliflower style growth morphology with an agglomeration of many particles of dimension 20 – 60 nm which are in turn made up of clusters of nanoparticles of diameter 5 nm. After the formation of one or two complete monolayers, island growth is adopted. The affinity of the film particles is dependant on the strength of binding between the adsorbate and the substrate, but also on other parameters such as lattice mismatch and orientational effects of overlayers. This growth behaviour was repeated across the sample and yielded the same morphology across the substrate, indicating that a uniform films deposits with no change in particle size, shape or distribution across the substrate. There was no change in the EDAX analysis or growth morphology for the films deposited in a layer by layer fashion.

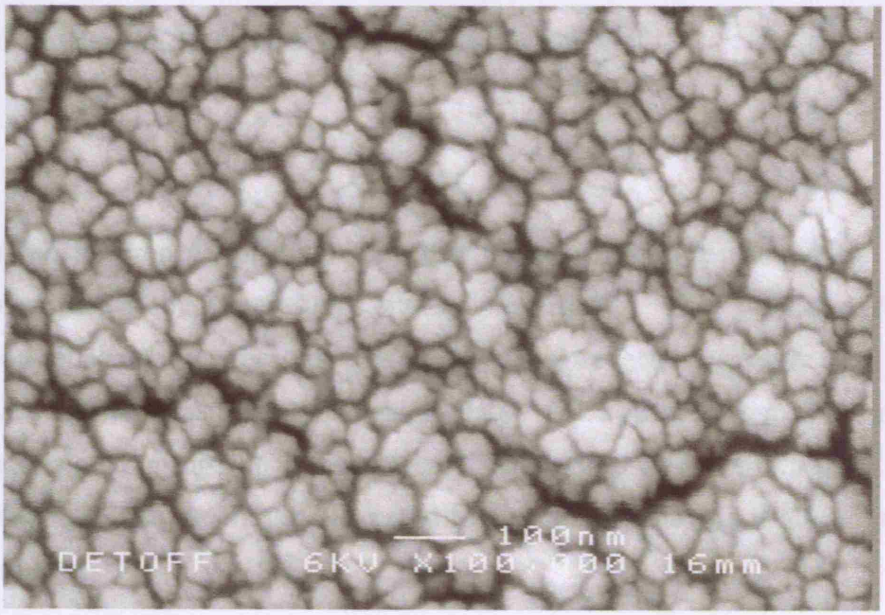

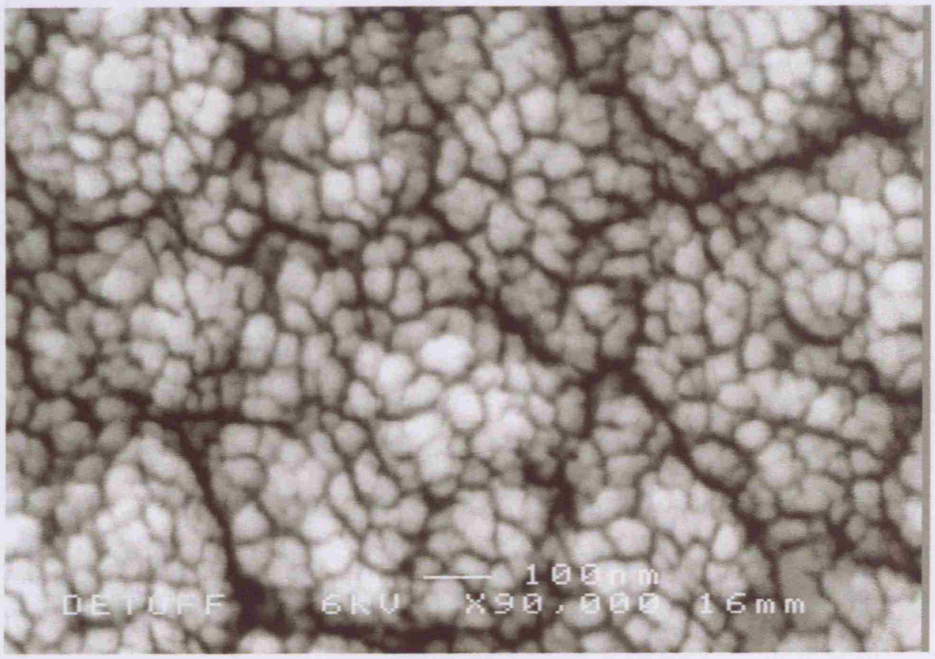


Figure 120. Au nanoparticle/ZnO thin films deposited by AACVD.

One characteristic property of zinc oxide that makes it a useful material for intelligent window coatings is the interesting optical properties[114]. This was investigated by transmission-reflection spectroscopy. The transmittance-reflectance spectra of a zinc oxide thin film at room temperature are shown in Figure 121. At room temperature, the film showed increasing transmission at the near infra-red to 85%, with the reflection increasing no more that 30%. This result is as expected for nanoparticulate thin films and shows that they are coherent.

A

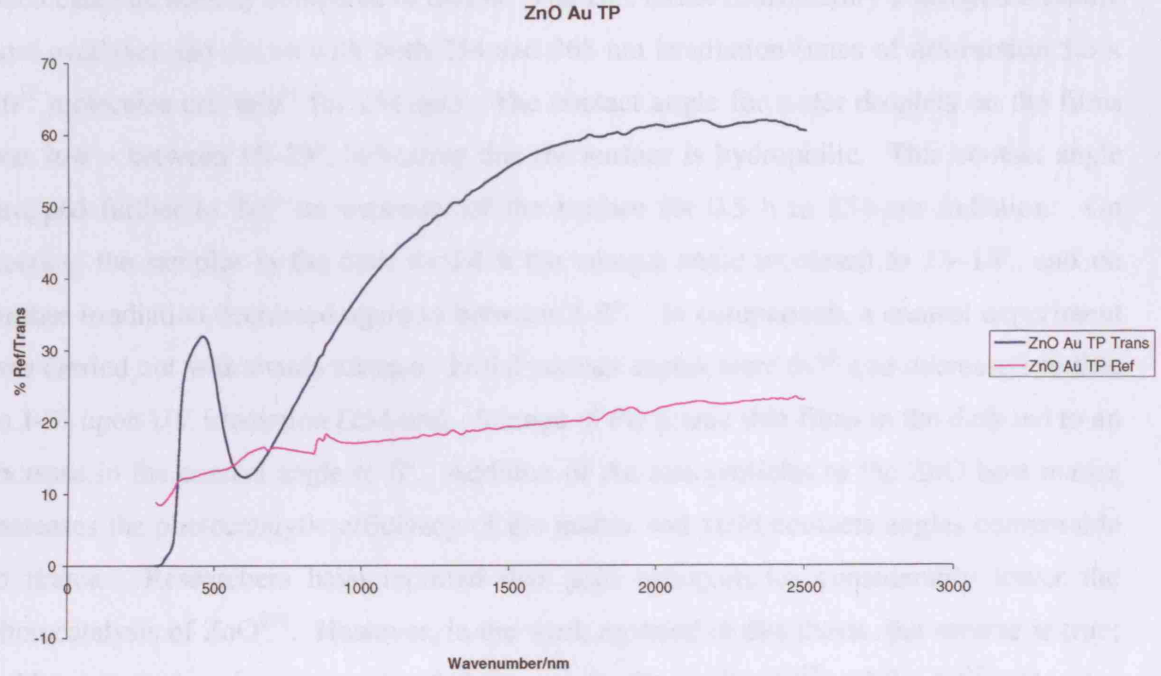


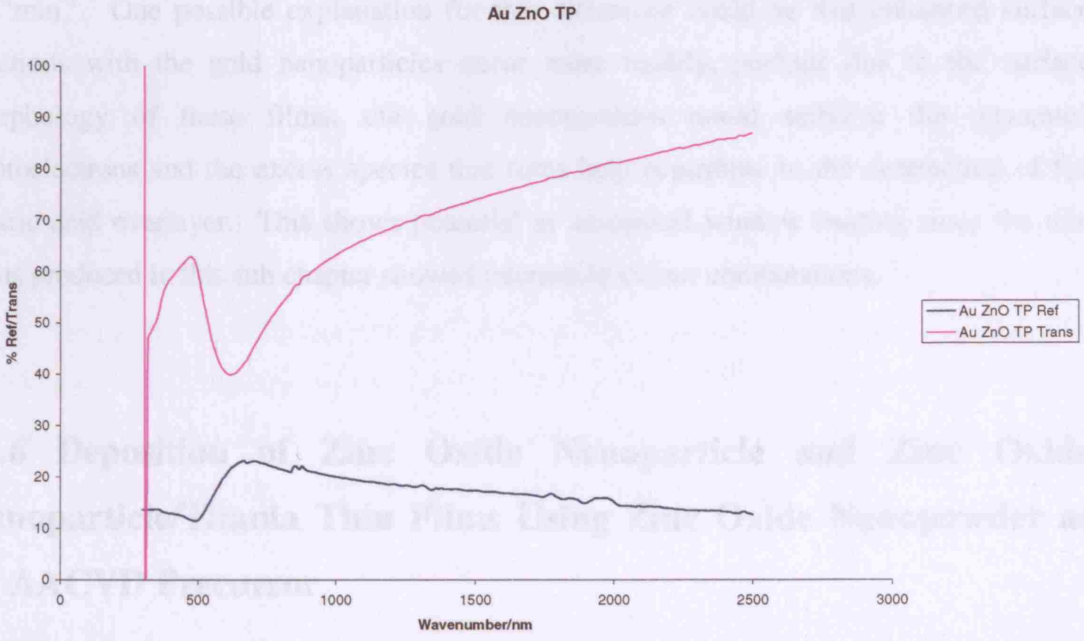


B

Figure 121. Reflectance/transmittance behaviour for Au nanoparticle/ZnO thin films. A) This film type deposited a ZnO layer beneath a layer of Au nanoparticles. B) This film type deposited a layer of Au nanoparticles beneath a layer of ZnO.

The Au nanoparticle/ZnO thin films synthesized in this study displayed enhanced photocatalytic activity compared to titania. The zinc oxide films readily destroyed a stearic acid overlayer and did so with both 254 and 365 nm irradiation (rates of destruction 5.3 x $10^{12}$ molecules $cm^{-1}min^{-1}$ for 254 nm). The contact angle for water droplets on the films was low – between 15–19°, indicating that the surface is hydrophilic. This contact angle dropped further to 2-3° on exposure of the surface for 0.5 h to 254-nm radiation. On keeping the samples in the dark for 24 h the contact angle increased to 13–18°, and on further irradiation decreased again to between 2–4°. In comparison, a control experiment was carried out with titania anatase. Initial contact angles were 6-7° and decreased further to 1-3° upon UV irradiation (254 nm). Storage of the titania thin films in the dark led to an increase in the contact angle to 6°. Addition of Au nanoparticles to the ZnO host matrix increases the photocatalytic efficiency of the matrix and yield contacts angles comparable to titania. Researchers have reported that gold nanoparticles considerably lower the photocatalysis of ZnO[293]. However, in the work reported in this thesis, the reverse is true; gold nanoparticle enhance the rate of photocatalysis from 1.8 x $10^{12}$ to 5.3 x $10^{12}$ molecules $cm^{-1}min^{-1}$. One possible explanation for this difference could be that enhanced surface reactions with the gold nanoparticles occur more readily, perhaps due to the surface morphology of these films; the gold nanoparticles could stabilise the generated photoelectrons and the excess species that form help contribute to the destruction of the stearic acid overlayer. This shows potential as an optical window coating since the thin films produced in this sub chapter showed interesting colour combinations.

## 10.6 Deposition of Zinc Oxide Nanoparticle and Zinc Oxide Nanoparticle/Titania Thin Films Using Zinc Oxide Nanopowder as an AACVD Precursor

ZnO nanoparticles are studied due to their enhanced optical properties- the reference band gap for ZnO is tunable from its normal position of 3.3 eV[293]. Aerosol assisted deposition (AAD) was used to deposit thin films of ZnO from a suspension of solid nanoparticulate

ZnO in methanol. These solid nanoparticles were used in a conventional CVD experiment using an aerosol as a carrier medium. A separate set of experiments investigated what happened when the ZnO nanoparticles were added to a titanium dioxide AACVD precursor and transformed into an adhesive thin film without the use of plasma spraying.

A deposition time of 55 minutes, enabled both the ZnO to be transferred to the glass substrate and also in a separate experiment, incorporated into a titiania host matrix. ZnO nanoparticles and titanium isopropoxide were co-deposited (Table 14). All films were deposited at a substrate temperature of 450 °C. Both the ZnO nanopowder and ZnO nanopowder/$TiO_2$ thin films were adhesive, continuous and also transparent. The nanoparticles could not be removed by any physical method indicating that the nanoparticles are strongly bound to the film or firmly contained in it. The films passed the Scotch tape test but could be scratched with both a brass and steel stylus. The films were stored and handled in air with no apparent degradation. The film could not be removed by immersion of the film in common solvents and acid and alkali (2M).

X-ray diffraction studies for ZnO nanopowder thin films confirmed that ZnO was indeed deposited. The values correspond well with reference values, however; peaks are missing at 47.5, 56.5, 63, 67 and 73°. This shows that the films are preferentially orientated on the (100), (002) and (101) planes (Figure 122). The X-ray spectrum for the starting nanopowder was taken and showed all reflections for ZnO. Figure 123 shows the X-ray diffraction pattern for ZnO nanopowder/$TiO_2$ thin films on glass. Peaks are seen at 25, 49, 55 and 64°. These correspond to the (101), (200) and (211) reflections for anatase titania and are comparable to the literature reference values. No evidence is seen for incorporation of ZnO nanoparticles. However EDAX was able to detect Zn.

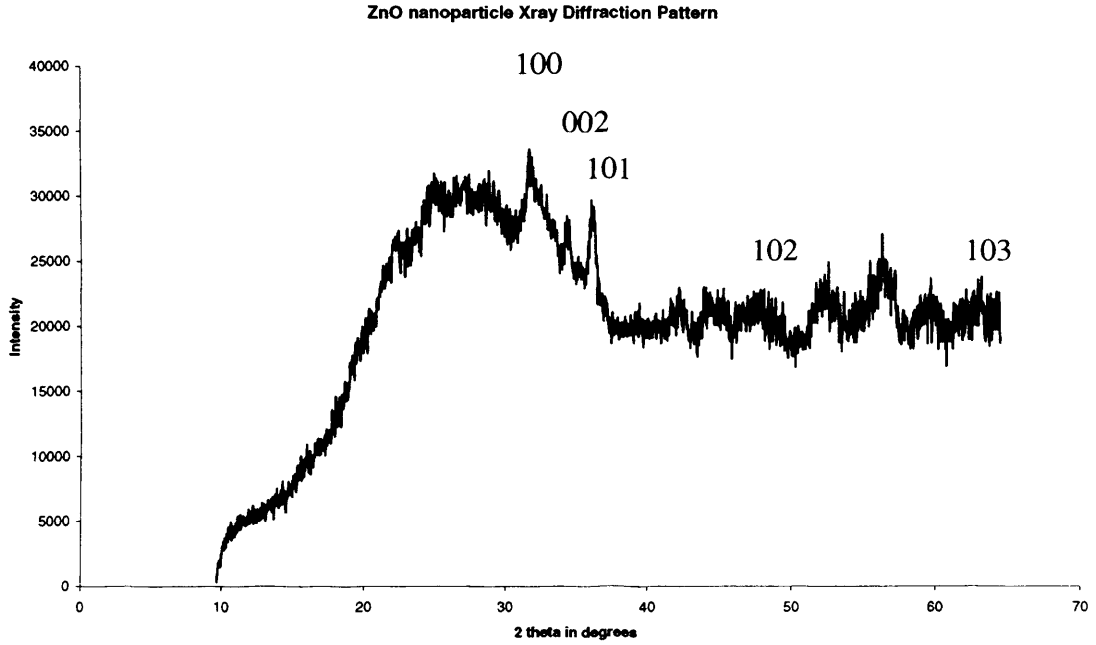


Figure 122. X-ray diffraction pattern for a ZnO nanoparticle thin film showing preferential orientation for the 100, 002 and 101 planes. This film was deposited from zinc oxide nanopowder at 425°.

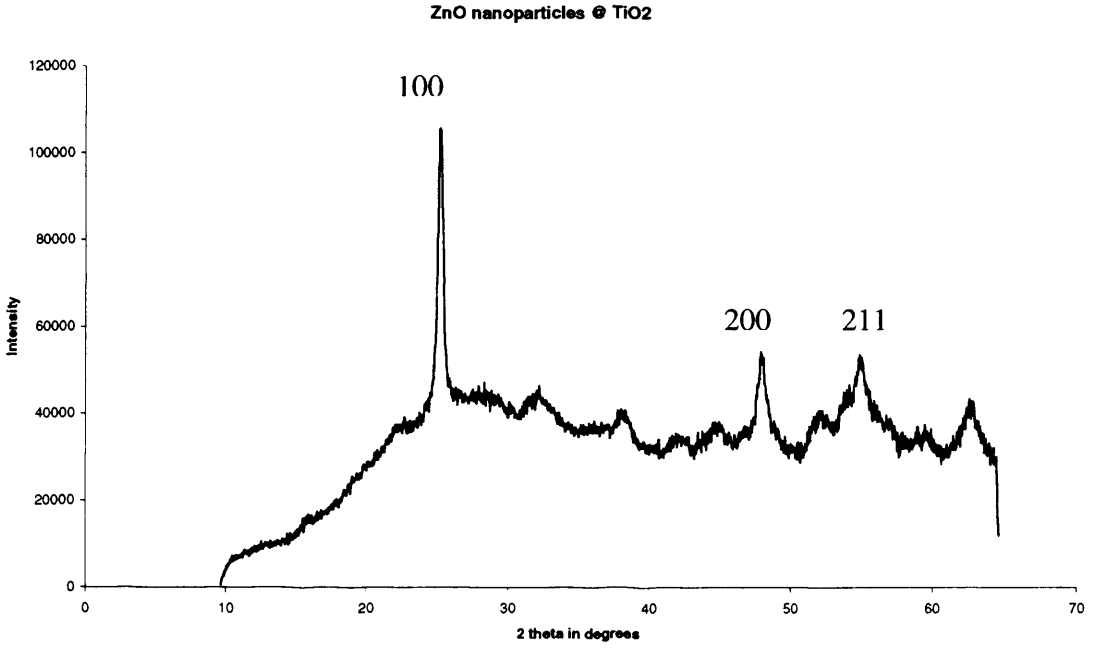


Figure 123. X-ray diffraction pattern for ZnO nanopowder/$TiO_2$ thin films formed from zinc oxide nanopowder and titanium isopropoxide at 425°. The indices correspond to titania.

EDAX analysis confirmed that indeed Zn was present in the ZnO thin films and also that Zn and Ti existed in the ZnO nanopowder-$TiO_2$ thin films in a 2:13 ratio. SEM images for ZnO nanopowder films showed fused nanoparticles of dimension 10 nm existing in islands 300nm in size (Figure 124). SEM images of a ZnO nanopowder/$TiO_2$ co-deposited thin film showed a change in morphology to plate like particles 20nm in size.

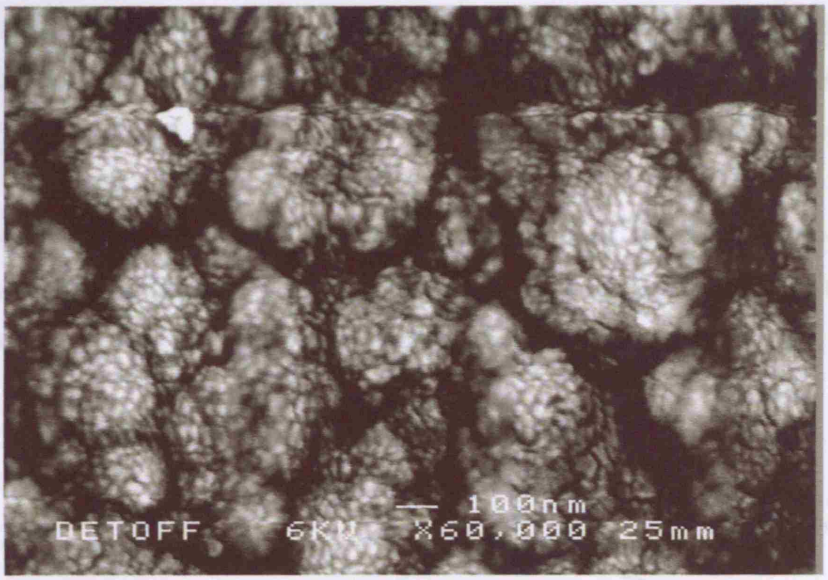


Figure 124. Transparent ZnO thin films deposited from ZnO nanopowder. A particle size of approximately 15 nm is observed.

The ZnO nanopowder/$TiO_2$ thin films synthesized in this study displayed enhanced photocatalytic activity compared to titania and were both active photocatalysts and showed photo-induced super-hydrophilicity. The zinc oxide nanopowder thin films readily destroyed a stearic acid overlayer at a rate of $6.6 \times 10^{12}$ molecules $cm^{-1}min^{-1}$ using 254 nm. This rate is enhanced compared to that of the ZnO thin films deposited from $[Zn(acac)_2]$[293]. The rate was further enhanced for ZnO nanopowder-$TiO_2$ thin films were the stearic acid overlayer was destroyed at a rate of $8.4 \times 10^{12}$ molecules $cm^{-1}min^{-1}$. This shows that addition of ZnO nanoparticles enhances the photocatalytic activity of titania films.

The contact angles for water droplets on the ZnO nanopowder-$TiO_2$ thin films were 8-10°, indicating that the surface is hydrophilic. This contact angle dropped further to 2-3° on exposure of the surface for 0.5 h to 254-nm radiation. On keeping the samples in the dark for 24 h the contact angle increased to 8°, and on further irradiation decreased again to between 2–3°. These compare well with the control experiment carried out with titania.

The reflectance/transmittance studies showed high interference patterns for the reflectance (Figure 125). The films transmitted at 65 - 75% across the spectrum and reflected at 20 - 35 %.

The Swanepoel method was used to determine film thickness. Here, all peaks and troughs were measured and tabulated in an Excel spreadsheet. A series of calculations then enabled a film thickness of 1067.5 nm for ZnO nanoparticle/titania anatase thin films to be estimated.

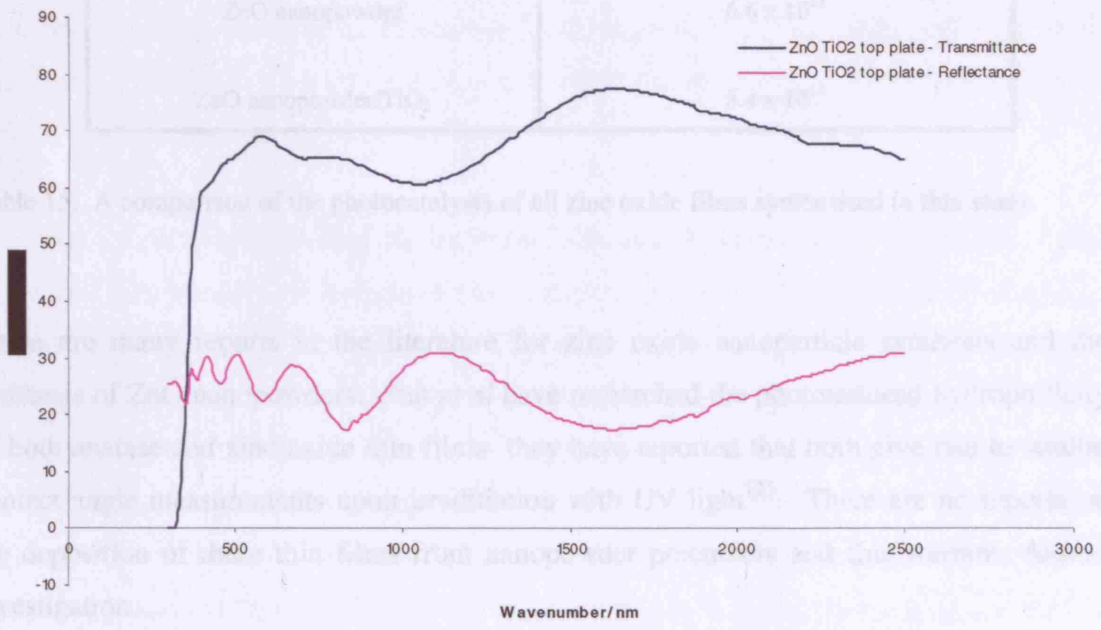


Figure 125. Reflectance/transmittance data for a ZnO nanoparticle/$TiO_2$ thin film. This film was deposited from zinc oxide nanopowder and titanium isoproxide at 450 °C.

## 10.7 Discussion

This work shows that addition of ZnO nanoparticles greatly enhances the photocatalytic activity of titania films. Table 15 shows the stearic acid degradation rate for the films deposited in this study. The highest degradation rate was for the zinc oxide nanopowder and zinc oxide nanopowder/titania thin films on glass. It is thought that the enhanced rate of catalysis at the nanoscale contributes towards this photocatalytic efficiency.

| Film type | Degradation rate / molecules $cm^{-1}min^{-1}$ |
|---|---|
| ZnO | $1.8 \times 10^{12}$ |
| Au nanoparticle/ZnO | $5.3 \times 10^{12}$ |
| ZnO nanopowder | $6.6 \times 10^{12}$ |
| ZnO nanopowder/$TiO_2$ | $8.4 \times 10^{12}$ |

Table 15. A comparison of the photocatalysis of all zinc oxide films synthesised in this study.

There are many reports in the literature for zinc oxide nanoparticle synthesis and the synthesis of ZnO nanopowders. Sun *et al* have researched the photoinduced hydrophilicity of both anatase and zinc oxide thin films- they have reported that both give rise to similar contact angle measurements upon irraditiation with UV light[123]. There are no reports on the deposition of these thin films from nanopowder precursors and this warrants further investigation.

Previously, researchers have studied zinc oxide thin films as transparent conducting devices[116]. Here aluminium, indium or zinc are added to induce n-doping which in turn results in oxygen vacancies and increased conductivity. Zinc oxide films can be doped with fluorine, boron, gallium and indium[117]. Magnetron sputtering has deposited aluminum,

gallium, and indium doped zinc oxide films[118]. Atmospheric pressure metal-organic chemical vapor deposition can also incorporate aluminium into a growing ZnO film[119].

ZnO layers are mainly deposited by sputter deposition and chemical vapor deposition (CVD)[120]. The latter method allows the growth of a rough layer, which has applications in solar cells as this allows the efficient diffusion of light by scattering. On the other hand, crystalline ZnO films with very smooth surfaces have also been deposited by sputtering (Zhu et al)[293]. In this thesis, an aerosol mist was successfully used to transfer the precursors onto the glass substrate depositing uniform nanoparticulate thin films.

## 10.8 Conclusion

Aerosol assisted chemical vapour deposition (AACVD) was used to deposit zinc oxide thin films and ZnO/$TiO_2$ composites. In addition ZnO nanopowders were transferred on to glass, depositing a thin film and also subsequently incorporated within a $TiO_2$ host matrix by aerosol assisted chemical vapour deposition.

No work has yet been published on the aerosol assisted chemical vapour deposition of zinc oxide thin film matrices incorporating nanoparticles. Here, AACVD was used to deposit a range of different zinc oxide thin films. This route also enabled films of Au nanoparticles within a host zinc oxide matrix to be grown from a solution of auric acid and zinc acetate to enhance the colour and impart some useful optical properties to the zinc oxide matrix. In addition ZnO nanopowder was transferred on to glass, depositing a thin film and also subsequently incorporated within a $TiO_2$ host matrix. This was completed to impart the useful properties exhibited by zinc oxide nanoparticles to a titania host matrix and to fine tune properties already known for titania, in particular to improve the optical, photocatalytic and photo induced super hydrophilicity of the titania thin films. Furthermore, one of the key aims was to develop a new and novel method for transferring semiconductor nanoparticles using solid nanoparticulate starting materials as precursors for

the formation of thin films. This would allow important technologocial advances, particularly for the deposition of zinc oxide thin films.

The ZnO thin films were transparent with uniform transparency (80%) across the substrate. Previously, zinc oxide has been used to grow thin films that are highly transparent (>80 %) and conductive as compared to commercial rivals such as fluorine doped tin oxide films[113]. Hence this report ties in well with the results researched in the literature. Another useful property shown by the films in this thesis is that they did not change colour upon exposure to UV light[115].

The Au nanoparticle/ZnO composite thin films however despite being transparent, showed a fusion of green, yellow and purple/blue interference colours. The zinc oxide nanoparticle composite titania thin films were also transparent with rainbow interference fringes due to the differing thickness across the substrate.

Addition of Au nanoparticles to the ZnO host matrix increased the photocatalytic efficiency of the matrix and yielded contact angles comparable to titania. This shows potential as an optical window coating since the thin films produced showed interesting colour combinations. It is thought that the greater activity is due to the generation of free radical and ionic species; the greater free radical and ionic presence contributes to the enhanced photocatalytic rate for titania anatase.

The concentration of gold in these films could be widely tuned, and the optical properties could of these films tailored according to application. Both these films and the films deposited in this study display enhanced optical properties, surface plasmon resonance effects and metal like reflectivity and this has great potential for use as optical window coatings, self cleaning glass and other applications of photocatalysis mentioned in Chapter 1. This research not only improves the optical, photocatalytic and photo induced super hydrophilicity of the zinc oxide and titania host thin films but also the colour. Furthermore, a new and novel approach was adapted by using solid nanoparticulate starting materials as precursors for the formation of thin films.

# Chapter 11: Conclusion

This research project explored the new idea of depositing nanoparticles within a host thin film in order to improve properties such as photocatalytic efficiency, solar control properties, colour, durability, thermochromic response and photo-induced super hydrophilicity. The primary aim of the project was to test these functional properties and the growth morphology imparted by the secondary nanoparticulate phase; particularly the effects of combinations of the bulk material and nanoparticles. In order to achieve this, new thin film deposition methods were developed, namely an aerosol assisted transport technique and an aerosol into atmospheric pressure chemical vapour deposition system.

Aerosol assisted chemical vapour deposition (AACVD) was used to deposit eight series of thin films on glass. Five different nanoparticles were tested to successfully deposit thin films incorporating nanoparticles within a host matrix; silver, gold, ceria, tungsten oxide and zinc oxide nanoparticles. These nanoparticle types were each unique with their own interesting chemistry. The nanoparticle preparations reported in this thesis were easy to prepare, inexpensive, non-toxic and available in a wide range of compositions that could yield a variety of doped metal oxide thin films. In general, it was found that the nanoparticles agglomerated into larger units, so protecting groups and capping agents were used throughout this study to aid stable dispersions.

Silver nanoparticles are important industrial materials due to their anti-bacterial properties. In chapter 3, silver nanoparticle/titania thin films were researched to test a number of important factors- photocatalytic activity which is imperative to enable the effective degradation of bacteria, photo-induced super hydrophilicity, optical properties and more importantly, to test the interesting colour combinations of silver nanoparticles and titania. It was found that silver nanoparticles greatly enhanced the photocatalytic activity and water contact angles for a titania thin film. Furthermore, these films allowed a yellow tint to be imparted into a titania thin film. As expected, silver nanoshaped thin films exhibited interesting optical properties due to the tuneable surface plasmon resonance bands. However some agglomeration of the rods, rectangles

and cubes did occur and this is something for researchers to build upon for future investigations.

A new combined chemical vapour deposition method was developed using simultaneously aerosol assisted and conventional atmospheric pressure chemical vapour deposition. A number of experimental designs were tested and it was found that the concentric tubing transport method was by far the more efficient design for co-transferring the aerosol and atmospheric pressure flows from two separate sources. The apparatus was designed 'in-house' and may allow incorporation into float glass production lines as the aerosol set up can be integrated into current APCVD coaters used in commercial glass production lines. This could allow commercialisation of the interesting optical and functional properties of a range of nanoparticles for use in window coating applications.

It was proven that preformed gold nanoparticles can be transported in an aerosol generated ultrasonically, and deposited into a growing film alongside transport of the titania precursor by APCVD. The Au/$TiO_2$ films formed in this process give rise to unusual optical properties, appearing red in reflected light and the Au nanoparticles depositing as nanocubes. The Au nanoparticle/ $TiO_2$ thin films were photoactive and superhydrophilic. These films showed unusual microstructures - gold nanocubes incorporated within the titania host matrix - not obtained by sol-gel or evaporation routes. Furthermore, the high reflectance generated by these films means they have potential for solar control applications. These films displayed enhanced optical properties, surface plasmon resonance effects and metal-like reflectivity and this has great potential for use as an optical window coating, self-cleaning glass and other applications of photocatalysis mentioned in Chapter 1.

Extensive research through this project has enabled the conclusion that many solid phase nanoparticles can be transferred into an adhesive thin film provided that they can be dissolved/suspended in an appropriate carrier solvent. It is thought that in some cases, the nanoparticulates tuned the morphology of the thin film yielding highly unusual microstructures. The use of solid nanoparticulate starting materials as precursors for the formation of thin films is therefore technologically important and warrants further research.

The preparation, morphology and structure study of $WO_3$ nanoparticle and titania films using preformed commercially available solid $WO_3$ was compared to conventional chemical vapour deposition routes. This generated thin films with growth rates of 3 - 7 $\mu m\ hour^{-1}$ and conformal coverage of the substrate. Hence this growth process has the potential to form thin films of material from involatile nanoscaled solid precursor and so a molecular volatile precursor is not required. Another benefit is that the nanopowder used did not require the use of charged or ligand stabilized materials and capping groups e.g. thiols. Furthermore, all films were very adhesive and superhydrophillic. Titania films formed in the presence of $WO_3$ nanoparticles showed unique morphology in addition to exhibiting photocatalysis and photoinduced super hydrophilicity. The initial water contact angles of these films were considerably lower than that seen for $TiO_2$ films prepared in the absence of nanoparticles and is attributed to the highly porous microstructure. This indicates that these nanoparticle incorporated host matrix thin films show promise as intelligent window coatings. The $WO_3$ nanoparticle incorporated titania thin films display properties which could be used in anti-misting applications.

This idea was also tested for zinc oxide since it is an important thin-film material that is used in a wide range of applications such as photocatalysis, varistor technology and sensing. Previously, no work has been published on the aerosol assisted chemical vapour deposition of zinc oxide thin film matrices incorporating nanoparticles. Here, the aerosol assisted chemical vapour deposition of zinc oxide thin films from zinc acetate powder was completed. This route also enabled films of Au nanoparticles within a host zinc oxide matrix to be grown from a solution of auric acid and zinc acetate. To extend this study further, ZnO nanopowder was transferred on to glass, depositing a thin film and also subsequently incorporated within a $TiO_2$ host matrix. This was completed to impart the useful properties exhibited by zinc oxide nanoparticles to a titania host matrix and to fine tune properties already known for titania, in particular to improve the optical, photocatalytic and photo-induced super hydrophilicity of the titania thin films. Furthermore, one of the key aims was to develop a new and novel method for transferring semiconductor nanoparticles using solid nanoparticulate starting materials as precursors for the formation of thin films. This allows important potential technological advances, particularly for the deposition of

zinc oxide thin films. All films exhibited interesting microstructures which could not be obtained by sol-gel or evaporation routes.

Addition of Au nanoparticles to the ZnO host matrix increased the photocatalytic efficiency of the matrix and yielded contact angles comparable to titania. This shows potential as an optical window coating since the thin-films produced showed interesting colour combinations. It is thought that the greater activity is due to the generation of free radical species; the greater free radical presence contributes to the enhanced photocatalytic rate for titania anatase. This work also shows that addition of ZnO nanoparticles greatly enhanced the photocatalytic activity of titania films. Furthermore, the concentration of gold in these films could be widely tuned, and the optical properties of these films tailored according to application. Hence by using a commercial solid nanoparticulate powder as a CVD precursor, it has been proven that nanoparticulate adherent-thin films can be synthesised, and that the presence of these nanoparticles can affect the surface morphology of the host matrix. This allows important technological advances, particularly for the deposition of thin films.

Thin films of $CeO_2$ nanoparticles were successfully deposited and thereafter $CeO_2$ nanoparticles were incorporated into a titania host matrix. The approach adopted here was to show that the as made nanoparticles can be transported by an aerosol in an AACVD process and that the films formed were composed of essentially the same nanoparticles that went into the initial process. In the $TiO_2/CeO_2$ deposition it was proven that preformed nanoparticles from solution could be embedded into a host matrix thin-film by using a conventional CVD precursor. This technique is different to those currently used to form nanoparticulate thin films and will have widespread applicability to a range of thin films. Furthermore the nanoparticulate cerium oxide thin films show marked photo-induced superhydrophilicity and good photocatalytic performance for the destruction of a stearic acid overlayer. There are conflicting reports on the photoactivity of ceria in the literature, but in this thesis, numerous repeat photocatalysis tests were carried out to ensure the reproducibility of the positive result. Therefore $CeO_2$ shows promise as a both as a photocatalyst and for use in solar control window coatings and merits further investigation and is a very promising material for future. Moreover, its high refractive index and excellent transmission in the visible and infrared regions will allow its application as a successful window coating. Furthermore

ceria is mechanically stable i.e. adhesive and stable against mechanical abrasion, chemical attack and high temperatures.

Thin films of $Fe_2O_3$ nanoparticles attract interest due to their technological and fundamental importance, such as information storage. Previously, little work has been completed on the aerosol assisted deposited of iron oxide nanoparticles and their subsequent incorporation into a host titania matrix. In this study, the properties of aerosol assisted chemical vapour deposition (AACVD) deposited $Fe_2O_3$ nanoparticle thin films on glass were investigated and thereafter thin films of $Fe_2O_3$ nanoparticles incorporated into a host $TiO_2$ matrix deposited. This allowed greater control over the optical properties of the thin films on glass, enhanced the reflectance-transmission properties, reduced the haze associated with the coating and improving on the coating colour. Interestingly, these films displayed enhanced photo-induced super-hydrophilicity compared to titania; the initial water contact angles of these films are lower than that seen for $TiO_2$ films prepared in the absence of nanoparticles and is attributed to the presence of $Fe_2O_3$ nanoparticles. The contact angle is probably a consequence of the surface being both partially hydroxylated and hence able to hydrogen bond effectively to the water, and having high porosity engendered by having a very fine microstructural form of nano-scaled particles. This shows potential for applications making use of the magnetic properties of iron oxide thin films and also for anti-misting optical coatings. Another interesting application would be for colour- where the tone of the thin film can be tuned to a transparent yellow colour.

Vanadium dioxide has been popular in the literature for some time now, due to the tuneable semiconductor to metal phase transition. Here, a number of ideas were tested to importantly, improve the colour of the vanadium oxide, the reflectance/transmittance properties, and induce a surface plasmon resonance effect to the host matrix through the use of gold nanoparticles.

In this research, gold nanoparticles were doped into a composite vanadium dioxide host matrix in order to decrease the transition temperature, enhance the optical properties and improve the coating colour. Au nanoparticle/$VO_2$ thin films were successfully deposited on glass by aerosol assisted CVD. Gold nanoparticles were incorporated into

a $VO_2$ host matrix by aerosol assisted chemical vapour deposition. The purpose of this study was limited to the preparation of Au nanoparticle doped $VO_2$ thin films and the influence of varying the Au/V molar ratio upon optical switching properties. Both ideas are new and have not been reported in the literature; vanadium dioxide was first deposited using AACVD by Parkin *et al* and there are no reports on doping a vanadium dioxide host matrix with nanoparticles by AACVD. Previously, metallic gold has been doped into the vanadium dioxide host matrix by the sol-gel process and a reduction in the thermochromic temperature to 49 °C resulted. In this thesis, addition of gold nanoparticles to the vanadium dioxide matrix greatly enhanced thermochromic, optical, colour and photocatalytic properties; the composite films formed show three useful functional properties – photocatalysis, enhanced optical properties and some significant reduction in thermochromic switching temperature by 37 °C. It also shows that composite films of this kind do not interfere with the functionality of each individual component and that solid solutions are not formed. Furthermore the improvement in the colour of the vanadium oxide host matrix by the gold nanoparticles has important industrial potential. Additionally, aerosol assisted chemical vapour deposition was used to deposit these thin films, and this technique is easily incorporated into float glass production lines. These film properties have excellent potential for future applications as window coatings and warrant further research in this class of coatings.

It was decided to explore these properties with the presence of a titania phase within the matrix. It is possible that the presence of titania will allow greater control of the tuning of the vanadium dioxide host matrix properties and perhaps allow the transition temperature to be modified by the doping effects of the gold nanoparticles. The aerosol assisted chemical vapour deposition of both $TiO_2/VO_2$ and $TiO_2/VO_2$ composite thin films with embedded nanoparticulate Au particles and their optical switching properties were reported. The aim was to assess whether or not the amounts of gold in the $TiO_2/VO_2$ host matrix altered the colour, optical properties and thermochromic switching properties of the host matrix. The films were deposited via the AACVD reaction of vanadium acetate, titanium isopropoxide and auric acid. The composite films formed show enhanced photocatalysis, photo-induced superhydrophilicity and a reduction in the thermochromic switching temperature to 47 °C. The photocatalysis for a $VO_2/TiO_2$ thin film is less than a pure CVD prepared anatase $TiO_2$ thin film – about

40% of the activity. This level of activity scales exactly with the titania content of the film. Although this photoactivity is relatively low it is still sufficient for self-cleaning action. It should be noted that gold nanoparticles significantly enhanced the photo catalytic activity of composite vanadium dioxide/titania thin films.

All nanoparticulate and nanoparticle/composite films gave interesting colour properties. The silver films imparted a yellow colour to the titania matrix, the gold colours reflected red and transmitted blue. This colour was also imparted to the vanadium oxide, titania and zinc oxide host matrices. This was particularly important for developing vanadium dioxide coatings with improved colour for applications as optical window coatings. In this thesis the vanadium dioxide colour was tuned to blue/purple/red. Silver nanorectangles and nanorods, gave a bottle green colour, and further work could be carried to impart this colour to the desired host matrix. $Fe_2O_3$ nanoparticles also gave a deep orange colour which was transferred as to titania whilst maintaining the transparent nature of the thin film.

The thin films reported in this thesis gave some unusual microstructures. In particular the titania films deposited in the presence of tungsten oxide nanoparticles gave striking needle and oval growth rather like a "wedding cake" structure. Interestingly, silver nanorectangles and micron sized rods were also deposited- these retained their shape upon transfer to the glass substrate. Surprisingly, in Chapter 4, spherical gold nanoparticles converted to nanocubes and in Chapter 8 and 9, gold nanocubes were deposited from auric acid. This suggests that certain CVD dynamics favour formation of gold nanocubes as compared to spherical nanoparticle deposition. It is thought that cube formation occurs either whilst the aerosol mist undergoes transformation to gaseous intermediate species or upon deposition/nucleation on the glass substrate.

Iron oxide/titania composite and also titania films deposited in the presence of tungsten oxide nanoparticles gave rise to very low initial contact angles and marked decrease in contact angles upon irradiation with both 365 and 254 nm UV light. Both films exhibited contact angles of less than 1° and it is thought that these low contact angles arise from the very fine and porous microstructure exhibited by both films types.

All other thin film types exhibited photo-induced hydrophilicity at a level comparable to titania. It should be noted that gold nanoparticles significantly enhanced the photo catalytic activity of composite vanadium dioxide/titania, zinc oxide and titania thin films. Silver nanoparticles however showed the greatest photocatalytic activity and also greatly enhanced the rate of photocatalysis for titania and this is comparable to literature reports.

The metallic nanoparticles in particular showed improved optical properties due to their tuneable surface plasmon resonance band. Changes in the shape, size and concentration of all films improved the reflectance/transmittance, particularly for gold nanoparticle/$VO_2$ thin films that showed heat mirror properties. The silver nanoparticle thin film surface plasmon resonance peak was investigated by using spherical particles and rectangular shapes. Gold nanocube thin films were also deposited, and generally, changing the shape of the nanoparticles allowed the extension of the surface plasmon resonance tail into the infra-red. The surface plasmon resonance bands were relatively strong as compared to the starting nanoparticle solutions, since there is a scale down to the thin film, which is only a few hundred microns in thickness. The nanoparticle thin film and nanoparticle/host matrix thin film UV surface plasmon resonances bands were also comparable with no marked decrease in the intensity of the bands upon incorporation into a host matrix.

Furthermore, all films deposited with gold nanoparticles, appeared red in reflected light and exhibited metal like reflectivity. Films deposited with silver nanoparticles however, were not so reflective.

The aerosol assisted chemical vapour deposition process yielded crystalline thin films, except where the deposition temperature was at 400 °C for titania anatase thin film deposition (crystalline anatase is deposited at higher deposition temperatures). Generally all films deposited in this thesis showed a transmission ranging from 30-80 %. The highest transmission was for zinc oxide related films and also ceria related thin films, where the maximum of the range was observed. Generally these films showed minimal haze.

All nanoparticle/host matrix composite films were adhesive, and in some instances, the top layers of the nanoparticle alone films could be wiped off. The majority of nanocomposite films passed the Scotch tape test, which is an important finding for future industrial applications. Furthermore all nanocomposite films were stable against chemical attack and high temperatures. Storage of the films over a period of 12 months did not result in a change in the composition, structure or physical properties and characteristics of the thin films.

The deposition parameters used were industrially acceptable; a temperature range of 400 – 575 °C was used, flow rates were 0.1 – 2 $Lmin^{-1}$ to deposit all nanocomposite thin films on glass. This allowed for a greater range of precursors usage for high quality deposition at low costs. Deposition rates were generally high, due to the high mass transport rate. Furthermore, a more flexible environment was used since AACVD operates at atmospheric pressure. Good stoichiometric control of the thin films was obtained and generally there was a good transfer of the nanoparticle/precursor amounts to the thin film comparable to the original precursor ratios used with little or no carbon contamination. Deposition of films in Chapters 4, 8 and 9 resulted in gold nanocube formation- this was due to complex reactor dynamics. Deposition of composite thin films from synthesised nanoparticle solutions also gave a good transfer of the nanoparticles to the thin film on glass- in a few cases nanoparticle growth did occur, but the majority of nanoparticles were transferred intact with slight agglomeration. All nanocomposite films covered atleast 2/3 of the glass substrate so good coverage was obtained overall.

Furthermore, this thesis used delivery methods not previously reported for nanocomposite thin films on glass- there are no reports on the aerosol assisted deposition of preformed solid nanoparticles. In this work, solid tungsten oxide and zinc oxide preformed nanopowders were used to deposit both nanoparticle and nanoparticle/metal oxide thin films. This is technologically important since nanopowders can be used as purchased in order to deposit a thin film by aerosol assisted chemical vapour deposition. The new combined chemical vapour deposition method was developed using simultaneously aerosol assisted and conventional atmospheric pressure chemical vapour deposition. This new process will allow commercialisation of the interesting optical and functional properties of a range of nanoparticles for use in

window coating applications. Moreover, auric acid was a new CVD precursor used in this research, first introduced very recently by Parkin *et al* and it has been proven through this work that auric acid can be used dissolved in a number of solvents for successful incorporation of gold nanoparticles into a host thin film.

The commercial applications of nanoparticle/host matrix thin films have been studied by many research groups, but this has mainly been using a non-CVD based process. CVD has the advantage of being incorporated into industrial float glass lines. In general, the use of both semiconductor and metallic nanoparticles enhanced the properties of the host matrices investigated in this thesis; titania, vanadium dioxide and zinc oxide. The two new processes developed, namely the combined aerosol assisted and atmospheric pressure CVD set up and aerosol assisted transport- were effective in transferring both the nanoparticles and the precursors to deposit composite films that contained nanoparticle films. Both the zinc oxide and tungsten oxide nanopowders were successfully transferred to glass and also incorporated within a titania host matrix. This result has not been reported in the literature. Furthermore, prior to this research there are no reports using an aerosol assisted chemical vapour deposition process to deposit mixed nanocomposite thin films. This thesis reported the deposition of nanocomposite thin films using a range of different nanoparticles.

In conclusion, the ideas, chemistry and methods explored in this thesis have potential for technological impact for the future. Extending this work further would provide insights for industry.

## References:


1) www.ngimat.com/technology/ccvd.html
2) www.solgel.com
3) Handbook of Physical Vapour Deposition *By* Donald M Mattox
4) Taken from Troy Manning's PhD thesis, University of London 2004, with permission
5) Aerosol Assisted Chemical Vapour Deposition *By* Kodas and Hampden-Smith
6) Taken from Warren Cross' PhD thesis, University of London 2002, with permission
7) Protective Coatings and Thin Films *By* Peter B Barna
8) www.pilkington.com
9) C. Park, J. Huang, M. Huang and T. Aderson, *Thin Solid Films*, 2002, **409**, 88
10) The Science of Crystallisation *By* William A Tiller
11) Chemical Vapour Deposition For Microelectronics *By* Arthur Sherman
12) www.iue.tulien.ac.at/phd/fleischmann/node70.html
13) The Chemistry of Metal CVD By T Todas and M Hampton Smith, VCH, New York, 1994
14) C. Park, J. Huang, M. Huang and T. Anderson, *Thin Solid Films*, 2002, **409**, 88
15) The Chemistry of Non-Metal CVD By W Rees Jnr, VCH, New York 1996
16) Photo taken in the materials research laboratory
17) www.wikipedia.org/wiki/nanotechnology
18) www.thenakedscientist.com/html/content/interviews/interview/4391
19) ao.osa.org/abstract.cfm?id=83871
20) www.ici.com
21) L.S. Moon and G. Chao, *Materials Science and Engineering C*, 2004, 24, 301
22) www.kimforesight.gov.uk
23) Y. Peng, X. Lu and J Luo, *Journal of Tribology,* 2004, **126**, 347
24) R. Messler, *Assembly Automation,* 2003, **23(2)**, 130
25) en.wiki.books.org/wiki/Nanotechnology/top_down_and_bottom_up_approaches
26) Nanoparticles: From Theory to Application *By* Gunter Schmid
27) http://www.nanomat.de.english/dalenblaether/12000.htm
28) www.nanosic.com.au/index.php.a=industry_focus.consumer
29) W. Zhang, L. Li, S. Yao and G. Zheng, *Corrosion Science*, 2007, **49**, 654

30) www.materialstoday.com/pdfs_7_2/warheit.pdf

31) K. Lin, H. Cheng, H. Hsu, L. Lin and W. Hsieh, *Chemical Physics Letters*, 2005, **409**, 208

32) Semiconductor and Metal Nanocrystals *By* Victor I Klimov

33) I. Bedja, P. Kamat, *Journal of Physical Chemistry B*, 1999, **103**, 8410

34) Nanoparticles: Synthesis, Properties and Applications *By* Springer Berlin, Heidelberg

35) Y. Wang and H. Yang, *Chemical Communications,* 2006, **25**, 45

36) Nanoparticles and Nanostructured Films *By* Janos H Fendler

37) F. Bensebaa, N. Patrito, Y. Page and D. Wang, *Journal of Materials Chemistry,* 2004, **14**, 3378

38) K. Kuwana and K. Saito, *Carbon,* 2005, **43(10)**, 2088

39) E. Wolf, *Journal of Physical Chemistry B*, 2001, **105**, No 5

40) The Chemistry of Nanostructured Materials *By Peidong Yang*

41) K. Fukushit and T. Sato, *Environmental Science and Technology*, 2005, **39(5)**, 1250

42) J. Zhang, X .Li, K. Lui and B. Zhao, *Journal of Colloid and Interface Science,* 2002, **255**, 115

43) M. Faraday, *Philos. Trans. R. Soc. London,* 1857, **147**, 145

44) J. Turkevich and G. Kim, *Science*, 1970, **169**, 873

45) S. Link, M. El-Sayed, *International Reviews in Physical Chemistry,* 2000, **38**, 409

46) www.nims.go.jp/heavyion/English/e_tutorial/tutorialnano.htm

47) www.en.wikipedia.org/wiki/surface_plasmon_resonance

48) www.users.path.ox.ac.uk/~vdmerwe/internal/spr.pdf

49) M. Garcia, J. Dela Verta, P. Grespo and J Llopis, *Physical Review B*, 2005, **72**, 2414

50) W. Weber and S. McCarthy, *Physical Review B*, 1975, **12**, 5643

51) J. Zia, L. Huang, J. Zhao, Y. Wang, Y. Zhao and L. Ha, *Materials Science and Engineering B*, 2005, **15**, 199

52) Z. Jian, H. Liqing, W. Yongchang and L. Yimin, *Physica E: Low Dimensional Systems and Nanostructures*, 2004, 25, 114

53) J. Turkevich, P. Stevenson and J. Hiller, *Discussion Farday Society*, 1951, **11**, 55

54) www.en.wikipedia.org/wiki/gold

55) X. Xu, M. Hen and C. Mirkin, *Angewandte Chemie International Edition*, 2007, **46**, 3468

56) www.geo.ucalgary.ca

57) Photo taken at the Materials Research Laboratory, UCL

58) L. Limsavam, V. Sritaveesinsub and S. Dubas, *Materials Letters,* 2007, **61**, 3048

59) Nanoparticles and Nanostructured Films: Preparation, Characterisation and Applications *Edited By* Janos H Fendler

60) R.G. Palgrave and I.P Parkin, *Journal of the American Chemical Society*, 2006, **128**, 1587

61) www.tyndall.ie/research/ams-group/aerosol.ppt

62) E. Gyorgy, G. Sauthier and A. Figueras, *Journal of Applied Physics,* 2006, **100**, 14302

63) C. Baker, A. Pradhan, L. Pakstis and S. Shah, *Journal of Nanoscience and Technology*, 2005, 5 244

64) smarteconomy.typepad.com

65) A. Hoonacker and P. Englebienne, *Current Nanoscience,* 2006, **2**, 359

66) Y. Sun and Y. Xia, *Science*, 2002, **13**, 2176

67) The Effect of Viscosity and Kinetics on Formation of Silver Nanoparticles *By* D.O. Shah and B.S. Parmar

68) Y. Mari and N. Masami, *Journal of Materials Chemistry*, 2003, **13**, 2064

69) J. Prashant and T. Pradeep, *Biotechnology and Bioengineering*, 2005, **90**, 59

70) www.patentstorm.us/patents-by-date/2003/1028-41.html

71) www.patentstorm.us/patents/5397485_description.html

72) K. Page, R. Palgrave and I. P. Parkin, *Journal of Materials Chemistry*, 2007, **17**, 95

73) adsabs.havard.edu/abs/2004SPIE.5520.206G

74) www.piers.mit.edu/piersonline/pdf/vol1NO6page634to637.pdf

75) H. Lee, S. Yeo, and S. Jeong, *Journal of Materials Science*, 2003, **38**, 2199

76) L. Wang, J. Luo, M. Maye, Q. Fan, Q. Rendeng, M. Engelhard and Y. Lin, *Journal of Materials Chemistry,* 2005, **15**, 1821

77) S. Sun, C.B. Murray, D. Weller, L. Folks and A. Moser, *Science*, 2000, **287**, 1989

78) M. Mikhaylova, D. Kim, N. Bobrysheva and M. Muhammad, *Langmuir*, 2004, **20**, 2472

79) S.H. Sun and H. Zeng, *Journal of the American Chemical Society,* 2002, **124**, 8204

80) B. Pal and M. Sharon, *Thin Solid Films,* 2000, **379**, 83

81) C. Lin, T. Liedl, R. Speling and H. Chang, *Journal of Materials Chemistry*, 2007, **17**, 1343

82) Figure adapted from Semiconductor and Metal Nanocrystals *By* Victor I Klimov

83) en.wikipedia.org/wiki/cerium(IV)_oxide

84) www.testbourne.co.uk

85) B. Eldrisci, M. Addou and C. Monty, *Thin Solid Films*, 2000, **379**, 23

86) R.P. Netterfield, W.G. Saintry, P.J. Martin and S.H. Sie, *Applied Optics,* 1985, **24**, 2267

57) T. Ami, Y. Yoshida, N. Nagasawa, A. Machida and M. Suzuki, *Applied Physics Letters*, 2001, **78**, 1361

88) G.R. Bamwenda, K. Sayama, H. Arakawa, *Chemical Letters*, 1996, **30**, 157

89) J.M. Coronado, A. Maira, A. Martinez, A. Arias, J. Carlos Conesa and Javier Soria, *Journal of Photochemistry and Photobiology A,* 2002, Chemistry **150**, 213

90) M.S. Al-Robaee, K.N. Rao and S. Mohan, *Journal of Applied Physics*, 1992, **71**, 2380

91) I. Kosacki, T. Suzuki, H. Anderson and P. Colomban, *Solid State Ionics*, 2002, **149**, 99

92) I. Porqueras, C. Person, C. Corbella, M. Vives, A. Pinyol and E. Bertran, *Solid State Ionics*, 2003, **165**, 131

93) D. Eyidi, M. Croitoni, O. Eibl and W. Prisseit, *Materials Research Society*, 2003, **18**, 14

94) M. Pan, G. Meng, H. Xin and C. Chen, *Thin Solid Films*, 1998, **324**, 89

95) A. Wang and T. Golden, *Journal of the Electrochemical Society,* 2003, **150**, 616

96) J. Kurian and M. Naito, *Physica C,* 2004, **402**, 31

97) I. Porqueras, C. Person and E. Bertran, *Thin Solid Films,* 2004, **447**, 119

98) P.M. Woodward, A.W. Sleight, T. Vogt, *Journal of Physical* Chemistry, 1995, **56**, 1305

99) P.M. Woodward, A.W. Sleight, T. Vogt, *Journal of Solid State* Chemistry, 1997, **131**, 9

100) T. Vogt, P.M. Woodward and B.A. Hunter, *Journal of Solid State Chemistry*, 1999, **144**, 209

101) C. G. Granqvist, *Solid Energy Material Solar Cells*, 2000, **60**, 201

102) G. Hallinger and T. Duc, *Physics Review Letters*, 1976, **37**, 1564

103) S. Bugaev, A.N. Zakharov and K. Oskomov, *Russian Physics Journal*, 1996, **39**, 395

104) S.H. Lee, H.M. Cheong, C.E. Tracy, A. Macarenhas, A.W. Czanderna and S.K Debb, *Applied Physics,* 1999, **75**, 1541

105) A.R.West, Basic Solid State Chemistry, 2nd Edition, 1999

106) A.G. Filno, J. Filno, V. Freire, A. Ayala and F. Melo, *Journal of Raman Spectroscopy,* 2001, **32**, 695

107) M. Sun, N. Xu, Y. Cao and J. Yao, *Materials Research Society,* 2000, **15**, 927

108) Photo taken of AACVD synthesised $WO_3$

109) H. Funk and G. Mohaupt, *Z.Anorg. Allg. Chem,* 1962, **315**, 204

110) R. Palgrave and I.P. Parkin, *Journal of the American Chemical Society,* 2006, **30**, 505

111) W. Run amd J. Wu, *Materials Science and Engineering A*, 2002, **328**, 196

112) A.P. Alivisatos, *Science,* 1996, **271**, 933

113) B.T. Khuri-yakub, G.S. Kino, and P. Gallo, *Journal of Applied Physics,* 1975, **46**, 3266

114) R. Groenen, J. Loffler, J. Lindler, R. Schropp and M. Van de Sanden, *Thin Solid Films*, 2005, **492**, 298

115) M.N. Kamalasanan, *Thin Solid Films,* 1996, **288**, 112

116) H Cheng, C Chen and C Tsay, *Applied Physics Letters,* 2007, **90**, 012113

117) E. Fortunato, A. Marques, H. Aguas and R. Martins, *Thin Solid Films*, 2004, **45**, 443

118) Y. Zhou, P.J. Kelly and O. Abu-Zeid, *Thin Solid Films*, 2004, **447**, 33

119) J.T. Sujino, N. Homma and Y. Abe, *Thin Soild Films,* 2002, **407**, 86

120) J.S. Kim, H.A. Marzouk, P.J. Rencroft and C Hamrin, *Thin Soild Films,* 1992, **217**, 133

121) S. Zhu, C.H. Su, S.L. Lehouzky, P. Peters and M.A. George, *Journal of Crystal Growth,* 2000, **211**, 106

122) www.nanowerk.com/spotlight/spotid=912.php

123) R. Sun, A. Nakajima, T. Watanabe and K Hashimoto, *Journal of Physical Chemistry B,* 2001, **105**, 1984

124) http://www.azom.com/details.asp?articleID=1179

125) www.en.wikipedia.org.wiki/anatase

126) www.ruby.Colorado.edu

127) T. Xu and C. Song, *Science*, 2006, **7(4)**, 299

128) H. Choi, E. Stathatos and D. Dionysiou, *Desalination*, 2007, **207**, 395

129) K. Hashimoto, H. Irie and A. Fujishima, *Japanese Journal of Applied Physics,* 2005, **44**, 8269

130) $TiO_2$ Photocatalysis Fundamentals and Applications *By* A. Fujishima, K. Hashimoto and K. Watanabe, Tokyo: BKC, Inc, 1999

131) Sequence adapted from Ashti Rampauls' PhD, University of London 2007, with permission

132) A. Granqvist, *Thin Solid Films,* 1990, **193**, 730

132) N.F. Mott, *Review of Modern Physics*, 1968, **40**, 677

133) D. Adler, *Review of Modern Physics,* 1968, **40**, 714

134) F.J. Morin, *Physics Review Letters,* 1959, **3**, 34

135) F.J. Morin, *Physics Review Letters,* 1959, **14**, 54

136) Y. Sato, T. Nomura, H. Tanka and K. Kobayakawa, *Journal of the Electrochemical Society,* 1991, **138**, 37

137) Taken from Troy Manning's PhD thesis, University of London 2004, with permission

138) A.S. Barker, H.W. Verleur and H.J. Guggenheim, *Physics Review Letters,* 1996, **17**, 26

139) H.S. Choi, J.S. Ahn, J.H. Jung and T.W. Noh, *Physical Review B,* 1996, **54**, 4621

140) www.solgel.com/articles/August00/thermo/Guzman.htm

141) T.D. Manning and I.P. Parkin, *Journal of Materials Chemistry,* 2004, **14**, 2554

142) J.B. Goodenough, *Journal of Solid State Chemistry*, 1971, **3**, 490

143) D. Adler, *Physical Review*, 1967, **155**, 826

144) T. Christmann, B. Felde, W. Neissner, D. Schalch and A Scharmann, *Thin Solid Films,* 1996, **287**, 134

145) W. Burkhardt, T. Christmann, B.K. Meyer, W. Neissner, D. Schalch and A. Scharmann, *Thin Solid Films,* 1999, **345**, 229

146) M. Gupta and A.J. Freeman, *Physical Review B*, 1997, **16**, 3338

147) A. Zylbersztejn, *Physical Review B*, 1975, **11**, 4383

148) Taken from Troy Manning's PhD thesis, University of London 2004, with permission

149) Chemical Vapour Deposition, By M.L. Hitchman and K.F. Jensen

150) The CVD of Thin Films, By W.S. Rees, Jr

151) I.P. Parkin and T.D. Manning, *Journal of Materials Chemistry*,

152) T. Maruyama and Y. Ikuta, *Journal of Materials Science,* 1990, **28**, 5073

153) F. Guinneton, L. Sauques, J.C. Valmalette and F. Cross, *Thin Solid Films*, 2004, **446**, 287

154) F. Beteille and J. Livage, *Journal of Sol Gel Science and Technology*, 1998, **13**, 915

155) F. Beteille, R. Morineau and J. Livage, *Materials Research Bulletin*, 1997, **32**, 1109

156) T.J. Hanlon, J.A. Coath and M. Richardson, *Thin Solid Films,* 2003, **436**, 269

157) T.J. Hanlon, R. Walker, J.A. Coath and M. Richardson, *Thin Solid Films,* 2002, **405**, 234

158) E. Cavanna, J. Segaud and J. Livage, *Materials Research Bulletin,* 1999, **34**, 167

159) www.opticsjournal.net:9999/getarticle.aspx?id=13812

160) I.P. Parkin and T.D. Manning, *Journal of Materials Chemistry*, 2002, **12**, 2936

161) W. Burkhardt, *Thin Solid Films*, 2002, **402**, 226

162) Precursors for Electronic Materials By P.O. Brien, D. Bruce and D. O'Hare, J. Wiley, London 1996, 523

163) www.azom.com/details.asp?articleID=1552

164) www.mrs.org/s_mrs/sec_subscribe.asp?CID=2735&DID=155680&action=detail

165) Taken from Troy Manning's PhD thesis, University of London 2004, with permission

166) www.ees.ufl.edu/homepp/cywu/ENV6130/materials%20synthesis.pdf

167) http://patentstorm.us/patents/6883724-description.html

168) Taken from Warren Cross' PhD thesis, University of London 2002, with permission

169) Taken from Troy Mannings' PhD thesis, University of London 2004, with permission

170) Taken from Russel Binions' PhD thesis, University of London 2005, with permission

171) http://faculty.uscs.edu/cbender/nl0341178.pdf
K. Caswell, C.M. Bender, C.J. Murphy, *Nanoletters*, 2003

172) N. Jana, L. Geaheart and C. Murphy, *Chemical Communications*, 2001, **21**, 617

173) T.C. Deivaraj, N.L. Lala and J.Y. Lee, *Journal of Colloidal Science*, 2005, **289**, 402

174) J. Zhu, C. Kan, X. Zu, J. Guo, M. Hon and G. Wang, *Materials Research Society*, 2007, **6**, 1479

175) J. Park and E. Lee, *Angewandte Chemie*, 2005, **44**, 2872

176) S. Yamamuro, T. Ando, K. Sumiyamai, T. Uchida and I. Kojima, *Japenese Journal of Applied Physics,* 2004, **43 7A**, 4458

177) rruff.geo.Arizona.edu/rruff

178) K. Page and I.P. Parkin, *Journal of Materials Chemistry*, 2007, **17**, 95

179) A. Sarkar, S. Kapoor and T. Mukherjee, *Journal of Colloid and Interface Science,* 2005, **287**, 496

180) X. Yang, Y. Su, *Materials Letters*, 2005, **59**, 2484

181) F. Liu, P. Huang, Y. Chang, C. Ko and T. Chu, *Journal of Crystal Growth*, 2005, **273**, 439

182) J. Mock, M. Barbic, D. Smith, D. Schultz and S. Schultz, *The Journal of Chemical Physics*, 2002, **116**, 6755

183) J. Zhu, L. Huang, J. Zhao, Y. Wang, Y. Zhao, L. Ho and Y. Lu, *Materials Science and Engineering B*, 2005, **121**, 199

184) Y.H. Chee, R.P. Rooney, R.F. Howe and P.A.W. van der Heide, *Journal of Raman Spectroscopy*, 1992, **23**, 243

185) The Material Science of Thin Film *By* M. Ohring

186) D. Shchukin, E. Ustinovich, D. Svindov and P. Pichat, *Photochemical and Biological Sciences,* 2004, **3**, 142

187) A. Vohra, D. Goswami, D. Deshpade and S. Block, *Journal of Industrial Microbiology and Biotechnology,* 2005, **32**, 364

188) S. Senthi-Kumar, K. Porkodi, R. Gomathi, G. Maheswari and N. Manonmani, *Dyes and Pigments*, 2006, **69**, 22

189) H.E. Chao, Y. Yun and H. Xingfang, *Journal of the European Ceramic Society*, 2003, **23**, 1457

190) S. Rengaraj and X.Z. Li, *Journal of Materials Catalysis A: Chemical*, 2006, **2**, 60

191) C. He, Y. Yu, X. Hu and A. Larbot, *Applied Surface Science,* 2002, **200**, 239

192) H.E. Chao, Y.U. Yun, H.U. Xingfang and A. Larbot, *Journal of the European Ceramic Society,* 2003, **23**, 1457

193) S.W. Ryu, E.J. Kim, S.K. Ko and S.H. Hahn, *Materials Letters*, 2004, 58, 582

194) T. Klar, T.M. Perner, S. Grosse, G. Von Plessen, W. Spirkl and J. Feldman, *Physical Review Letters*, 1998, **80**, 4249

195) R. Salvati, A. Longo, S. Nicola, G. Pepe, N. Nicolais and A. Barone, *Applied Surface Science*, 2005, **248**, 28

196) S. Chattopadhyay and A. Datta, *Synthetic Metals*, 2005, **155**, 365

197) D. Lim, I. Lopez-Salido, R. Dietsche and Y. Kim, *Surface Science*, 2006, **600**, 507

198) H. Chowdhury, X. Xu, P. Huyah and M. Cortie, *Journal of Solar Energy Engineering*, **127**, 2005, 70

199) J. Lim, R. Titon, A. Eggeman and S. Majetch, *Journal of Magnetism and Magnetic Materials,* 2007, **311**, 78

200) H. Masai, T. Fujiwara and H. Mori, *Applied Physics Letters*, 2007, **90**, 907

201) R.G. Palgrave and I.P Parkin, *Journal of the American Chemical Society,* 2006, **128**, 1587

202) K.R. Brown and M.J. Natan, *Langmuir*, 1998, **14**, 726

203) G. Silver-Smit, G. De Doncker and R. De Gryse, *Surface Science Spectra*, 2002, **9**, 21

204) Z. Pinter, Z. Sassi, S. Kornely, Ch. Pion, I.V. Perczel, R. Bene and F. Reti, *Thin Solid Films,* 2000, **391**, 243

205) S. Nagamine and E. Sasaoka, *Journal of Porous Materials*, 2002, **9**, 167

206) R. Wang, K. Hashimoto, A. Fujishima, A. Kitamura and T. Watanabe, *Thin Solid Films,* 1999, **351**, 260

207) Nanoscale Materials *By* L.M. Liz-Marzan and P.V. Kamat

208) H. Takele, U. Schurman, H. Creve and F. Fauret, *European Physical Journal-Applied Physics,* 2006, **33**, 83

209) K. Liu, *Nanotechnology*, 2005, **16**, 3006

210) G. Fang, Z. Liu, C. Sun and K. Yao, *Physica Status Solidi (A)*, 2001, **184**, 129

211) P.M Woodward, A.W. Sleight, J. Voight, *Journal of Physical Chemistry Solid, 1995, **56**, 1305*

212) C. Blackman and I.P. Parkin, *Chemistry of Materials, 2005, **17**, 1583*

213) R. Diehl, G. Brandt and E. Saije, *Acta Crystallographica Section B*, 1978, **B34**, 1105

214) S. O'Neill, I.P. Parkin, R. Clark, A. Mills and N. Elliot, *Journal of Materials Chemistry*, 2003, **13**, 56

215) R. Chein and W. Liao, *Heat and Mass Transfer*, 2005, **42**, 71

216) A.C. Larson and R.B. Van Dreele, "General Structure Analysis System (GSAS)". Los Alamos National Laboratory Report LAUR, 2000, 86-748

217) A. Mills, A. Lepre, N. Elliott, S. Bhopal, I.P. Parkin and S.A. O'Neill, *Journal of Photochemistry and Photobiology A*, 2003, **160**, 185

218) www.chem.lsu.edu/htdocs/people/SFWatkins/ch4570/lattices/lattice.html

219) S.A. O'Neill, I.P. Pakin, R.J.H Clark, A. Mills and N. Elliot, *Journal of Materials Chemistry,* 2003, **13**, 56

220) K.L. Choy, *Progress in Materials Science,* 2003, **48**, 57

221) A. Fuishima, T. Rao and D. Tryk, *Electrochimica Acta*, 2000, **45**, 4683

222) T. Sumita, H. Otsuka, K. Kubota, M. Nagata, Y. Honda and Y. Miyagawa, *Nuclear Instruments and Methods in Physics Research B,* 1999, **148**, 758

223) C.V. Romana, R.C. Ewing and V. Becker, *Journal of Physics B,* 2006, **110**, 10430

224) T. He, Y. Ma, Y. Cao, W. Yang and J. Yao, *Journal of Electroanalytical Chemistry,* 2001, **514**, 129

225) S. Badilescu and P. Ashrit, *Solid State Ionics*, 2003, **158**, 187

226) http://science24.com/paper/11316

227) S. Pavasupree, Y. Suzuki, S. Pivsa-Art and S. Yoshikawa, *Journal of Solid State Chemistry,* 2005, **178**, 128

228) R. Toro, G. Malandrino and I. Fragala, *Journal of Physical Chemistry B,* 2004, **108**, 16357

229) Raman Scattering in Materials Science *By* H. Willes

230) M. Miyauchi, A. Nakajima, T. Watanabe and K Hashimoto, *Chemistry of Materials,* 2002, **14**, 2812

231) J. Coronado, A. Mavier, A. Martinez-Arias, J. Conesa and J. Soria, *Journal of Photochemistry and Photobiology A: Chemistry,* 2002, **150**, 213

232) A. Fujishima, T.N. Rao and D. Tryk, *Journal of Photochemistry and Photobiology,* 2000, **1**, 1

233) M. Qi, Z. Bao-Zhu, Z. Zhi-Qiang and R. Jian-Guo, *Yingyong Huagong,* 2005, **34(3)**, 153

234) H. Yang, K. Zhang, K.Shi and A. Tang, *Journal of the American Chemical Society,* 2007, **90**, 1370

235) C.T Campbell and C.H.F. Peden, *Science*, 2005, **309**, 713

236) S. Amirhaghi, I. Boyd and Y. Li, *Materials Science and Engineering B,* 1995, **34**, 192

237) www.sciencemag.org/cgi/content/full/sci;309/5735/713

238) A. Trovarelli, *Catal. Rev. Sci. Eng*, 1996, **38**, 439

239) J. Lin and J.C. Yu, *Journal of Photochemistry and Photobiology A,* 1998, **63**, 116

240) J. Kurian and M. Naito, *Physica C,* 2004, **402**, 31

241) I. Porqueras, C. Person and E. Bertran, *Thin Solid Films,* 2004, **447-448**, 119

242) K.C. Krogman, T. Druffel and M. Sunkara, *Nanotechnology,* 2005, **16**, 338

243) G.R. Bamwenda, K. Sayama and H. Arakawa, *Chemical Letters*, 1996, **30**, 157

244) R.P. Netterfield, W.G. Saintry, P.J. Martin and S.H. Sie, *Applied Optics*, 1985, **24**, 2267

245) T. Feng and J.M. Vohs, *Journal of Catalysis*, 2004, **221**, 619

246) S. Sun and C.B. Murray, *Journal of Applied Physics,* 1999, **85**, 4325

247) M. Giersig and M. Hilgendorff, *Journal of Applied Physics D,* 1999, **32**, 111

248) C. Petit, A. Taleb and M.P. Pileni, *Journal of Physical Chemistry B,* 1999, **103** 1805

249) S. Sun, C.B. Murray, D. Weller, L. Folks and A. Moser, *Science*, 2000, **287**, 1989

250) L. Guo, Q. Huang, X. Li and S. Yang, *Physical Chemistry and Chemical Physics*, 2001, **3**, 1661

251) www.eng.uc.edu/~gbeaucag/classes/XRD/SathishScherrer/SathishScherrerEqn.html

252) T. Sumita, H. Otsuka, K. Kubota, M. Nagata, Y. Honda and Y. Miyagawa, *Nuclear Instruments and Methods in Physics Research B*, 1999, **148**, 758

253) P. Tartaj, M.D. Morales, S. Veintemillas-Verdaguer and T. Gonzalez-Carreno and C. J. Serna, *Journal of Physics D- Applied Physics,* 2003, **36**, 182

254) L. Wang, J. Luo, M. Maye, Q. Fan and Q. Rendeng, *Journal of Materials Chemistry,* **15**, 1821

255) Y. Hida and H. Kozuka, *Thin Solid Films,* 2005, **476**, 264

256) R. Goswami, G. Kioseoglou, A.t. Hanbicki and G. Spanos, *Applied Physics Letters,* 2005, **86**, 032509

257) J. Gu, J. Shi, L. Xiong, H. Chen and M. Ruan, *Microporous and Mesoporous Materials*, 2004, **74**, 199

258) W. Wang, G. Yang, Z. Chen, Y. Zhou and H. Lu, *Journal of Applied Physics,* 2002, **92**, 7242

259) E. Cavanna, J. Segaud and J. Livage, *Materials Research Bulletin,* 1999, **34**, 167

260) E. Cavanna, J. Segaud and J. Livage, *Materials Research Bulletin,* 1999, **34**, 167

261) A. Magneli and G. Andersson, *Acta Chemistry Scandinavia*, 1995, **9**, 1378

262) K.D. Rogers, *Powder Diffraction*, 1993, **8**, 240

263) P. Mulvaney, *Langmuir*, 1996, **12**, 788

264) www.webelements.com/webelements/text/auindex.html

265) www.wulixb.phy.ac.cn/en.cn/common/create_pdf.aspx?file_no=200706378&flag=1

266) A.G. Aranov, D.N. Mirlin, I.I. Reshina and F.A. Chudrovski, *Fiz Tverd Tela (Leningrad),* 1977, **19**, 193

267) J.C. Parker, *Physical Review B,* 1990, **42**, 3164

268) E. Cavanna, J. Segaud and J. Livage, *Materials Research Bulletin*, 1999, **34**, 167

269) T. Maruyama and Y. Ikuta, *Journal of Materials Science*, 1990, **28**, 5073

270) F. Beteille, R. Morineau and J. Livage, *Materials Research Bulletin*, 1997, **32**, 1109; G. Zhao, G. Han, M. Takahasi and T. Yoko, *Thin Solid Films*, 2002, **410**, 14; Y. Muraoka and Z. Hiroi, *Applied Physics Letters*, 2002, **80**, 583.

271) F.J. Morin, *Physics Review Letters*, 1959, **14**, 34

272) H.S. Choi, J.S. Ahn, J.H. Tung and T.W. Noh, *Physical Review B*, 1996, **54**, 4621

273) Chemical Vapour Deposition *By* M.L. Hitchman and K.F. Jemsen

274) I.P. Parkin and T.D. Manning, *Journal of Materials Chemistry,* 2002, **12**, 2936

275) J.P. Segaud, O. Giraudo, C. Indrigo, E. Cavanna and J. Livage, *Non-Linear Optics,* 1999, **34**, 167

276) A. Magneli and G. Andersson, *Acta Chemistry Scandinavia*, 1995, **9**, 1378

277) K.D. Rogers, *Powder Diffraction*, 1993, **8**, 240

278) J.C. Parker, *Physical Review B*, 1990, **42**, 3164

279) A.G. Aronov, D.N. Mirlin, I.I. Reshina and F.A. Chudrovski, *Fiz Tverd Tela (Leningrad),* 1977, **19**, 193

A.G. Aronov, D.N. Mirlin, I.I. Reshina and F.A. Chudrovski, *Soviet Physics Solid State (English translation),* 1977, **19**, 110

280) F. Theobold, R. Cabala and J. Bernard, *Journal of Solid State Chemistry*, 1976, **17**, 431

281) Practical Surface Analysis, 2nd edn., vol. 1 *By* C. D. Wagner
Auger and X-Ray Photoelectron Spectroscopy *By* D. Briggs and M. P. Seah, Wiley, Chichester, 1990

282) Nanoparticles and Nanostructured Films *By* Janos H Fendler

283) P. Mulvaney, *Langmuir*, 1996, **12**, 788

284) J. Lim, R. Tilton, A. Eggeman and S. Majetich, *Journal of Magnetism and Magnetic Materials,* 2007, **311**, 78

285) A. Schuler, D. Dutta and C. Roecker, *Solar Energy Materials and Solar Cells,* 2006, **90**, 2894

286) Y. Yang, J. Shi, W. Huang, S. Dai and L. Wang, *Journal of Materials Science*, 2003, **38**, 1243

287) F. Theobold, R. Cabala and J. Bernard, *Journal of Solid State Chemistry*, 1976, **17**, 431

288) E. Cavanna, J. Segaud and J. Livage, *Materials Research Bulletin,* 1999, **34**, 167

289) T. Maruyama and Y. Ikuta, *Journal of Materials Science*, 1990, **28**, 5073

290) S. Ren-De, N. Akira, W. Toshiya and H. Kazuhito, *Journal of Physical Chemistry B,* 2001, **105**, 1984

291) Y. Zeng, L. Juntao, W. Wei and C. Ding, *Surface Coatings and Technology*, 2005, **200**, 2398

292) G. Liu, X. Zhang, J. Xu, X. Niu, L. Zheng and X. Ding, 2004, **55(9)**, 1287

293) www.ias.ac.in/matersci/bmsjun2002/227.pdf